Evaluation of aerosol representation by ACCESS-CM2 with increased aerosol-chemistry complexity in the Southern Ocean

Imogen Wadlow 978348

Supervised by: Dr Robyn Schofield, Dr Matthew Woodhouse and Professor Todd Lane

Masters Research Report submitted as part of the M.Sc. degree in the School of Earth Sciences, University of Melbourne

Submitted 11/09/2020

I certify that this thesis contains less than 25,000 words.
Imogen Wadlow

Acknowledgements

Thank you firstly to my supervisors for providing me with the independence to follow my own ideas, invaluable discussions, guidance towards useful research tracks, and for their support and patience as I struggled through some difficult circumstances.

I would like to thank my supervisor, Robyn Schofield, for facilitating my berth on an Antarctic voyage for two months. Aside from fulfilling a lifetime dream to voyage South, acting as the caretaker for the types of instruments I would use in this thesis provided invaluable first-hand experience that assisted my interpretation of observational data.

Thank you to Scott Wales for the hours spent working through the endless errors that come with running a climate model. Progressing from no prior python knowledge to running multiple modified simulations of a fully coupled Global Climate Model was a steep learning curve, and one that I could not have achieved without Scott's help. Thank you also to the Centre of Excellence for Climate Extremes (CLEX) CMS team for helping me with coding problems and storage issues.

Thank you also to:
CLEX for providing me with a scholarship and funding to attend multiple conferences and workshops throughout my degree. Conversations at these conferences led to exciting directions in my research and the inclusion of new datasets.

The Rayner-Schofield research group for useful help, advice and companionship.

Ruhi Humphries, Joel Alroe, Luke Cravigan, Marc Mallet and the Southern Ocean research group for providing me with CCN and size distribution data, and valuable insight regarding their use.

Melita Keywood for providing Cape Grim CCN data.

Steve Wilson for providing Cape Grim AOD data.

Julia Schmale for providing ACE voyage CCN data.

Finally, my friends, family, office-mates and house-mates for keeping morale high. Writing a thesis in isolation during a pandemic lockdown was a daunting prospect, but your continued support has made this journey all the more enjoyable. Thank you also to my mother who found endless care to give despite her own battles with cancer this year.

Contents

1 Introduction **12**

1.1 Background to Aerosols . . . 12
1.2 Sources of Southern Ocean Aerosol . . . 12
1.3 Aerosol chemical composition . . . 14
1.4 Aerosol size . . . 15
1.5 Aerosol transformation processes . . . 16
1.5.1 Cloud Condensation Nuclei . . . 16
1.5.2 Chemical mechanisms and processes . . . 17
1.6 Aerosol effects on clouds and radiation . . . 20
1.7 Aerosol Optical Depth . . . 22

2 Aerosol Representation in Climate Modelling **23**

2.1 Previous modelling studies . . . 23
2.2 Implementation of more complex aerosol-chemistry schemes . . . 23
2.2.1 Primary Marine Organic Aerosol (PMOA) schemes . . . 23
2.2.2 Sea-salt schemes . . . 24
2.2.3 Online chemistry schemes . . . 25

3 Model description **25**

3.1 Aerosol & Chemistry schemes in ACCESS-CM2 . . . 26
3.1.1 GLOMAP . . . 26
3.1.2 Chemistry scheme . . . 27
3.1.3 Sea-salt emissions . . . 30
3.2 Previous model-observation evaluations . . . 30
3.2.1 AOD bias in previous aerosol-chemistry models . . . 31
3.2.2 CCN bias in previous aerosol-chemistry models . . . 32

4 Motivation **33**

4.1 Aims . . . 35
4.2 Significance and Innovation . . . 35
4.2.1 Evaluation of ACCESS-CM2 . . . 35
4.2.2 Focus on the Southern Ocean spatial domain . . . 35
4.2.3 Use of a comprehensive suite of ground-based observations for model evaluation . . . 36
4.2.4 Exploration of increased model complexity . . . 37

5 Methods: Running ACCESS-CM2 **38**

5.1 Model configuration . . . 38
5.2 Model simulation runs . . . 39
5.2.1 Model output . . . 42

6 Methods: Collection of observational data 43
6.1 Meteorological observations . . . 43
6.2 Chemical composition and particle size observations . . . 45
6.3 Aerosol Optical Depth observations . . . 46
6.4 Cloud Condensation Nuclei observations . . . 48
6.5 Radiation and Cloud Fraction observations . . . 49
6.6 Statistical analysis . . . 49

7 Results 52
7.1 Meteorological validation . . . 52
7.1.1 Wind speed: . . . 52
7.1.2 Wind direction . . . 56
7.2 Model Chemistry . . . 59
7.2.1 Chemical species . . . 59
7.2.2 Oxidation pathways . . . 65
7.3 Size distributions . . . 70
7.3.1 Comparison of simulated size-distributions . . . 70
7.3.2 Comparison against observational size distribution . . . 73
7.3.3 Seasonal simulated size distributions . . . 75
7.4 Evaluation of Aerosol Optical Depth . . . 79
7.4.1 Magnitude of AOD . . . 79
7.4.2 Relationship between wind-direction and AOD bias . . . 82
7.4.3 Relationship between wind-speed and AOD bias . . . 83
7.4.4 Seasonal representation of AOD . . . 86
7.4.5 Spatial representation of AOD . . . 88
7.4.6 Aerosol mode contribution to AOD . . . 92
7.4.7 Comparison against observational aerosol-mode AOD . . . 95
7.5 Cloud Condensation Nuclei . . . 98
7.5.1 Magnitude of CCN . . . 98
7.5.2 Seasonal representation of CCN . . . 101
7.5.3 Spatial representation of CCN . . . 104
7.6 Aerosol-chemistry interactions with cloud and radiation schemes . . . 107
7.6.1 Cloud Droplet Number Concentration . . . 107
7.6.2 SW TOA ↑ radiation . . . 109

7.6.3 Low Cloud Fraction . . . 114

8 Discussion of Research Questions 118

8.1 How well does ACCESS-CM2 represent aerosols over the Southern Ocean in terms of AOD and CCN bias? . . . 118

8.2 Does increasing the complexity of aerosol-chemistry schemes result in a more accurate representation of AOD and CCN? . . . 124

8.2.1 Implications for AOD bias . . . 124

8.2.2 Implications for CCN bias . . . 127

8.3 Can the overall radiation and cloud fraction bias in the Southern Ocean be improved through increasing the complexity of aerosol-chemistry schemes? 132

9 Conclusion 134

A Appendix 137

A.1 Köhler theory . . . 137

A.1.1 Calculation of AOD and CCN from model output . . . 137

A.2 Calculation of AOD in observations . . . 139

A.3 Measurement of AOD . . . 140

A.4 Model nudging . . . 141

A.5 A-factors . . . 142

A.6 Drawbacks of using ground-based observations . . . 143

A.7 Observational and simulated uncertainty . . . 144

A.8 Challenges facing observations in field campaigns . . . 146

A.9 Summary of observational ground-based datasets . . . 148

A.9.1 Summary of observational satellite datasets . . . 150

A.10 Observational data processing . . . 150

A.10.1 Introduced Statistical metrics; NMBF and NMAEF . . . 152

A.11 Meteorology . . . 153

A.11.1 Statistical summaries of simulated and observed wind-speed . . . 153

A.11.2 Land-Ocean Fraction as a source of simulated wind-speed bias . . . 157

A.12 Size distributions . . . 158

A.13 AOD . . . 160

A.13.1 Average simulated and observed AOD statistical comparisons . . . 160

A.13.2 Seasonal simulated and observed AOD statistical comparisons . . . 162

A.13.3 Relationship between wind-direction and AOD bias . . . 165

A.13.4 Simulated inter-annual variability of AOD . . . 167

A.13.5 Comparison of zonal simulated AOD against Revell et al. [2019] results . . . 169
A.14 CCN . . . 170
A.14.1 Average simulated and observed CCN statistical comparisons . . . 170
A.14.2 Probability Density Functions, Southern Ocean CCN . . . 173
A.14.3 Monthly mean CCN time-series, Cape Grim and Macquarie Island . 174
A.14.4 Seasonal simulated and observed CCN statistical comparisons . . . 175
A.15 CDNC, Radiation & Low Cloud Fraction . . . 180
A.15.1 Seasonal simulated CDNC statistical comparisons . . . 180
A.15.2 Seasonal simulated and observed SW TOA ↑ radiation statistical comparisons . . . 182
A.15.3 Seasonal simulated Low Cloud Fraction statistical comparisons . . . 184
A.15.4 Seasonal simulated and observed Low Cloud Fraction statistical comparisons . . . 186

List of Figures

1 Cape Grim aerosol sources . . . 13
2 Sea-salt aerosol generation mechanisms . . . 13
3 Schematic of aerosol size distributions . . . 15
4 Modes of aerosol size distributions . . . 16
5 Spatial distribution of CCN . . . 17
6 Binary nucleation of H_2SO_4 . . . 18
7 Hoppel minimum . . . 19
8 Sources and transformations of aerosols . . . 20
9 Radiative climate forcing between 1750 and 2011 . . . 21
10 Global distribution of AOD at 550 nm . . . 22
11 Mode distribution of aerosols in GLOMAP . . . 27
12 AOD at 550nm for the period 2003-2006 . . . 32
13 Schematic of radiation biases in GCMs . . . 33
14 Mean errors on absorbed surface SW↓ radiation in CMIP5 climate models 34
15 Nighttime all-sky zonal mean 532nm aerosol extinction . . . 37
16 Cape Grim baseline sector . . . 44
17 Voyage tracks CAPRICORN II & I2E . . . 45
18 Location of Southern Ocean observation stations . . . 46
19 AERONET MAN Voyage Tracks . . . 47
20 ACE and MARCUS Voyage Tracks . . . 48

21 Southern Ocean seasonal observed and simulated wind-speed 53
22 Cape Grim wind roses 57
23 Macquarie Island wind roses 57
24 Seasonal concentration of modelled chemical species 62
25 Concentration of DMSO, OH, and HO_2 on two axes 63
26 Comparison of modelled sea-salt and observed Cl^-. 64
27 Seasonal and zonal distribution of gas-phase SO_2 oxidation flux 66
28 Zonal distribution of simulated SO_2 and OH concentrations 67
29 Seasonal cycles of simulated aqueous sulfur oxidation 68
30 Zonal distribution of aqueous sulfur oxidation 69
31 Zonal distribution of simulated H_2O_2 and O_3 69
32 Southern Ocean average modelled size distribution 72
33 Comparison of model size distribution and observations 74
34 Seasonal simulated nucleation-mode aerosol number density 76
35 Seasonal Southern Ocean average size distributions 77
36 Boxplot comparison of simulated and observed AOD 80
37 Probability Density Histograms of simulated and observed AOD 82
38 Cape Grim AOD pollution rose 83
39 Comparison of modelled AOD and wind-speed relationships 85
40 Seasonal cycles of observed and modelled AOD 87
41 PMO-enriched region location 88
42 Seasonal spatial AOD differences between simulations 89
43 MODIS-Aqua seasonal [chl-a 90
44 ACCESS-CM2 seasonal wind-speed output 92
45 Aerosol mode contribution to AOD boxplot 93
46 Stacked bar graph of AOD modal contributions 94
47 Annual cycle of observed and modelled fine and coarse mode AOD 96
48 Boxplot comparison of simulated and observed CCN 99
49 Probability density functions of simulated and observed CCN 101
50 Seasonal cycle of simulated and observed CCN 103
51 Seasonal spatial CCN differences between simulations 105
52 Comparison of simulated CDNC between models 108
53 Comparison of simulated SW TOA ↑ radiation 111
54 Comparison between simulated SW TOA ↑ radiation and CERES-EBAF observations. 113
55 Low cloud fraction differences between simulations 115
56 Comparison of simulated low cloud fraction and CALIPSO-GOCCP 116

57 Calculation of CCN from model output 138
58 Scattering efficiency of green light 140
59 Schematic of sun-photometer 141
60 Availability of AOD_{550nm} measurements in the SO 143
61 Land fraction of meteorological stations 157
62 Macquarie Island AOD pollution rose 165
63 Cape Grim Conditional Probability Function plot 166
64 Observed and simulated AOD inter-annual variability at Cape Grim 167
65 Observed and simulated AOD inter-annual variability at Macquarie Island 167
66 Observed and simulated AOD inter-annual variability at Amsterdam Island 168
67 Aerosol mode contribution to AOD, Cape Grim. 168
68 ACCESS-CM2-simulated zonal averages of AOD_{550nm} 169
69 HadGEM3-GA7.1-simulated zonal averages of AOD_{550nm} 169
70 Probability Density Function of simulated and observed CCN 173
71 Monthly-averaged timeseries of simulated and observed CCN 174
72 Simulated and observed inter-annual variability, Cape Grim 179
73 Simulated and observed inter-annual variability, Macquarie Island 179
74 Simulated and inter-annual variability averaged over the Southern Ocean . 180

Abstract

This thesis identifies the inherent biases of aerosol parameters within the next-generation Global Climate Model (GCM); the Australian Community Climate and Earth System Simulator Coupled Model (ACCESS-CM2). GCMs poorly represent clouds and aerosols over the Southern Ocean, resulting in systematic shortwave (SW) radiation biases with widespread global energy budget impacts. This research determines whether a more complex, physically-representative aerosol-chemistry scheme may reduce the Southern Ocean radiation bias, and the inherent aerosol biases established within ACCESS-CM2.

Southern Ocean aerosols are dominated by sea-salt and biogenic products. This study ran a control ACCESS-CM2 simulation and three perturbation simulations, which altered either the representation of Primary Marine Organic aerosols, sea-salt, or implemented a fully interactive chemistry scheme respectively. A suite of ground-based and satellite observations was collected and compared against each simulation to establish model bias respective to key aerosol metrics including Aerosol Optical Depth (AOD), Cloud Condensation Nuclei (CCN) and SW radiation. Simulation biases were explained through model-observation comparisons of aerosol chemistry, size and number parameters.

Overall, ACCESS-CM2 exhibited a substantial positive bias in Aerosol Optical Depth (AOD) and SW radiation, and underestimated Cloud Condensation Nuclei concentration. This research suggests that increasing the complexity of aerosol schemes was able to provide a closer model agreement with observed aerosol metrics of AOD and CCN. Fully interactive chemistry provided the best reduction in both AOD and CCN bias. However, modified aerosol schemes have negligible effects upon the inherent SW radiation bias in ACCESS-CM2, suggesting further research into cloud schemes is necessary.

Abbreviations

12E	Ice Edge to Equator (Voyage)
ACCESS	Australian Community Climate and Earth System Simulator
ACCMIP	Atmospheric Chemistry and Climate Model Inter-comparison Project
ACE	Antarctic Circumnavigation Expedition
ACI	Aerosol-Cloud Interactions
ACSM	Aerosol Chemical Speciation Monitor
AERONET	Aerosol Robotic Network
AOD	Aerosol Optical Depth
APS	Aerodynamic Particle Sizer
ARI	Aerosol-Radiation Interactions
CABLE	Community Atmosphere Biosphere Land Exchange
CALIPSO	Cloud-Aerosol Lidar and Infrared Pathfinder Satellite Observation
CALIPSO-GOCCP	GCM-Oriented CALIPSO Cloud Product
CAPRICORN	Clouds, Aerosols, Precipitation, Radiation, and Atmospheric Composition over the Southern Ocean
CCN	Cloud Condensation Nuclei
CDNC	Cloud Droplet Number Concentration
CERES-EBAF	Clouds and the Earth's Radiant Energy System - Energy Balanced and Filled
CFMIP	Cloud Feedback Model Inter-comparison Project
CheST	Chemistry for the Stratosphere and Troposphere
COSP	CFMIP Observation Simulator Package
CPF	Conditional Probability Function
DMS	Dimethyl Sulfide
DMSO	Dimethyl Sulfoxide
ERA-I	ERA-Interim
ERF	Effective Radiative Forcing
GCM	Global Climate Model
GLOMAP	Global Model of Aerosol Processes
IOA	Index Of Agreement
MARCUS	Measurements of Aerosols, Radiation and Clouds over the Southern Ocean
MBL	Marine Boundary Layer
MODIS	Moderate resolution Imaging Spectroradiometer
MSA	Methane Sulfonic Acid
NMAEF	Normalised Mean Absolute Error Factor

Continued on the next page...

NMB	Normalised Mean Bias
NMBF	Normalised Mean Bias Factor
NSS	Non Sea-Salt
OM	Organic Mass (OM_{frac} determines the Organic Mass Fraction)
PDF	Probability Density Function
PMO	Primary Marine Organic
PMOA	Primary Marine Organic Aerosol
RH	Relative Humidity
RMSE	Root Mean Square Error
SDA	Spectral Deconvolution Algorithm
SIC	Sea Ice Concentration
SMPS	Scanning Mobility Particle Sizer
SS	Super-Saturation
SSA	Sea-Salt Aerosol
SSP	Shared Socioeconomic Pathway
SST	Sea Surface Temperature
SW	Short-Wave
TOA	Top Of Atmosphere
UKCA	United Kingdom Chemistry and Aerosols

1 Introduction

1.1 Background to Aerosols

Aerosols, defined as a suspension of liquid or solid particles in a gas, play a significant role in numerous atmospheric processes in the Earth's climate. They interact with radiation and cloud processes and provide a surface which is important for many atmospheric chemical reactions. Aerosols are described as primary (emitted directly in particle form) or secondary (formed in the atmosphere by chemical, condensation or nucleation processes from precursor gases). Removal (also termed 'scavenging') mechanisms include wet and dry deposition; where smaller aerosols grow large enough to precipitate as raindrops (see Section 1.5), or are deposited to the ground as larger aerosols in the dry mechanism. Varying atmospheric lifetimes enable aerosols to be transported over large distances via wind advection [Winker et al., 2013], hence it is possible to observe continental aerosols over marine environments. During the transportation of aerosols, microphysical properties can change, including aerosol number, size, and volume concentrations. This results in large variations in aerosol distribution on spatial and temporal scales [Boucher, 2015].

1.2 Sources of Southern Ocean Aerosol

Primary aerosols dominate Southern Ocean aerosol populations. Aerosol composition analysis undertaken at a monitoring site representative of the Southern Ocean (Cape Grim, 40.6833°S, 144.6833°E), reported that the majority of fine particles (smaller than 2.5 μm in diameter) were dominated by sea salt (72%) and secondary sulfate aerosols (10%) [Crawford et al., 2017] (Figure 1). Sea-salt, originating from sea-spray aerosols (SSA), is produced from the bursting of bubbles at the ocean surface. These bubbles are generated from the interaction of wind stress and the ocean surface, often at wind speeds over approximately 4 ms^{-1} [Seinfeld and Pandis, 2016a] (see Figure 2 SSA generation description). SSA dominate global aerosol emissions, estimated between 1400-6800 $\mathrm{Tg\,y}^{-1}$, in comparison to natural emissions of dust which range from 1000-4000 $\mathrm{Tg\,y}^{-1}$ [Boucher, 2015, Lewis, 2004, Jaeglé et al., 2011a].

Unlike primary sea-salt aerosols, secondary aerosols may contain an organic element and are largely comprised of non-sea-salt (nss) sulfates. Secondary aerosols are largely produced by the oxidation of dimethylsulfide (DMS, CH_3SCH_3); a sulfur-containing species emitted from marine organisms. DMS is an important source of marine aerosols as it contributes ∼19% of global sulfur emissions [Carslaw et al., 2013] with an estimated flux of $15-32\,\mathrm{Tg\ yr}^{-1}$ [Elliott, 2009, Woodhouse et al., 2010]. Nss sulfates have both natural and anthropogenic sources, therefore Southern Ocean observations utilise sampling methods

to remove data with anthropogenic sources (described in Section 6.1 & Appendix A.13.3).

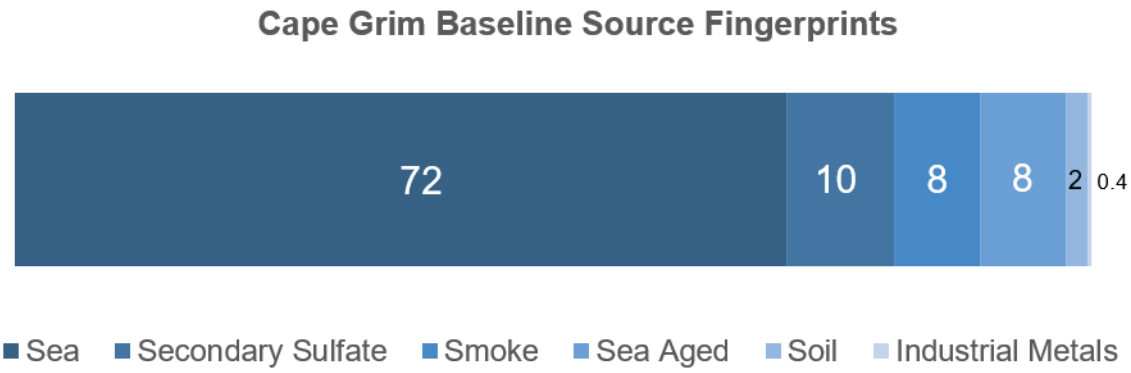


Figure 1: Source of aerosol fingerprints at Cape Grim (units in %). Adapted from Crawford et al. [2017]. Sea Aged = sea-sourced aerosols which have undergone chemical reactions over time.

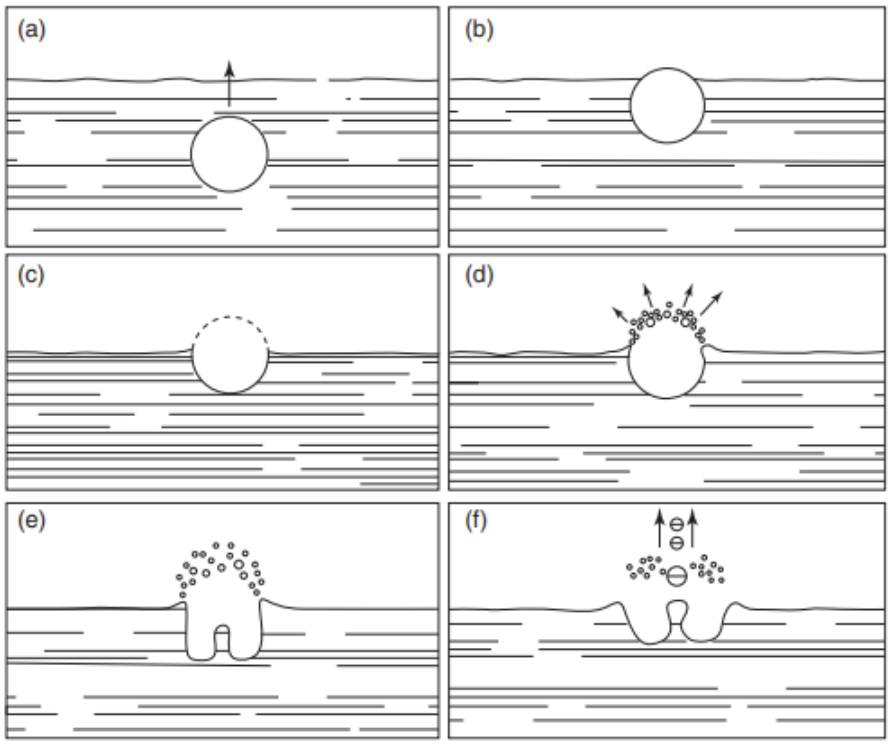


Figure 2: Schematic sequence of sea-salt aerosol generation through bubble-bursting mechanisms: (a) air bubble rises to the sea surface; (b) air bubble reaches the surface; (c) sea water film starts to break; (d) droplets form (~5-30 μm diameter) where the exposed portion of the bubble film bursts; (e) film droplets evaporate leaving sea-salt particles (with diameter >2 μm suspended; (f) larger droplets break away from the jet formed during bubble-bursting (in a size range ~15% of the bubble diameter). It is during this process that organic matter form part of the SSA. As a bubble rises in the water column, various hydrophobic molecules are attracted to the air-bubble interface which partition into the spray once the bubble reaches the surface [Seinfeld and Pandis, 2016a]

1.3 Aerosol chemical composition

The composition of aerosols has important implications for their microphysical, hygroscopic (the ability of aerosols to uptake water from the surrounding environment) and optical properties. These properties determine how aerosols interact in larger scale atmospheric processes (discussed in Section 1.5). Tropospheric aerosols have a diverse chemical composition and are dominated by sulfur species in the Southern Ocean. Most model aerosol schemes represent chemical composition through six categories summarised in Table 1 [Seinfeld and Pandis, 2016b].

SSAs which contain quantities of inorganic (e.g: sulfate, $SO_4{}^{2-}$) and organic matter (such as phytoplankton cell fragments and lipids) are termed Primary Marine Organic Aerosols (PMOA) [Gantt and Meskhidze, 2013]. Southern Ocean SSA studies have shown the average organic mass (OM) fraction (OM_{frac}) of SSA was approximately 10%, where OM_{frac} was largest at smaller aerosol diameters [Law et al., 2017, Middlebrook et al., 1998]. The distribution of PMOAs varies with time, areas of primary production and seasonality, where PMOA concentration increases in biologically-active summertime months [Gantt and Meskhidze, 2013].

Aerosol species	**Formation processes**	**Atmospheric lifetime**
Sulfate	*Primary:* emitted from volcanic and marine sources. *Secondary:* Oxidation of atmospheric SO_2 to H_2SO_4 and condensation/nucleation processes to particulate form.	1 week
Nitrate	Oxidation of NO_x	∼1 week
Black carbon	Emitted from combustion processes as soot.	7-10 days
Organic aerosols	*Primary:* Combustion of fuels & biomass, contintental & marine ecosystems). *Secondary:* Organic gas condensation.	1 week
Sea salt	Bubbles bursting in breaking waves	1 day − 1 week (size dependent)
Mineral dust	Natural erosion or industrial/agricultural processes	1 day − 1 week (size dependent)

Table 1: Summary of aerosol modes and properties as categorised by aerosol models. SO_4 = sulfate, BC = black carbon, OC = organic carbon, SS = sea salt, DU = dust. [Abraham et al., 2016]

1.4 Aerosol size

Particle size determines the effect of aerosols on clouds and radiation, and the microphysical processes that an aerosol is involved in (discussed in Section 1.5). Aerosols are categorised by size in four modes; nucleation, Aitken, accumulation and coarse. Within each mode, aerosols are described by solubility characteristics, soluble or insoluble. Aerosols may change modes with increasing size due to absorption of water by hygroscopic particles, or coagulation with other particles (see Figure 3). These processes are discussed in Section 1.5.

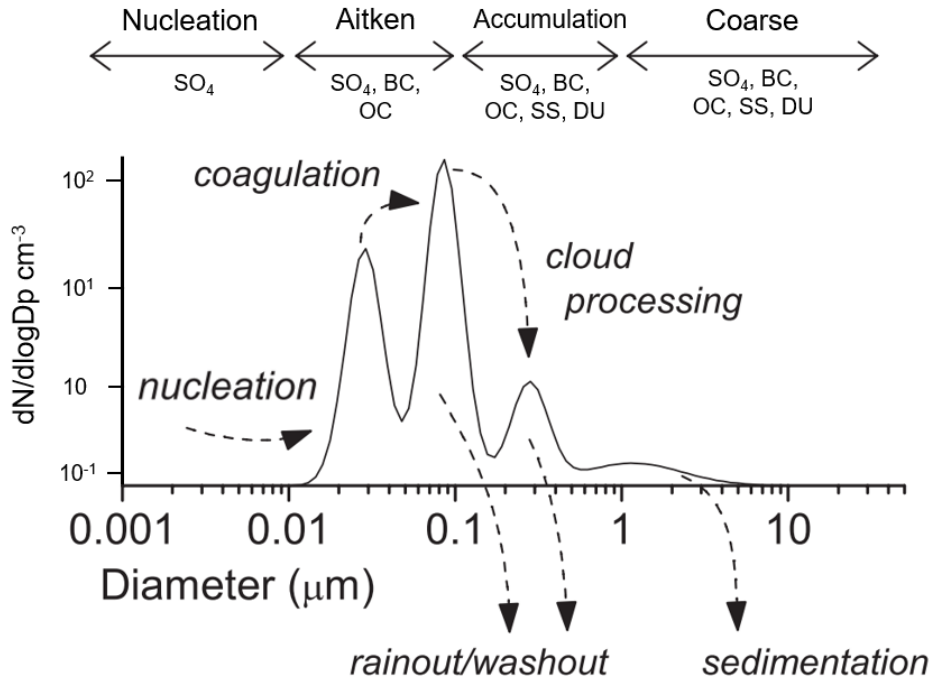


Figure 3: Schematic of aerosol mode size distribution. BC = Black Carbon, OC = Organic Carbon, SS = Sea Salt. PMOAs exist largely within the Aitken and accumulation modes, and SSA ranges between 0.05–10μm diameter and dominates the coarse mode [O'Dowd et al., 2004]. The units of size distribution on the y-axis, dN/dlogD cm^{-3} (or dN/dlogDp cm^{-3}) indicate the number of particles per micron per cm^3. The area integrated underneath the curves of the size distribution represents the total number of particles within the aerosol population. Image adapted from [Saltzman, 2013].

Accumulation and coarse aerosol modes account for the majority of atmospheric aerosol mass and volume, although the smaller Aitken and nucleation modes are more numerous (as shown in Figure 4). Size distribution is represented by the function $n(r)$ which represents the number of particles per unit volume whose radius is between r and $r + dr$. The total aerosol population can be obtained by integrating over the size distribution: $N_0 = \int n(r)dr$.

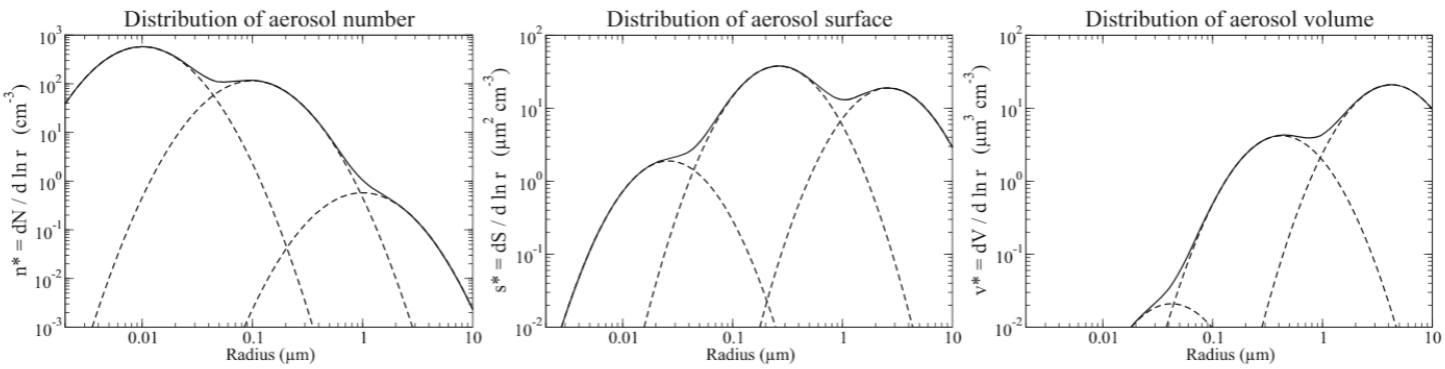


Figure 4: Schematic of three modes of aerosol size distribution, separated into fine (Aitken), accumulation and coarse modes [Boucher, 2015]. Aerosol modes are represented as three log-normal distributions with a mean geometric radius corresponding to the maximum diameter of the three modes (0.01, 0.1 and 1 μm) with a geometric standard deviation of 2. This diagram indicates how the fine mode dominates aerosol number distribution, accumulation mode dominates the aerosol surface area distribution and the coarse mode dominates the aerosol volume

1.5 Aerosol transformation processes

This section discusses how aerosols change in size and chemical composition through the processes identified in Figure 3; nucleation, coagulation, and cloud-processing.

1.5.1 Cloud Condensation Nuclei

To understand the role of aerosols in larger climate systems, we must first understand how aerosols interact with clouds. When an aerosol enters a region of elevated relative humidity (RH), it can grow to form a cloud droplet. This depends on numerous factors including the chemical composition, soluble matter content, size, shape and age of the particle [Seinfeld and Pandis, 2016a, Andreae and Rosenfeld, 2008]. These particles, termed Cloud Condensation Nuclei (CCN), are the subset of the total aerosol population that are activated to form cloud droplets. Aerosol activation occurs at and above a critical supersaturation value (SS) where an increasing number of particles become activated into CCN progressing from low to high SS [Andreae and Rosenfeld, 2008]. The concept of CCN is based in Köhler theory, which is described in Appendix A.1. CCN concentration varies from $<100\,\mathrm{cm}^{-3}$ in remote marine regions to many thousand cm^{-3} in polluted urban areas (see Figure 5 for spatial distribution).

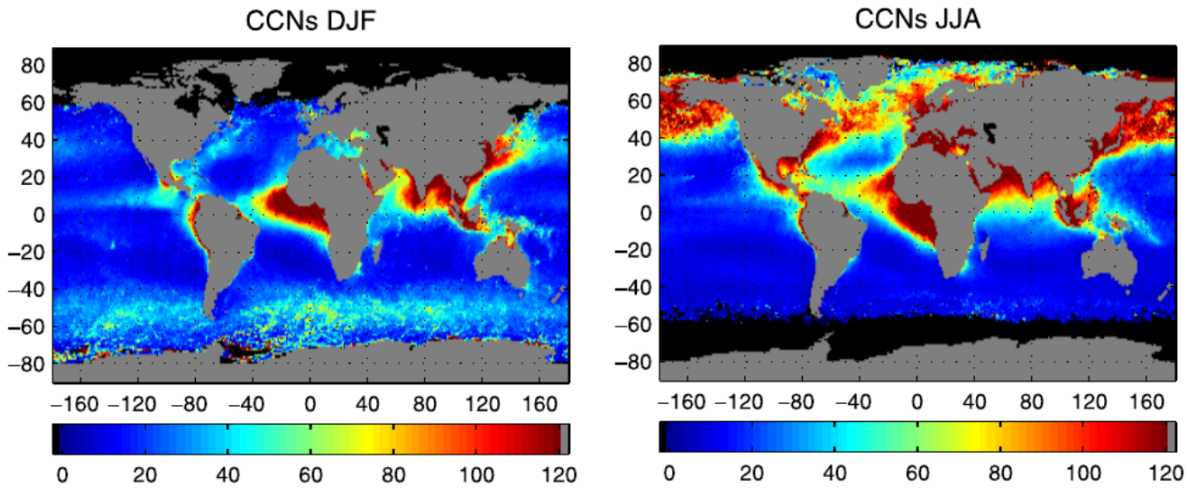


Figure 5: Global distribution of monthly climatological satellite-derived CCN concentrations (particles cm^{-2}), adapted from [Vallina et al., 2007].

For a constant liquid water content, increasing CCN concentration within a cloud-topped boundary layer generally results in an increase of cloud droplets (cloud droplet number concentration, CDNC). Natural aerosols contribute substantially to CDNC, accounting for over half of the spatiotemporal variability of observed CDNC [Mccoy et al., 2015a] The presence of PMOAs have complex interactions in the activation of aerosols into cloud droplets, and can facilitate or inhibit this process depending on the inorganic-organic chemical mixture [Ovadnevaite et al., 2011, 2017]. PMOAs can increase CCN concentration, as surfactants within the aerosols can lower the surface tension of nucleating cloud droplets and reduce the critical supersaturation required for CCN formation [Lowe et al., 2019] (see Appendix A.1 for details).

1.5.2 Chemical mechanisms and processes

Next, we outline the processes and transformations aerosols undergo in their lifetime to form clouds or leave the atmosphere through deposition processes (summarised in Figure 8). In Section 1.2, we identified the source of primary marine aerosols as wind-driven sea-spray. Secondary aerosols begin their life as precursor gases - in marine environments this is dominated by SO_2, which results from air/sea gas transfer of biologically-produced DMS. DMS is oxidised by OH (and to a lesser extent, NO_3) to produce SO_2, dimethyl-sulfoxide (DMSO), and methanesulfonic acid (MSA). The oxidation pathway that sulfate aerosols take has important implications for the aerosol size distribution and future chemical reactions. If DMS oxidises to SO_2, the pathway has the potential for gas-phase oxidation to sulfuric acid (shown in Equation 1). Sulfuric acid then provides the basis for new particle formation, shown in Figure 6.

$$
\begin{aligned}
DMS_{(g)} + OH_{(g)} &\longrightarrow SO_{2(g)} + CH_3O_2 + HCHO \\
DMS_{(g)} + OH_{(g)} &\longrightarrow SO_{2(g)} + DMSO + CH_3O_2 \\
SO_{2(g)} + OH_{(g)} &\longrightarrow H_2SO_{4(g)} + HO_{2(g)}
\end{aligned} \tag{1}
$$

H_2SO_4 condenses readily onto pre-existing particles resulting in particle size growth. In the absence of pre-existing particles, H_2SO_4 clusters with water-vapour to form new particles, a process known as binary nucleation (Figure 6). Mixing between the marine boundary layer (MBL) above the sea-surface and the free troposphere (FT) provides a source of precursor gases in the free troposphere where new particle formation occurs (in the nucleation mode). Entrainment of FT air masses provides the MBL with a source of secondary aerosols, and thus provides the main source of DMS-derived CCN [Merikanto et al., 2009].

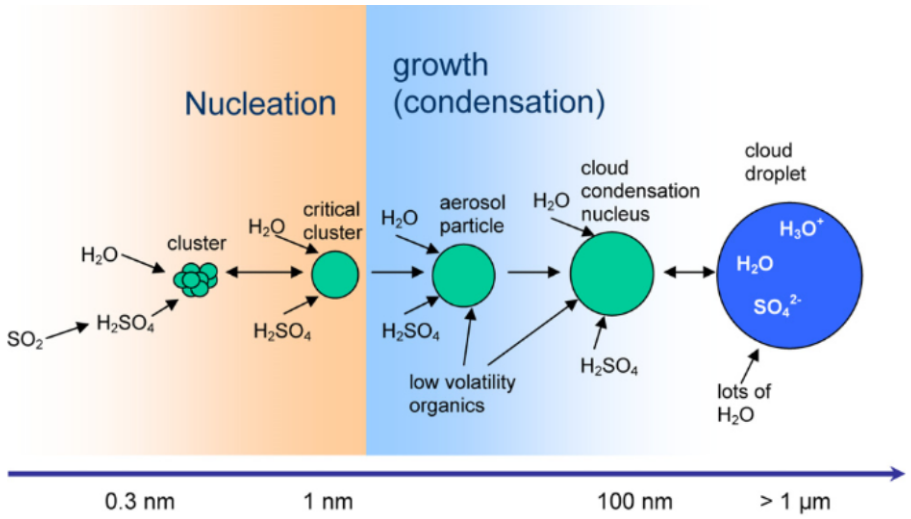


Figure 6: Schematic of the binary nucleation and growth processes of H_2SO_4 and H_2O. Once a cluster has formed, other species such as organics play a role in this growth process. [Curtius, 2006]

Nucleation mode aerosols then grow into the Aitken and accumulation modes through continued coagulation of particles, condensation of gas-phase species and cloud-processing. Cloud-processing refers to an important mechanism that modifies the size and chemical characteristics of aerosols through cloud droplet activation and growth, and aqueous-phase chemical processes. When aerosols form cloud droplets, they are able to absorb soluble gases such as SO_2 and undergo aqueous-phase oxidation through the establishment of equilibrium between SO_2, H_2O, HSO_3^-, and SO_3^{2-} as follows:

$$
\begin{aligned}
SO_{2(g)} &\rightleftharpoons SO_{2(aq)} \\
SO_{2(aq)} + H_2O &\overset{pK\ 4}{\rightleftharpoons} HSO_3^- + H^+ \\
HSO_3^- + H_2O &\overset{pK\ 8}{\rightleftharpoons} SO_3^- + H^+
\end{aligned} \tag{2}
$$

Within this equilibrium, HSO_3^- is then oxidised by H_2O_2 and O_3 to form sulfate as follows:

$$
\begin{aligned}
HSO_3^- + H_2O_2 &\longrightarrow SO_4^{2-} \\
HSO_3^- + O_3 &\longrightarrow SO_4^{2-}
\end{aligned} \tag{3}
$$

When these oxidised cloud droplets evaporate, they create aerosols that are larger than the original CCN and hence have a reduced critical supersaturation. This process forms a major pathway for aerosols into the accumulation-mode by increasing the aerosol mass and consequently size. Cloud-processed aerosols are distinct from their neighbours on a size distribution plot (as in Figure 3) by a minimum, termed the Hoppel minimum (shown in Figure 7).

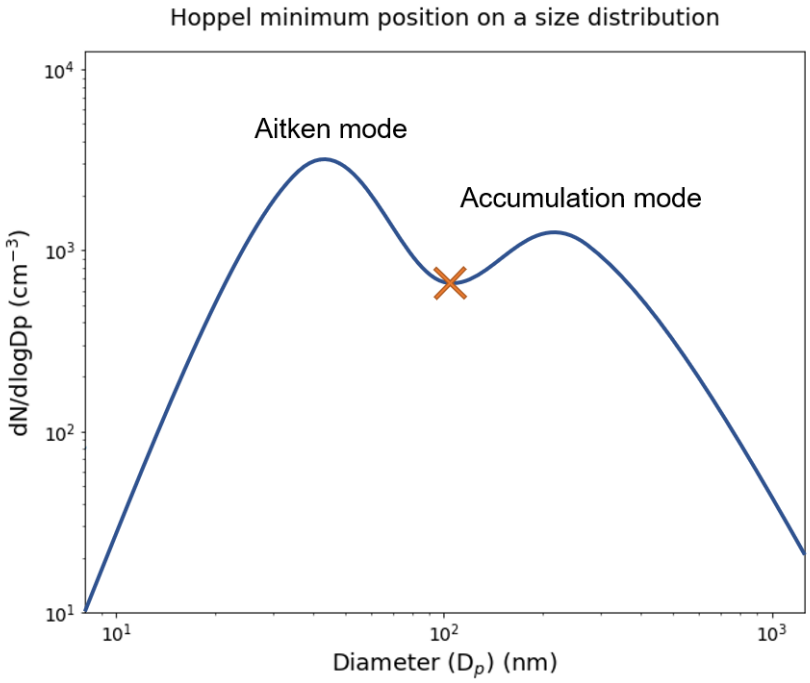


Figure 7: Schematic of the location of the Hoppel minimum which is located between Aitken and accumulation modes, indicated by the orange X (Image self-generated).

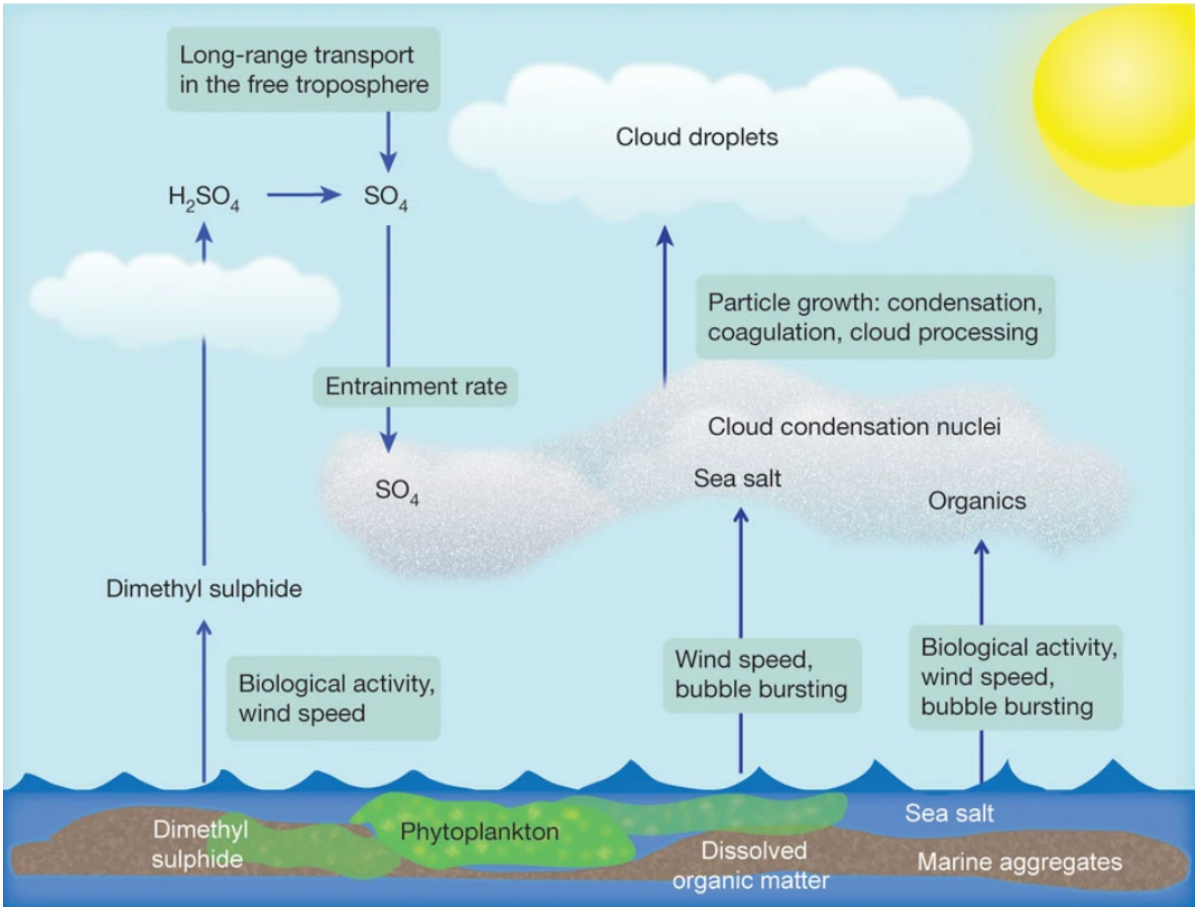


Figure 8: This figure depicts sources of primary marine aerosol of wind-driven SSA, and phytoplankton-produced DMS. Equation 1 is depicted through the formation of H_2SO_4 from DMS, and the resulting input of secondary aerosols into the MBL through FT entrainment. The formation of CCN from SSA is depicted, and the process of cloud-processing which forms cloud droplets [Quinn and Bates, 2011].

1.6 Aerosol effects on clouds and radiation

Radiative forcing is defined as the net downward radiative flux at the top of the atmosphere (TOA), and provides an indication of the radiative impact of atmospheric processes. Aerosols are the largest contributor to uncertainty in radiative forcing through interactions with clouds (termed Aerosol-Cloud Interactions, ACIs), and radiation (termed Aerosol-Radiation Interactions, ARIs) (Figure 9).

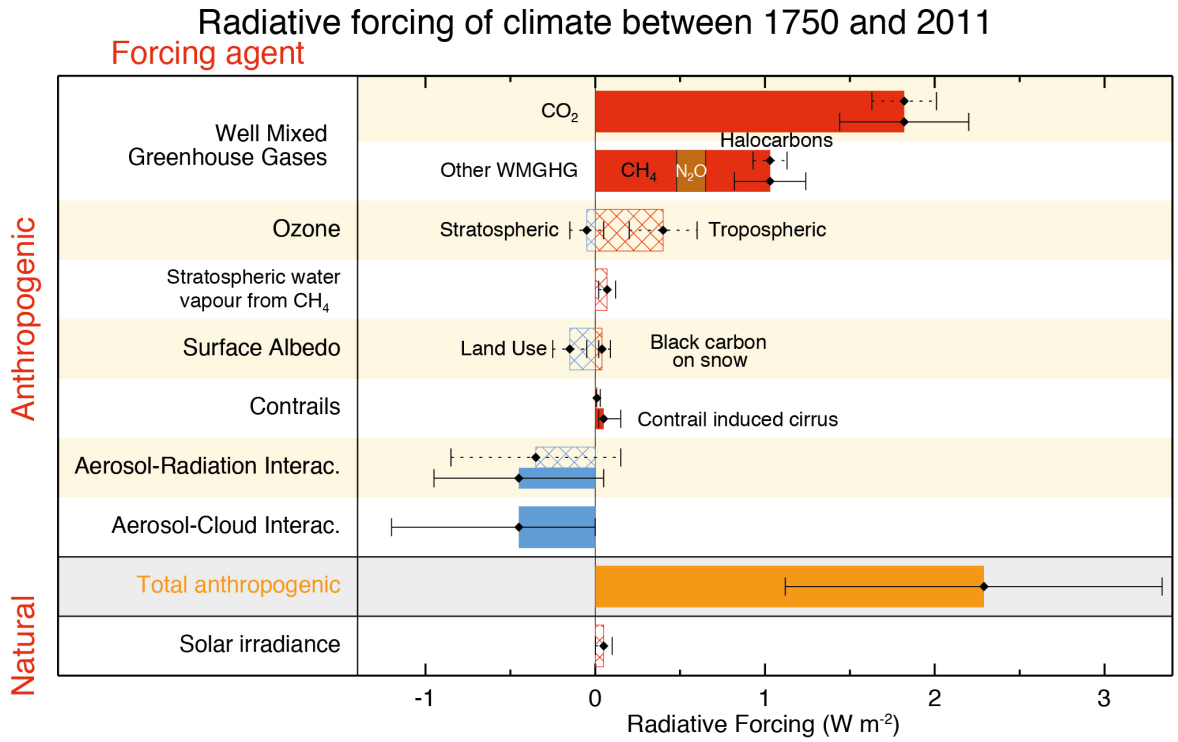


Figure 9: Bar chart showing radiative forcing (hatched) and Effective Radiative Forcing (ERF) (solid) for the period 1750-2011. ERF is defined as radiative forcing which accounts for changes to the TOA energy budget but are uncoupled to to surface warming changes [Smith et al., 2018]. This figure demonstrates the large uncertainty plotted for ARIs and ACIs in comparison to other forcing agents. Whiskers denote the 5–95% confidence range [Myhre et al., 2013]

ARIs describe the direct effect of aerosols which scatter or absorb radiation. The direct effect is dependent on the environment's relative humidity, and particle size, shape, and chemical composition [Mishra et al., 2015]. Scattering aerosols such as sulfates (characteristic of the SO) reflect larger proportions of incident radiation back out to space, resulting in a net radiative cooling of the surface climate estimated globally at -0.35 (-0.85 to +0.15) Wm^{-2}.

ACIs include two effects; the first indirect 'Twomey effect' and the second indirect effect. The first indirect effect describes how an increase of CCN with smaller radius sizes (and hence increased surface area) increases cloud albedo (brightness). Increased cloud albedo increases the amount of SW reflected radiation received at the TOA [Twomey, 1974]. The second indirect effect describes how smaller droplets may act as precipitation suppressants due to smaller collision efficiencies and fall speeds, thus increasing cloud longevity [Koren et al., 2015]. This effect also describes the role of aerosols as ice-nucleating particles (INPs) in supercooled clouds, although analysis of this effect has been regarded as out of the scope of this thesis.

1.7 Aerosol Optical Depth

This thesis utilises measurements of chemical composition, CCN, radiation and cloud fraction to characterise aerosol populations which are easily understood in concept, although the metric Aerosol Optical Depth (AOD) requires some explanation. AOD describes the amount of solar irradiance prevented from reaching the ground due to scattering/absorption from aerosol particles. AOD measurements are column-integrated (provide no indication of the vertical distribution of aerosols) and are weighted preferentially toward larger particles from the accumulation mode that attenuate light more strongly (see Appendix Figure 58). AOD is a mass-dominated metric, hence larger values of AOD could be representative of either an increased number or size of aerosols. Clean marine atmospheres are characterised by relatively low AOD values compared to polluted regions (Figure 10). The use of AOD has limitations, including the restriction of measurements to clear-sky conditions to avoid contamination by strongly-reflecting clouds [Martins et al., 2002]. See Appendix Section A.2 for details on the calculation of AOD.

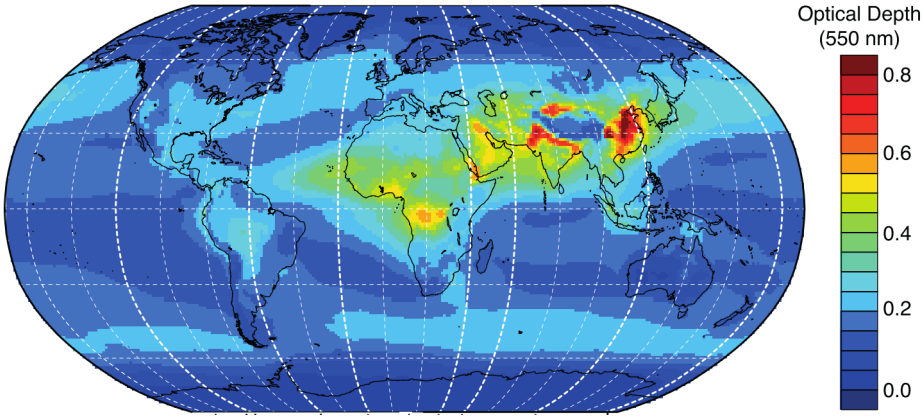


Figure 10: Spatial distribution of 550 nm AOD from the European Centre for Medium-Range Weather Forecasts Integrated Forecast System model, assimilated with Moderate Resolution Imaging Spectroradiometer (MODIS) satellite AOD retrievals (averaged over the period 2003–2010). Regions of increased AOD correspond to areas of high aerosol content (e.g: biomass burning in lower latitudes) [Benedetti et al., 2009, Morcrette et al., 2011]

This chapter has introduced fundamental concepts and processes relevant to Southern Ocean aerosol populations. The following chapter will describe how aerosols are represented in Global Climate Models (GCMs), and establish the AOD and CCN bias in current GCMs.

2 Aerosol Representation in Climate Modelling

This chapter outlines how aerosols have been implemented and parameterised within GCMs, and provides a background to the atmospheric and aerosol-chemistry schemes used within this thesis. The ability of previous models to represent observed AOD and CCN is summarised to provide context to the performance of the model investigated in this thesis, ACCESS-CM2.

2.1 Previous modelling studies

The complexity and variety of aerosol representations in GCMs is extensive and has been summarised in inter-comparison projects [Lamarque et al., 2013, Shindell et al., 2013, Collins et al., 2017]. Most aerosol schemes represent a combination of major aerosol components; dust, nitrates, sulfates and sea-salt in discrete size bins (introduced in Figure 3). Schemes range from a simple 'bulk' approach with prescribed size and mass distributions through to more complex 'modal' approaches where aerosol number, mass and particle size evolve via growth/condensation processes between modes with fixed distribution shapes. The chemical emissions supplied to models varies largely too, which is discussed in Section 2.2.3.

2.2 Implementation of more complex aerosol-chemistry schemes

Recent approaches in aerosol-chemistry modelling has shifted towards implementing increasingly complex emission parameterisations and chemistry schemes within GCMs. The goal of increasing complexity is to provide a more realistic representation of the physical atmosphere. Areas of interest include increasing the physical representation of PMOAs, sea-salt emissions, and the use of fully interactive chemistry schemes, which are summarised below.

2.2.1 Primary Marine Organic Aerosol (PMOA) schemes

PMOA schemes range in complexity from specifying a global marine organic aerosol emission (in $\mathrm{Tg\,yr^{-1}}$), through to complex parameterisations involving zonal 10 m wind-speed ($\mathrm{U_{10}}$), particle diameter (D_p) and chlorophyll-a concentration [chl-a]. Chlorophyll-a is often used as a proxy for marine organic aerosol due to similar seasonal cycles and good correlation [O'Dowd et al., 2004, Long et al., 2011, Vignati et al., 2010]. Recent studies have, however, suggested this relationship does not accurately represent the organic enrichment of SSA. [Frossard et al., 2014, Quinn et al., 2014]. Roelofs [2008] increased the global PMOA emission source within the ECHAM5-HAM Global Aerosol-Climate Model,

which increased CDNC by a factor of 3–4 and improved agreement with observed CCN and CDNC over the North Atlantic. Westervelt et al. [2012] used a [chl-a] scaling technique and saw a decrease in simulated CCN (0.2% SS) by up to 5% regionally. Meskhidze et al. [2011] implemented more complex parameterisations (utilising [chl-a], D_p and U_{10}) and saw a 20% increase in simulated CCN (0.2% SS) over biologically productive waters. Gantt et al. [2012b] found the implementation of a complex PMOA scheme resulted in a 7% reduction in global average Aerosol Indirect Forcing (the combination of both first and second indirect effects mentioned in 1.6) due to increases in low-level CDNC. The inclusion of complex PMOA schemes within GCMs has demonstrated the potential for a more physically-representative scheme to account for biogenic-related changes in CCN and radiation. The implementation of such schemes has yet to be fully explored in the Southern Ocean region.

2.2.2 Sea-salt schemes

Model emissions of sea-salt vary widely; the AeroCom intercomparison project found that simulated sea-salt had the highest inter-model difference of all studied aerosol types with global burdens ranging from 3–18 Tg (± 4 Tg) [Textor et al., 2006]. Most parameterisations utilise a relationship of SSA to wind-speed, hence differences in simulated wind-speed have significant impacts in calculated SSA bias. A multitude of SSA source emission schemes have been developed, although the most widely implemented scheme is the Gong 2003 function [Spracklen et al., 2008, Fan and Toon, 2011, Kipling et al., 2016, Tegen et al., 2019, Witek et al., 2016, Gong, 2003], this is discussed in more detail in Section 5.2.

Increasing evidence within literature has highlighted issues with the Gong [2003] sea-spray function. Spada et al. [2015] found this source function overestimated sea-salt surface concentrations in the Southern Ocean region compared to observations. Jaeglé et al. [2011a] found that at high wind speeds, coarse-mode SSA was overestimated by a factor of 2–3 and Madry et al. [2011] reported this overestimation increased discrepancies between simulated and observed AOD. Revell et al. [2019] used a modified sea-spray emission source function in the GLOMAP-HadGEM3-GA7.1 climate model and observed improved agreement between simulated and observed AOD during wintertime over the Southern Ocean (discussed later in Section 5.2).

2.2.3 Online chemistry schemes

Atmospheric chemistry processes involve constant interactions between aerosols, clouds and meteorological dynamics. To more fully capture these inter-connected schemes, interactive ('online') aerosol-chemistry schemes were created which provide a more realistic representation of simulated atmospheres. Online chemistry schemes feature a range of tropospheric and stratospheric chemical mechanisms whereby concentrations of important chemical species are updated based on a suite of reactions, rather than using set input and output rates parameterised in an offline scheme (described in Section 3.1.2). Justification for online coupled-chemistry schemes in GCMs remains controversial. Online chemistry schemes have been shown to improve air quality prediction in numerical models and the representation of seasonal sulfate aerosol cycles [Werner et al., 2018, Dhomse et al., 2016]. Hu et al. [2018] found that online chemistry simulations improved model bias in some spatial regions but worsened it in others (in the case of simulated ozone). Colarco et al. [2010] found online schemes could at best reproduce similar values as the offline version.

A World Meteorological Organization report (2015) concluded that implementation of full online chemistry remains too computationally expensive to be feasible for GCMs, combined with poor performance in studies aforementioned [World Meteorological Organization et al., 2015]. However, the evaluation of online chemistry in the SO has been limited. Sessions et al. [2015] evaluated the AOD bias of multiple online models, but used only one available observational station in the Southern Ocean and provided no reference simulations (without online chemistry) for comparison (discussed further in Section 8.1). Given the unique aerosol environment in the SO, it remains to be seen whether improvements in model aerosol bias could be made using online chemistry. The following section will provide a background to the model used in this thesis, ACCESS-CM2, and how this model represents PMOAs, sea-salt and chemistry schemes.

3 Model description

The Australian Community Climate and Earth System Simulator Coupled Model (ACCESS-CM2) is a next-generation coupled GCM which will contribute simulations to the next Coupled Model Intercomparison Project (CMIP6) ensemble. ACCESS-CM2 features a more advanced atmospheric configuration, dynamics and physics schemes, and increased vertical resolution in comparison to its predecessors, ACCESS1.x models used in CMIP5 [Hirst et al., 2015]. Aerosol and chemistry schemes used within ACCESS-CM2 are outlined below, and model specifications are provided in Table 5.

3.1 Aerosol & Chemistry schemes in ACCESS-CM2

Aerosol and chemistry routines are handled through two connected frameworks; United Kingdom Chemistry and Aerosol (UKCA) [Abraham et al., 2016] which simulates chemical processes and transformations, and the detailed aerosol microphysical scheme 'Global Model of Aerosol Processes' (GLOMAP) [Mann et al., 2010] (see Section 3.1.1). UKCA and GLOMAP code are incorporated in ACCESS-CM2 after the atmospheric time-step at a rate of once per hour [Abraham et al., 2016]. UKCA is coupled to GLOMAP and the radiation scheme through the Edwards-Slingo radiation code which utilises both radiatively active trace gases and aerosol optical properties to calculate direct radiative effects (see Abraham et al. [2016]) for full description of the radiation scheme). The activation of aerosols to form CDNC is performed through the coupling of GLOMAP to a Köhler theory-based parameterisation [Abdul-Razzak and Ghan, 2000]. Based on atmospheric saturation and updraught velocity conditions, calculated CDNC is passed to the radiation code which determines the first indirect aerosol effect (cloud albedo) and precipitation processes [Abraham et al., 2016].

Cloud schemes are handled separately from UKCA and calculated within ACCESS-CM2. Specifically, cloud fraction which is used in this thesis is calculated using parameters such as liquid water content, total specific humidity, temperature and pressure within the convective and large-scale cloud scheme [Bi et al., 2020, Wilson et al., 2008, Morcrette, 2012].

3.1.1 GLOMAP

GLOMAP simulates aerosol size distribution through a suite of microphysical processes including aerosol nucleation, coagulation, cloud-processing and condensation. The scheme has been implemented widely in GCMs and evaluated against a combination of satellite [Mccoy et al., 2015b, Crippa et al., 2013] and largely Northern-Hemispheric ground-based observations [Korhonen et al., 2008, Pringle et al., 2009, Spracklen et al., 2010, Reddington et al., 2011, Mann et al., 2010]. The modal version of GLOMAP used in this thesis simulates aerosol components within modes of a fixed distribution shape. Within these modes, aerosol number, mass, mean particle size and the amount of water (for soluble aerosols) varies [Mann, 2014] (see Figure 11). Transportation and deposition processes, and dust emissions are handled separately and separated into six size bins [Woodward, 2011]. GLOMAP calculates respective sources and sinks of aerosol mass and number, with removal processes including sedimentation, dry deposition, nucleation (in-cloud) and impact (below-cloud) scavenging [Abraham et al., 2016].

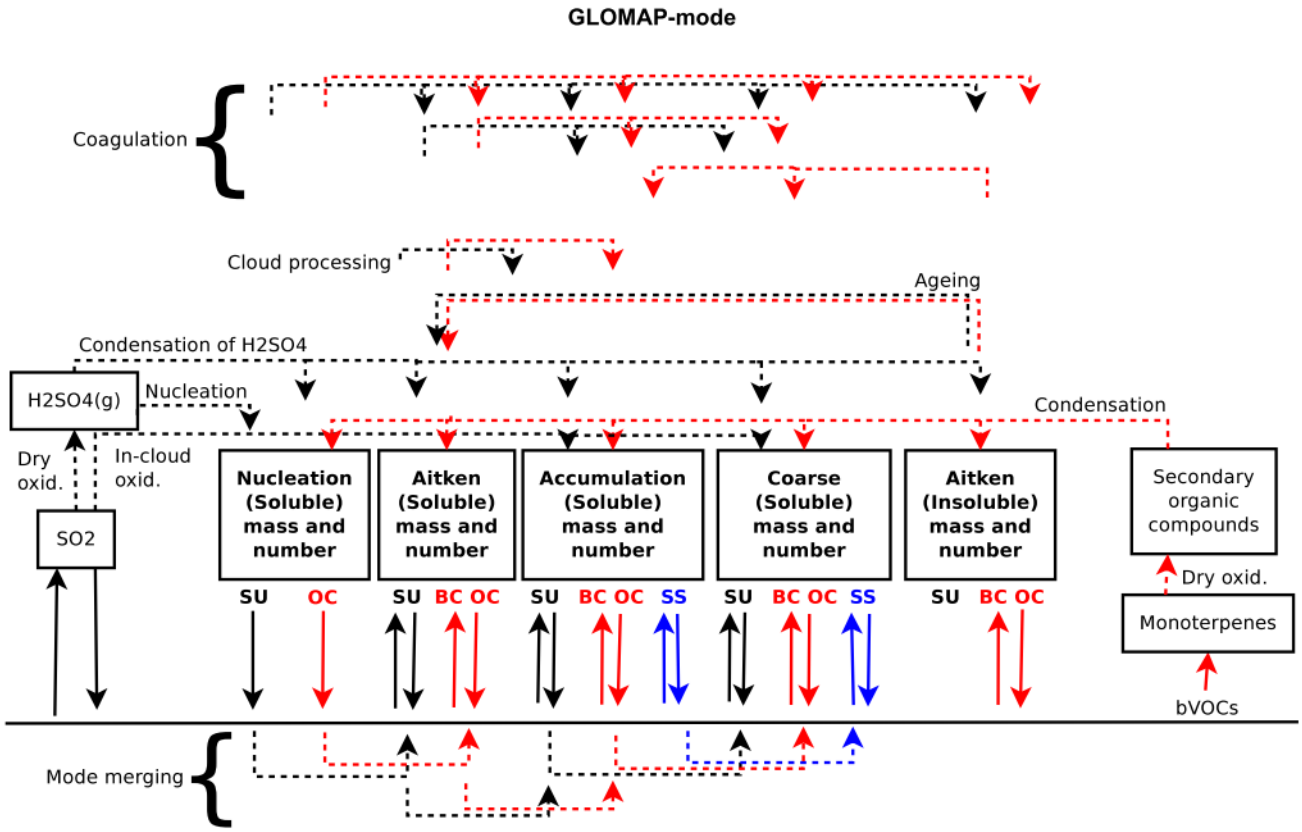


Figure 11: Mode distribution of aerosol components and chemical transformations in GLOMAP. GLOMAP simulates the number and mass of aerosols in five aerosol modes. Within each mode, sulfate (SU), black and organic carbon (BC and OC), and sea-salt (SS) are internally mixed. Solid arrows show the total emission and deposition mass fluxes, and dashed arrows represent mass fluxes [Bellouin et al., 2013b]. For example, this figure illustrates the gas-phase ('dry') oxidation of SO_2 to form H_2SO_4, and the condensation of H_2SO_4 into the nucleation mode.

3.1.2 Chemistry scheme

Offline chemistry is the default scheme in ACCESS-CM2 which uses a monthly climatology of oxidant fields as emissions, and features 11 species which take part in 14 chemical reactions. These emission files have been pre-computed using a more complex stratospheric-tropospheric chemistry scheme, such as the online scheme described in Section 2.2.3. Offline chemistry restricts advected tracers to seven aerosol precursor species, provided in Table 2.

UKCA Species	**Dry**	**Wet**	**Type**
H_2O_2	Yes	Yes	Advected tracer
DMS	-	-	Advected tracer
SO_2	Yes	Yes	Advected tracer
H_2SO_4	Yes	-	Advected tracer
$(CH_3)_2SO$ (DMSO)	Yes	Yes	Advected tracer
Monoterpene	Yes	-	Advected tracer
Secondary Organic	Yes	Yes	Advected tracer
O_3	-	-	Offline oxidant
OH	-	-	Offline oxidant
NO_3	-	-	Offline oxidant
HO_2	-	-	Offline oxidant

Table 2: Advected tracers and offline oxidants (diagnostic species) used in the offline chemistry scheme. Species identified as offline oxidants are established from ancillary files in the model. Table adapted from [Abraham et al., 2016].

Oxidants are supplied as a constant monthly field, with short-lived species such as OH, HO_2, and NO_3 having a parameterised diurnal cycle superimposed on the monthly climatological fields. Offline oxidants fields are used within a chemical mechanism involving the gaseous and aqueous oxidation of sulfur, detailed in table 3 below. Nucleation rates are parameterised using the concentration of H_2SO_4 following a binary homogenous sulfate nucleation scheme outlined in Vehkamäki et al. [2002] (described in Section 1.5).

Gas-phase reactions	**A-factor**	**Reference**
DMS + OH $\longrightarrow$ SO_2	9.60e-12	Pham et al. [1995]
DMS + OH $\longrightarrow$ 0.6 SO_2 + 0.4 DMSO + CH_3O_2	3.04e-12	Pham et al. [1995]
DMS + NO_3 $\longrightarrow$ SO_2 + HNO_3 + CH_3O_2 + HCHO	-1.90e-13	Pham et al. [1995]
DMSO + OH $\longrightarrow$ SO_2	5.80e-11	IUPAC [2006]
SO_2 + OH $\longrightarrow$ H_2SO_4 + HO_2	3.00e-31	Pham et al. [1995]
MONOTERPENE + OH $\longrightarrow$ F_{SOA} 0.13 SEC-ORG	1.20e-11	IUPAC [2006], Spracklen et al. [2006]
MONOTERPENE + O_3 $\longrightarrow$ F_{SOA} 0.13 SEC-ORG	1.01e-15	IUPAC [2006], Spracklen et al. [2006]
MONOTERPENE + NO_3 $\longrightarrow$ 0.13 SEC-ORG	1.19e-12	IUPAC [2006], Spracklen et al. [2006]
HO_2 + HO_2 $\longrightarrow$ H_2O_2	2.20e-13	IUPAC [2006]
OH + H_2O_2 $\longrightarrow$ H_2O	2.90e-12	IUPAC [2006]
Aqueous-phase reactions	**A-factor**	**Reference**
HSO_3^- + H_2O_2 $\longrightarrow$ SO_4^{2-}	2.13e+14	Kreidenwies et al. [2003]
HSO_3^- + O_3 $\longrightarrow$ SO_4^{2-}	4.01e+13	Kreidenwies et al. [2003]
SO_3^{2-} + O_3 $\longrightarrow$ SO_4^{2-}	7.43e+16	Kreidenwies et al. [2003]

Table 3: Sulfur and monoterpene oxidation scheme used in ACCESS-CM2 (offline chemistry). SEC-ORG = secondary organic product generated from monoterpene oxidation [Mann et al., 2010]. The aqueous-phase oxidation reactions shown in this table describe cloud-processing mechanisms (discussed in Section 1.5) and have no traceable product, but output a flux term of sulfate produced by each oxidant. The reaction fluxes produced by these oxidation processes are passed to GLOMAP which updates the accumulation and coarse soluble modes (proportional to the number concentration in each mode). See Appendix A.5 for the description of A-factor.

Updated chemical products from the chemical reactions outlined in Table 3 are used to update the particle number concentration in each size mode (e.g: Aitken, accumulation, etc.), and the mass of each aerosol component within GLOMAP (e.g: sulfate and sea-salt). Based on updated particle number and mass, GLOMAP applies aerosol growth and deposition processes.

A source of uncertainty within UKCA that must be noted lies within the constant cloud-water pH assumed to be five everywhere. Variable cloud pH values determines the dissociation of $SO_{2(aq)}$ at $pK \sim 4$ and $HSO^{-}_{3(aq)}$ at $pK \sim 8$ (Equation 1.5.2). Cloud pH which has important implications for aqueous-phase oxidation and has been shown to contribute substantially to uncertainty surrounding simulated CCN and radiative forcing [Lee et al., 2013, Turnock et al., 2019].

3.1.3 Sea-salt emissions

Sea-salt emissions are calculated using the Gong [2003] sea-spray source function (mentioned in Section 2.2.2), which describes the surface emission rate of sea-salt aerosols as a function of surface wind speed (U_{10}) and particle size. Equation 4 describes the number of seawater droplets generated per square metre of sea surface per particle radius over 20 size bins, as follows:

$$\frac{dF}{dr} = 1.373 u_{10}^{3.41} r^{-A} (1 + 0.057 r^{3.45}) \times 10^{1.607 e^{-B^2}} \tag{4}$$

where $A = 4.7(1 + \Theta r)^{-0.017 r^{-1.44}}$, $B = (0.433 - logr)/0.433$, and Θ is an adjustable parameter that controls the shape of the sub-micron size distributions [Gong, 2003]. Sea-salt is emitted into the accumulation and coarse modes, and is assumed to be purely sea-salt (NaCl). Hence, the standard configuration of ACCESS-CM2 lacks primary marine emissions in the submicron size range, and does not include organic matter within this sea-spray.

3.2 Previous model-observation evaluations

This section describes how well previous modelling efforts have performed in representing observed AOD and CCN to provide context to the performance of ACCESS-CM2. Mann et al. [2010] evaluated the bias and correlation of key aerosol parameters simulated in GLOMAP against various, predominantly Northern hemispheric, global observations (Table 4). Aerosol precursor gases, chemically speciated particle mass, sea-salt, and CCN were found to perform well against observations.

3.2.1 AOD bias in previous aerosol-chemistry models

Modelled bias of AOD varies largely; the Atmospheric Chemistry and Climate Model Intercomparison Project (ACCMIP) of 10 GCMs resulted in simulated AOD biases ranging from -22% to 77% compared to satellite observations [Shindell et al., 2013]. Bellouin et al. [2013a] incorporated GLOMAP into the Hadley Centre GLobal Environmental Model (HadGEM3) and reported an global AOD underestimation of approximately 30% compared to the satellite-based Monitoring Atmosphere Composition and Climate reanalysis dataset [Inness et al., 2012], with a positive bias noted in high latitudes (Figure 12). Compared against predominantly Northern Hemispheric ground-based sun-photometers, the GLOMAP-HadGEM3 model reported a mean AOD bias of -0.039 [Bellouin et al., 2013a].

Parameter	**Normalised mean bias (b)**	**Pearson regression coefficient (R)**	**Reference**
Surface DMS	Amst.Isl: -0.45 Cape Grim: 0.28 Dumont Durville: -0.56	Amst.Isl: 0.72 Cape Grim: 0.65 Dumont Durville: 0.62	Nguyen et al. [1992] Ayers et al. [1991] Jourdain and Legrand [2001]
Surface SO_2	Amst.Isl: -0.39 Cape Grim: 4.22	Amst.Isl: 0.60 Cape Grim: 0.45	Nguyen et al. [1992] Ayers et al. [1991]
Sulfate	0.25	0.92	Malm et al. [2002] Stier et al. [2005]
Sea-salt	0.22	0.13	Stier et al. [2005]
CN	Cape Grim:-0.75 Neumayer: -0.11	Cape Grim: 0.41 Neumayer: 0.88	Ayers et al. [1991] Rolf [1999]
CCN	Cape Grim (S=1.2%): 0.20 Cape Grim (S=0.23%): 0.78	Cape Grim (S=1.2%): 0.68 Cape Grim (S=0.23%): 0.41	Ayers et al. [1997a]
Aitken mode	0.10	0.54	Heintzenberg et al. [2000]
Accumulation mode	-0.46	0.77	Heintzenberg et al. [2000]

Table 4: Evaluation of key aerosol parameters in GLOMAP, adapted from Mann et al. [2010]. Single bias and correlation values are provided when evaluation used a multi-station dataset. Bias and correlation values have been presented for individual stations in the SO where available.

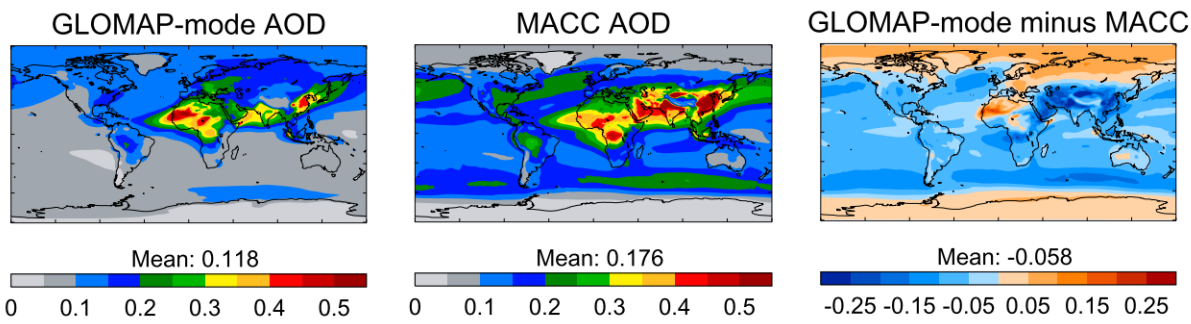


Figure 12: GLOMAP-simulated AOD at 550nm for the period 2003-2006 and subtracted from MACC reanalysis, adapted from [Bellouin et al., 2013b].

Revell et al. [2019] compared simulated AOD in a GLOMAP-HadGEM3-GA7.1 climate model against satellite observations with altered sulfate chemistry. The model reported an overall positive bias between 40°-60°S, with an average AOD reported as 15.7% larger than satellite measurements. Simulated AOD was positively biased in wintertime and negatively biased in summertime with an RMSE of 0.032 [Revell et al., 2019].

3.2.2 CCN bias in previous aerosol-chemistry models

Mann et al. [2010] evaluated GLOMAP-simulated CCN against ground-based observations and found a positive CCN model bias at Cape Grim (see Table 4, and Table 8 for NMB equation). Conversely, Spracklen et al. [2011] evaluated GLOMAP-simulated CCN against a suite of largely Northern-Hemisphere ground-based observations (CCN SS ranged from 0.02–0.5%) and found the model was biased low with a normalised mean bias of -77% . Schmale et al. [2019] compared observations from a voyage in the Southern Ocean to GLOMAP simulations, and similarly reported an underestimation of CCN (0.2% SS) by approximately 50% in regions which corresponded to high concentrations of gas-phase MSA (a product of DMS oxidation). In marine environments, this suggests that GLOMAP may be missing a marine aerosol source or under-represents sea-spray or DMS emission fluxes. Additionally, this may indicate a lack of cloud-processing (which increases CCN concentrations), or an overestimation of deposition/precipitation processes [Schmale et al., 2019]. Further evidence for a potential missing marine aerosol source was noted in an underprediction of GLOMAP-simulated aerosol number in comparison with size-distribution observations collected on a Southern Ocean voyage [Law et al., 2017, Woodhouse et al., 2020].

This chapter outlined the ACCESS-CM2 model framework, and provided a background of previous models' performances in simulating AOD and CCN metrics. The next chapter presents why such biases must be remedied in GCMs, and establishes the aims of this research.

4 Motivation

Aerosols form the largest contribution to uncertainty in radiative forcing, as discussed in Section 1.6. Limited datasets, compounded by the use of predominantly Northern Hemisphere data for model microphysical parameterisations has resulted in biases within aerosol, cloud and radiation schemes in GCMs, particularly in the SO [Marchand et al., 2014]. GCMs struggle to represent observational aerosol parameters; Section 3.2 and Table 4 described the wide range of biases for simulated AOD and CCN.

GCMs often underestimate cloud fraction (CF) and albedo in the SO [Wang, 2015]. Fan et al. [2018] showed that current GCMs underestimated satellite CF by 15.2% globally. Underestimations in CF result in positive short-wave (SW) ↓ radiation biases and underestimations in SW TOA ↑ radiation, particularly during the Austral summer [Li et al., 2013] (Figure 13). While TOA SW↑ radiation biases were reduced in the CMIP5 ensemble by up to 56%, a systematic bias still persists in the overestimation of SW↓ radiation and the underestimation of TOA SW↑ radiation.

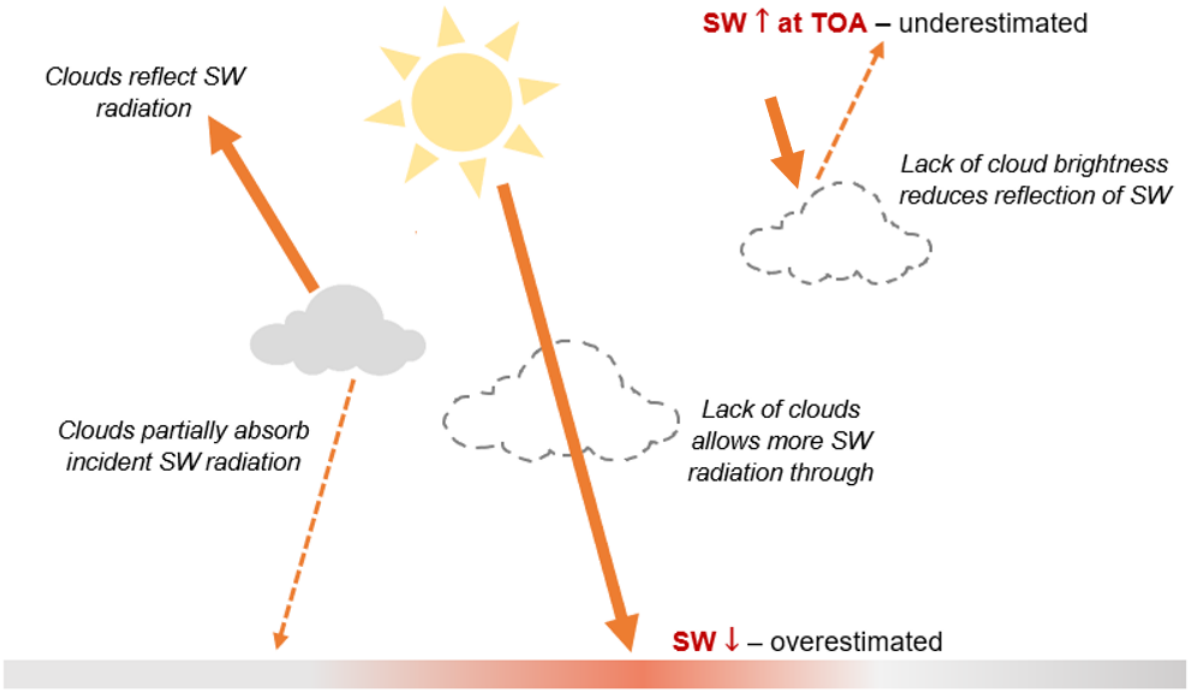


Figure 13: Schematic of radiation biases in GCMs (figure self-made). SW↑ = Outgoing TOA Shortwave Radiation, SW↓ = Incoming Shortwave Radiation

Reducing this radiation bias has been identified as a key goal for the modelling community, as it induces warm sea-surface temperature (SST) biases which have wide-spread consequences in the global energy budget, carbon cycle and circulation systems [Hawcroft et al., 2017] (see Figure 13). SW biases have been attributed to multiple factors based around aerosol representation including insufficient parameterisations of mixed-phase and supercooled clouds, Ice-Nucleating Particles (INPs) (introduced in Section 1.6), and a poor representation of annual/seasonal cycles of CCN [McFarquhar, 2016]. Complex ACIs and ARIs suggest improvements in simulated aerosol representation could improve model SW biases.

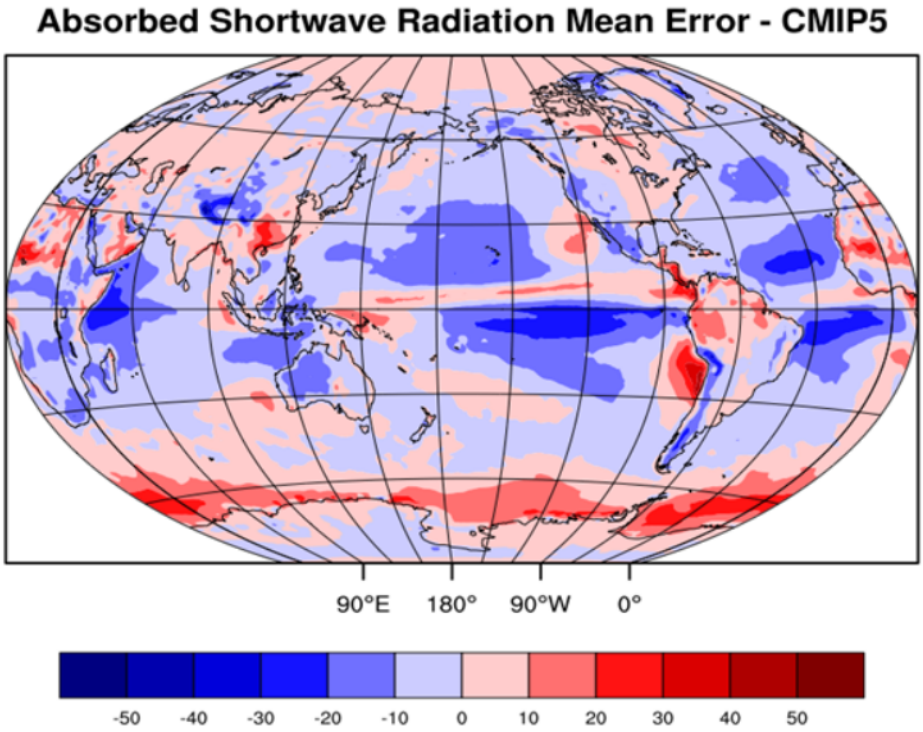


Figure 14: Mean errors of absorbed surface SW↓ radiation in CMIP5 climate models. Positive values indicate an excess of SW↓ radiation absorbed [Marchand et al., 2014]

With the introduction of Australia's newest GCM, ACCESS-CM2, it must be determined to what extent this model is subject to the same biases in the aerosol-chemistry schemes, and how these biases can be improved. The next section defines the aims of this thesis to address such questions.

4.1 Aims

Climate modelling communities have made efforts to improve the aforementioned biases by incorporating more physically-representative aerosol schemes or tailored parameterisations for PMOAs, sea-salt and online chemistry (discussed in Sections 4.2.4 & 2.2), although these efforts have been limited in the SO region. This research aims to successfully run a suite of perturbation simulations of ACCESS-CM2 with modifications to the PMOA, SSA, and chemistry schemes. Ultimately, this research aims to answer the following research questions:

1. How well does ACCESS-CM2 represent aerosols over the Southern Ocean in terms of AOD and CCN bias?

2. Does increasing the complexity of aerosol-chemistry schemes result in a more accurate representation of AOD and CCN?

3. Can the overall radiation and cloud fraction bias in the Southern Ocean be improved through increasing the complexity of aerosol-chemistry schemes?

4.2 Significance and Innovation

4.2.1 Evaluation of ACCESS-CM2

ACCESS-CM2 constitutes the atmosphere-only version of Australia's submission to the next CMIP6 evaluation. Understanding the model's inherent biases in aerosol, cloud and radiation representation will be crucial in underpinning future simulations using this model. This thesis constitutes one of the first efforts to evaluate aerosol representation in ACCESS-CM2 and to run a series of perturbation experiments (outlined in Chapter 5). Figure 9 indicated that aerosol ARIs have made a substantial contribution to mitigation of anthropogenic increased radiative forcing (RF), hence reducing the RF uncertainty surrounding ARIs and ACIs is crucial in understanding future climate change outcomes.

4.2.2 Focus on the Southern Ocean spatial domain

The Southern Ocean has been identified as a region of priority research within the aerosol modelling community as it exhibits the largest SW radiation bias in GCMs [Marchand et al., 2014]. When GCM evaluation studies utilise ground-based observations, these efforts are largely focused in the Northern-Hemisphere due to increased availability of data temporally and spatially. When satellites are used, data is often lacking in the SO region due to factors including high cloud cover (discussed in Section 4.2.3). Recent research efforts that have aimed to address the SO model SW bias have done so by

focusing attention on model cloud schemes [Hyder et al., 2018, Vergara-Temprado et al., 2018, Kuma et al., 2019, Mason et al., 2015, Neubauer et al., 2019]. However, while these studies have identified clouds as a large source of error in remedying the SW radiation bias, a comprehensive evaluation of aerosols, the precursor to clouds, is lacking. There is a clear need for aerosol model evaluation studies within the SO region, despite the relative scarcity of measurements in the region.

4.2.3 Use of a comprehensive suite of ground-based observations for model evaluation

This thesis uses a suite of ground-based observations for model evaluation which facilitate a more comprehensive analysis of aerosol populations. Variables such as chemical composition, size-distribution and CCN are most effectively measured using laboratory instruments, although there are a number of limitations which must be accounted for (see Appendix A.6). Hence, this research provides a departure from most GCM-evaluation studies which utilise satellite products that provide global gridded output at a high temporal and spatial resolution [Sockol and Small Griswold, 2017, Misra et al., 2016, Bender et al., 2019]. Numerous challenges result in satellite retrievals having a higher uncertainty than ground-based observations such as white-capping surface brightening (produced by high wind speeds and large waves), difficulties detecting low-concentration aerosols and in penetrating through the complete atmosphere (Figure 15) [Giles et al., 2019, Levy et al., 2013, Sayer et al., 2013, Witek et al., 2013, Guzman et al., 2017, Thorsen and Fu, 2015]. While satellite measurements of CCN exist, retrievals have an accuracy between ±25%–±30% and may only be observed in specific meteorological conditions that excluding the dominant cirrus cloud type over the SO [Rosenfeld et al., 2016]. Observational data largely provides lower uncertainty values, which is beneficial for increasing the accuracy of model-evaluation studies. For example, observational AOD data used in this thesis has an estimated uncertainty between 0.01–0.02 (unitless), compared to satellite products which range from 0.03-0.09 (unitless) [Holben et al., 1998, Sayer et al., 2013], this is discussed further in Chapter 6.

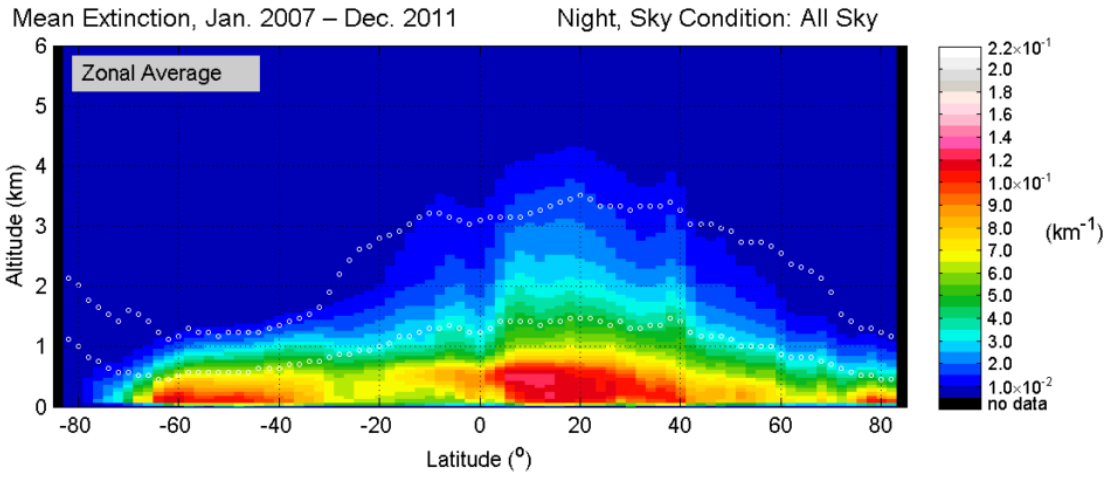


Figure 15: Nighttime all-sky zonal mean 532nm aerosol extinction (km^{-1}) from Jan 2007-Dec 2011. Note lower altitudes are reached in high-latitude regions [Winker et al., 2013]. This figure demonstrates that aerosols reach lower altitudes over the SO than mid-latitude aerosols, hence making it more difficult for satellites to effectively measure surface aerosols. Satellite retrievals often only record above the aerosol layer; an analysis of CALIPSO measurements showed that only 69% of vertical profiles penetrated through the complete atmosphere [Guzman et al., 2017]

4.2.4 Exploration of increased model complexity

More complex aerosol and chemistry schemes are seldom included in GCMs due to additional computational expense. The majority of models in ACCMIP utilised the more simple 'bulk' approach (defined in Section) and largely output at a temporal resolution of monthly means [Shindell et al., 2013]. Next generation climate models are increasingly incorporating more complex parameterisations, which is required to capture the complexity of inter-connected atmospheric systems. Model simulations described in Section 5.2 utilise more complex aerosol-chemistry schemes and output at a temporal resolution of 1 hour. This increased resolution facilitates meaningful comparison with the short time periods of campaign and voyage observational data described in Section 6, which is essential in capturing the relatively short atmospheric lifetimes of aerosols.

5 Methods: Running ACCESS-CM2

This chapter includes details on the configuration of ACCESS-CM2 combined with UKCA and GLOMAP, changes made to the model in perturbation runs, and describes how AOD and CCN were calculated from model output.

5.1 Model configuration

The configuration of ACCESS-CM2 has been summarised in Table 5 below. The Shared Socioeconomic Pathway 2-4.5 used to prescribe anthropogenic emissions was selected as a 'middle of the road' option, although disparities in anthropogenic emissions are negligible over the model run times used in this thesis [Riahi et al., 2017].

Parameter	**ACCESS-CM2 model setup**
Physical Atmosphere	Met Office Unified Model General Atmosphere 7.1 (GA 7.1) [Walters et al., 2019]
Model configuration	Atmosphere only
Code Version	Unified Model 10.6 (UM 10.6) [Abraham et al., 2016]
Land-surface scheme	Community Atmosphere Biosphere Land Exchange (CABLE) [Kowalczyk et al., 2013]
Model grid spacing	1.25° Latitude by 1.85° Longitude
Vertical Levels	85
Model Top	85km
Meteorology	Nudged at 6-hourly intervals to ERA-Interim
Aerosol -Chemistry scheme	UKCA Offline Chemistry (Backward-Euler Solver) for the BASE run, and UKCA Chemistry for Stratosphere and Troposphere (CheST) for the online chemistry run [Abraham et al., 2016], combined with aerosol scheme GLOMAP-mode [Mann et al., 2010].
SSTs and SIC	Atmospheric Model Intercomparison Project (AMIP) [Taylor et al., 2015])
Anthropogenic emissions	SSP2-4.5 forcing [Riahi et al., 2017]

Table 5: Description of base ACCESS-CM2 model parameters. SST = Sea Surface Temperatures, SIC = Sea Ice Concentration.

5.2 Model simulation runs

ACCESS-CM2 was run in this study for years 2016-2018, with a one-year spin-up run through 2015. Meteorology in the simulations was nudged to ERA-Interim (ERA-I) reanalysis data products of zonal (U) and meridional (V) wind components, and potential temperature (Θ) at 6-hourly intervals in the free troposphere. While nudging interferes with a GCM's ability to respond to dynamic feedback systems, it is necessary to ensure consistent 'real-world' meteorology when performing multiple simulations over the same time period (see Appendix A.4). Model data was output at an hourly temporal resolution to capture the short atmospheric lifetime of aerosols and increase the number of data points in a relatively short run time. Data was output in a spatial domain of 30°S to 90°S to accommodate storage and computing time limitations. One control simulation and three perturbation simulations were run, where each simulation used the same model configuration as the control run (Table 5) but changed one aspect of the aerosol or chemistry scheme:

Simulation name	**Simulation description**	**PMOA/sea-salt/chemistry schemes**
1. BASE	Control simulation (ACCESS-CM2).	• Primary sea-salt emissions assumed to be purely NaCl • Sea-salt emitted using the Gong [2003] function • Offline chemistry scheme used (outlined in Section 3.1.2)
2. PMO	Addition of Primary Marine Organics scheme.	• Sea-salt includes organic fraction (PMOA scheme) • Sea-salt emitted using the Gong [2003] function • Offline chemistry scheme used
3. CHEM	Online chemistry scheme	• Primary sea-salt emissions assumed to be purely NaCl • Sea-salt emitted using the Gong [2003] function • Online UKCA CheST chemistry scheme used
4. SSALT	Altered sea-salt emission source function	• Primary sea-salt emissions assumed to be purely NaCl • Sea-salt emitted using the Hartery et al. [2020] function • Offline chemistry scheme used

Table 6: Description of ACCESS-CM2 control run and perturbation simulations.

Control run, BASE: The first model run, BASE, was run in the standard configuration outlined above in Section 5.1 & Chapter 3.

PMO: The PMO run includes an empirically-derived emission parameterisation that introduces organic matter within simulated Sea Salt Aerosols (OM_{SSA}), which has been found to improve the seasonal representation of simulated organic aerosols [Gantt et al., 2012a, Meskhidze et al., 2011]. This parameterisation calculates the size-resolved organic mass fraction of sea-spray (OM_{frac}) as a function of MODIS/Aqua satellite-derived [chl-*a*], 10m zonal wind speeds (U_{10}) and the sea spray particle dry diameter (D_p, in units μm) as follows:

$$\mathrm{OM}_{frac}(\text{chl } a, U_{10}, D_p) = \frac{(1+\exp(3(-2.63[chl\,a]) + 3(0.18(U_{10})))^{-1}}{1+0.03\exp(6.81D_p)} + \frac{0.03}{1+\exp(3(-2.63[\text{chl } a] + 3(0.18(U_{10}))))} \quad (5)$$

The organic mass fraction (OM_{frac}) calculated in Equation 5 is then applied to the volume flux of SSA (V_{SSA}) to calculate the mass flux of PMO carbon (OM_{flux}, units g $m^2 s^{-1}$) as follows:

$$\mathrm{OM}_{flux} = \mathrm{OM}_{frac} \times V_{SSA} \times \rho_{SSA} \quad (6)$$

where ρ_{SSA} is the apparent density of SSA ($\mathrm{g\,cm^{-3}}$). This parameterisation makes a number of assumptions. The sea-spray emissions are defined to occur at 160nm, in the Aitken soluble (25% of mass) and insoluble (75% of mass) modes. These ratios are based on observational findings of marine organic aerosol solubility [O'Dowd et al., 2004]. Organic aerosol is emitted into the Aitken mode as organic carbon, which is immediately transferred to the accumulation mode at the next chemistry timestep (1 hour).

CHEM: The third run, CHEM, utilises a fully online UKCA CheST chemistry scheme which features a combination of stratospheric and tropospheric schemes outlined in Morgenstern et al. [2009], UKCA [2011], & O'Connor et al. [2014]. This scheme defines 75 species in 283 chemical reactions, and features 70 chemical tracers including O_3, NO_3, and H_2O_2; an increase in tracer species by a factor of 10 compared to offline chemistry (Section 3.1.2). An excerpt of online chemistry reactions relevant to marine sulfur chemistry have been presented in Table 7 below.

Gas-phase reactions	A-factor	*Reference*
DMS + OH $\longrightarrow$ SO_2	1.2e-11	Pham et al. [1995]
DMS + OH $\longrightarrow$ MSA + SO_2	3.04e-12	IUPAC [2006]
DMS + NO_3 $\longrightarrow$ SO_2 + HNO_3 + CH_3O_2 + HCHO	1.90e-13	Pham et al. [1995]
SO_2 + O_3 $\longrightarrow$ SO_3	3.00e-12	IUPAC [2006]
SO_3 + H_2O $\longrightarrow$ H_2SO_4 + H_2O	8.50e-41	IUPAC [2006]
MONOTERPENE + OH $\longrightarrow$ F_{SOA} 0.13 SEC-ORG	1.20e-11	IUPAC [2006], Spracklen et al. [2006]
MONOTERPENE + O_3 $\longrightarrow$ F_{SOA} 0.13 SEC-ORG	1.01e-15	IUPAC [2006], Spracklen et al. [2006]
MONOTERPENE + NO_3 $\longrightarrow$ 0.13 SEC-ORG	1.19e-12	IUPAC [2006], Spracklen et al. [2006]
Aqueous phase reactions	A-factor	*Reference*
HSO_3^- + H_2O_2 $\longrightarrow$ $SO_4{}^{2-}$	2.13e+14	Kreidenwies et al. [2003]
HSO_3^- + O_3 $\longrightarrow$ $SO_4{}^{2-}$	4.01e+13	Kreidenwies et al. [2003]
$SO_3{}^{2-}$ + O_3 $\longrightarrow$ $SO_4{}^{2-}$	7.43e+16	Kreidenwies et al. [2003]

Table 7: Sulfur and monoterpene oxidation scheme used in ACCESS-CM2 (UKCA CheST online chemistry). SEC-ORG = secondary organic product generated from monoterpene oxidation [Mann et al., 2010].

Online chemistry utilises fully interactive oxidant species where emission inputs are computed in real-time during the simulation using interactive meteorological variables at each chemical timestep (1 hour). This is compared to the use of prescribed, pre-computed monthly oxidant values in the offline chemistry scheme. Relevant online emissions include DMS, and lightning-generated NO_x.

The online and offline schemes have similarities in the oxidation pathways, but have some notable differences. For example, the online scheme has no production of DMSO as the offline scheme does. Additionally, the A-factors are different (Tables 3 & 7). For example, the online oxidation of DMS by OH has a larger A-factor by a factor of 10, hence we could expect a faster rate of DMS oxidation in online chemistry. See Appendix A.5 for the definition of the A-factor and its effect on reaction rates.

SSALT: The fourth model run addresses concerns in the modelling community regarding the use of the Gong [2003] sea-spray function (described in Section 3.1.3). This simulation implements a modified sea-spray source function which is based on in-situ measurements of total suspended sea-spray concentration from a voyage departing Wellington, New Zealand to the Ross Sea [Hartery et al., 2020, Revell et al., 2019]. The modified SSA function reduces the U_{10} wind speed exponent term from 3.14 (as in the Gong [2003] function given in Equation 4) to 2.8 as follows:

$$\frac{dF}{dr} = 2.6u_{10}^{2.8}r^{-A}(1 + 0.057r^{3.45}) \times 10^{1.607e^{-B^2}} \tag{7}$$

5.2.1 Model output

Output for all models was carefully selected to balance the cost of computing time and storage limitations of costly chemistry runs at high temporal output resolution. Both CCN and AOD_{550nm} (AOD calculated at a wavelength of 550nm) were calculated from a number of variables required for multiple routines to reduce computational cost and storage. These calculations have been described in Appendix A.1.1.

6 Methods: Collection of observational data

This section describes how observational datasets used in the evaluation of ACCESS-CM2 were located, collected, and processed for comparison against modelled variables. All observational datasets and the appropriate references have been summarised in Appendix Tables 28 and 29. Firstly, the spatial domain of the Southern Ocean region was defined. There is no consensus regarding the geographic bounds of the Southern Ocean (SO), which has been defined in literature as ranging anywhere between 35°-70°S [Mccoy et al., 2015b, Bodas-Salcedo et al., 2016, Revell et al., 2019, Vergara-Temprado et al., 2018, Swart et al., 2019]. The SO has been defined in this study ranging between 40-60°S to utilise available stations and voyages in that range and align with the spatial output of the Revell et al. [2019] study which also utilises the Hartery et al. [2020] modified SSA source function to facilitate comparison.

6.1 Meteorological observations

Meteorological observation data was sourced from monitoring stations which were both within the defined SO region and deemed as capable of receiving an oceanic signal. These conditions vastly limited available monitoring stations to King Island (TAS), Cape Grim (TAS), and the sub-Antarctic Macquarie Island which were either within 1 km of the coastline, or were represented in the model grid as completely ocean (discussed in Section 7.1). Observational wind-speed was converted to ms^{-1} and resampled to an hourly temporal resolution (from half-hourly) to align with model data. Simulated wind-speed and wind-direction were extracted for meteorological stations by selecting the nearest grid-box. Model and simulated wind-speed and wind-direction were joined on the same dataframe, and model values that did not match with an observational value were dropped to ensure the same length of data for observational and simulated datasets. This approach of selecting for the nearest station, joining on the same dataframe and dropping values lacking an matching observation was applied for all observational comparisons in this thesis.

The Cape Grim station was screened for baseline conditions to avoid terrestrial influence, defined as wind-directions between 190° to 280° which is discussed further in Section 7.1.2 and Appendix A.13.3 (see Figure 16) [Slemr et al., 2015].

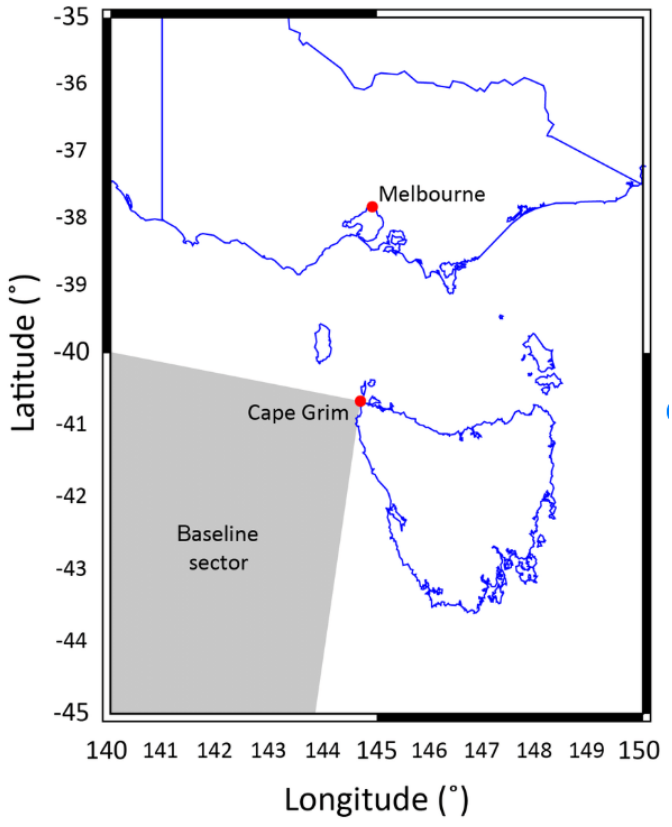


Figure 16: Data at Cape Grim is screened to be within the baseline sector when observed wind-directions are between 190° to 280°. In this baseline sector, data recorded at Cape Grim is considered representative of the Southern Ocean.

Section 7.1.2 compares simulated wind-direction against observed values to evaluate how representative the model is of Southern Ocean conditions. For this evaluation, a metric of model skill was devised as follows. If the wind-direction simulated by the model was within 45° of the observed value (22.5° either side) at a particular timestep, a model skill 'win' array would be awarded with a value of 1 as follows (when applied to all matching observational/simulated timesteps):

$$\text{Model skill} = \frac{\text{wins}}{\text{wins} + \text{losses}} \tag{8}$$

The value of 45° was chosen as a nominal value to identify whether the model and observations were both within the bounds of a cardinal sector.

6.2 Chemical composition and particle size observations

Scarcity of available chemical observations within the simulated timeframe prevents model-observation comparison for the majority of chemical outputs discussed in Section 7.2. For example, the most recently available measurements of DMS were recorded at Cape Grim in 1993 [Ayers et al., 1997b]. Available observational data includes a measure of Chloride ions as a proxy for sea-salt, and a size distribution dataset, which were both measured on voyage campaigns. The first dataset of Chloride ions was recorded half-hourly using an Aerosol Chemical Speciation Monitor (ACSM) on the CAPRICORN II voyage (see Figure 17). An ACSM measures chemical composition and particle mass loading of non-refractory sub-micron aerosol particles including sulfate and chloride (instrument details have been documented in Watson [2017]). Measuring sea-salt using an ACSM faces a number of challenges (outlined in Appendix A.8), but it is possible to obtain a sea-salt signal by using a scaling factor of 51 [Ovadnevaite et al., 2012] which has been successfully implemented in Alroe et al. [2020].

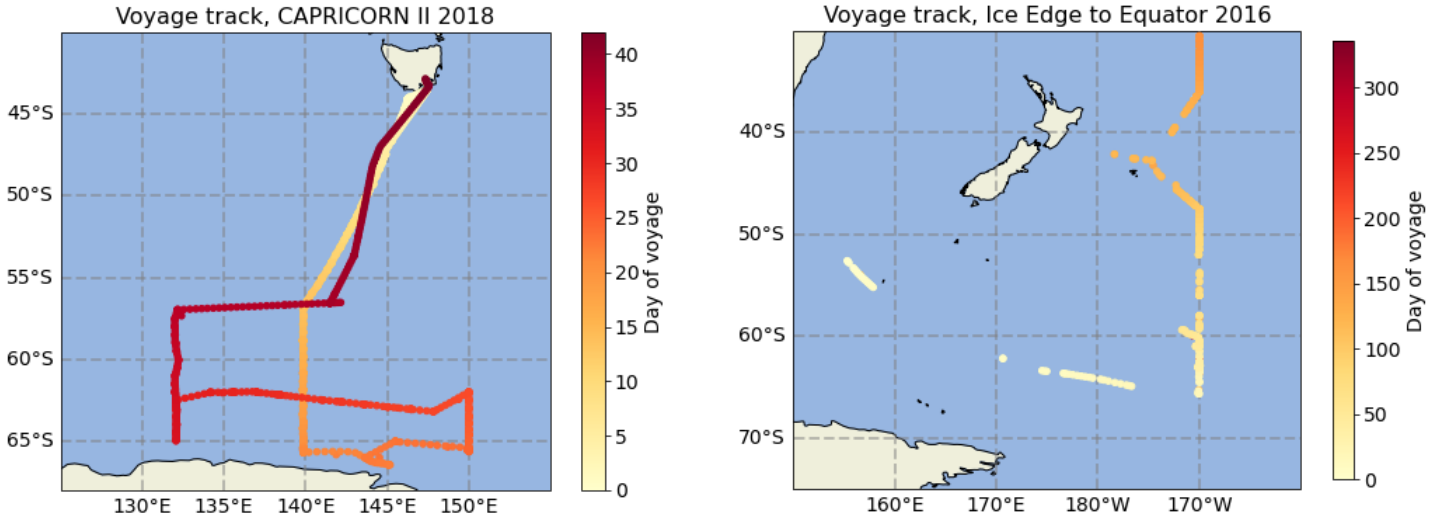


Figure 17: Voyage tracks of CAPRICORN II, and Ice Edge to Equator (I2E) voyages. The CAPRICORN II voyage departed from Hobart (TAS) and reached a maximum latitude of 66.5°S from 11/01/2018 - 22/02/2018. The Ice Edge to Equator voyage departed from Hobart, reached a maximum latitude of 65.7°S and voyaged North towards the equator between 29/04/2016 - 28/05/2016. Each dot represents where an observation has been made, and has passed quality-control screening along the voyage of the respective datasets.

The second observational dataset used within this chemical processes analysis is a measure of size distribution taken on the Ice Edge to Equator (I2E) voyage (see Figure 17) [Law et al., 2017]. This dataset consists of Aerodynamic Particle Sizer (APS) spectrometer measurements which provided data on the size of submicrometer particles up 598nm in diameter, and the remainder was provided by a Scanning Mobility Particle Sizer (SMPS)

instrument. See Appendix A.10 for instrument details. Both ACSM and size-distribution datasets were screened for ship exhaust and continental influence, and resampled to average hourly resolution aligned with model output (see Appendix A.10 for information on data processing and quality control). Peaks in simulated and observed size distributions were located using the python function *scipy.signal.find_peaks*. This function was was able to detect most aerosol modal peaks but struggled for less clearly-defined peaks often simulated in the nucleation mode (shown in Section 7.3).

6.3 Aerosol Optical Depth observations

AOD observations include three monitoring stations and 14 voyage-based measurements. Station-based observations include Cape Grim and two stations at Macquarie Island and Amsterdam Island as part of the Aerosol Robotic Network (AERONET). AOD was measured using a Carter-Scott SPO2 sun photometer at Cape Grim, with an estimated uncertainty of ±0.01 (unitless) [Wilson, 2019]. Both AERONET stations use a Cimel sun-photometer to derive total column AOD with an uncertainty of ±0.01 (unitless) based on a radiative transfer inversion algorithm described in Holben et al. [1998]. See Appendix A.10 for instrumental details and data-processing.

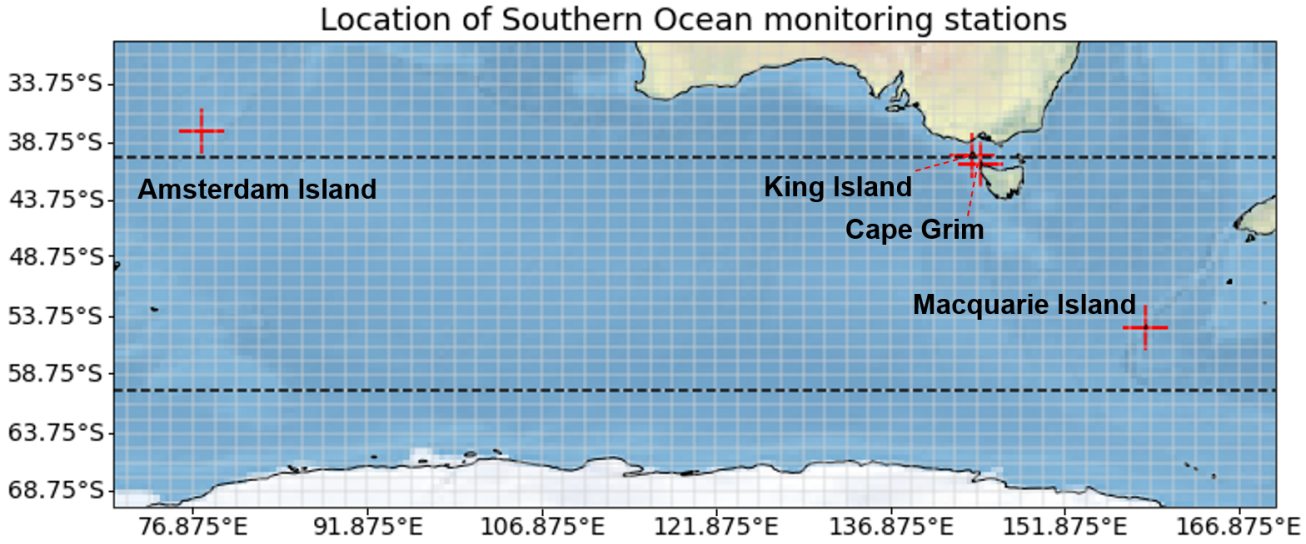


Figure 18: Location of station monitoring stations in the Southern Ocean region. While Amsterdam Island remains slightly above the threshold defined as the Southern Ocean, it has been included within this analysis due to overwhelming long-term observational scarcity. Black dotted lines show the threshold for the Southern Ocean defined in this study as between 40-60°S. White gridded lines provide an representation of the model grid size (1.25° Latitude by 1.875° Longitude). King Island has been plotted in this figure to show location, but only provides meteorological information, not AOD, as described in Section 6.1.

AOD data was collected from 14 voyages which are part of the AERONET Maritime Aerosol network (MAN) (see Figure 19). MAN voyages measured AOD using Microtops II sun-photometers, which have an accuracy to ±0.02 (See Appendix A.10 for quality control and data processing) [Smirnov et al., 2009]. Additionally, fine and coarse-mode AOD data was extracted at the only available long-term station, Macquarie Island. This AERONET product uses a Spectral Deconvolution Algorithm (SDA) to extract modal AOD under the assumption of a bimodal aerosol size distribution (see Appendix A.3). While AOD observational data has come from a variety of sources, all AERONET data was selected at a Level 2 quality which represents cloud-screened data where instruments have been calibrated both pre- and post- field deployment. AOD and SDA-AOD data at all sites and voyages was measured at 500nm, and has been converted to the model-output wavelength of 550nm as follows:

$$AOD_{550nm} = AOD_{500nm}(\frac{550}{500})^{-a} \tag{9}$$

Equation 9: Conversion of AOD_{500nm} to AOD_{550nm}, where a is the Ångström exponent, 1.2.

All AERONET (& Cape Grim) AOD and SDA measurements were averaged hourly with a minimum threshold of 5 observations per month to align with model temporal output. Model values without a matching observation were dropped from analysis datasets (see Appendix A.10 for further details on data processing).

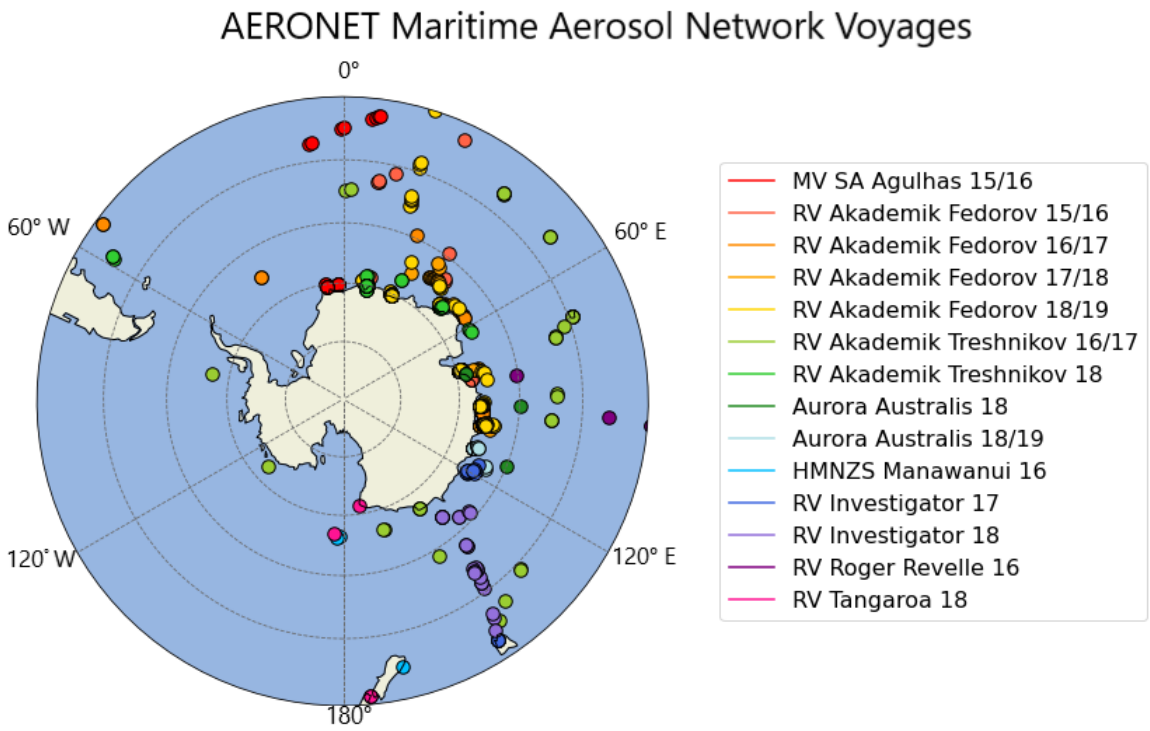


Figure 19: Voyage tracks of AERONET MAN Voyages over the time period 2016–2018. Each dot is representative of where an available AOD measurement has been made, colour-coded for each voyage to indicate the spatial distribution of data.

6.4 Cloud Condensation Nuclei observations

CCN data was collected from two voyages and two stations within the study temporal and spatial bounds. Voyage CCN data at 0.5% SS was collected using CCN-110 CCN counters on both the Antarctic Circumnavigation Expedition (ACE), and the Measurement of Aerosols, Radiation, and Clouds over the Southern Ocean (MARCUS) voyages (see Figure 20). CCN measurements were collected from Cape Grim at 0.5% SS, and Macquarie Island at 0.45% SS and 0.55% SS using similar CCN-100 counters. An estimate of CCN at 0.5% SS at Macquarie Island cannot be made by averaging 0.45%SS and 0.55%SS measurements and instead these observations may be used broadly to determine overall bias, evaluated against the model separately. If a significant proportion of measured aerosols had sizes close to the critical diameter, small changes in the specified SS% may lead to substantial changes in CCN depending on atmospheric conditions (discussed in Section 1.5) [Duplissy et al., 2008, Fossum et al., 2018]. At all stations and voyages, data was quality controlled by standardised filtering and flagging processes (see Stratmann and Gysel [2015] and Appendix A.10).

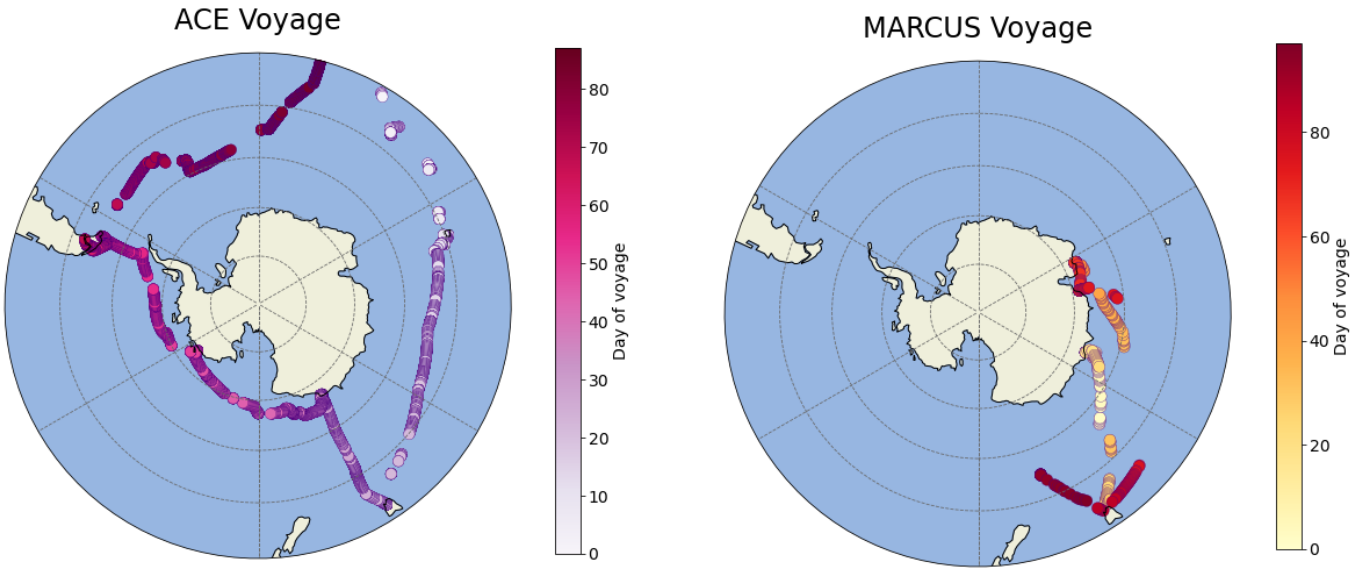


Figure 20: Tracks of the ACE and MARCUS Voyages. Each dot is representative where a CCN measurement has been made and passed through quality-control methods outlined in Appendix A.10. The ACE voyage completed a circumnavigation of Antarctica from 20/12/2016 to 19/3/2017 in the Southern Ocean. The MARCUS voyage collected CCN data from 29/10/2017 to 25/03/2018, departing from Hobart (TAS), and completed four resupply missions to the four Antarctic/sub-Antarctic stations. The individual lines on the right plot show the four resupply voyages within the MARCUS voyage scheme - these have been grouped together in the MARCUS dataset to increase the total data points and facilitate a meaningful comparison with the model as voyages occurred within a similar timeframe.

6.5 Radiation and Cloud Fraction observations

Observational SW TOA All-Sky radiation flux data was obtained from the Clouds and Earth's Radiant Energy System (CERES)-Energy Balanced and Filled (EBAF)-TOA Edition 4.1 product [Loeb et al., 2018]. The TOA SW ↑ Flux defines TOA at 20km altitude, outputs monthly averaged data at a spatial resolution of 1° x 1° Latitude/Longitude and has a uncertainty defined as ±2.5 W/m^2 (see Appendix A.7 for discussion on managing model-observation uncertainty) [Loeb et al., 2018].

Low cloud fraction (defined as between 680-1000hPa) was downloaded from the GCM-Oriented Cloud-Aerosol Lidar and Infrared Pathfinder Satellite Observation Cloud Product (CALIPSO-GOCCP) at a resolution of 2° x 2° Latitude/Longitude [Chepfer et al., 2010]. Direct comparison of model output and satellite-based data is limited in that it does not account for satellite measurement biases. It is recommended to run the Cloud Feedback Model Intercomparison Program (CFMIP) Observation Simulator Package (COSP) online with the model to account for such biases and enable direct model-observation comparison [Bodas-Salcedo et al., 2011]. The implementation of COSP within ACCESS-CM2 was unavailable, but nevertheless a useful comparison may be made. To align with output model values, the CERES-EBAF and CALIPSO-GOCCP data was regridded to the model grid at a 1.25° x 1.85 ° resolution using a bilinear interpolation method (Climate Data Operators function *cdo remapbil*) [Schulzweida, 2019].

This thesis assimilates multiple sources of observational data. While this thesis undertakes efforts to ensure the uncertainty of each observational dataset is accounted for, each instrument used will have differing inherent biases through instrumental setup and calibration factors. See Appendix A.7 for a discussion on uncertainty within observations and model simulations in this thesis.

6.6 Statistical analysis

This thesis follows the lead of atmospheric chemistry model-observation evaluation studies which use common statistical metrics to determine bias, correlation, error, and agreement (as described in Table 8) [Lamarque et al., 2013, Bowman et al., 2013, Gueymard and Yang, 2020, Gliß et al., 2020]. Chapter 7 uses Probability Density Function Histograms to illustrate differences in data distribution, and uses standard deviation as a measure of inter-annual variability.

The lack of ensemble members in this thesis prevents the spatial testing of significance often seen in multi-model evaluations. Meaningful results are hence interpreted through whether model-observation differences fall within the observations' range of uncertainty (see Appendix A.7). As reducing model bias is the key focus within the SO modelling community, this thesis largely focuses on bias metrics in result discussions.

Metric	**Mathematical expression**
Correlation coefficient	$r = \frac{\sum(M_i - \bar{M})(O_i - \bar{O})}{\sqrt{\sum(M_i - \bar{M})^2 \sum(O_i - \bar{O})^2}}$
Mean Bias	$MB = \frac{1}{N}\sum(M_i - O_i) = \bar{M} - \bar{O}$
Root Mean Square Error	$RMSE = \sqrt{\frac{1}{N}\sum(M_i - O_i)^2}$
Normalised Mean Bias	$NMB = \frac{\sum(M_i - O_i)}{\sum O_i} = (\frac{\bar{M}}{\bar{O}} - 1)$
Index of Agreement	$1 - \frac{\sum_{i=1}^{N}(M_i - O_i)^2}{\sum_{i=1}^{N}(\lvert M_i - \bar{O}\rvert^2 + \lvert O_i - \bar{O}\rvert^2)}$

Table 8: Statistical evaluation metrics, adapted from [Yu et al., 2006, Hayman et al., 2014]. The statistic, Index of Agreement, provides a standardised measure of the degree of model prediction error which does not rely on a linear relationship (as does standard metrics of correlation) and is widely implemented for cross-comparisons of different models' performances. This is because the statistic is easily-understood through its range from 0 to 1, where 0 indicates no agreement and 1 indicates perfect model performance [Willmott, 1982, Hayman et al., 2014].

Traditional metrics of bias (NMB) and error (Mean Normalised Absolute Error) create issues of asymmetry and inflation, depending on the sign of the model bias. The statistics, Normalised Mean Bias Factor (NMBF) and Normalised Mean Absolute Error Factor (NMAEF) address both issues and are particularly recommended for use in atmospheric chemistry contexts (discussed in Appendix A.10.1) [Yu et al., 2006]. NMBF is defined as follows:

$$\text{If}\bar{(M)} \geq \bar{O} : NMBF = \frac{\sum M_i}{\sum O_i} - 1 = \frac{\sum(M_i - O_i)}{\sum O_i} = \frac{\bar{M}}{\bar{O}} - 1 \tag{10}$$

$$\text{If}\bar{(M)} \leq \bar{O} : NMBF = \left(1 - \frac{\sum O_i}{\sum M_i}\right) = \frac{\sum(M_i - O_i)}{\sum M_i} = \left(1 - \frac{\bar{O}}{\bar{M}}\right) \tag{11}$$

NMAEF is defined as follows:

$$\text{If}(\bar{M}) \geq \bar{O} : NMAEF = \frac{\sum |M_i - O_i|}{\sum O_i} \tag{12}$$

$$\text{If}(\bar{M}) \leq \bar{O} : NMAEF = \frac{\sum |M_i - O_i|}{\sum M_i} \tag{13}$$

where M = model & O = observed values.

NMBF is interpreted where if NMBF is positive, the model overestimates observations by a factor of NMBF + 1. If NMBF is negative, the model underestimates observations by a factor of 1-NMBF. For example, an NMBF of 1.1 indicates that the model overestimates observations by a factor of 2.1, and a NMBF of -1.1 indicates the model underestimates observations by a factor of 2.1. While NMBF has been used as an improved metric of bias, NMB has also been calculated where necessary to ensure evaluation against previous studies is possible (see Table 4).

7 Results

Based on the methodologies outlined in Chapter 6, Section 7.1 compares simulated wind-speed and direction against observations. Section 7.2 compares the output concentration of chemical species between simulations and evaluates simulated sea-salt concentrations and size-distributions against available observations. Sections 7.4 and 7.5 compare simulated AOD and CCN against observations seasonally and spatially, respectively. Finally, Section 7.6 compares modelled CDNC, TOA SW ↑ radiation, and Cloud Fraction between simulations and against satellite-based observations. Results have been discussed as they are presented in context of study findings.

7.1 Meteorological validation

The modelled meteorological variables, wind-speed and wind-direction, are compared to the reanalysis dataset used in the model nudging routine (described in Appendix A.4). Descriptions of ACCESS-CM2 meteorology in this section refer to BASE run output. All model data at a station-level has been subset using the nearest model gridbox. Simulated wind-speed was analysed to ensure that the nudging routine in ACCESS-CM2 was functioning correctly, and to evaluate whether the model realistically represented observed wind-speed as both the PMOA and sea-salt emission routines utilise wind-speed (see Section 5.2). Simulated wind-direction was evaluated against observations to determine whether the model captured the same provenance of air parcels as observations, and how accurately the model would be able to screen for baseline conditions at Cape Grim.

7.1.1 Wind speed:

This section demonstrates that ACCESS-CM2 reproduced consistent wind-speed across perturbation simulations, indicating a successful implementation of the nudging routine. ACCESS-CM2 exhibited considerable bias compared to station observations dependent on the station and season; this bias was greatest in summer and smallest in winter. Underestimation of wind-speed by the model would result in fewer wind-generated SSA, which would likely reduce mass-dominated AOD and number-dominated CCN values.

The BASE and perturbation simulations exhibited mean wind-speeds within a maximum difference of 0.131% of each other, representing the nudging functioning as anticipated. Consistent meteorology between simulations was important to ensure that changes in aerosols were the result of changes to aerosol/chemistry schemes, not fluctuations in meteorology. ACCESS-CM2 exhibited good correlation of 0.995 and agreement (IOA=0.747)

with ERA-I nudging data averaged over the SO, shown in Figure 21. However, the model underestimated wind-speed by approximately 5.10% (Table 9). Discrepancy between reanalysis and simulated surface wind-speed can be expected as nudging occurs within the free troposphere; boundary-layer meteorology is dependent on model meteorological dynamics.

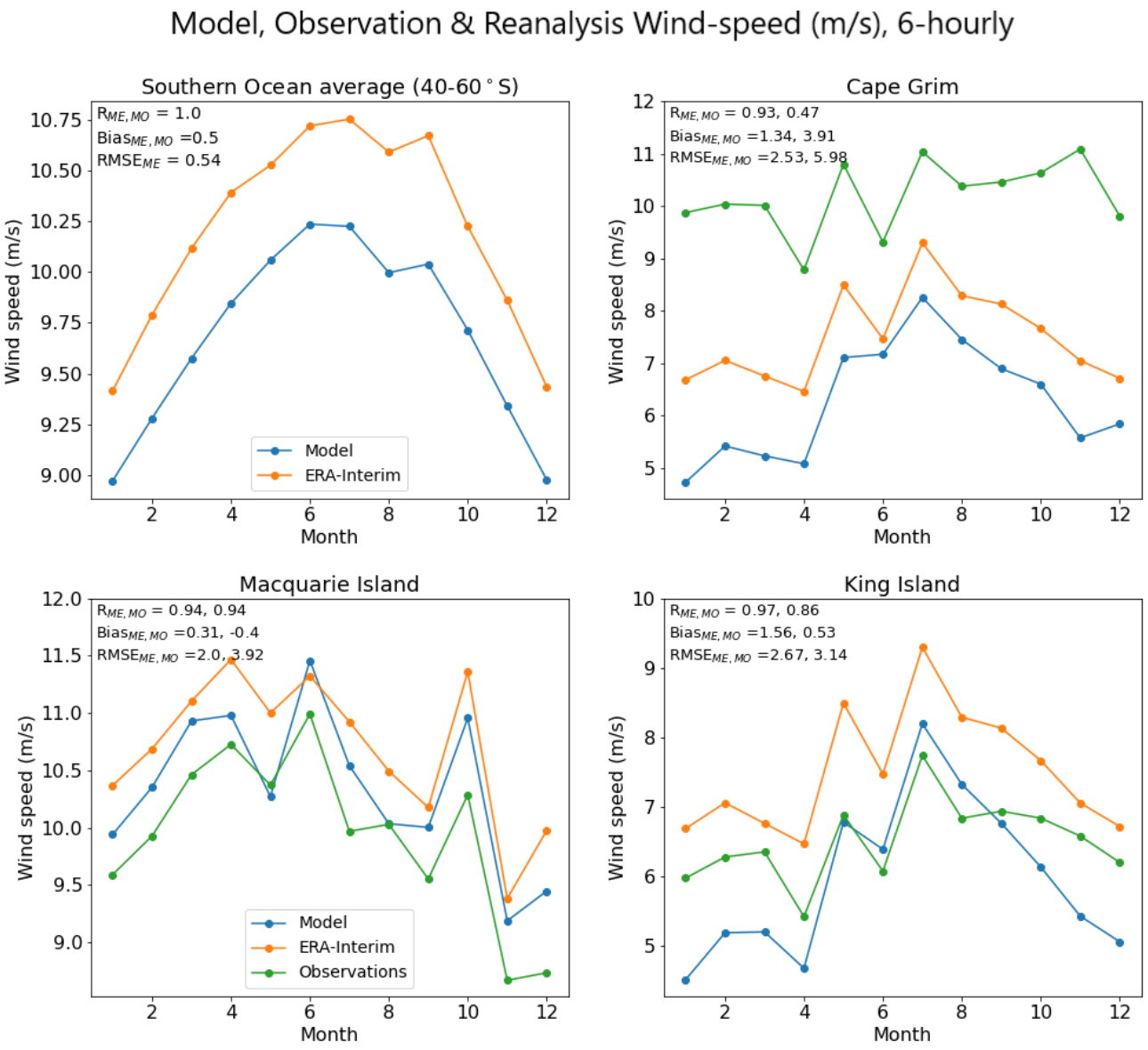


Figure 21: Average model, reanalysis and observational surface wind-speed averaged over the Southern Ocean (40–60°S), and selected for the nearest gridpoint at Cape Grim, Macquarie Island, and King Island. Data was selected at 6-hourly intervals to align with the nudging routine and grouped monthly from 2016–2018. Similar bias metrics were observed when data was averaged 6-hourly. ME = comparison of ACCESS-CM2 model and ERA-I, MO = comparison of ACCESS-CM2 and observations, R = correlation, RMSE = Root Mean Square Error (defined in Table 8).

ACCESS-CM2 exhibited increased bias when compared against observations, and exhibited further decreases in agreement at all stations (compared to ACCESS-CM2-ERA-I statistics) (Tables 10, 11, & 12). Model-observation bias was not consistently negative (as in comparisons with ERA-I). ACCESS-CM2 reported a negative bias at Cape Grim (NMBF= -0.621) and positive bias at Macquarie Island (NMBF= 0.0402). The model performed particularly poorly at Cape Grim with a correlation of 0.468 and IOA of 0.075, compared to a correlation of 0.940 and IOA of 0.885 at Macquarie Island. NMBF between ACCESS-CM2 & observations improved at all stations in winter due to increases in standard deviation; this brought simulated and observed wind-speed values to closer agreement (Tables 33, 35, & 37). For example, at Cape Grim the model standard deviation was 1.6 times larger than the observed variability. This analysis has shown that ACCESS-CM2 under-simulates wind-speed compared to Cape Grim and King Island observations, particularly so in summer-time. Therefore, a reduced flux of wind-generated aerosols could be expected in summer which would reduce both simulated AOD and CCN, and vice versa for overestimations of wind-speed (and consequently wind-generated aerosols) at Macquarie Island.

Southern Ocean Average	BASE	ERA-I
Mean	9.69	10.2
Minimum	8.97	9.41
Maximum	10.2	10.8
Standard deviation	0.438	0.465
Relative Difference		-5.10
Correlation		0.995
Bias		-0.521
NMBF		-0.0538
RMSE		0.523
NMAEF		0.0538
IOA		0.747

Table 9: Statistical summary of model, reanalysis and observational wind-speed averaged spatially over the Southern Ocean (data selected every 6 hours, averaged 2016–2018).

Cape Grim	BASE	ERA-I	OBS
Mean	6.28	7.51	10.2
Minimum	4.73	6.46	8.78
Maximum	8.26	9.30	11.1
Standard deviation	1.06	0.845	0.661
Relative Difference		-16.7	-38.4
Correlation		0.930	0.468
Bias		-1.22	-3.90
NMBF		-0.195	-0.621
RMSE		1.29	4.02
NMAEF		0.195	0.621
IOA		0.667	0.075

Table 10: Statistical summary of model, reanalysis and observational wind-speed at Cape Grim (data selected every 6 hours, averaged 2016-01-01 to 2018-10-22 with available data, N = 21460).

Macquarie Island	BASE	ERA-I	OBS
Mean	10.3	10.7	9.94
Minimum	9.19	9.38	8.67
Maximum	11.5	11.5	11.0
Standard deviation	0.641	0.606	0.687
Relative Difference		-3.25	4.10
Correlation		0.944	0.940
Bias		-0.347	0.400
NMBF		-0.0335	0.0402
RMSE		0.407	0.463
NMAEF		0.0357	0.0419
IOA		0.899	0.885

Table 11: Statistical summary of model, reanalysis and observational wind-speed at Macquarie Island (data selected every 6 hours, averaged 2016-01-01 to 2018-12-31, N = 24077).

King Island	BASE	ERA-I	OBS
Mean	5.97	7.51	6.51
Minimum	4.51	6.46	5.41
Maximum	8.19	9.30	7.74
Standard deviation	1.10	0.845	0.570
Relative Difference		-21.1	-8.83
Correlation		0.972	0.859
Bias		-1.54	-0.539
NMBF		-0.258	-0.0904
RMSE		1.58	0.863
NMAEF		0.258	0.126
IOA		0.592	0.743

Table 12: Statistical summary of model, reanalysis and observational wind-speed at King Island (data selected every 6 hours, averaged 2016-01-01 to 2018-12-31, N = 24194).

The ratio of land to ocean within a model gridbox was investigated in Appendix A.11.2 as a source of simulated wind-speed bias. A negative relationship was noted between the amount of land within a gridbox and model-observation wind-speed correlation, although limited station data prevents this relationship from being stated with confidence.

7.1.2 Wind direction

This section shows that ACCESS-CM2 was only able to capture observed wind-direction within 45° under half of the time. This has important implications for future modelling work screening for baseline conditions at Cape Grim, and informs baseline-screening methods used in this research.

The following discussion evaluates how well simulated wind-direction agrees with observations through the metric of model skill defined in Chapter 6 at Macquarie Island and Cape Grim which have available aerosol data for the remaining analysis. ACCESS-CM2 was able to capture the dominant South-West (SW) wind-direction at Cape Grim but underestimated wind-speeds (Figure 22). Similarly, the model was able to capture dominant observed wind-directions at Macquarie Island, but exhibited skew towards SW directions (Figure 23). Model skill has been calculated for cardinal and inter-cardinal wind-directions within a maximum angle of 45°, 22.5° either side of the simulated angle. At Cape Grim and Macquarie Island, model skill was averaged at 0.427 and 0.401 respectively, with increased model skill in the SW (largely baseline) sector reported as 0.431 at Cape Grim and 0.418 at Macquarie Island. Thus, ACCESS-CM2 captures observed wind-direction less than half the time at both stations.

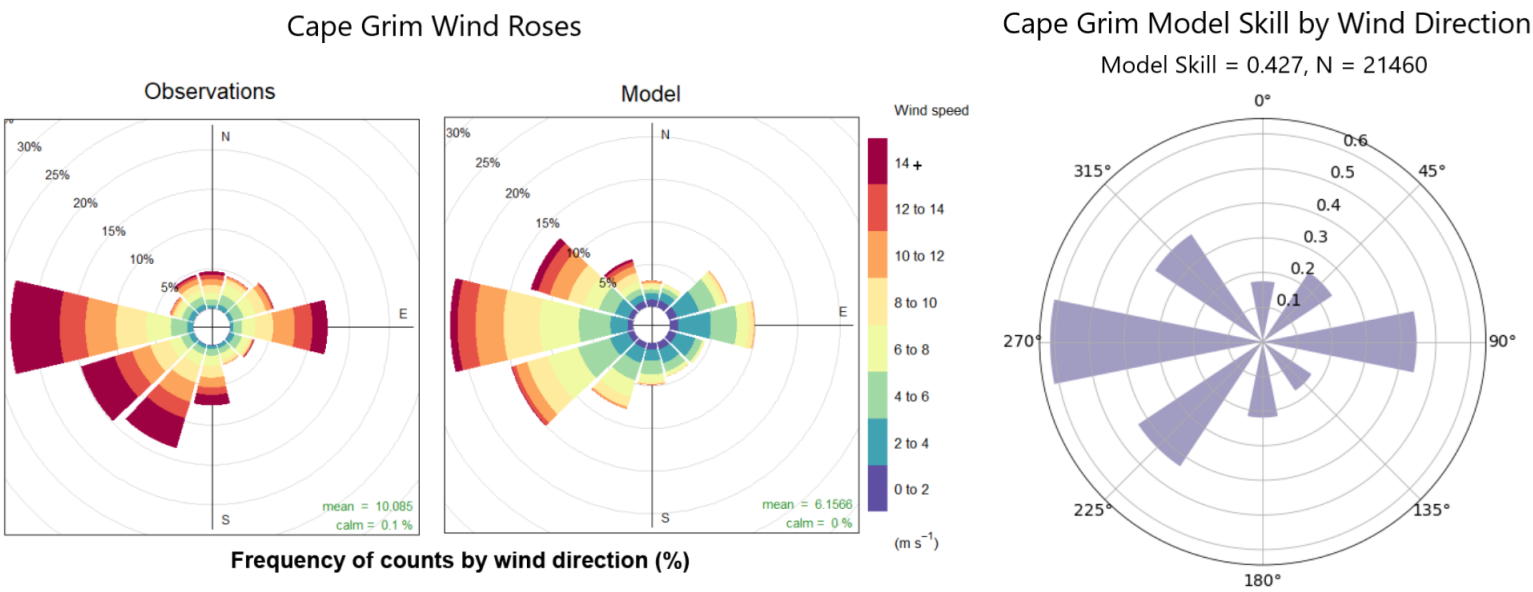


Figure 22: Wind roses of observational and simulated wind-speed and direction. The dominance of green and yellow colours in the 'Model' plot show that the model over-represented lower wind-speeds compared to the model, which had a larger proportion of wind-speeds in red colours (faster wind-speeds). The figure on the right shows the model skill grouped by wind direction. This plot shows how frequently the model captured the observed wind direction within a maximum angle of 45° (22.5° either side of the simulated angle).

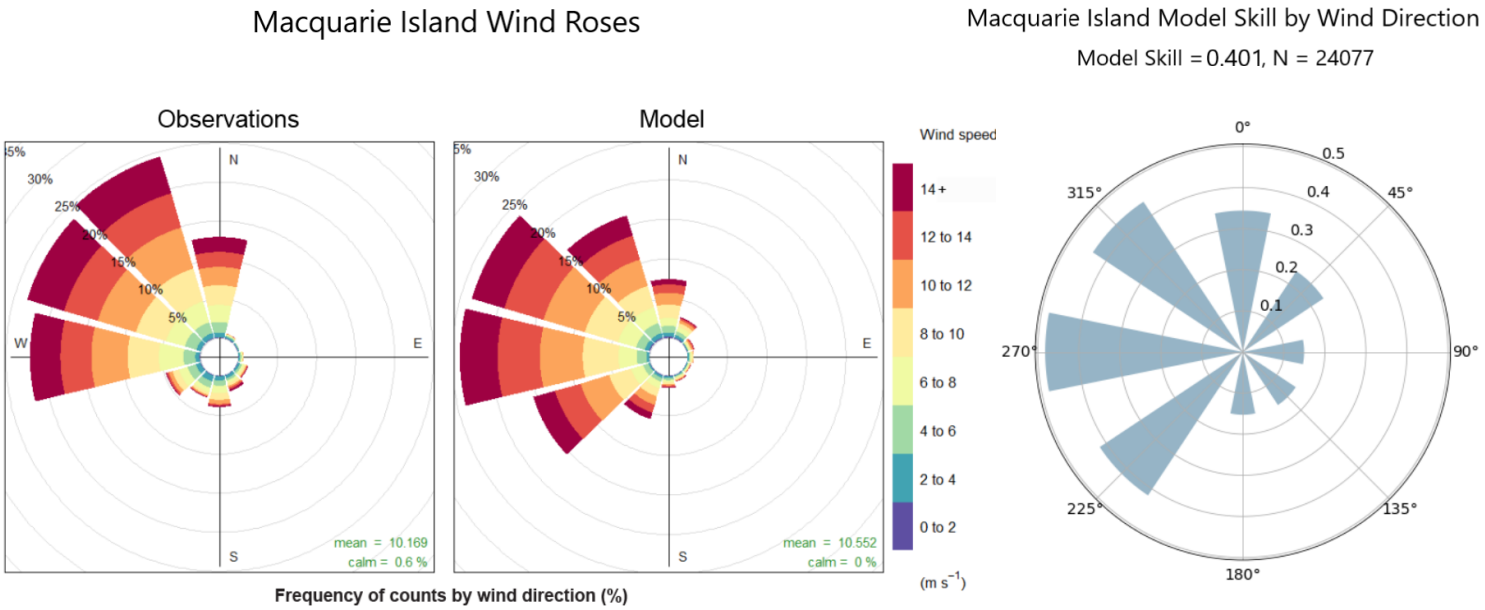


Figure 23: Wind roses of observational and simulated wind-speed and direction. The figure on the right shows the model skill grouped by wind direction.

Poor model skill in wind-direction ensures ACCESS-CM2 cannot be screened for baseline conditions at Cape Grim using simulated wind-direction. Instead, all datasets at Cape Grim have been aligned on matching time-steps and screened using observational wind-directions. All other stations and voyages are unable to use baseline screening methods (see Appendix A.13.3 for an example). For these observations, poor model wind-direction skill suggests that ACCESS-CM2 may sample air masses with different provenances than observed. While sea-salt has a largely homogeneous source over the SO (over aerosol lifetimes), biogenic aerosols such as PMOAs have strong regional variations. Poor simulated wind-direction may result in different aerosol populations being sampled from varying spatial sources between the model and observations. Sampling different air-masses compared to observations is discussed in reference to AOD and CCN Probability Density Function distributions in Figures 37 & 49 later.

Summary of model meteorological evaluation:
Based on the preliminary analysis conducted in this section, we conclude:

- The nudging routine was successfully implemented in ACCESS-CM2 as all perturbation runs exhibited mean wind-speeds within 0.13% of each other ($0.02\,\mathrm{ms}^{-1}$)
- Model bias varied between observational stations subject to seasonal variations with increased model skill in winter
- Underestimation of observed wind-speed at Cape Grim would result in lower simulated emissions of sea-salt. Conversely, at Macquarie Island, overestimation of wind-speed would lead to too much modelled sea-salt. This is important for AOD and CCN interpretations later (Sections 7.4 & 7.5)
- ACCESS-CM2 cannot be screened for baseline conditions at Cape Grim with high confidence due to low skill in wind-direction simulation
- These findings have informed future methods in this thesis where all model baseline Cape Grim datasets have been screened using observational wind-direction

7.2 Model Chemistry

This section provides an analysis of chemical composition and processes within ACCESS-CM2, and how these features have changed with perturbations to the model. Firstly, this section compares how perturbations in the model affect the concentration of chemical species, and utilises available observations of sea-salt to draw a conclusion of model sea-salt bias. Secondly, oxidation processes are investigated both seasonally and zonally, and aerosol size distributions are compared against observations to identify biases.

7.2.1 Chemical species

This section demonstrates that using online or offline chemistry schemes produces vastly different chemical concentrations, particularly DMS and its oxidation products. Online chemistry increased emissions of oxidants, resulting in suppressed sea-salt concentrations. The following analysis focuses on sulfur-containing compounds that are most relevant to Southern Ocean aerosols. Output chemical concentrations were extracted, converted to the most commonly used units, averaged over the Southern Ocean and plotted to facilitate inter-simulation comparison in Figure 24. It is important to note that the output concentrations shown in Figure 24 are the result of competing source and sink processes.

DMS: Models followed the well-known seasonal cycle of DMS with a maximum in summer and a minimum in winter [Ayers et al., 1997a]. The PMO and BASE models utilise the same offline DMS scheme and exhibit a similar seasonal DMS distribution that differed by 0.239% annually. The CHEM run, which used an online DMS emission scheme, departed from this pattern and exhibited increased concentrations from autumn despite an increased A-factor for DMS oxidation by OH (Tables 3 & 7). CHEM DMS concentrations reached a maximum difference from the BASE run in winter (183% larger) and returned to BASE/PMO values in spring (relative difference -4.02%). The increase in CHEM-simulated DMS in autumn and winter months may be representative of increases in online DMS emissions compared to offline pre-computed DMS emissions in the BASE & PMO runs. Alternatively, this may be due to a decreased DMS sink through a lack of DMSO production in the CHEM run, despite having an additional DMS oxidation reaction compared to offline chemistry (Tables 3 & 7).

SO_2: All simulations captured the seasonal cycle of SO_2, which exhibits a similar cycle to DMS mentioned above [Ayers et al., 1997b]. Opposite to DMS, the CHEM run simulated lower concentrations of SO_2 in Autumn by 11.2% (compared to the BASE run), and increased to be 7.97% larger than the BASE run in summer. Both offline schemes simulated similar SO_2 seasonal distributions and differed by 1.66% annually. Interpreting simulated

SO_2 concentration is difficult as it is involved in multiple chemical processes as both a reactant and a product. Decreased SO_2 values in the CHEM run could be indicative of an increased sink term from autumn to spring, such as increased gas-phase oxidation (SO_2 + OH $\rightarrow$ H_2SO_4 + HO_2). Additionally, decreased concentrations may be the result of deficiencies in source terms such as the lack of DMSO (which produces SO_2) in online chemistry, or a reduction in cloud-processing (see Equation 2). Section 7.2.2 investigates these potential causes further.

H_2SO_4: H_2SO_4 concentrations showed the largest discrepancy between simulations, with maximum differences occurring in summer. All models captured seasonal trends following what is expected of nss-sulfates (maximum in summer, minimum in winter). The BASE run had the highest average concentration of $1.54e^{10}$ molec cm^{-3} in summer, and a minimum concentration of $0.285e^{10}$ molec cm^{-3} in winter. Relative to the BASE run, the PMO and CHEM runs exhibited differences of -22.7% and -85.4% in summer, and -15.2% and -66.3% in winter respectively. Decreases in CHEM-simulated H_2SO_4 may represent decreased gas-phase SO_2 oxidation, or increased nucleation processes which consume H_2SO_4 (described in Section 3.1.2). Injection of OM into the PMO-run Aitken-mode increases Aitken-mode surface area which may act as a condensation sink for H_2SO_4. This may explain the decreased PMO-run output of H_2SO_4 in biologically-active spring and summer seasons.

Oxidants:
For all oxidant species (OH, H_2O_2, O_3, and NO_3), the BASE & PMO runs share the same prescribed oxidant emission outputs, hence comparison is conducted between online chemistry (CHEM) and offline chemistry.

OH: Offline and online simulations exhibited a similar seasonal cycle of differing magnitudes where online chemistry was biased higher by a factor of 2507 (NMBF = 2506) (seen more clearly in Figure 25). It would be difficult to attribute increased concentrations of CHEM-simulated OH to any particular reaction, as OH is involved in numerous reactions (Table 7). Due to the relatively constant annual bias, it is likely that online chemistry has increased OH emissions.

O_3: Expected seasonal distributions of O_3 are simulated in both online and offline chemistry (minimum in summer and maximum in winter) [Oltmans et al., 2006]. Online chemistry exhibited increased O_3 output concentrations by 67.3% in summer and 32.4% in winter relative to offline chemistry, with an annual NMBF of 0.417. The role of O_3 in offline and online chemistry is discussed further in Section 7.2.2.

NO_3: Offline and online simulations followed a similar seasonal distribution of NO_3, but instead online chemistry reported a consistent negative bias with a relative difference of -91.6% in summer and -90.5% in winter compared to offline chemistry (annual NMBF=-9.43).

DMSO: The seasonal cycle of DMSO was captured by both offline models, BASE and PMO, and differed by -0.433% annually due to a shared DMS chemistry scheme. The BASE run exhibited an maximum average value of 13.6 ppt in summer, and a minimum of 0.540 ppt in Winter. While the CHEM run exhibited trace amounts of DMSO, this is a remnant of the model file used to initialise the CHEM simulation at the first timestep, and is negligible as it is not included within the chemistry scheme (Figure 25).

HO_2: Offline and online simulations represented the seasonal distribution expected of HO_2 (peak in summer, minimum in winter). Again, online chemistry exhibited substantially higher concentrations of HO_2 by a factor of e^5; 1450 times larger in summer and 1903 times larger in winter relative to offline chemistry (annual NMBF = 1542). As the product of gaseous SO_2 oxidation, it may be concluded that the online scheme simulates increased gas-phase oxidation. However, this bias was relatively consistent seasonally hence further analysis in Section 7.2.2 has determined whether this is the case, or whether increased online-simulated HO_2 is the artefact of increased online oxidant emissions.

Sea-salt: Averaged over the SO, sea-salt concentration was fairly constant seasonally in all models, although a seasonal cycle would be expected. The PMO had the highest output sea-salt concentration with an average value of 14.3 $\mu g/m^3$, and differed from the BASE run by 0.0885% annually as both simulations share offline sea-salt emissions. The CHEM and SSALT runs simulated average values of 10.8 $\mu g/m^3$ and 6.30 $\mu g/m^3$, 24.5% and 55.9% lower than the BASE run respectively. Decreased CHEM sea-salt concentrations are discussed further in Section 7.3.

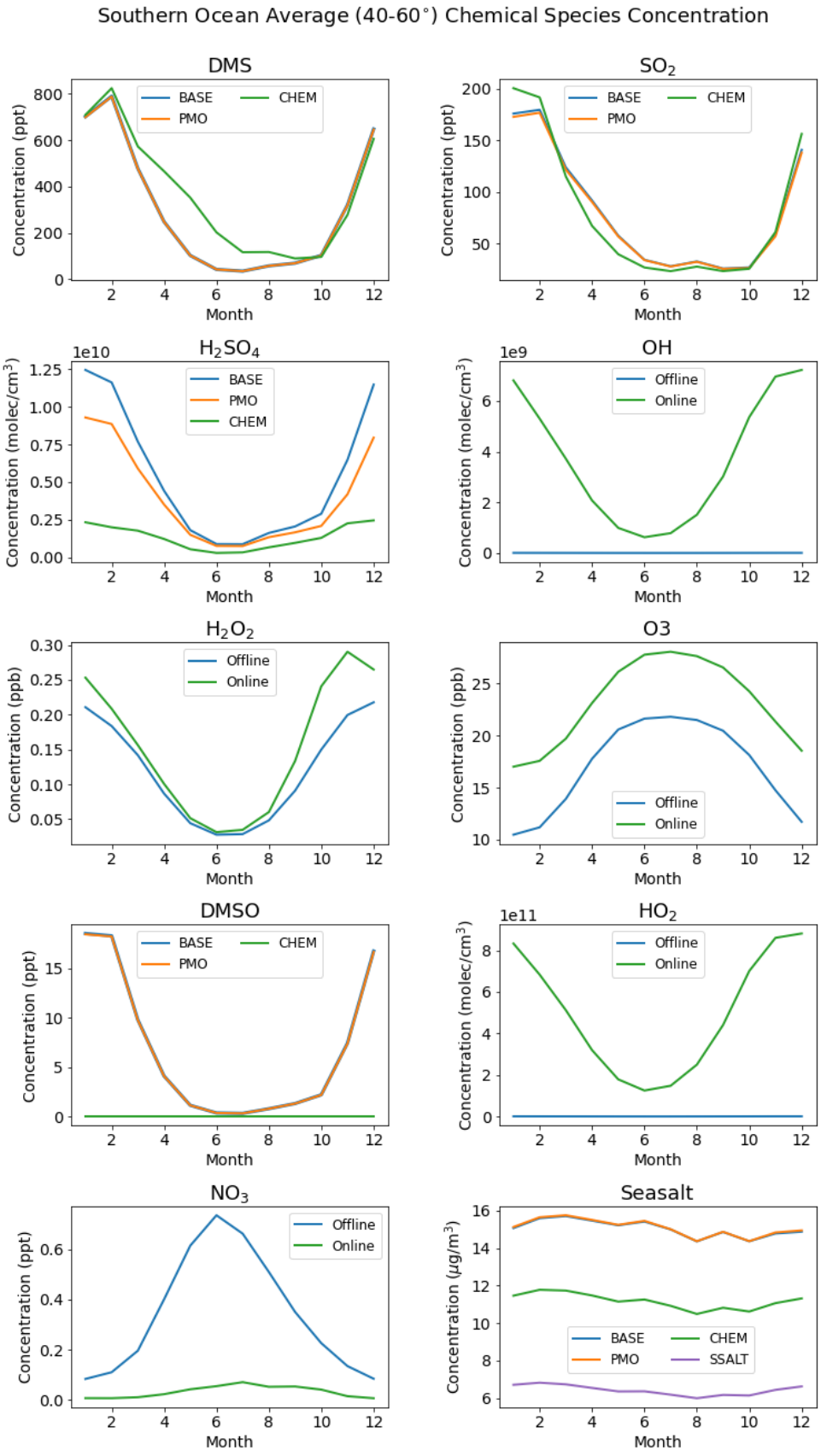


Figure 24: Annual cycle of output chemical species for the BASE, PMO, CHEM, and SSALT model. Data utilises the hourly model output from 2016–2018 for each simulation, grouped by month and averaged accordingly.

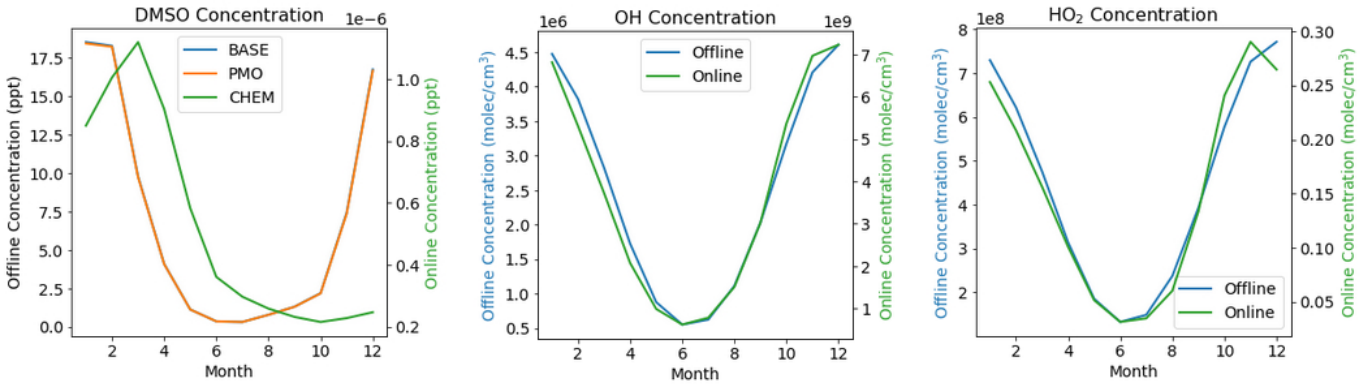


Figure 25: DMSO, OH, and HO_2 model output concentration plotted on two axes to identify seasonal cycles. The colour of the axis text corresponds to the colour of the line plotted.

Having established changes to mean sea-salt incurred via model perturbations, we next compare simulated sea-salt against observations to establish bias. Figure 26 shows a comparison of observed ACSM Cl^- multiplied by a factor of 51 as outlined in Section 6.2, and simulated accumulation-mode sea-salt corresponding to the track of the CAPRICORN II Voyage. All simulations underestimated both mean accumulation-mode sea-salt concentration and variability compared against observations. Appendix A.7 describes the limitations of the ACSM instrument and explains why comparison against accumulation-mode particles is most suitable as the ACSM is unable to capture larger particle sizes. While all simulations reported good correlations against observations above 0.76, the BASE, PMO, CHEM and SSALT runs underestimated accumulation-mode sea-salt concentrations by 79.9%, 80.2%, 85.2% and 89.1% respectively (13). Figure 26 also shows the lack of variability in all simulations compared to observations, most notably seen in the modified sea-salt source function SSALT run with a standard deviation of 0.0350 compared to observations of 0.937.

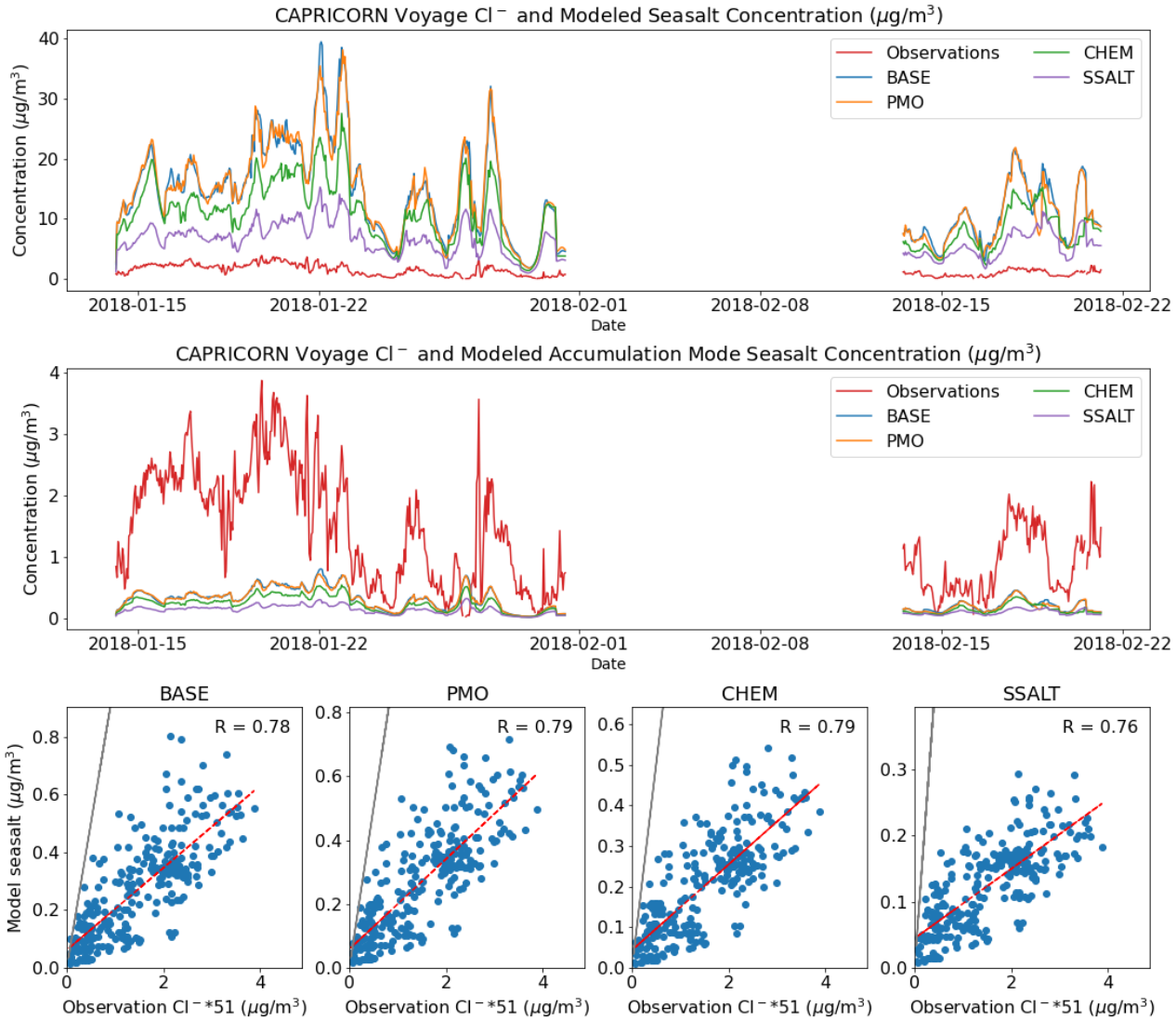


Figure 26: Comparison of observed Cl^- recorded on an ACSM on the CAPRICORN II Voyage. The top panel shows observed Cl^- compared against total output sea-salt for all model runs, which is the sum of the accumulation and coarse mode sea-salt. The middle panel shows observations compared to simulated accumulation-mode sea-salt. The bottom panel shows correlation plots comparing observed Cl^- with simulated accumulation-mode sea-salt respective for each model simulation, as the accumulation mode provided a fairer comparison with ACSM data.

It is clear that all ACCESS-CM2 simulations underestimated both the magnitude and variability of mean observed sub-micron sea-salt concentration. Perturbation simulations worsened simulated accumulation-mode sea-salt bias, where the BASE run performed the best and the SSALT run exhibited the worst bias (Table 13). As coarse-mode sea-salt observations were unavailable for comparison to models at this stage, clear conclusions of the overall sea-salt bias cannot be drawn yet. Section 7.4.6 provides a proxy for coarse-mode sea-salt and discusses model bias further.

CAPRICORN II sea-salt	OBS	BASE	PMO	CHEM	SSALT
Mean	1.53	0.278	0.274	0.204	0.125
Min	0.0340	0.0163	0.0177	0.0118	0.00874
Max	3.88	0.802	0.717	0.541	0.294
Relative Difference (%)		-1.25 (-77.6%)	-1.25 (-78.1%)	-1.32 (-83.6%)	-1.40 (-89.1%)
Correlation		0.782	0.792	0.788	0.763
Bias		-1.25	-1.25	-1.32	-1.40
NMB		-0.817	-0.820	-0.866	-0.918
NMBF		-4.48	-4.57	-6.47	-11.2
RMSE		1.49	1.49	1.57	1.66
NMAEF		4.48	4.57	6.47	11.2
IOA		0.184	0.182	0.131	0.0628
Standard deviation		0.170	0.167	0.125	0.0645

Table 13: Statistical summary of observed ACSM Cl^{-}**51 and simulated accumulation-mode sea-salt over the CAPRICORN II Voyage. All mean model-observation differences are outside the threshold of observational variability defined in Appendix A.7 (0.0174).

Comparison of chemical output species has indicated contradictory suggestions for how sulfur is transformed differently using online chemistry in ACCESS-CM2. Decreased SO_2 and increased HO_2 concentration outputs suggested a potential increase in gas-phase oxidation or merely an increase in oxidant species concentration, while decreased H_2SO_4 concentration suggested decreased gas-phase oxidation. The next section clarifies these relationships by examining sulfur oxidation pathways.

7.2.2 Oxidation pathways

Implementation of online chemistry resulted in increased gas-phase and aqueous-phase oxidation by H_2O_2, associated with increased oxidant availability as rate-limiting reagents. Increased gas-phase oxidation and cloud-processing would likely result in increased particle size/number, and CCN size respectively. Despite increased availability of O_3, online chemistry decreased aqueous-phase oxidation via O_3, suggesting the involvement of further factors such as cloud fraction.

Comparison of gaseous and aqueous oxidation reactions in each simulation can provide insight into how sulfur is transformed, which has important implications for aerosol size and formation. As described in Section 1.5, gas-phase oxidation forms H_2SO_4 via the reaction in Equation 1, ($SO_{2(g)} + OH_{(g)} \longrightarrow H_2SO_{4(g)} + HO_{2(g)}$). Gas-phase oxidation can increase particle size or number depending on whether the molecule condenses with existing particles (size) or water-vapour (number). The CHEM run exhibited a substantial increase in total-column gas-phase SO_2 oxidation by an average of 68.9% in summer and 89.5% in spring compared to the BASE run (Figure 27). All model runs represented the expected seasonal cycle with a winter minimum and summer maximum coinciding with maximum availability of the photolytically-produced OH reactant. Decreased OH oxidant availability in winter (shown in Figure 24) saw the CHEM run reduce to only 27.4% larger than the BASE run. Both offline models exhibited a similar flux and hence differed by only -1.97% annually.

Zonally averaged gas-phase oxidation flux followed the zonal distribution of the rate-limiting oxidant OH with decreasing flux towards higher latitudes as oxidant concentration reduced (Figure 28). The CHEM run flux was 58.1% larger at 40°S and 43.5% larger at 60°S relative to the BASE run. A potential reason for increased gas-phase oxidation in the CHEM run is increased OH oxidant concentration compared to the BASE run, particularly in summer months and lower latitudes with higher photolytic production of OH. However, we note that the output concentration is following the chemistry timestep, and is the result of both source and sink processes (so this does not provide the value of OH before gaseous oxidation reactions).

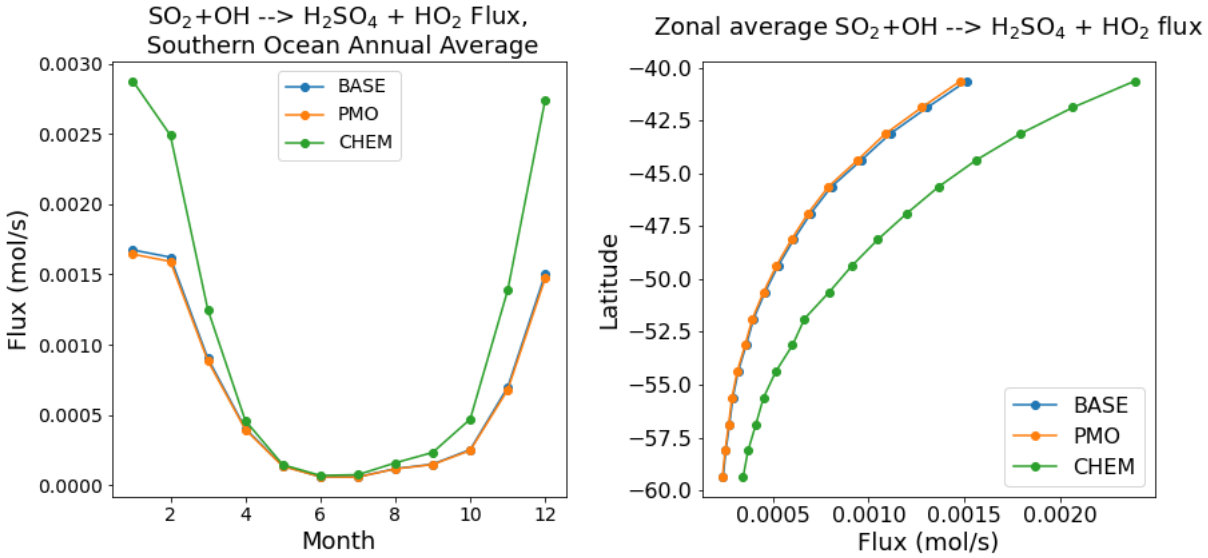


Figure 27: Seasonal and zonal distribution of total-column gas-phase SO_2 oxidation flux ($\mathrm{mol\,s^{-1}}$). These values are indicative of the total sulfate flux produced by the reaction of SO_2 with OH.

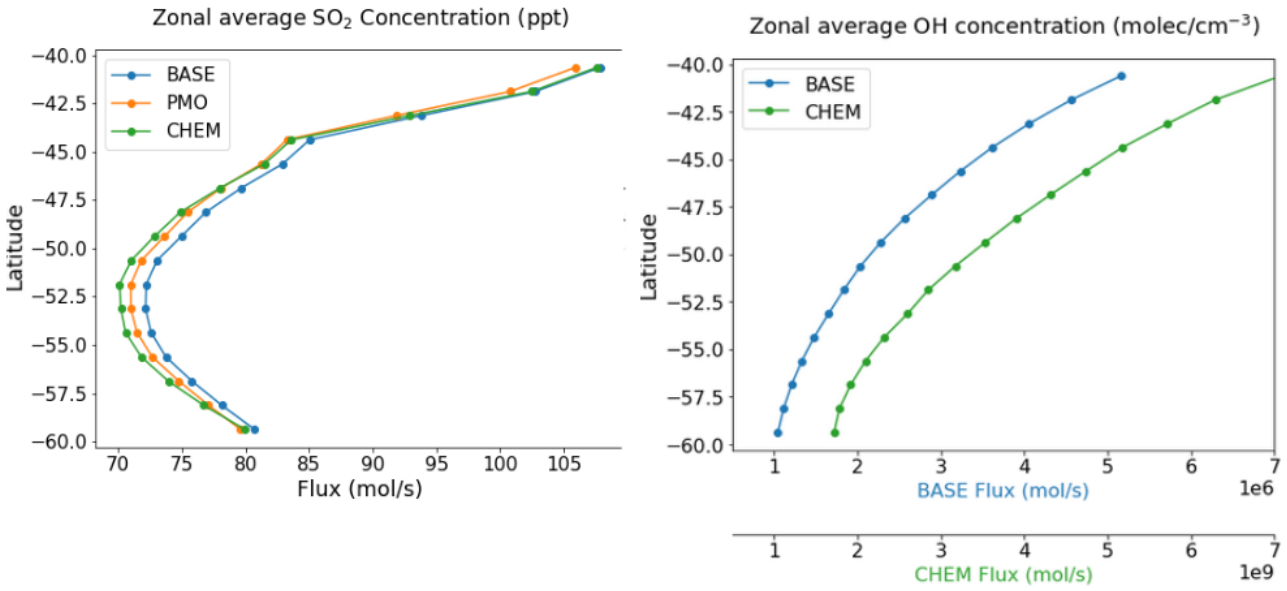


Figure 28: Zonal distribution of simulated SO_2 and OH (output following source and sink processes). Note the different magnitudes on the x-axis for the offline (BASE) and online (CHEM) model where the online oxidant concentration is a magnidue of three times larger.

Aqueous-phase oxidation provides an indication of chemical cloud-processing via H_2O_2 and O_3 and informs interpretation of Hoppel minimums on size distributions (illustrated later in Section 7.3). Changes in oxidation pathways are important to understand as aqueous-phase oxidation is more efficient at producing sulfate aerosols than gas-phase oxidation, and will therefore have larger impacts on AOD and CCN [Revell et al., 2019]. The CHEM run exhibited increased oxidation by H_2O_2 annually, and was larger than the BASE run by 21.7% in summer, and by 54.7% in winter. Oxidation by O_3 saw an increased summer-time flux in the CHEM run, but decreased to 32.9% lower than the BASE run in winter months. Both offline simulations exhibited similar flux values which differed annually by 1.08% and 2.44% for oxidation by H_2O_2 and O_3 respectively.

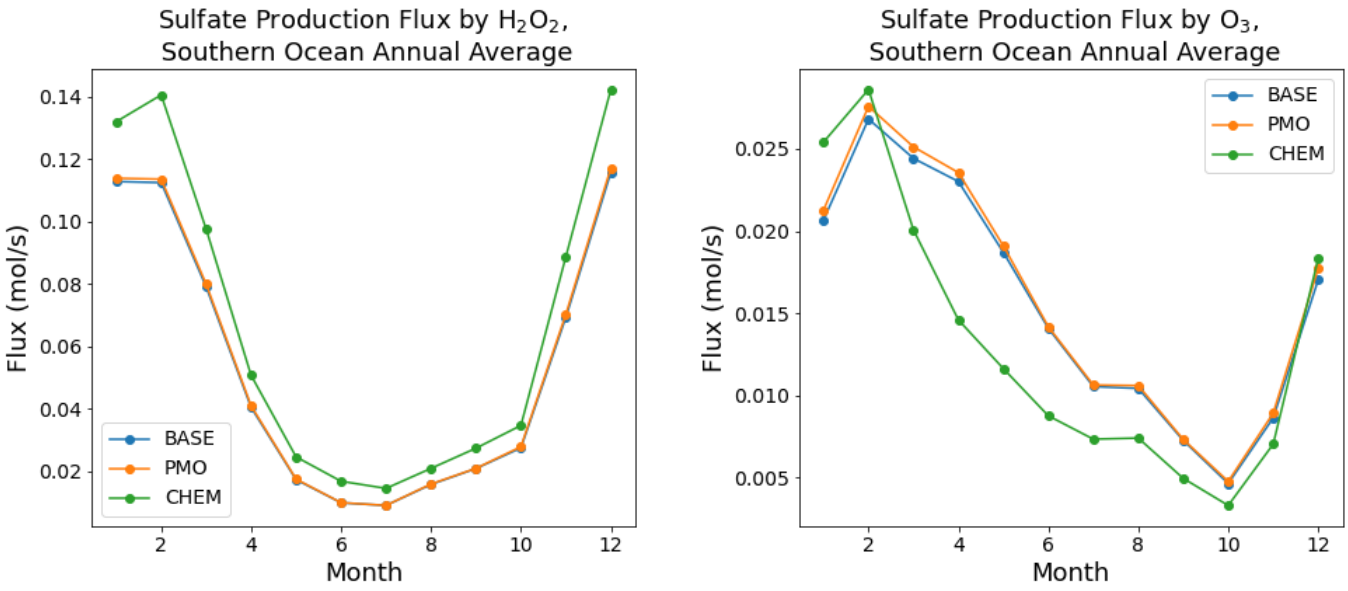


Figure 29: Seasonal cycles of simulated sulfate production flux by H_2O_2 and O_3.

The distribution of reactants and oxidants were examined zonally to identify influencing factors in changed oxidation pathways. Figures 29 & 31 identified increased aqueous-phase oxidation in the PMO run compared to the BASE run, particularly in summer-time and at lower latitudes. As both the PMO and BASE run utilise the same chemistry scheme, these changes will be discussed further utilising the size distribution in Section 7.3.

Increased H_2O_2 aqueous-phase oxidation in the CHEM run was accompanied by increased oxidant availability, particularly at lower latitudes. Zonally averaged at 40°S, H_2O_2-sulfate production flux was larger by a factor of ∼2 and output H_2O_2 concentration was larger by a factor of ∼6 compared to at 60°S. The positive relationship between sulfate production flux and oxidant availability becomes more complicated for O_3-based oxidation. Figures 30 & 31 show the CHEM run exhibited consistent zonal increases in oxidant (O_3) and reactant availability compared to the BASE run, including reactant precursors, OH and SO_2. Despite increased oxidant availability, the CHEM run exhibited decreased O_3-sulfate production by 24.3% at 40°S and was continually lower than the BASE run up to 57.5°S. We then consider why the CHEM run exhibits decreased oxidation by O_3, but increased oxidation by H_2O_2.

Within UKCA, aqueous-oxidation by H_2O_2 ($HSO_3^- + H_2O_2 \longrightarrow SO_4^{2-}$) proceeds preferentially compared to aqueous-oxidation by O_3, and hence forms the rate-limiting factor for sulfate production by O_3. H_2O_2-mediated oxidation consumes the available HSO_3^- first, resulting in a lower amount of available reactant for oxidation by O_3. What must be considered is that the output for sulfate production by O_3 describes two reactions in both offline and online chemistry schemes; the reaction of HSO_3^- with O_3 ($HSO_3^- + O_3 \longrightarrow SO_4^{2-}$),

and of SO_3^{2-} with O_3 ($SO_3^{2-} + O_3 \longrightarrow SO_4^{2-}$) (Tables 3 & 7). The contribution of each reaction to total sulfate output cannot be ascertained due to lacking model complexity. Differences in oxidation between the BASE and CHEM runs may also be a function of cloud fraction, which is required in the calculation of cloud-processing equations within UKCA [Abraham et al., 2016]. Differences in simulated cloud-fraction are discussed in Section 7.6.3.

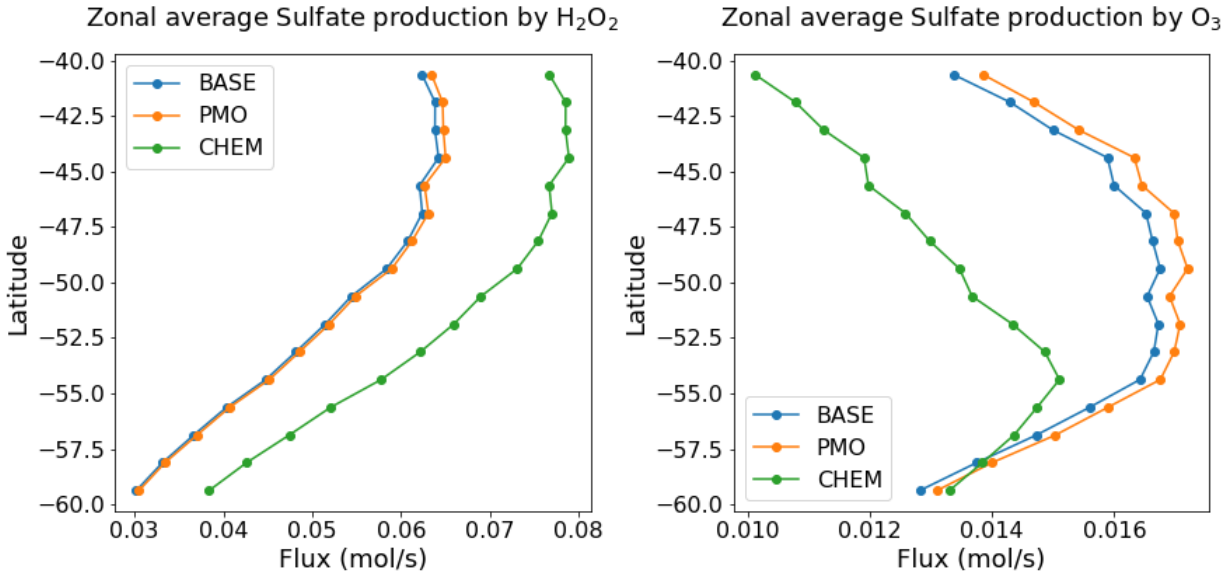


Figure 30: Zonal distribution of simulated sulfate production flux by H_2O_2 and O_3.

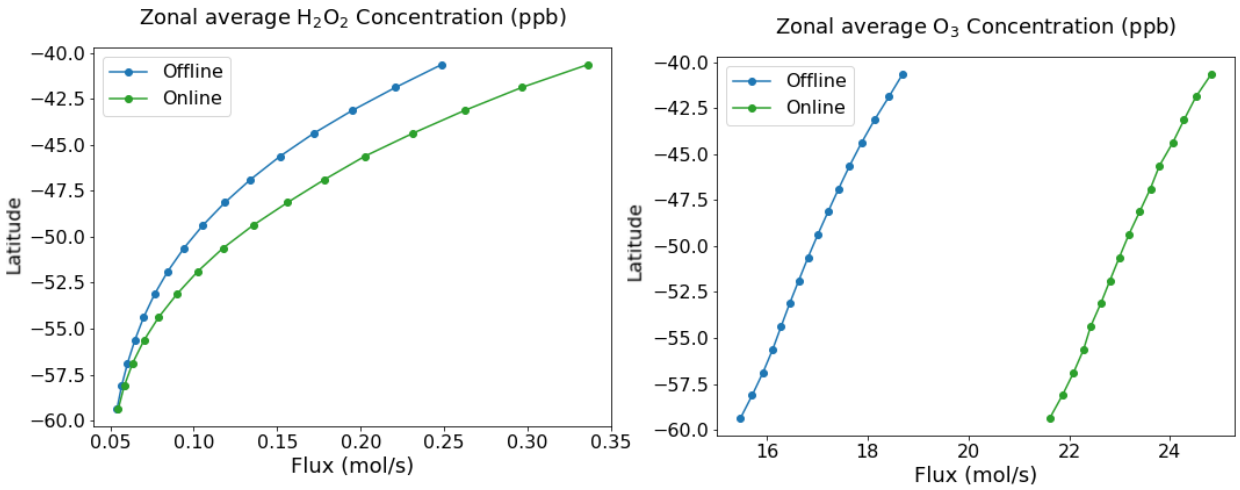


Figure 31: Zonal distribution of simulated H_2O_2 and O_3 (output following source and sink processes), averaged longitudinally over the Southern Ocean.

This section has identified how the inclusion of online chemistry resulted in changed oxidation pathways. The next section illustrates how these changes have been manifested in the simulated size distribution. We could expect to see an increase in the Hoppel minimum in the CHEM run due to increased aqueous-phase oxidation by H_2O_2, but also a reduced minimum due to decreased aqueous-phase oxidation by O_3.

7.3 Size distributions

Size distribution plots illustrate the size and number of aerosols within each mode. Comparing simulated size distribution plots can aid interpretation of how each simulation changed chemical concentration and oxidation pathways as suggested in Section 7.2. We may hypothesise the effect of each perturbation simulation on AOD and CCN due to changes to simulated modal aerosol number and size and verify these changes in later comparisons (Sections 7.4 & 7.5). Section 7.2.1 noted changes in simulated H_2SO_4, which may be informed through analysis of the nucleation mode peak. Similarly, we can more fully interpret changes in larger aerosols, such as sea-salt, through changes in the accumulation and coarse modes. Changes in gas and aqueous-phase oxidation noted in Section 7.2.2 may be informed through analysis of the Hoppel minimum and both the peak height and mean radius of the accumulation-mode peak. Size distributions have been calculated averaged over the Southern Ocean and notable features in each simulation have been described below.

7.3.1 Comparison of simulated size-distributions

Online chemistry exhibited increased aqueous-phase oxidation through increased accumulation-mode peak height and decreased mean radius. Previously, Figures 27 & 29 demonstrated that the CHEM run exhibited increased gas- and aqueous-phase oxidation by H_2O_2, and decreased O_3-based aqueous-phase oxidation. Increases in aqueous oxidation would manifest in the size distribution through an increase in the accumulation-mode peak, as cloud-processing adds increased particle number and hence mass to the mode. Increases in cloud-processing would also result in more Aitken-mode particles growing to enter the accumulation-mode. This would be represented on a size-distribution plot through the shifting of the accumulation-mode peak towards the Aitken-mode. Averaged over the Southern Ocean, the CHEM run reported an accumulation-mode peak which was 5.39% larger in particle number and 14 nm smaller in mean diameter (5.26%) compared to the BASE run, likely confirming an increase in cloud-processing in the CHEM run.

Online chemistry exhibited a lower coarse-mode mean radius, indicative of decreased sea-salt. The CHEM coarse-mode peak was 10.1% larger in particle number but 13.7% lower in mean diameter compared to the BASE run. Section 7.2.1 reported a decreased sea-salt output in the CHEM run, hence it may seem counter-intuitive that the CHEM run would have an increased coarse-mode peak height. Rather, the mean diameter bias towards smaller particles represents the lack of larger sea-salt particles, and the increased particle height is likely the result of increased nss-sulfate products (potentially from increased CHEM-emissions suggested in Section 7.2) that have grown to coarse-mode sizes. Both offline simulations exhibited similar coarse-mode distributions due to similar sea-salt emissions which dominate the coarse-mode (shown in Figure 24).

Decreased H_2SO_4 output in online chemistry was likely explained by increased nucleation-mode particle number. The CHEM run exhibited the lowest output H_2SO_4 concentration of all compared simulations (Figure 24). H_2SO_4 can be consumed through condensation processes in the nucleation mode, which would manifest as a larger nucleation-mode peak in a size distribution. The CHEM run exhibited a nucleation-mode peak particle number that was 16.2% larger than the BASE run. Increased particle number originating from the nucleation-mode progressed through aerosol modes, with CHEM-simulated peaks larger by 24.7%, 5.39% and 9.09% compared to BASE run for the Aitken, accumulation and coarse modes respectively (Figure 32).

Introduction of OM mass through the PMO parameterisation increased Aitken-mode particle size and accumulation-mode particle number. These changes will likely increase simulated AOD and CCN. The Gantt et al. [2012a] parameterisation in the PMO simulation injects OM mass into the upper Aitken-mode that is rapidly transferred to the accumulation-mode. On the size distribution plot, we would expect to see the Aitken-mode peak shifting to larger diameters through introduction of larger sized Aitken particles, and a resulting increase in peak accumulation-mode number. In the PMO run, the mean Aitken-mode diameter increased by 80.3% and the accumulation-mode peak height increased by 51.8% compared to the BASE run. Figure 32 shows the resulting increase in the PMO-simulated Hoppel minima as a result of these changes. This increased Hoppel minima may also account for increased aqueous-phase oxidation (cloud-processing) seen in the PMO run compared to the BASE run observed in Figure 30, which could otherwise not be attributed to chemical differences due to both runs using offline chemistry (seen in Figures 28 & 31).

PMO run formed a condensation sink for H_2SO_4, accounting for the decreased PMO-simulated H_2SO_4 output observed in Figure 24. The introduction of OM in the PMO run increased Aitken-mode surface area which acts as a condensation sink for H_2SO_4 in the nucleation mode. H_2SO_4 condenses onto pre-existing organic aerosols in the Aitken-mode, and is therefore not available to nucleate new particles in the nucleation mode. The result is fewer nucleation-mode particles, and increased sulfate mass in the Aitken-mode. Increased condensation is accounted for in Figure 32, which shows a decrease in PMO-simulated nucleation mode particle number by 15.8% compared to the BASE run.

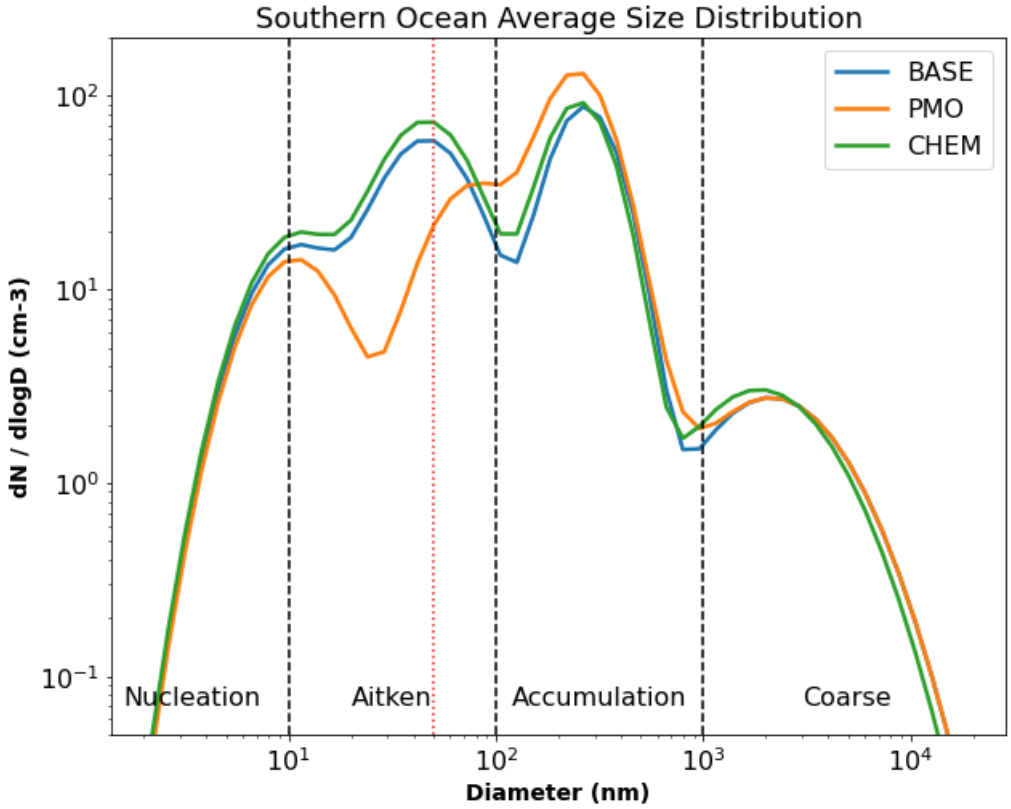


Figure 32: Southern Ocean size distribution, averaged spatially over the 40–60°S domain and temporally from 2016–2018, grouped into 50 size bins. Models identify clear peaks for the nucleation, Aitken, accumulation and coarse modes which have been labelled appropriately. As reference, the BASE run simulated mode peaks occurring at 11.4 nm, 46.2 nm, 266nm , and 2133 nm respectively for these modes (Table 15).

Aerosol Mode mean diameter (nm)	BASE	PMO	CHEM
Nucleation	11.4	10.8	11.6
Aitken	46.2	83.4	46.2
Accumulation	266	243	252
Coarse	2133	2133	1841

Table 14: Southern Ocean average of modal mean diameter (nm)

Aerosol Mode peak particle number (dN/dlogDp)	BASE	PMO	CHEM
Nucleation	17.1	14.4	19.8
Aitken	59.7	35.5	74.5
Accumulation	88.2	133.9	93.2
Coarse	2.76	2.76	3.04

Table 15: Southern Ocean average of modal peak particle number (dN/dlogDp cm^{-3})

7.3.2 Comparison against observational size distribution

All ACCESS-CM2 simulations overestimated particle size and underestimated particle number compared to observations. Figure 33 shows a comparison of model size distribution corresponding with observed SMPS & APS values from the Ice Edge to Equator Voyage (discussed in Section 6.2). Simulated coarse-mode aerosols exhibited a mean particle diameter that was larger than observations by a factor of 5.15, 5.15, and 4.29 for the BASE, PMO, and CHEM run respectively (Table 16). Simulated coarse-mode mean particle number was underestimated by 89.9%, 89.6%, and 88.9% compared to observations for the BASE, PMO and CHEM runs respectively (Table 17). However, due to inlet losses of large particles in the instrumental setup used in the field campaigns described in Appendix A.8, these conclusions may be stated only with limited confidence. There is higher confidence in the ability of the SMPS instrument to sample particles in the Aitken (above 0.01μm) and accumulation-mode, hence the following discussion focuses on these size modes.

The BASE and CHEM simulations underestimated Aitken-mode peak particle number by 89.3% and 90.6% respectively, and both overestimated mean particle diameter by 91.7% compared to observations. The PMO peak was not detected using the peak-detection method outlined in Section 6.2, but is shown to be larger than both simulations on Figure 33. All simulations of peak particle number exhibited closer agreement to observations in the accumulation-mode, but again reported increased particle sizes. Simulated

accumulation-mode particle numbers were still 40.7%, 26.7%, and 39.7% lower than observations for the BASE, PMO, and CHEM runs respectively, and particle diameters were overestimated by 177% by all simulations (Tables 16 & 17).

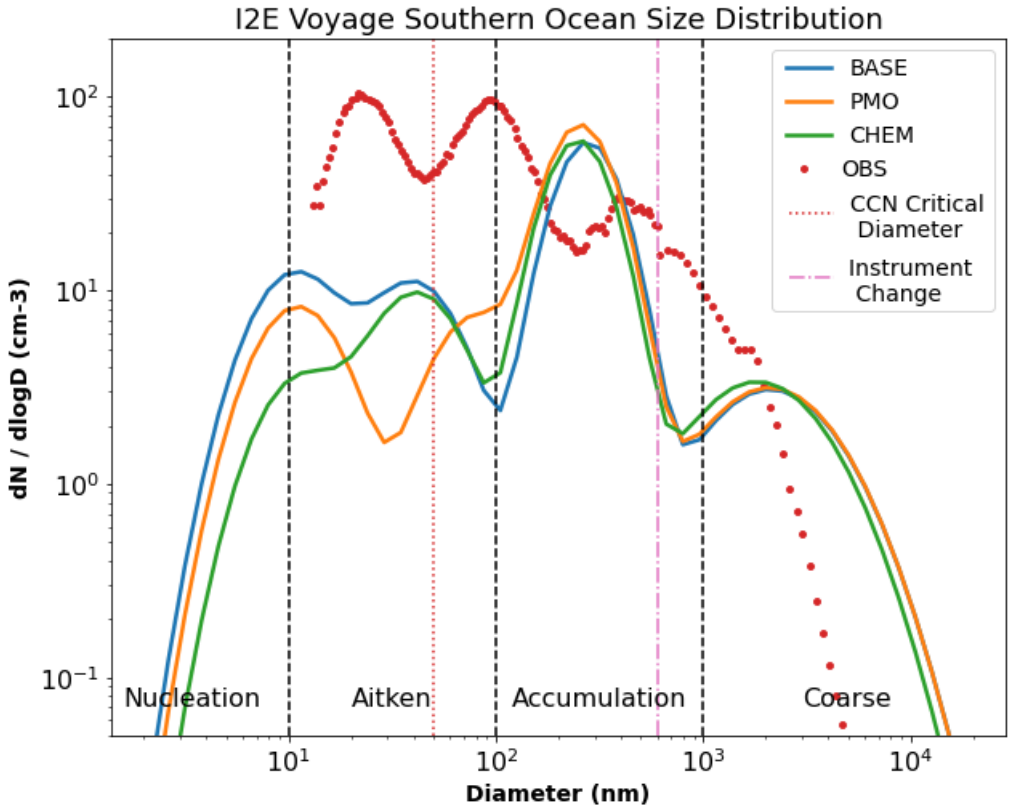


Figure 33: Size distribution averaged spatially and temporally over the Ice Edge to Equator Voyage plotted on a log-log scale. Model data has been grouped into 50 size bins. Observational values shown in the red dots consist of measurements from two instruments; the first section being SMPS observations up to 598 nm (denoted on the plot up to the pink dashed line), and the remainder are APS measurements. The cut-off for CCN at 0.5% SS is shown in the red dotted line at 50 nm, where the integral under the remainder of the size distribution curve provides the total simulated or observed CCN values.

Aerosol Mode mean diameter (nm)	OBS	BASE	PMO	CHEM
Nucleation	(not detected)	11.5	11.5	(not detected)
Aitken	21.8	41.8	(not detected)	41.8
Accumulation	95.4	264	264	264
Coarse	388	2000	2000	1664

Table 16: Ice Edge to Equator Voyage simulated and observed aerosol mode mean diameter (nm).

Aerosol Mode peak particle number (dN/dlogDp)	OBS	BASE	PMO	CHEM
Nucleation	(not detected)	12.51	8.25	(not detected)
Aitken	104	11.13	(not detected)	9.81
Accumulation	98.0	58.1	71.8	59.1
Coarse	30.3	3.07	3.14	3.35

Table 17: Ice Edge to Equator Voyage simulated and observed aerosol mode peak particle number (dN/dlogDp cm^{-3}).

7.3.3 Seasonal simulated size distributions

Comparison of seasonal size distributions enables interpretation of the different biological and photolytic influences between simulations. Increases in Aitken-mode particle size and accumulation-mode number were largely observed in biologically-active months within the PMO run. Increased nucleation-mode particle number simulated in the CHEM run was similarly largest in photolytically-active months, suggesting the role of OH and increased gas-phase oxidation in new particle formation suggested in Section 7.2.2.

Figure 35 clearly illustrates that the PMO run had the largest effects in biologically-active months; increases of [chl-*a*] in summer and spring are utilised by the Gantt et al. [2012a] parameterisation to increase the OM_{frac} in SSA (Equations 5 & 6). For example, the PMO-simulated Aitken-mode mean diameter was 64.4% larger than the BASE run in summer, and Aitken-mode peaks were not detected in winter for comparison. Similarly, accumulation-mode peak particle number was 69.8% larger in summer compared against 19.7% larger in less biologically-active winter months. Increased Aitken-mode peak diameters corresponded to decreased nucleation-mode peak numbers through increased Aitken-mode surface areas acting as a condensation sink. This was particularly noted in spring, where the PMO run saw a reduction in nucleation-mode aerosol number by a factor of 1.2 compared to the BASE run (Figure 35).

The CHEM run both increased and decreased aqueous-phase cloud processing via H_2O_2 and O_3, respectively (Section 7.2.2). While competing effects may result in a minimal effect on size-distributions, an enhanced Hoppel minimum was observed with increased accumulation-mode particle number in summer and spring months, coinciding with increases in simulated cloud-processing (Figure 35).

Increased nucleation was noted in the CHEM run in photolytically-active months of summer and spring. Figure 34 demonstrates the peak of CHEM-run nucleation-mode particle number which was 51.7% larger than the BASE in spring, compared to a comparative increase of 1.35% against the BASE run in winter (see Tables 38, 40, 42 & 44). Lower winter-time nucleation particle number corresponds to the minimum of H_2SO_4 reported by all models in Figure 24, although there are numerous factors involved in nucleation processes such as new particle formation within the free-troposphere (discussed in Section 1.5). Increased nucleation-mode particle number does not necessarily mean increased nucleation processes; this is discussed further in context with other variables examined in Chapter 8. Increases in nucleation particle number enhanced particle numbers in larger aerosol modes, particularly the neighbouring Aitken-mode. Aitken-mode particle number increased by 56.6% in spring and 32.0% in summer compared to the BASE run (Tables 38 & 44). Increased particle number would consequently increase CCN concentration (for particles above 50 nm), and therefore AOD would increase, which is dominated by larger-sized particles. Increased nucleation in summer and spring suggests an increased photo-chemical process, possibly attributable to increases in gas-phase oxidation forming nucleation-mode H_2SO_4 suggested in Section 7.2.2 due to increased OH availability.

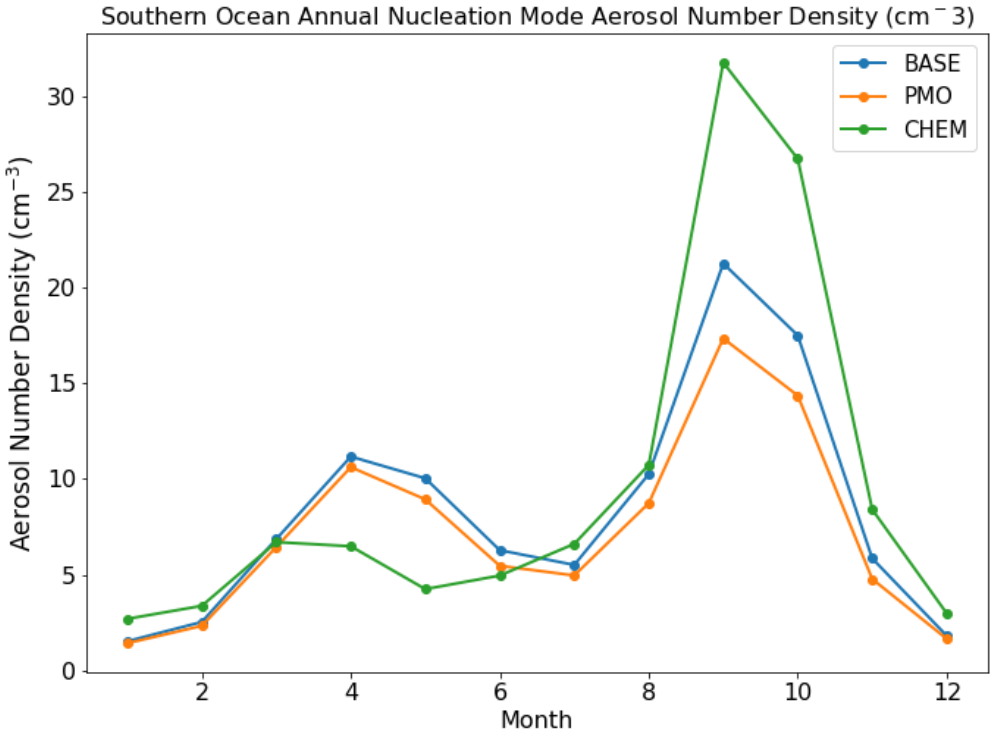


Figure 34: Nucleation mode aerosol number density of the BASE, PMO, and CHEM simulations. Data used was hourly output from 2016–2018, grouped by month and averaged temporally and spatially over the Southern Ocean domain (40-60°S).

It should be noted that not all Aitken particles may be explained through changes to nucleation in the CHEM run. Figure 35 showed a winter-time increase of Aitken-mode particles by 46.5% in the CHEM run compared to the BASE run, yet no substantial increase in nucleation-mode aerosols. This suggests that a source of winter-time Aitken-mode aerosols is missing, which is discussed in Section 8.1.

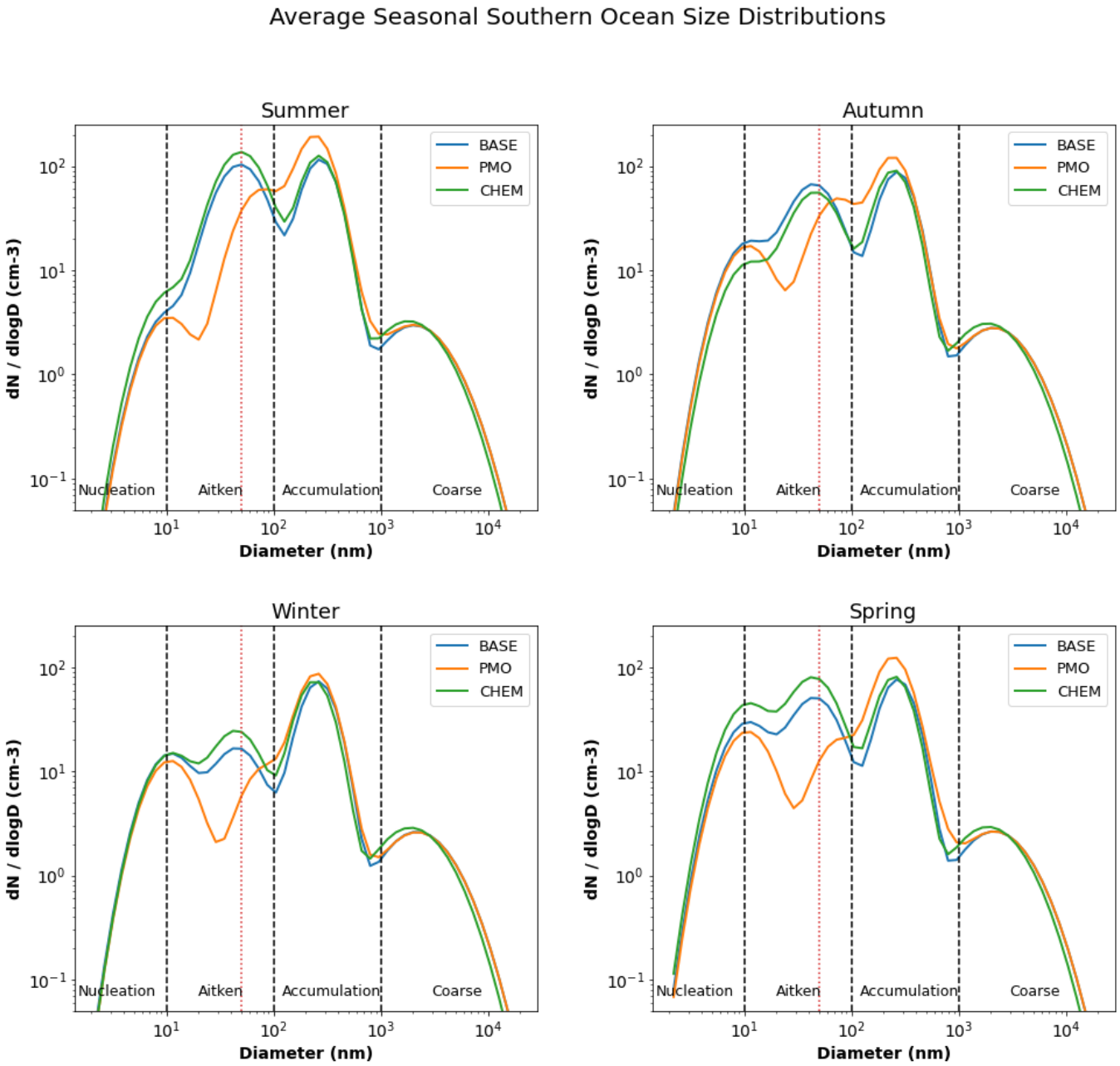


Figure 35: Southern Ocean seasonal size distributions. Hourly output data was grouped by season within 50 size bins and averaged spatially over the 40–60°S domain.

Summary of model chemistry analysis:
In this section, we conclude:

- Increased oxidant availability in the CHEM run increased gas-phase and H_2O_2 aqueous-phase oxidation. Preferential oxidation via H_2O_2 suppressed aqueous-phase O_3 oxidation, although other factors such as cloud-fraction are possibly involved.
- The PMO [Gantt et al., 2012a] scheme increased Aitken and accumulation particles in biologically-active months and therefore increased CCN and AOD values are predicted to be simulated.
- The CHEM run increased nucleation particle numbers, corresponding to increased production of H_2SO_4 through gas-phase oxidation. Increased particle number can be expected to increase CCN and AOD, however decreases in simulated sea-salt concentrations will likely counter these increases.
- All ACCESS-CM2 simulations were found to underestimate particle number and overestimate particle size compared to observations, which has also been noted in another GLOMAP Southern Ocean simulation [Woodhouse et al., 2020].

7.4 Evaluation of Aerosol Optical Depth

Sections 1.7 & 3.2 established the dependence of model evaluations upon AOD to identify bias and characterise aerosol populations. This section first establishes the AOD bias of ACCESS-CM2 using statistical metrics outlined in Section 6.6, and how perturbations to the aerosol-chemistry scheme have changed model bias. Next, this bias was examined using wind-speed and direction to determine any local terrestrial influences on simulated AOD at Cape Grim that must be accounted for. All simulations were explored to identify whether AOD seasonality was captured, and how model bias changed seasonally. Finally, model bias was investigated through identifying each aerosol mode contribution to AOD between simulations, and compared against observations.

7.4.1 Magnitude of AOD

As suggested in Section 7.3, this section confirms that the PMO and CHEM runs increased and decreased average simulated AOD respectively at all stations analysed. The SSALT run reduced simulated AOD with a more narrow distribution of data. Importantly, ACCESS-CM2 simulations largely exhibited a positive bias compared to observations across stations and voyages. Averaged over the Southern Ocean, the PMO, CHEM and SSALT runs reported relative differences from the BASE run of 1.83%, -13.9%, and -43.4%, respectively, where the CHEM run exhibited the lowest bias and the SSALT run simulated the highest bias (Table 18).

Southern Ocean Average	BASE	PMO	CHEM	SSALT
Mean	0.148	0.150	0.127	0.0836
Min	0.102	0.103	0.0843	0.0514
Max	0.210	0.214	0.178	0.124
Relative Difference		1.83%	-13.9%	-43.4%
Correlation		0.993	0.947	0.821
Bias		0.00268	-0.0204	-0.0641
NMBF		0.0182	-0.161	-0.768
RMSE		0.00350	0.0213	0.0649
NMAEF		0.0186	0.161	0.768

Table 18: Statistical summary of simulated AOD averaged spatially and temporally over the Southern Ocean. Statistical metrics have been described in Table 8, where NMBF = Normalised Mean Bias Factor, RMSE = Root Mean Square Error, NMAEF = Normalised Mean Absolute Error Factor.

Despite reductions in mean AOD reported by the CHEM and SSALT runs, ACCESS-CM2 simulations largely overestimated mean observed AOD. This indicates that even without perturbations, ACCESS-CM2 BASE run exhibits a systematic positive bias over the Southern Ocean region, which varied between stations. For example, mean BASE-simulated AOD was 55.0% larger than observations at Cape Grim and 25.1% larger at Macquarie Island. Boxplots shown in Figure 36 demonstrate the consistent AOD overestimation by the BASE, PMO, and CHEM runs, with a variable bias shown in the SSALT run. For example, simulated mean SSALT-AOD was 7.12% larger than observations at Cape Grim which reduced to -19.5% at Macquarie Island. Comparisons between voyage data showed the largest discrepancies in AOD bias (NMBF) and error (NMAEF), where the PMO run reported a mean simulated AOD 122% larger than observations, and mean SSALT-simulated AOD was 48.7% lower than observations (see Appendix tables 46, 47, & 48). As voyages largely occur during summer-months, seasonal AOD representation is examined in Section 7.4.4 to identify whether this increased-overestimation in summer is a consistent seasonal bias.

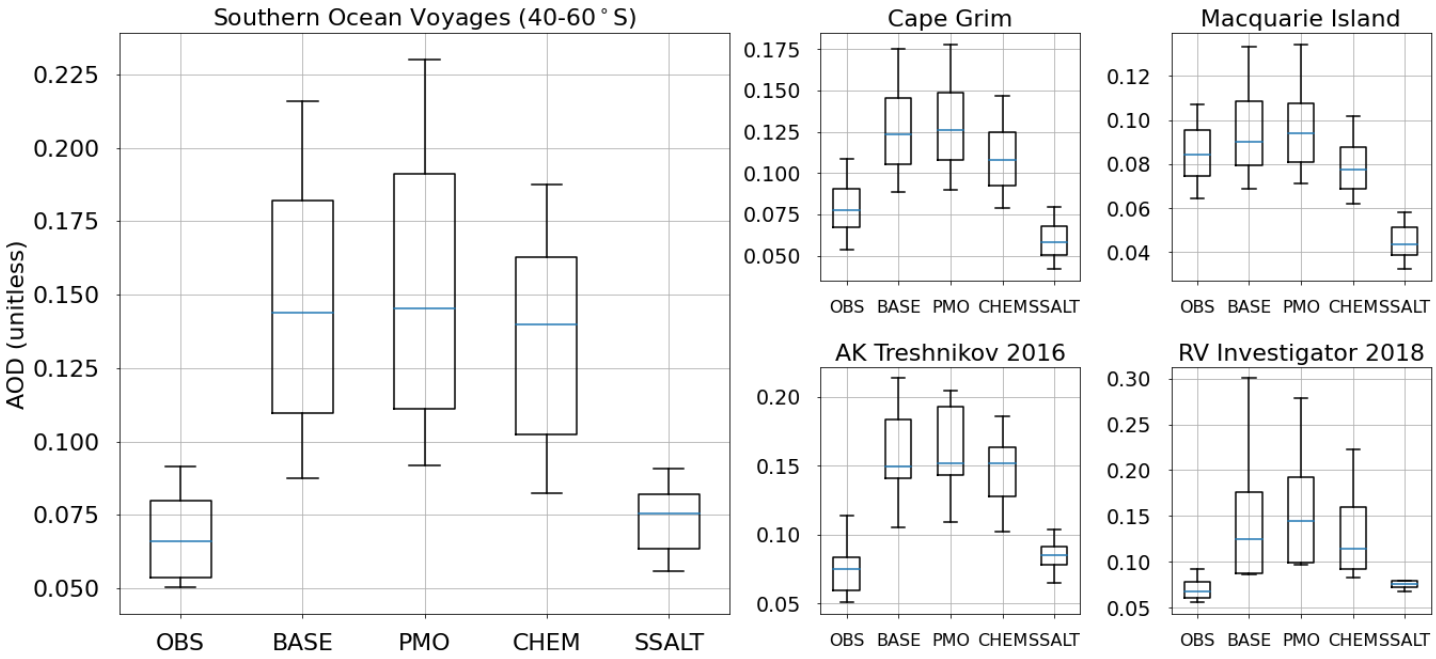


Figure 36: Boxplot comparison of simulated and observed AOD_{550nm} at AERONET stations over AERONET MAN voyages.

Probability density function histograms shown in Figure 37 provide a representation of data distribution within each simulation. Increased spread of data in all simulations resulted in larger maximum values compared to observations that skewed the mean simulated AOD towards higher values (Figure 37). All ACCESS-CM2 simulations did not capture low AOD values, particularly at Cape Grim where the BASE, PMO, and CHEM runs exhibited a positive skew. Compared to voyage data, the SSALT run performs well in terms of AOD distribution, but both the SSALT and CHEM runs feature a bimodal peak that was not present in observations. This likely represents the sampling of separate air masses with distinct aerosol populations, potentially a result of the poor wind-direction model-observation agreement as discussed in Section 7.1.2. It is important to note that the number of samples within this total Southern Ocean Voyage dataset was low due limited available data (N=86).

The SSALT run exhibited a narrower distribution of AOD with an increased peak centred at lower values compared to station-based observations. It could be expected that simulated distributions would have a wider, smoother distribution of AOD in comparison to observations, due to modeling limitations including a coarse spatial resolution, 6-hourly meteorology nudging to reanalysis data, and parameterised emissions. This is the case for the BASE, PMO and CHEM runs, but the modified sea-salt parameterisation in the SSALT run resulted in kurtosis values twice as large as observed. For example, the Cape Grim SSALT kurtosis was 18.6, compared to the observed value of 9.9. (Kurtosis provides a measure of the weight of a distribution's tails relative to the center, where increased kurtosis describes a steeper distribution peak).

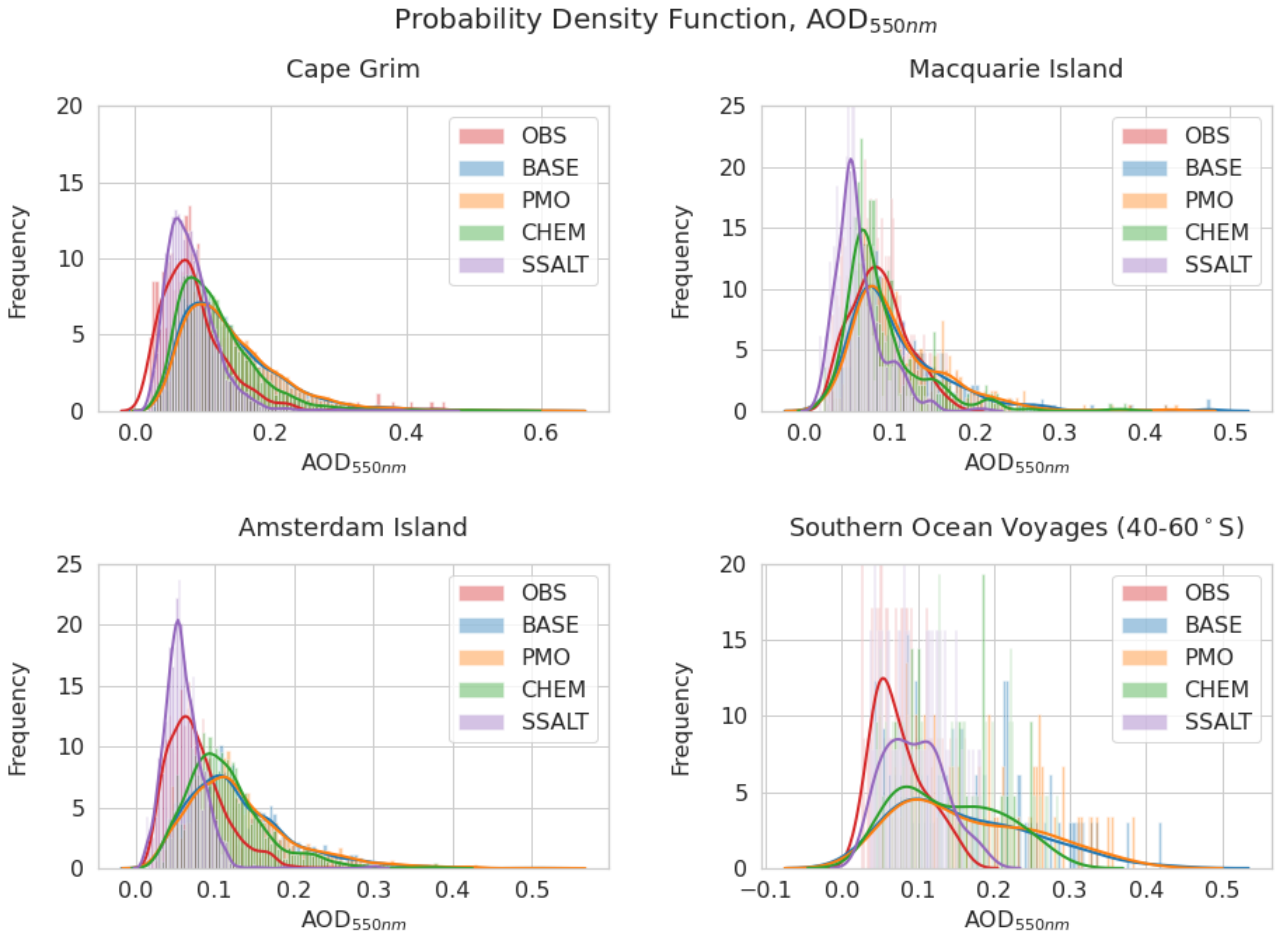


Figure 37: Probability Density Histograms: Comparison of modelled and observed AOD. Data presented in this plot is hourly-averages subset at each station, or corresponding with the time and GPS coordinates of the voyages. Southern Ocean Voyages corresponds to the amalgamated product of all 14 AERONET MAN voyages described in Section 6.3. The BASE and PMO runs exhibit similar distributions of AOD, where the blue line (BASE) is plotted directly beneath the orange line (PMO).

7.4.2 Relationship between wind-direction and AOD bias

Having identified a AOD positive bias within ACCESS-CM2 at Cape Grim, this section determines the source of this bias to be representative of the Southern Ocean, and not terrestrial influence. Cape Grim has the largest potential for local terrestrial influence, unlike Macquarie and Amsterdam Islands where the model assumes a completely oceanic gridbox (see Figure 61 & Appendix 62). While all Cape Grim data used in analysis within this thesis is screened for baseline conditions (discussed in Section 7.1.2), there is potential for terrestrial air parcels to be admitted within this baseline screening through re-circulation systems. Hence, this section aims to identify whether the baseline sector was the largest source of bias at Cape Grim, or whether other terrestrial influences exhibit a positive bias that must be considered.

The pollution-rose shown in Figure 38 demonstrates the strongest signal of AOD bias is located within the oceanic baseline sector of Cape Grim (defined in Section 6.1). AOD bias signal was calculated as the ratio of ACCESS-CM2 AOD to observed AOD, where the model overestimates AOD by over a factor of 2.5 in the baseline sector. There is also a source of AOD bias in the NWW sector; this suggests a potential source of AOD bias from continental outflow, although the bias magnitude is notably lower. This source has been further investigated using a Conditional Probability Function in Appendix A.13.3, which concluded that baseline wind-direction screening methods were suitable for this research.

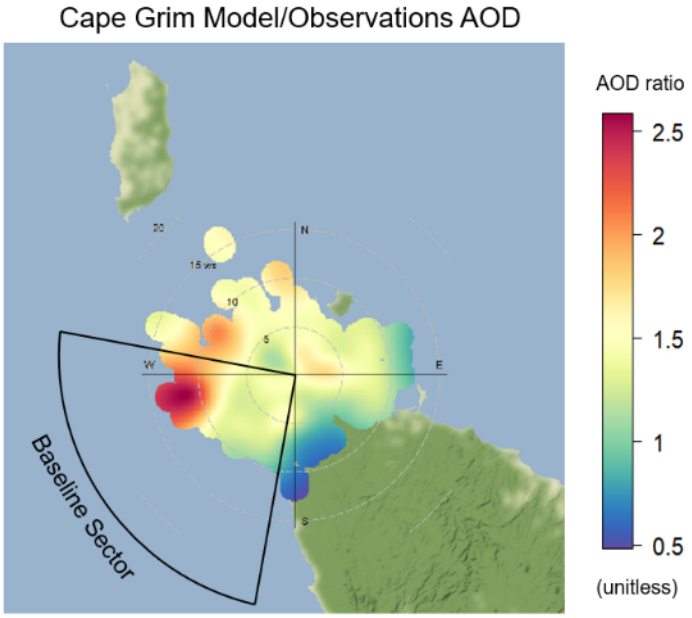


Figure 38: Pollution Rose of AOD_{550nm} at Cape Grim. AOD ratio calculated as the ratio of ACCESS-CM2 simulated AOD/Observed AOD for all data (not baseline-screened).

Having attributed the AOD model bias to Southern Ocean wind-directions, the following section evaluates the relationship between AOD and wind-speed.

7.4.3 Relationship between wind-speed and AOD bias

The SSALT Hartery et al. [2020] modified sea-salt source function was implemented in response to concerns regarding the overestimated relationship between AOD and wind-speed in the BASE Gong [2003] function. This section demonstrates that the SSALT run reduced this overestimation relative to observations at Cape Grim, although not as significantly at Macquarie Island which may be attributable to poor simulated meteorological representation.

A positive relationship is to be expected for AOD and wind speed due to increases in wind-produced sea-spray aerosols that dominate AOD. Figure 39 shows that the observed positive relationship is overestimated in the BASE run, with a slope over five times larger than observations at Cape Grim, and approximately two times larger at Macquarie Island (Table 19). The SSALT run improved this relationship, and simulated a slope that was a factor of 1.4 larger than observations at Cape Grim, but a factor of approximately two times smaller than observations at Macquarie Island. The reduction of AOD with increasing wind-speed was expected for the SSALT run; reducing the wind-speed driven sea-salt flux would reduce the number of heavy sea-salt aerosols and hence AOD, which is dominated by mass.

AOD & wind-speed relationship	OBS	BASE	SSALT
Cape Grim			
Slope	0.00330	0.018	0.00462
Y-intercept	0.0610	0.0399	0.0585
Macquarie Island			
Slope	0.00381	0.00740	0.00176
Y-intercept	0.0529	0.0529	0.0477

Table 19: Slope and y-intercept of AOD and wind-speed relationships at Cape Grim and Macquarie Island. The PMO and CHEM runs have been excluded from this analysis as meteorology-dependent sea-salt schemes remain unchanged and the meteorology was nudged.

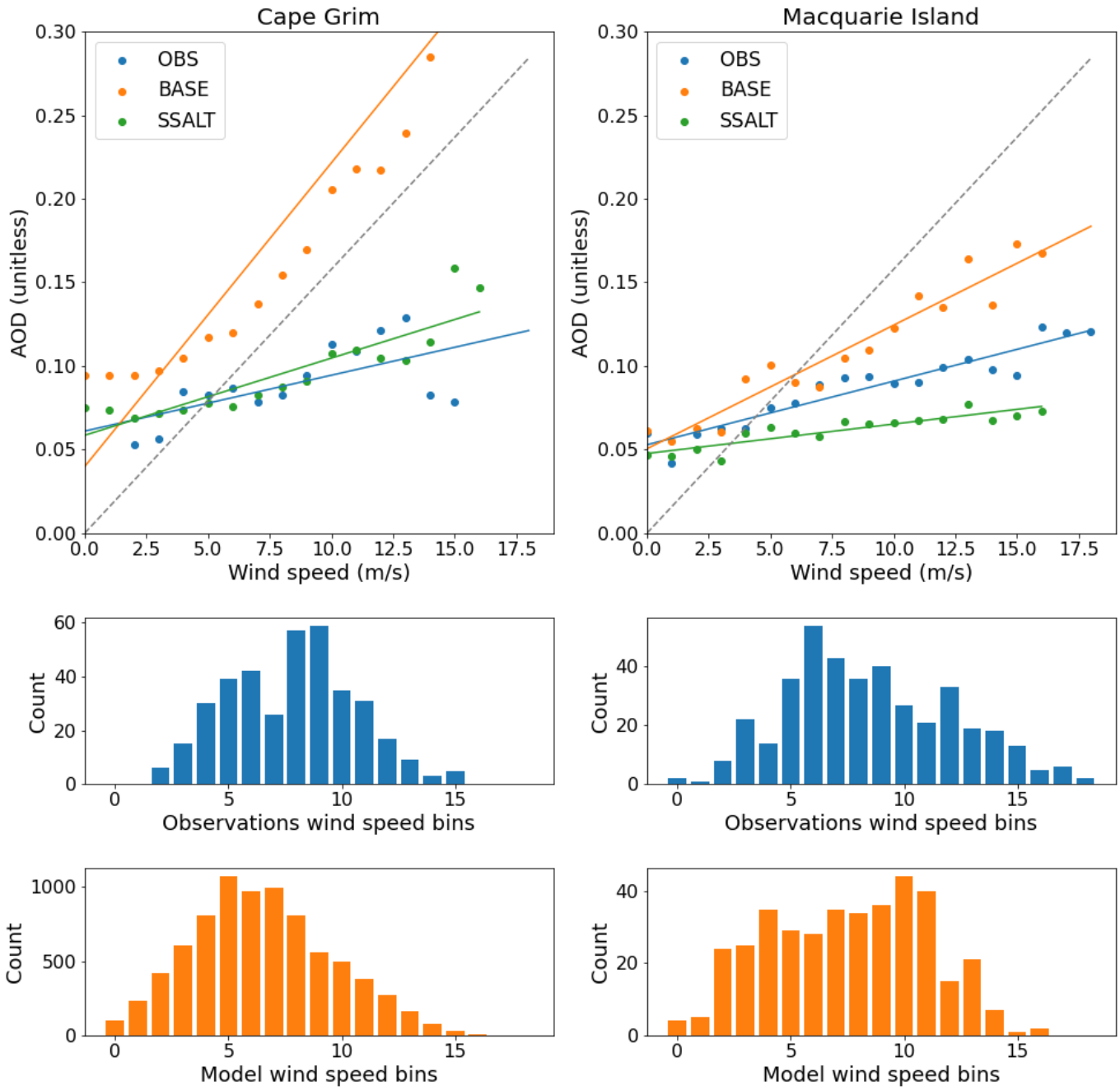


Figure 39: Relationship between AOD and winsdpeed for the BASE and modified sea-salt parameterisation SSALT simulations, compared against observations. Note the number of values in each wind speed bin (shown in the orange histogram) is the same for the BASE and SSALT runs. Improved wind-speed-AOD relationships at Macquarie Island may be due to a model under-representation of high observed wind-speeds, as the [Gong, 2003] production of SSA has been shown to struggle at increased wind-speeds [Revell et al., 2019].

Having established the relationships between wind-speed and AOD for both the BASE and SSALT sea-salt source functions, the following section evaluates the bias of each simulation seasonally with varying wind-speed, biological and photochemical processes between seasons.

7.4.4 Seasonal representation of AOD

For a model to be considered representative of observed values, it must capture both the observed distribution of AOD (shown in Section 7.4.1) and importantly, seasonal cycles and patterns. This section finds that all ACCESS-CM2 simulations represented seasonal patterns of observed AOD well, albeit with substantial seasonal bias. The perturbation simulations exhibited improved bias and correlation at different stations, with the exception of the SSALT run which consistently exhibited an increased positive bias in winter. Figure 40 shows that all simulations captured the overall shape of seasonal AOD at all sites; broadly speaking this includes a minimum AOD during winter-time which increases towards spring and summer. The performance of each simulation has been analysed per station in the following discussion.

Despite improvements in simulated wind-speed noted in Section 7.1.1 in winter, simulated AOD bias and error (NMAEF) worsened during winter for all model runs at Cape Grim. Model error bias (NMBF) increased by factors ranging from 3.3 in the SSALT run to 6.9 in the CHEM run, where the SSALT run changed sign from negative in summer to positive in winter. Notably, the increased winter-time AOD bias in SSALT-simulated AOD was still a factor of four lower than the BASE run (Tables 50 & 51).

In contrast to results at Cape Grim, winter- and spring-simulated AOD saw the closest model-observation agreement at Macquarie Island. Average winter NMBF values were lower by a factor of 6.7 and 9.2 in the BASE and PMO runs respectively, with a complete change of sign in the CHEM run from 0.307 in summer to -0.304 in winter. From June to December, BASE, PMO, and CHEM modelled AOD overlapped within ± 1 standard deviation of observed annual AOD at Macquarie Island. The SSALT run consistently underestimated AOD annually, but saw a worsening in bias by a substantial factor of 24 in winter.

Amsterdam Island reported the highest model-observation correlation values, where the seasonal pattern is shown replicated well in all simulations in Figure 40. The BASE, PMO, and CHEM models all reported a correlation over 0.975 which improved in winter, and a fairly constant NMBF across the year. Contrary to other simulations, the SSALT run saw a reduction in correlation from 0.999 in summer to 0.902 in winter with an increased winter-time bias that changed signs to negative value of -0.141. The SSALT run was able to reduce simulated AOD to within the range of observational uncertainty in summer and winter at Amsterdam Island, shown in Tables 54 & 55.

Intra-annual variability between seasons has previously been discussed for each simulation. This discussion focuses on inter-annual variability through the metric of standard deviation. Appendix figures 64, 65 & 66 demonstrate that across all stations, the BASE and PMO simulations exhibited a higher inter-annual variability annually and across all seasons for the study period; these differences were most noted at Macquarie Island and Amsterdam Island. In particular, the BASE, PMO, and CHEM runs largely exhibited an increased inter-annual variability for winter and spring compared against observations. Notably, the SSALT run exhibited a decreased variability compared to observations but showed increased variability in winter, which was also reflected in the reduced width of AOD distributions relative to observations, shown in Figure 37. The next section identifies whether seasonal variations in model-observation agreement were consistent spatially, or subject to changes regionally.

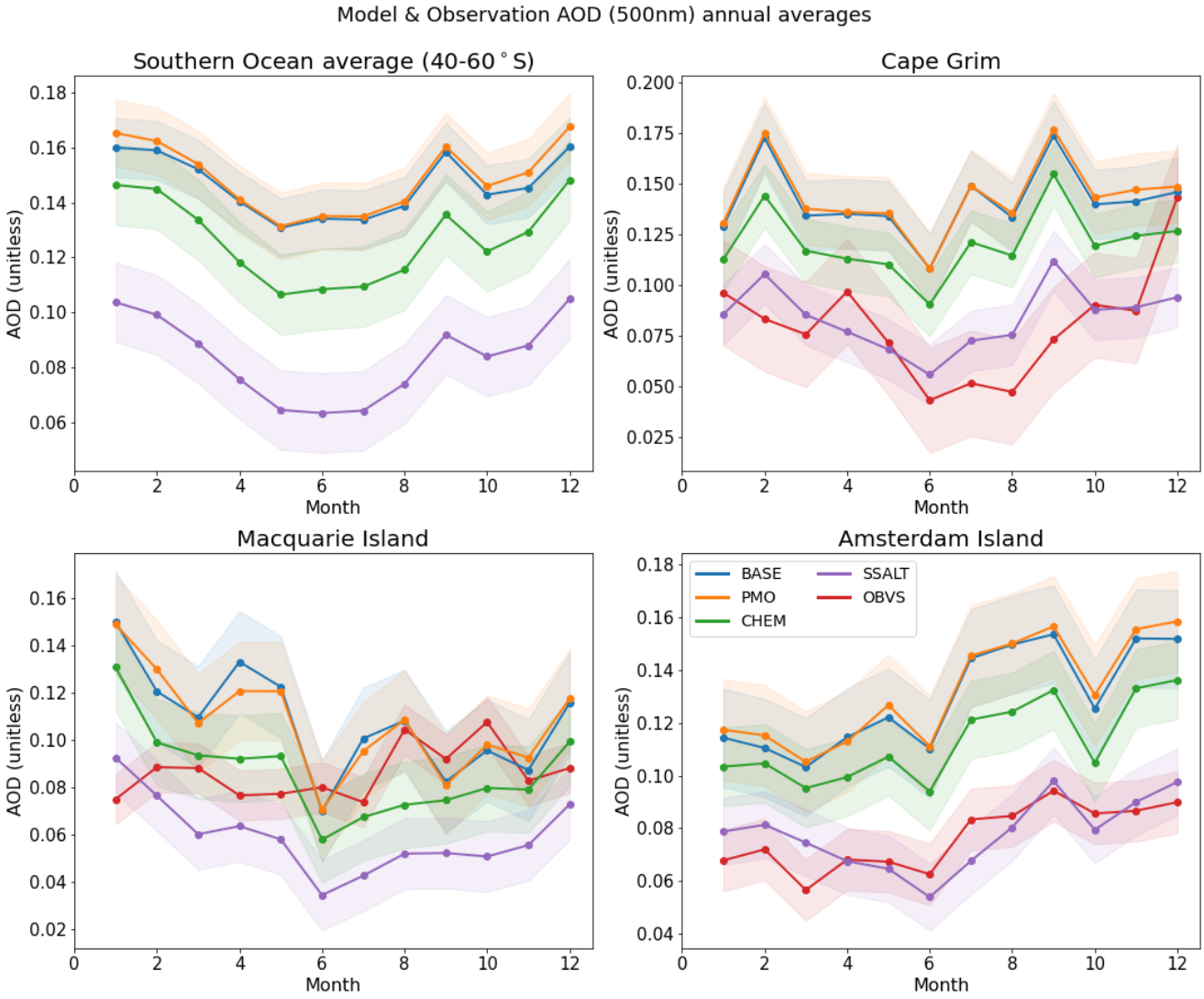


Figure 40: Annual patterns of modelled observed AOD, shaded ± 1 standard deviation. Values shown are the monthly averages of 2016–2018.

7.4.5 Spatial representation of AOD

Clear regional increases in PMO-simulated AOD were simulated in biologically-productive regions, likely as a result of the Gantt et al. [2012a] PMOA scheme dependency on [chl-*a*] to predict increased OM fraction in SSA. Zonal AOD reductions were simulated in the CHEM and SSALT simulations consistent with dominant wind-speed patterns in the Southern Ocean, hence AOD reductions are likely due to the decreased (wind-generated) sea-salt, as seen in Figure 24. Figure 42 shows a notable increase in PMO-simulated AOD by 10.3% in summer and 9.04% in spring compared to the BASE run between longitudes 60°W to 10°W, which has been illustrated in Figure 41. Such increases in this region were only a feature of the PMO run, as the CHEM and SSALT runs reported summer AOD differences of 2.13% and -0.867% compared to the BASE run.

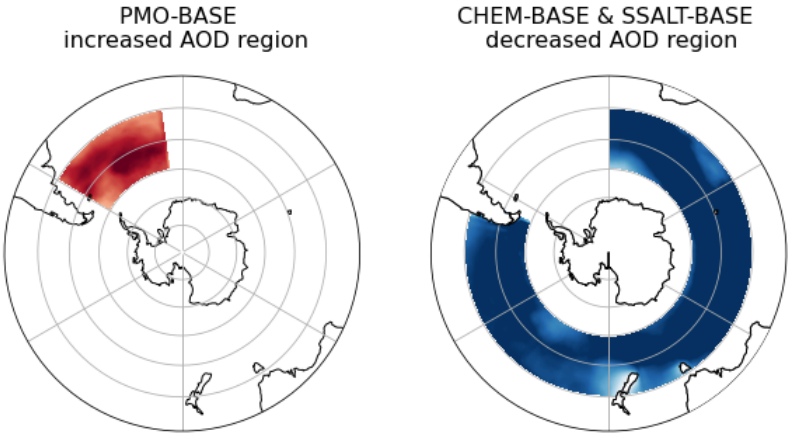


Figure 41: Areas subset to calculate maximum difference between perturbation simulations and the BASE run. The area of maximum increase in the PMO run is bounded by latitudes 40–60°S and longitudes 300-350°. Maximum decreases in AOD were noted in the CHEM and SSALT run between latitudes 40-60°S, and longitudes 0-290°.

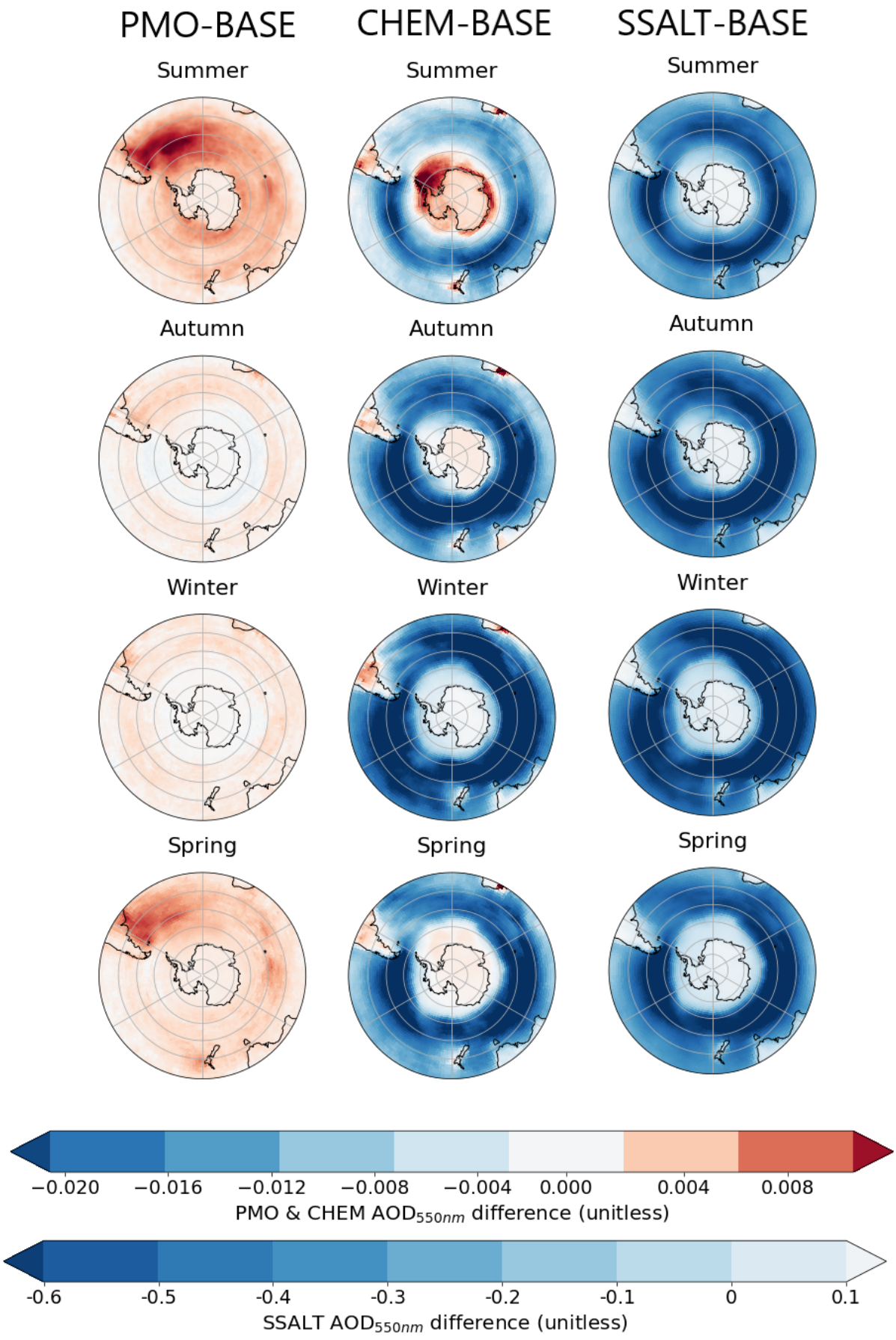


Figure 42: Seasonal spatial differences between the BASE model and perturbation simulations, shown as absolute (non-relative) differences. Land values have been kept in the figure to show entire model output but in statistical analysis, land values have been masked and removed.

The Gantt et al. [2012a] PMOA scheme utilises MODIS/Aqua satellite-derived [chl-a], zonal wind-speed, and the dry diameter of SSA to determine the organic mass fraction of SSA. With nudged meteorology and the same sea-salt emissions as the BASE run, the dependency on [chl-a] is therefore likely responsible for increases in regional AOD. Figure 43 shows the MODIS-Aqua [chl-a] product averaged seasonally. In this figure, it is evident that the regions that show the largest increase in spring/summer AOD correspond spatially to regions of high chlorophyll-a concentration. For example, the 'PMO-enriched' region illustrated in Figure 41 saw a summertime increase of [chl-a] by 235% and 166% in spring compared to a zonal region of background minimal [chl-a] (40–60°S, 80–170°W). In Section 7.5 later, we will also see that changes in CCN correspond to biologically-productive regions in the PMO model.

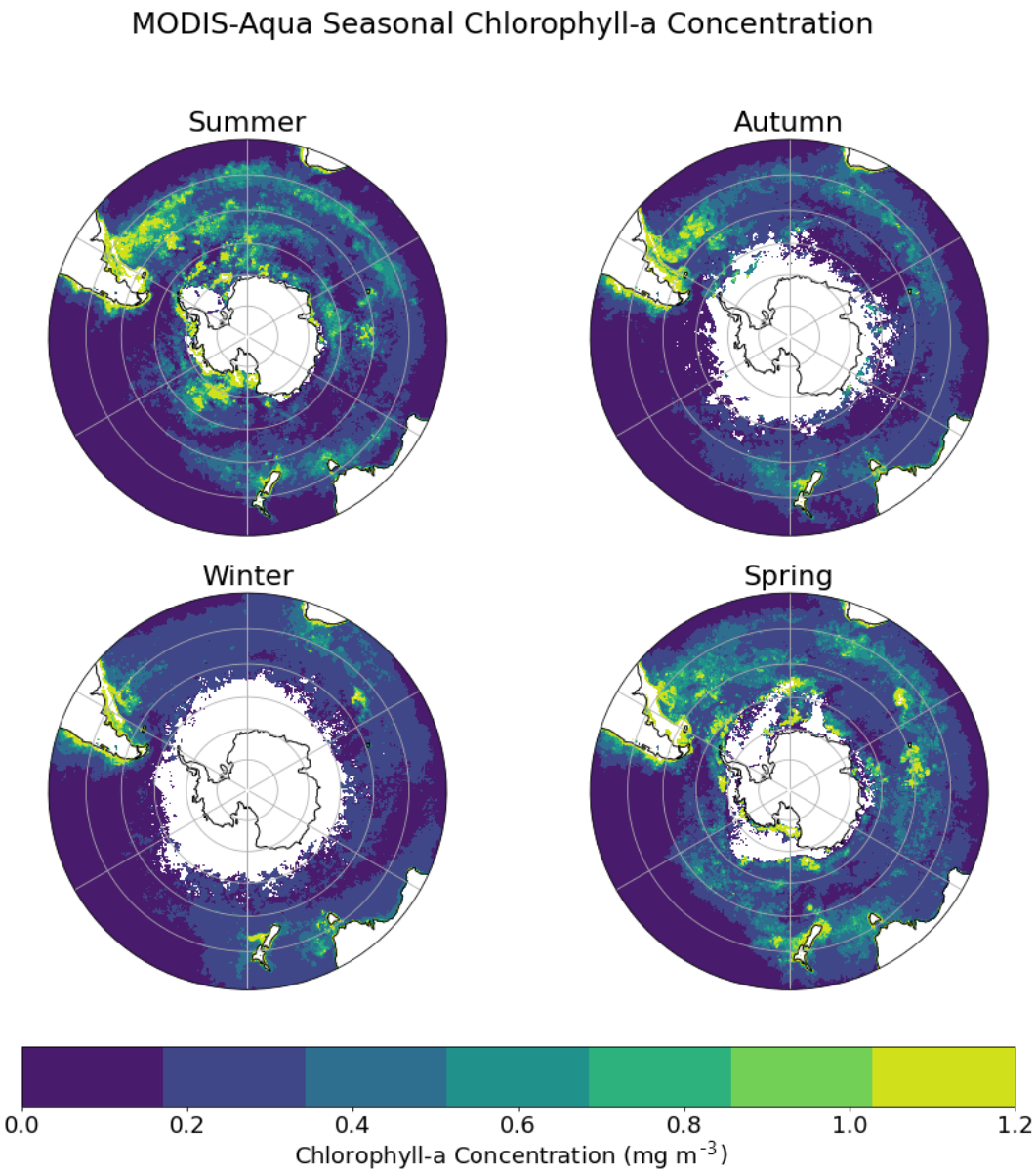


Figure 43: MODIS-Aqua Seasonal 9 km Chlorophyll-a concentration, 2016.

In contrast to the PMO run, both CHEM and SSALT runs exhibited an overall negative bias in AOD over the 40–60°S region, most notably so within longitudes of 0–290° in the CHEM run (excluding the area of highest AOD increase noted in the PMO run). Within this region (see Figure 41), the CHEM run reported a maximum seasonal averaged difference compared to the BASE run in summer of 7.55%, while the SSALT run reported the maximum average AOD difference of -32.2% in winter. Despite evidence of notable increases in AOD near Antarctica, evaluation of these changes are beyond the scope of this study (Figure 41). The next discussion identifies a potential physical mechanism responsible for spatial decreases in simulated AOD.

Section 7.2 described reductions in simulated sea-salt concentration in the CHEM run and to a greater extent, the SSALT run. Average reductions in sea-salt may contribute one aspect to the total reduction in simulated AOD. Seasonally, we may investigate wind-speed patterns to explain spatial changes in AOD due to the wind-generated nature of sea-salt. Zonal 10 m seasonal wind-speed plotted in Figure 44 shows how areas of greatest AOD change between the CHEM and SSALT runs and the BASE run correspond to areas of increased wind-speed. Similarly, the 'PMO-enriched' region which exhibited lower reductions of AOD in the CHEM and SSALT runs (Figure 41) corresponds to a marked decrease in mean wind-speed relative to the remainder of the 40–60°S zonal band by 3.16% in summer and 7.28% in winter. Due to the exponential nature of the sea-spray aerosol flux in the Hartery et al. [2020] source function, higher wind-speeds would result in the greatest difference between BASE and SSALT sea-salt AOD as seen in the reduced slopes seen in Figure 39.

Explaining spatial changes in the CHEM run is more complex; Section 7.2 concluded that increased oxidation processes would result in increased AOD, while decreased aqueous-phase oxidation and reduced sea-salt output would reduce simulated AOD. Therefore, while the CHEM-simulated AOD follows the spatial patterns of zonal 10 m wind-speed (as sea-salt generated by the Gong [2003] source function is dependent on wind-speed), there are more factors such as chemistry and cloud fraction involved that will be discussed in Section 8.1. In this analysis, we assume sea-salt plays the most important role in mass-dominated AOD as a large particle. The following section clarifies this assumption through analysis of the contribution of sea-salt and other size-specified aerosols towards total AOD.

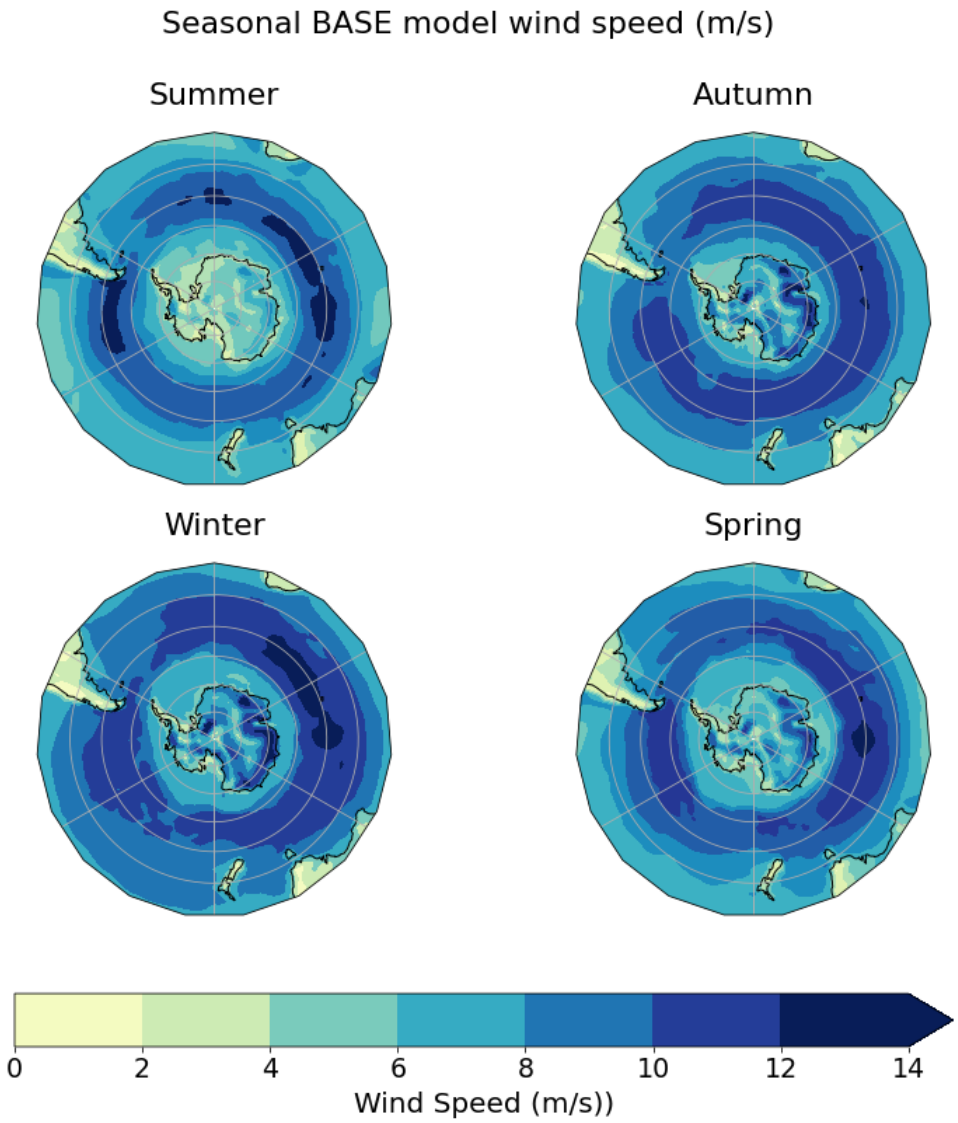


Figure 44: BASE run surface wind-speed output ($\mathrm{m\,s^{-1}}$) grouped seasonally and averaged.

7.4.6 Aerosol mode contribution to AOD

This section determined the role of sea-salt as a substantial contributor to total AOD where, combined with nss-sulfates, coarse-mode AOD accounted for nearly 60% of total AOD in the BASE run. As such, the most consequential changes in perturbation simulations were the reduction of sea-salt in the CHEM and AOD runs which reported decreases in coarse-mode AOD of 6% and 15% respectively. The contribution of each mode to total AOD when interpreted with size distributions (discussed in Section 7.3) can provide an important insight into why each perturbation exhibits a different mean AOD bias. Figure 45 shows changes made to each mode's AOD in different perturbation runs. The Gantt et al. [2012a] injection of OM mass into the Aitken insoluble mode saw an increase of 354% in the PMO run compared against the BASE run. (We recall the Gantt et al. [2012a] parameterisation

injects 75% of OM mass into the Aitken-insoluble mode, and 25% into the Aitken-soluble mode). This corresponds to the increased Aitken-mode peak particle size in the PMO run, which increased by 40.5% compared to the BASE run (Section 7.3).

Similarly, the Aitken-soluble mode AOD was 16.7% larger in the CHEM run compared to the BASE run, likely as a result of increase particle number from enhanced nucleation processes (discussed in Section 7.3). Changes in the accumulation and coarse soluble modes are largely dominated by sea-salt shown by the sensitivity of ACCESS-CM2 to the SSALT perturbation. The SSALT run exhibits a reduction in accumulation soluble AOD by 26.5% and coarse soluble AOD by 59.0% compared against the BASE run. Therefore, reductions in the CHEM coarse soluble mode by 22.4% are likely the result of a reduced sea-salt output (Figure 24). Reductions in CHEM accumulation soluble mode by 2.29% compared against the BASE run may either be the product of a shifting towards lower particle sizes due to cloud-processing (discussed in Section 7.3), or a reduction in accumulation-mode sea-salt. These changes to modal AOD have also been observed at a station basis (see Appendix Figure 67). The following discussion describes changes to modal AOD in the context of total AOD.

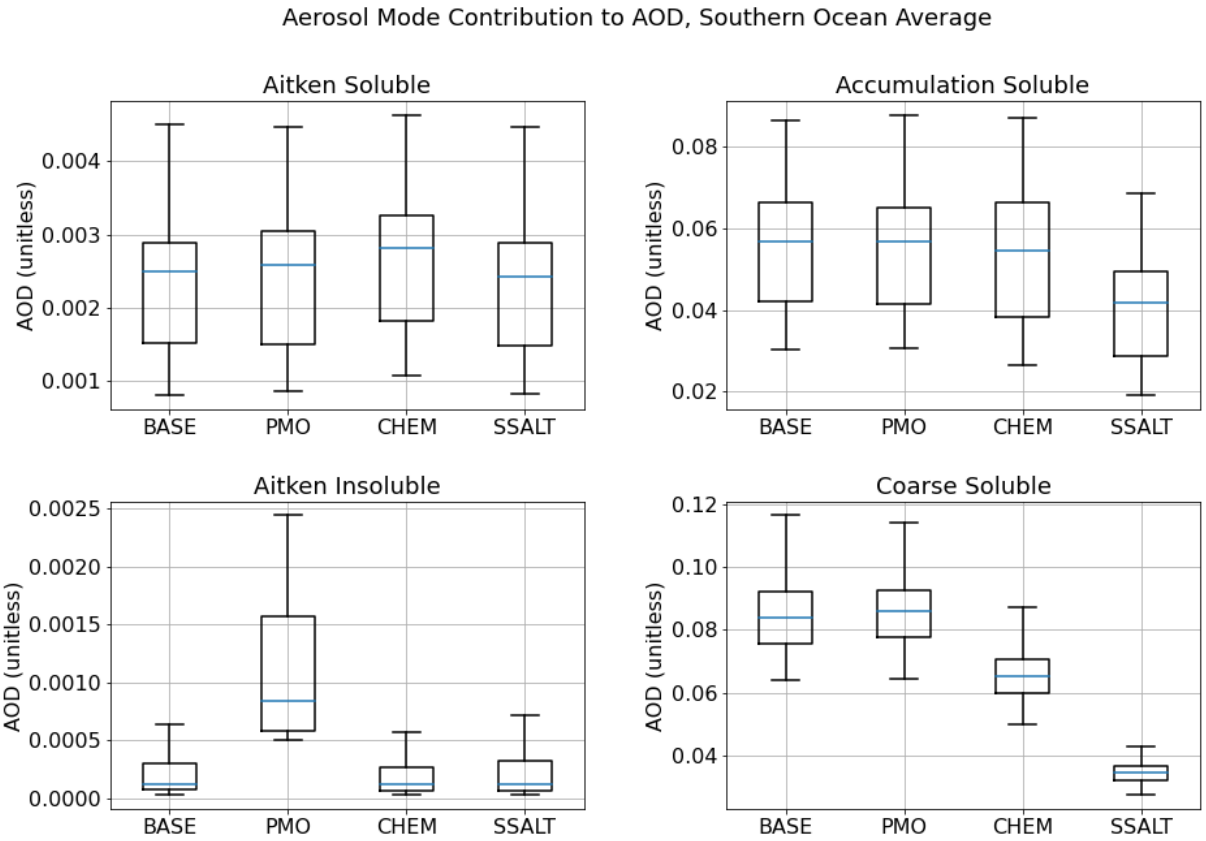


Figure 45: Changes in aerosol mode contribution to AOD between BASE model and pertubation runs. Data shown is averaged spatially over the Southern Ocean between years 2016–2018. The blue line shows the median and whiskers represent 1.5 × the Inter-Quartile Range.

The following discussion illustrates the contribution of each mode to total AOD, and demonstrates the dominant role of coarse-mode sea-salt in determining total AOD. Figure 46 below shows Southern Ocean average AOD of each aerosol mode which, when summed together create the total AOD. For the BASE run, Aitken-soluble and Aitken-insoluble modes contribute 1.63% and 0.161% respectively, whereas accumulation and coarse modes have the highest contribution to total AOD, at 38.8% and 58.9% respectively. Changes in the distribution of AOD within modes will have the largest impacts on total AOD in the accumulation and coarse modes. Hence, the significant increase in the PMO run Aitken-insoluble mode, seen in Figure 45, would not contribute substantially to AOD, as the particles are too small to be as optically active as larger particles. Larger particles such as sea-salt have a more substantial effect. Reductions in sea-salt and hence coarse-mode AOD shown in Figure 45 account for total AOD reductions of 6% and 15% for the CHEM and SSALT runs respectively.

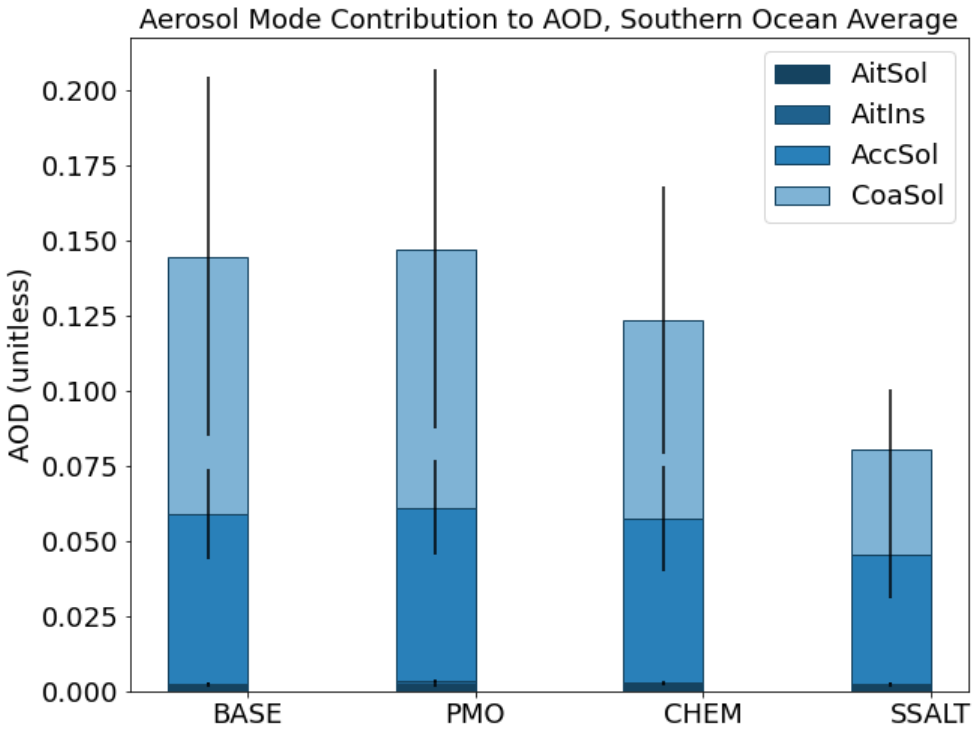


Figure 46: Stacked bar graph: AOD of each aerosol mode averaged over the Southern Ocean from years 2016–2018. The nucleation-soluble mode has been excluded in this figure as the contribution to AOD is negligible. Black lines extending from the bars show ±1 standard deviation.

7.4.7 Comparison against observational aerosol-mode AOD

The previous section outlined how model perturbations affected modal AOD. This section utilises size-resolved AOD observations to further identify model bias within fine and coarse mode AOD. All ACCESS-CM2 models overestimated fine-mode AOD, which is likely attributable to nss-sulfates. Nss-sulfates are the likely cause of fine-mode AOD overestimations due to the seasonal cycle not shown in observations, and the underestimation of accumulation-mode sea-salt, shown in Figure 26. This section provides evidence for the overestimation of coarse-mode sea-salt, proposed in Section 7.2, with the exception of the SSALT run. Figure 47 shows the seasonal cycle of simulated and observed fine and coarse mode contribution to AOD at Macquarie Island. With only one available observational station, limited data prevents an in-depth analysis but nevertheless a useful indication regarding model bias may be made (discussed in Section 6.3).

All ACCESS-CM2 simulations exhibited a positive NMBF in fine-mode AOD, with a maximum average summer NMBF of 3.65 in the BASE run and minimum of 2.65 in the SSALT run. In winter, this bias reduced in all models ranging from 1.08 in the PMO run to 0.347 in the SSALT run. Maximum NMBF values in the PMO run, combined with a seasonal cycle not represented in observations, and underestimations of accumulation-mode sea-salt (Figure 26) suggests this positive bias is due to biological nss-sulfates such as DMS oxidation products. Notably, the online DMS oxidation scheme in the CHEM run exhibited a reduced NMBF of 3.59 in summer and 0.793 in winter, potentially suggesting an improved representation of observed fine-mode nss-sulfates in online chemistry. Additional observations would be able to confirm whether reduced seasonal cycles are consistent across the SO, or only observed at Macquarie Island. Comparison against coarse-mode AOD shows differing model-observation bias between simulations.

Simulations that used the Gong [2003] sea-salt source function exhibited a positive bias against coarse-mode AOD. The CHEM run featuring online sea-salt emissions exhibited a lower annual NMBF of 0.161, and the modified sea-salt SSALT run exhibited a negative NMBF of -0.620. The sensitivity of simulated coarse-mode AOD to changes in sea-salt in the CHEM and SSALT suggest that coarse-mode AOD is largely representative of sea-salt. Despite the absence of coarse-mode sea-salt measurements for verification, it is therefore likely that the BASE, PMO, and CHEM overestimate coarse-mode AOD as suggested in Section 7.3.

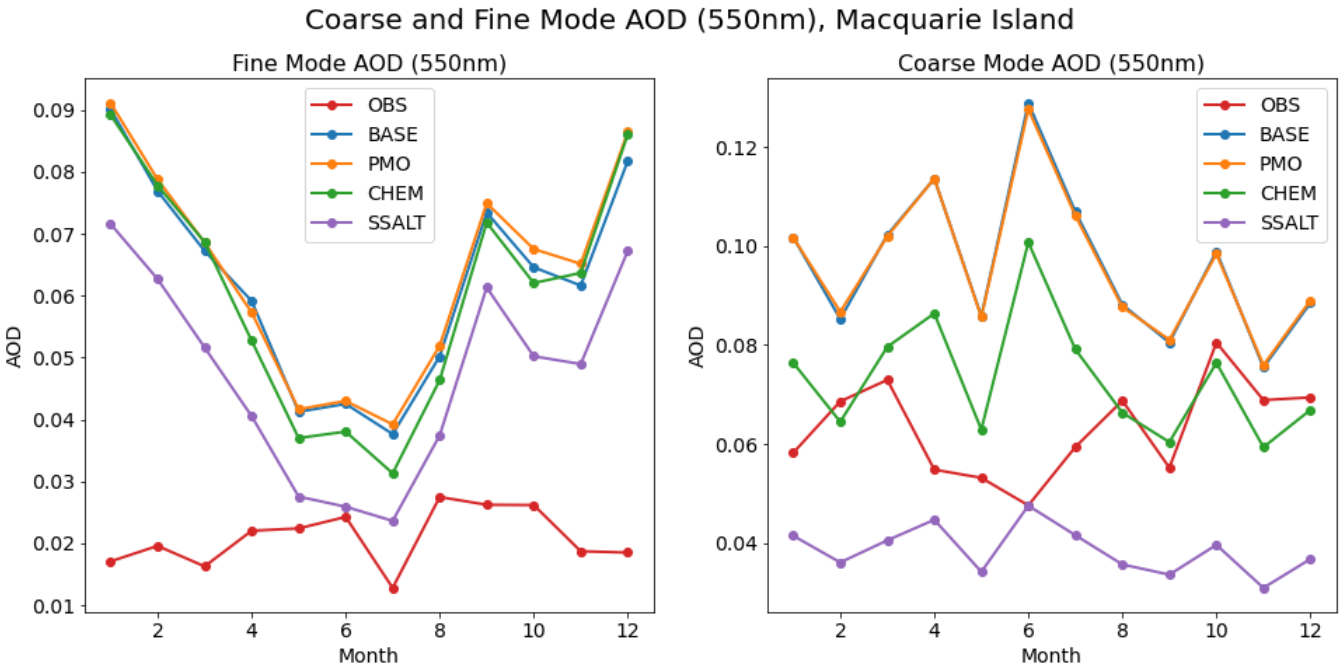


Figure 47: Annual cycle of observed and modelled fine and coarse mode AOD. The figure on the left shows the annual cycle of simulated and observed fine mode aerosol for all model runs at Macquarie Island. Fine mode aerosol has been calculated through an algorithm outlined in Section 6.3, and is defined in the model as the summed AOD contributions of nucleation, Aitken and accumulation modes. The figure on the right shows the annual cycle of simulated and observed coarse-mode aerosol for all model runs at Macquarie Island, where the observations have defined coarse mode AOD through an algorithm defined in 6.3, and model values refer to the coarse mode AOD output.

Summary of AOD analysis:

In this section, it was shown that:

- At all stations and voyages analysed, simulated AOD is positively biased in the BASE, PMO, and CHEM simulations, with the SSALT run returning lower or negatively biased AOD values.
- All simulations were able to successfully capture basic AOD seasonal patterns subject to bias, and the SSALT run consistently produced increased AOD bias in winter.
- The BASE, PMO, and CHEM simulations largely simulated increased inter-annual variability compared to observations, with the SSALT run under-simulating inter-annual variability.
- Implementation of the PMOA scheme saw regional increases in simulated AOD in biologically-active areas.

- Reductions in AOD largely followed dominant wind-speed patterns due to decreased sea-salt output in the CHEM and SSALT runs.
- Coarse-mode AOD was identified as the strongest contributor to total AOD, explaining why the reduced sea-salt output in the CHEM and SSALT runs is a likely cause of reduced AOD.
- All simulations were found to overestimate fine-mode AOD, which was likely the result of overestimated nss-sulfates. The BASE, PMO, and CHEM runs all overestimated coarse-mode AOD and the SSALT run underestimated coarse-mode AOD. This was attributed to respective over/underestimations of coarse mode sea-salt due to the sensitivity of ACCESS-CM2 simulated AOD to sea-salt.

7.5 Cloud Condensation Nuclei

Achieving an accurate representation of observed CCN in ACCESS-CM2 is important in reducing the substantial radiative uncertainty surrounding ACIs. The simulation of cloud droplets are dependent upon CCN, which drive both the cloud and radiation scheme (discussed in Section 3.1). Hence, this section establishes model bias in simulated CCN and identifies which perturbation simulations achieve an improved representation of observed CCN. Simulated CCN in each of the perturbation models is compared against the BASE run, and further compared against ground-based observations at two stations and two voyages. Following metrics described in Section 6.6, modelled CCN is evaluated in terms of capturing the magnitude and seasonality of observed CCN.

7.5.1 Magnitude of CCN

As hypothesised in Section 7.3, the PMO and CHEM runs increased simulated CCN compared to the BASE run. However, all ACCESS-CM2 simulations underestimated mean CCN compared against all stations and voyages. The CHEM run largely saw the greatest improvements in model-observation agreement in mean simulated CCN, and the SSALT run resulted in increased bias at all observational sites and voyages. Averaged over the Southern Ocean, the PMO and CHEM runs reported a relative increase of 34.1% and 44.5% in comparison to the BASE run, while the SSALT run reported an average CCN decrease of -15.8% (Table 20). These relationships to the BASE model were consistent at all stations and voyages analysed, with the PMO and CHEM both reporting increases and the SSALT model reporting decreased mean CCN values (Figure 48).

Compared against observations, all models underestimated observed CCN, despite increases in CCN values reported in the PMO and CHEM models. This suggests ACCESS-CM2 systematically underestimates observed CCN in the Southern Ocean. All simulations modelled mean CCN within the observational variability range reported at Cape Grim (Table 56). At Cape Grim, all models reported mean CCN values lower than observations by at least 30% with all IOA values under 0.491 (Table 56). Model-observation agreement worsened at Macquarie Island where all simulations reported mean CCN concentrations lower than observations by at least 68% and all IOA values below 0.218 relative to CCN observations (0.45% SS, written as 'OBS1' on Figure 48) (Table 57).

Southern Ocean models, N = 26280	BASE	PMO	CHEM	SSALT
Mean	56.5	76.4	82.4	48.1
Min	37.1	45.7	45.6	27.6
Max	95.7	129	147	89
Relative Difference (%)		19.9 (34.1%)	25.9 (44.5%)	-8.40 (-15.8%)
Correlation		0.937	0.936	0.996
Bias		19.9	25.9	-8.40
NMBF		0.353	0.459	-0.175
RMSE		22.5	28.9	8.51
NMAEF		0.353	0.459	0.175
IOA		0.659	0.567	0.899
Standard deviation	12.4	21.1	23.6	13.0

Table 20: Statistical summary of average modelled CCN, Southern Ocean Average (40–60S, 2016-2018).

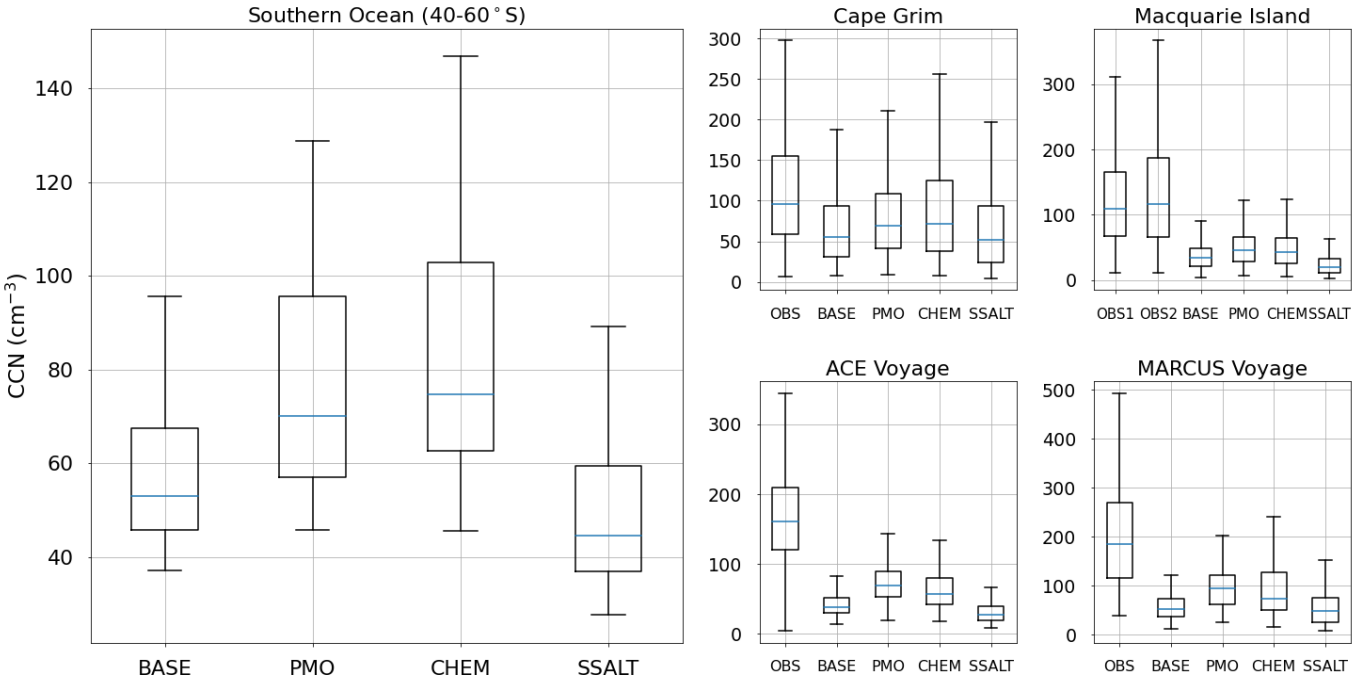


Figure 48: Boxplots comparison of simulated and observed CCN. The plot on the left shows all hourly output data averaged over the Southern Ocean spatial domain from 2016-2018. Figures on the right show model output data selected at the nearest gridpoint for Cape Grim and Macquarie Island, and subset for the nearest gridpoints and timestamps corresponding to the ACE Voyage and MARCUS Voyage GPS tracks. The blue line represents the median value, and the whiskers extend to 1.5 times the inter-quartile range.

Probability Density Function (PDF) plots shown in Figure 49 revealed further differences between simulated CCN and observations. At all sites/voyages, model PDFs displayed common features of higher frequency peaks, bias shifted towards lower values, and did not capture the full range of observed CCN. These features were observed in the monthly averaged time-series for both station observations, shown in Appendix Figure 71. All simulations exhibited the best fit against CCN distribution observations at Cape Grim. Despite decreased bias and improved IOA values compared to other stations (Table 56), the maximum modelled CCN values are still approximately a third of observations, evident in the lacking tail lengths in Appendix Figure 70.

At Macquarie Island, all models exhibited a far steeper PDF, with model standard deviations ranging from ∼2–4 times lower than observations (see Table 57). The BASE and PMO PDFs both exhibited bimodal peaks which were not represented in the observations, and the SSALT PDF reported a peak frequency at lower values, which was approximately seven times higher than the peak frequency in observations (see Appendix 70).

Examining the ACE Voyage, all models exhibited kurtosis values approximately four times higher than observations, indicating a lacking ability to capture the full range of observed CCN. Both observational voyage PDFs exhibit bimodal peaks which were captured to a limited extent by models. Multiple peaks in a PDF suggest the sampling of separate aerosol populations; Section 7.1.2 suggested poor model wind-direction skill means the model may struggle to capture observed air masses.

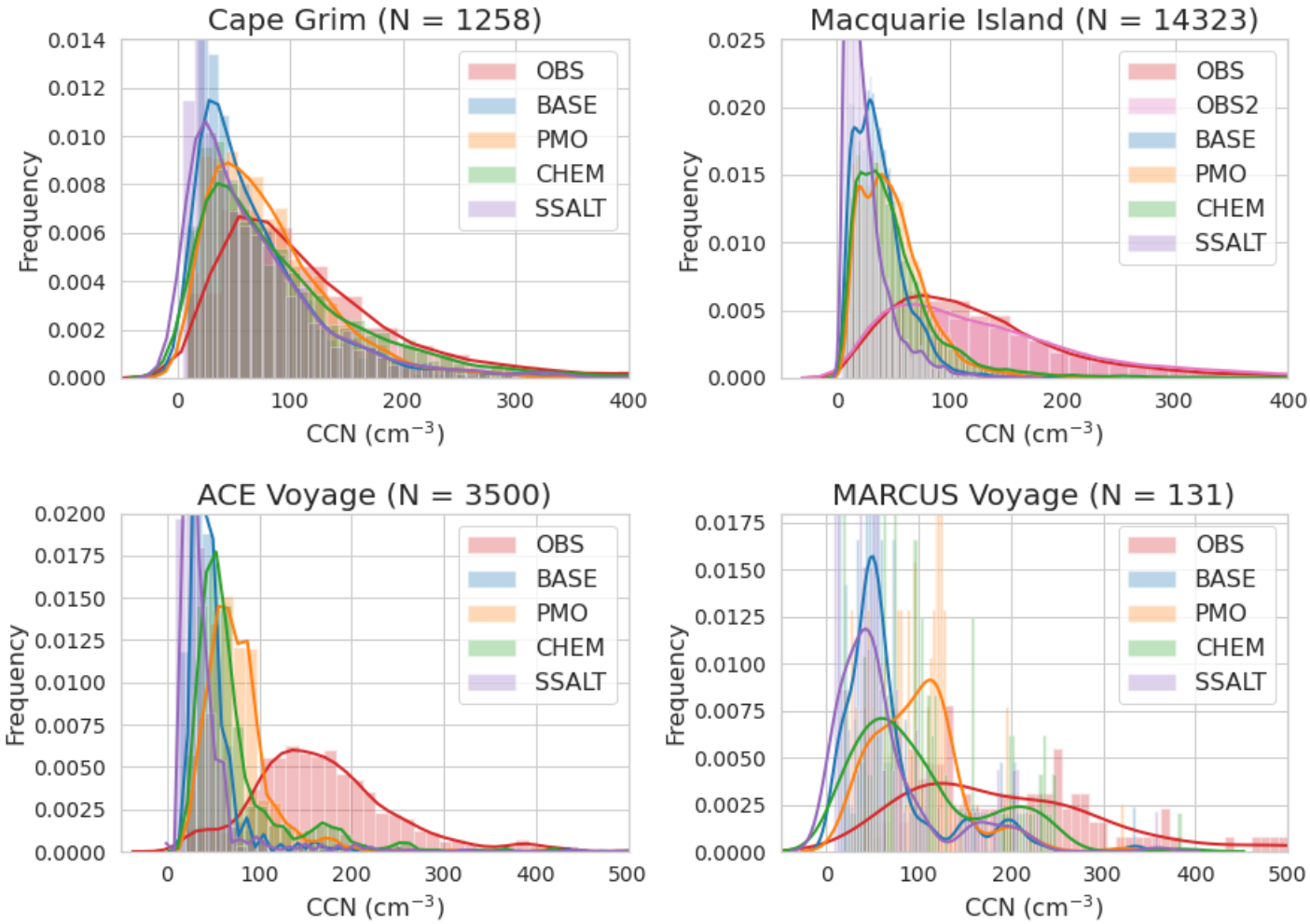


Figure 49: Probability Density Function histograms for observed and modelled CCN using a bin size of 100. Figure has been cropped to best compare the histogram peaks (see Figure 70 for the full image.)

7.5.2 Seasonal representation of CCN

Section 7.5.1 identified mean simulated bias between models. This section identifies whether those biases were consistent annually or subject to seasonal variations. All simulations captured the overall observed CCN seasonal pattern at Cape Grim and Macquarie Island but lacked increased summer and winter CCN signals. At both stations, all simulations exhibited a maximum bias in winter due to divergent model-observation patterns, and all simulations failed to capture observed inter-annual variability.

Monthly-averaged seasonal cycles are shown at Cape Grim, Macquarie Island and averaged over the Southern Ocean in Figure 50. At both Cape Grim and Macquarie Island, all simulations exhibited a consistent negative bias which worsened in winter due to increased CCN observations that were not captured by the model. At Cape Grim, winter-time NMBF values ranged from the -0.77 in the CHEM run, to -1.62 in the SSALT run (61 & 62). Despite notable bias, all models largely remained within ±1 standard-deviation of the observed annual temporal variability.

At Macquarie Island, all simulations exhibited a clear negative bias with no substantial overlap between modelled and observed annual temporal variability (within ±1 standard-deviation). Similarly to Cape Grim, all simulations at Macquarie Island underestimated winter-time CCN by up to a factor of 6.67 in the SSALT run (NMBF= -5.67), and the PMO run exhibited the least bias (NMBF=-2.19) (Table 66). Increased winter-time CCN observations have also been noted in a previous study but not attributed to a physical source [Murphy et al., 1998].

While all simulations demonstrated the expected seasonal cycle for CCN (maximum in summer, minimum in winter ([Gras and Keywood, 2017]), all runs failed to capture increased observed summer-time CCN, particularly at Cape Grim. The PMO and CHEM runs exhibited the largest summer CCN increase of 11.3% and 12.9% compared against the BASE run respectively. This suggests that ACCESS-CM2 is missing both summer and winter-time sources of CCN, which is discussed further in context with AOD in Section 8.1.

All models underestimated the inter-annual variability of observed CCN, particularly in the winter at both observational stations (Appendix Figures 72 & 73). For example, modelled standard deviations ranged from 5.28 (CHEM)–9.71 (SSALT) times lower than winter-time Macquarie Island observations. Of all models, the CHEM run exhibited both the lowest bias across all seasons and stations, and performed the best in predicting inter-annual variability particularly in summer (see Figure 73).

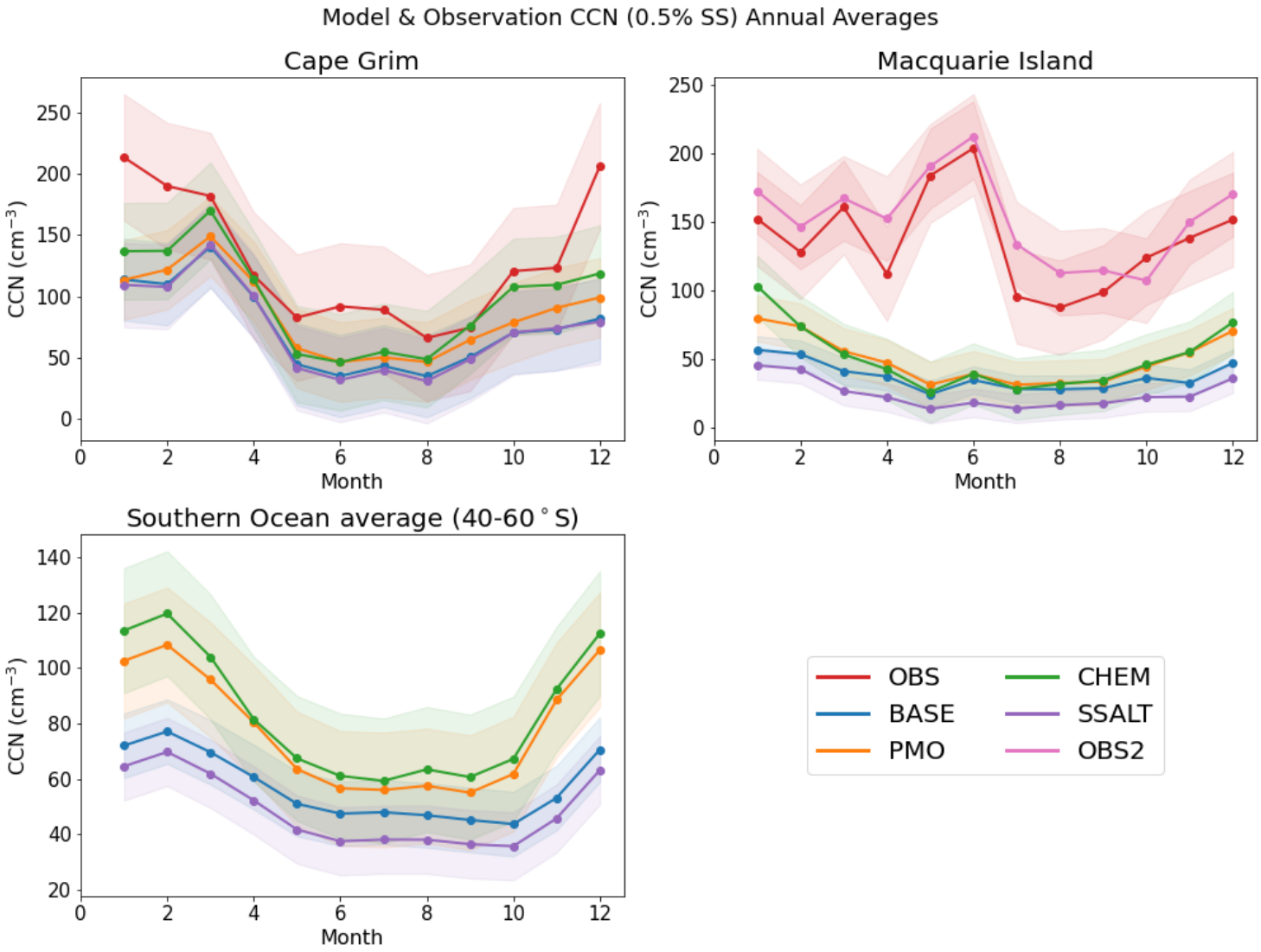


Figure 50: Seasonal cycle of observed and simulated CCN. Data has been grouped monthly and averaged temporally, and the shaded region denotes ±standard deviation.

This section has identified seasonal bias in each simulation compared against observations. The following section establishes whether those seasonal biases were consistent spatially, or featured regional variations similarly simulated to AOD in Section 7.4.5.

7.5.3 Spatial representation of CCN

Similarly to increases in AOD, the PMO run saw increased CCN in the PMO-enhanced region, particularly in summer and spring. Opposite to spatial changes in AOD, the CHEM run saw increases in CCN zonally, with the largest increase in summer by 44.5% compared to the BASE run. Finally, the SSALT run saw zonal decreases in CCN, which were consistent with dominant wind-patterns and spatial changes similarly in AOD.

Spatial differences between the perturbation runs and BASE run are shown in Figure 51. The PMO run exhibited increased CCN in the PMO-enhanced region by 120% in summer and 125% in spring relative to the BASE run. Increased CCN in this region is likely the result of increased [chl-a] observed in Figure 43 and discussed in Section 7.4.5.

The CHEM run exhibited the largest increases in CCN zonally (between 40–60°S) during the summer and spring with relative differences of 42.1% and 26.1% respectively compared against the BASE run. CHEM-simulated CCN exhibited the opposite sign to simulated AOD, and exhibited a more homogeneous increase of CCN spatially, hence does not exhibit the same wind-dominated spatial patterns as AOD discussed in Section 7.4.5. Instead, the largest increases of CCN were located near coastal environments of New Zealand and Antarctica, which are excluded from the scope of this study. This suggests that sea-salt, which played a dominant role in AOD bias, is not as significant in total CCN concentration. Instead, it is likely that Aitken and smaller accumulation-mode particles have determined the zonal increase of CHEM-simulated CCN, as they do not influence AOD substantially but do contribute to CCN number.

The SSALT run exhibited similar spatial patterns of CCN to the spatial AOD distribution discussed in Section 7.4.5. Zonal decreases of CCN were simulated, which were constricted towards higher latitudes in summer, and increased towards lower latitudes in winter, corresponding with seasonal zonal 10 m wind-speed distributions shown in Figure 44. The role of sea-salt in these CCN changes may be easily attributed as it is the only variable changed in the SSALT run, which has been discussed in context of size distributions and AOD in Section 8.1. SSALT-simulated CCN was a factor of 2.38 larger in summer compared to winter despite reduced summer-time zonal wind-speeds by 11.4% (compared to winter). This suggests a nss-element (non wind-speed driven) contributes to increased summer-time modelled CCN.

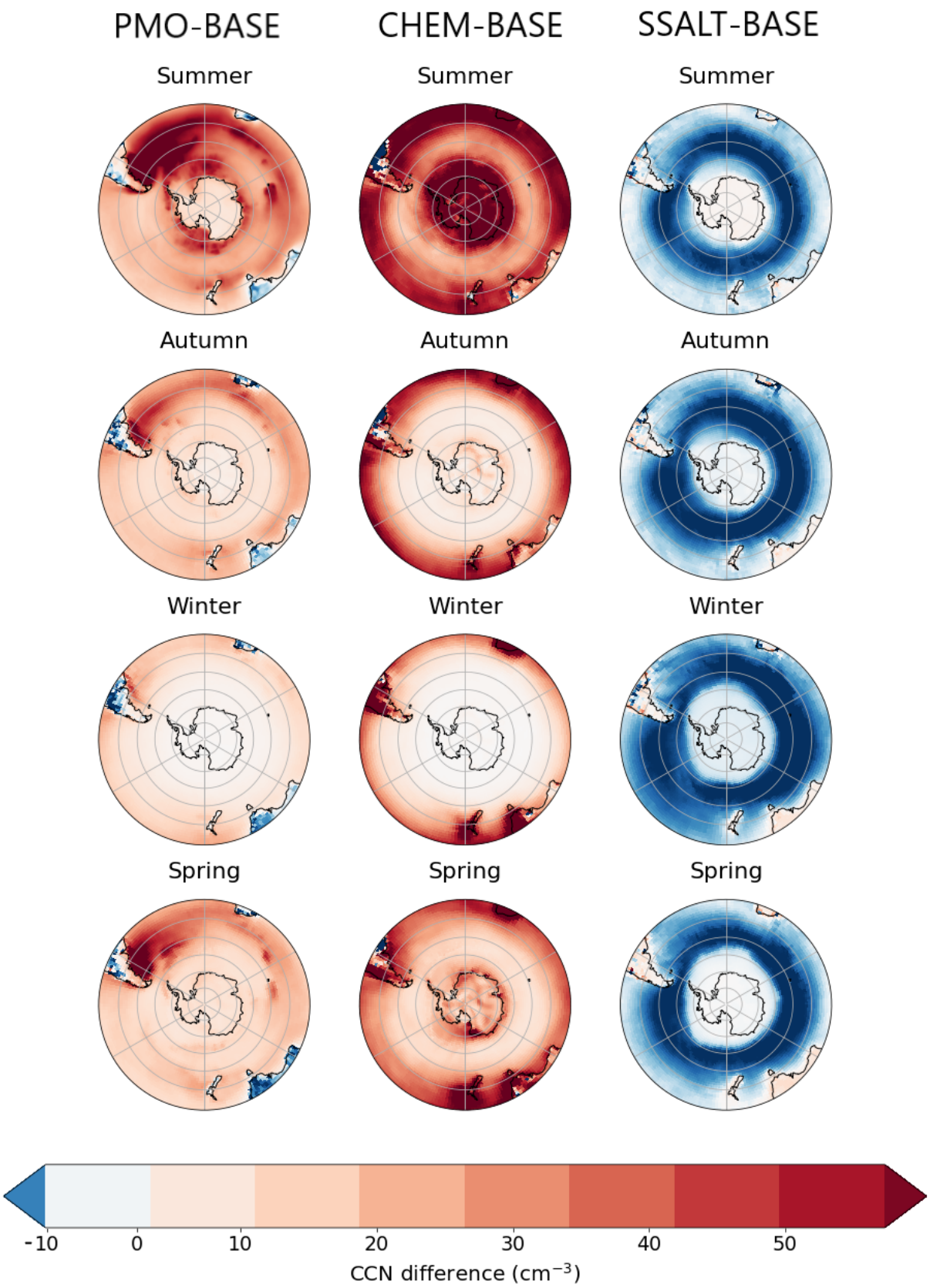


Figure 51: Spatial differences of CCN (0.5% SS), where the BASE run values have been subtracted from each perturbation simulation. Hourly output data has been grouped seasonally from 2016-2018 and averaged. The PMO run also exhibits regional areas of CCN increase which are coincident with increased [chl-a], but this thesis focuses on the PMO-enriched area for discussion.

CCN analysis summary:

Analysis in this section has showed that:

- All ACCESS-CM2 simulations overestimated CCN and underestimated inter-annual variability at all sites and voyages analysed, where the PMO and CCN runs increased simulated CCN concentration, and the SSALT run decreased CCN. Overall, the CHEM run exhibited the greatest reduction in model bias and best representation of inter-annual variability at all observational sites.
- The previous finding confirms predictions made from size-distributions regarding increased particle number and size in the PMO and CHEM runs (Section 7.3)
- All simulations were able to capture the seasonal cycle of Cape Grim CCN well but completely lacked seasonal representation of observations at Macquarie Island. All simulations lacked a summer and winter source of CCN.
- Spatially, the PMO run saw an increase in simulated CCN consistent with spatial increases in AOD, which corresponded to biologically-active areas.
- The CHEM run saw zonal increases of CCN (opposite to simulated AOD zonal decreases), likely as the result of more numerous Aitken and accumulation-mode particles shown in size distributions (Figure 32).
- Decreases in SSALT-simulated CCN were linked to seasonal variations in wind-speed, consistent with simulated AOD.

7.6 Aerosol-chemistry interactions with cloud and radiation schemes

The overall objective of improving simulated aerosol representation in the Southern Ocean is to amend the known radiation and Cloud Fraction (CF) bias in this area. Radiation in ACCESS-CM2 is calculated through numerous interacting schemes including ARIs in the aerosol-radiation scheme, ACIs in the aerosol-cloud scheme (defined in Chapter 4) and associated convective meteorology schemes calculated entirely separately to aerosols. We recall the Abdul-Razzak Ghan (2000) parameterisation scheme implemented within UKCA, which connects the aerosol and radiation schemes through prescribing the activation of aerosols into cloud droplets [Abraham et al., 2016]. While the role of clouds has largely been excluded from the scope of this study, this section examines simulated Cloud Droplet Number Condensation (CDNC) in ACCESS-CM2 and perturbation simulations. Next, the SW TOA ↑ bias in ACCESS-CM2 and perturbation simulations is evaluated, as SW TOA ↑ provides the best estimate for ACIs (cloud albedo). We identify whether the ACCESS-CM2 radiation bias can be attributed to aerosol influence through simulated CNDC. Finally, Section 7.6.3 evaluates the overall low CF bias of ACCESS-CM2, and how aerosol-chemistry perturbation simulations have altered this bias. Low cloud fraction has been selected as this would represent any surface aerosol-based changes to the cloud lifetime effect.

7.6.1 Cloud Droplet Number Concentration

This section has showed that all simulations reported a similar spatial distribution of CDNC and relationship to the BASE run as was observed in CCN. Compared against the BASE run, the PMO run increased mean simulated CDNC by 41.5%, particularly over biologically-active regions such as the PMO-enriched region. The CHEM run saw a largely consistent zonal increase of 9.7% between 40–60° compared against the BASE run. The SSALT run simulated decreased CDNC consistent with areas of increased simulated wind-speed, with a mean reduction of 18.4% averaged over the SO compared to the BASE run (Figure 52).

Figure 52 shows simulated CDNC for the BASE run and differences in perturbation simulations averaged from 2016–2018. It is common practise in model comparison studies to select CDNC values at a model height of 1 km as a representation of boundary layer clouds, hence model data has been selected at model level number 10 (defined as between 876–1037m above the surface).

Simulated bias varied seasonally. The greatest difference in model bias was noted in spring in the PMO run with a NMBF of 0.579, which would be expected due to the perturbation having the largest impacts on simulated CCN in biologically-active spring-time months. The lowest bias was observed in summer in the SSALT run with a NMBF of 0.087. The PMO and CHEM runs reported the lowest bias in winter-time months due to lower simulated CDNC. Reduced winter-time CDNC may be attributed to suppressed biogenic emissions (in the PMO run) and DMS oxidation processes (in the CHEM run), which limits the amount of nss-sulfate aerosols that grow into the CDNC population. The SSALT run exhibited an increased winter-time bias, which may be explained as the effects of the perturbation would have the largest impacts at high wind speeds observed in winter-time due to the exponent dependency of the Hartery et al. [2020] SSA source function on U_{10} wind-speed (see Equation 7).

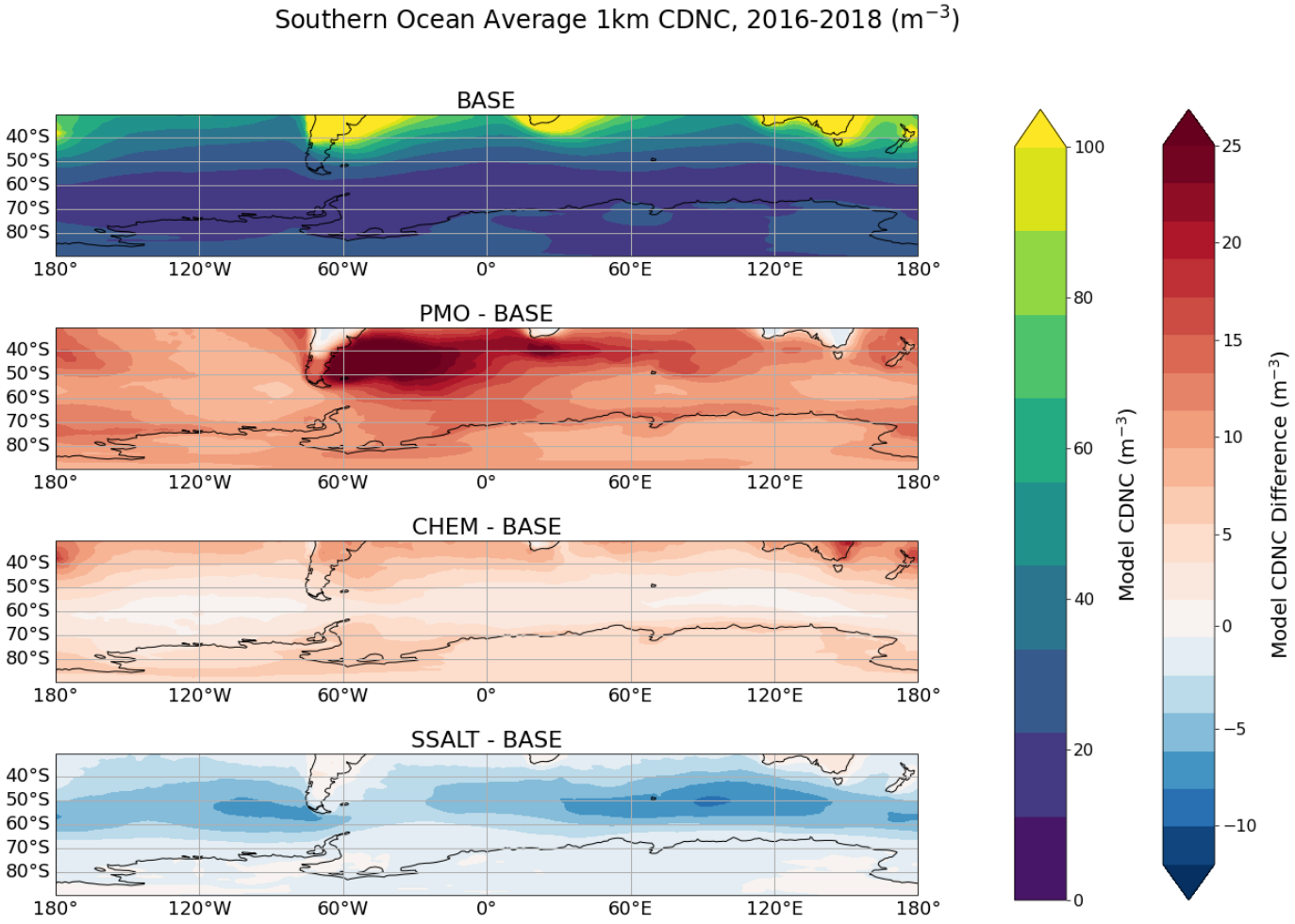


Figure 52: Comparison of simulated CDNC between models at a 1 km model height.

CDNC	BASE	PMO-BASE	CHEM-BASE	SSALT-BASE
Mean	31.2	44.8	34.8	26.3
Mean difference (%)		13.5(40.6%)	3.18 (9.7%)	-4.88 (-17.5%)
Correlation		0.936	0.995	0.998
Mean bias		13.5	3.18	-4.88
NMBF		0.433	0.100	-0.185
RMSE		16.2	3.6	5.0
NMAEF		0.433	0.100	0.185
IOA		0.676	0.966	0.932

Table 21: Comparison of simulated CNDC values between models, averaged over the Southern Ocean from 2016–2018.

This section established that the implementation of aerosol-chemistry perturbations had an substantial impact on CDNC, similarly to changes noted in CCN. The following section identifies the extent to which these impacts translate to appreciable changes in the radiation scheme.

7.6.2 SW TOA ↑ radiation

This section provides a brief overview of how perturbations to the aerosol-chemistry scheme have resulted in changes to overall simulated SW TOA ↑ radiation. In this section, the term radiation has been used to refer specifically to SW TOA ↑ radiation. First, the three perturbation simulations have been compared relative to the BASE run, and these model differences were compared seasonally. All simulations were then compared against the CERES-EBAF satellite TOA SW ↑ radiation product and evaluated for total and seasonal variations of model bias.

The PMO run produced a positive SW TOA ↑ radiation bias, while the CHEM and SSALT simulations were negatively biased compared to the BASE run. All ACCESS-CM2 simulations exhibited a clear positive zonal bias between ∼40–60°S compared to observations. However, the magnitude of changes to simulated radiation in perturbation runs only fell within 2.62% of the BASE-simulated radiation compared to observations. Therefore, aerosol-chemistry schemes have not made a substantial reduction in the SW TOA ↑ radiation bias of ACCESS-CM2.

Compared to the BASE model, the PMO run increased average SW TOA ↑ radiation by 3.05 W/m^2, and the CHEM and SSALT runs decreased average simulated radiation by -0.347 Wm^{-2} and -2.64 Wm^{-2} respectively over the SO (Table 22). The largest changes to radiation between simulations occurred within 40–60°S, the spatial domain of this study, shown in Figure 53.

Seasonally, the PMO simulated the largest increases in radiation in summer and spring with differences of 5.50 Wm^{-2} and 4.36 Wm^{-2} respectively (compared to the BASE run). Of all perturbation runs, the CHEM run had the least amount of change compared to the BASE run, with a maximum difference occurring in autumn of -0.686 Wm^{-2}, with the lowest difference occurring in summer of -0.130 Wm^{-2}. The SSALT run saw the largest decrease of simulated radiation in spring and summer, with differences of -3.85 Wm^{-2} and -3.31 respectively (compared to the BASE run). Spatially, these seasonal changes occurred zonally within the 40–60° latitudinal band observed in Figure 53, subject to changes in magnitude.

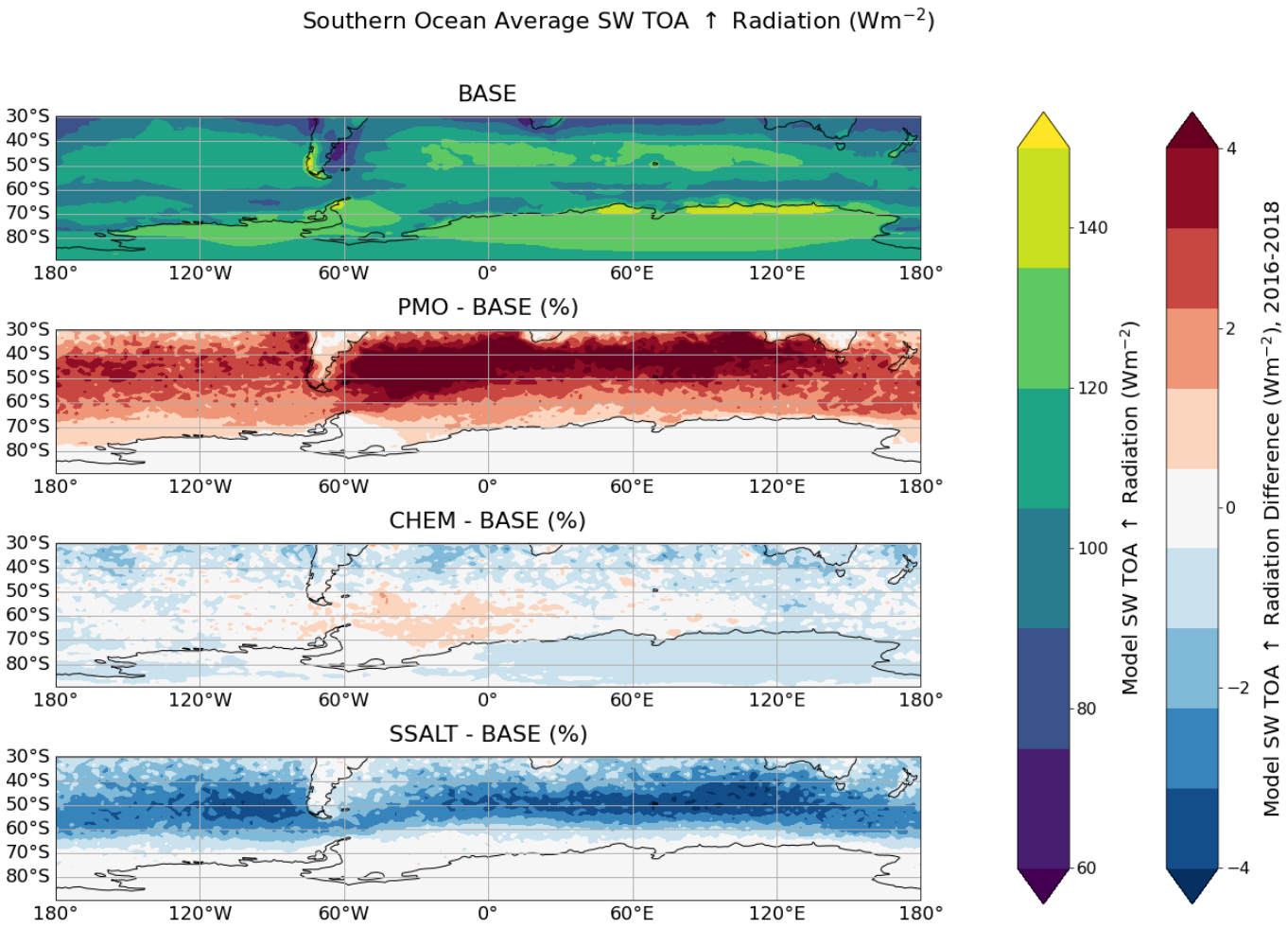


Figure 53: Comparison of simulated SW TOA ↑ radiation in the BASE and perturbation simulations. The top panel shows the absolute values of radiation output, and the following three panels show the difference of each perturbation simulation minus the BASE run values.

SW TOA ↑ Radiation	BASE	PMO-BASE	CHEM-BASE	SSALT-BASE
Mean	111.147	114.192	110.799	108.506
Mean difference (%)		3.045 (2.274%)	-0.347 (-0.497%)	-2.640 (-2.450%)
Correlation		1.000	1.000	1.000
Mean bias		3.045	-0.347	-2.640
NMBF		0.027	-0.003	-0.024
RMSE		3.924	0.516	2.853
NMAEF		0.027	0.004	0.024
IOA		0.998	1.000	0.999

Table 22: Comparison of simulated SW TOA ↑ Radiation between models.

Comparison against observations:

Figure 54 shows that compared to CERES-EBAF satellite observations, all simulations exhibited an average positive bias in SW TOA ↑ radiation in lower latitudes, and a negative bias in higher latitudes with an abrupt change at approximately 60°S. Averaged between 40–60°S, the BASE, PMO, CHEM, and SSALT runs reported a differences ranging from 4.09 W/m^2 in the CHEM run to 7.48 W/m^2 in the PMO run, the latter of which was outside of the observational uncertainty range (Table 23). Implementation of the SSALT run saw the greatest reduction in model bias, bringing simulated radiation values within the uncertainty of the satellite product ($\pm 2.5\,W/m^2$ [Loeb et al., 2018]).

The positive radiation bias between 40–60°S was consistent annually for all simulations, with the exception of the SSALT which simulated mean summer-time radiation as 1.87% lower than observations. Model bias (NMBF) worsened in winter in all simulations by factors of 25, 3.58, 18.8 and 6.33 for the BASE, PMO, CHEM, and SSALT runs respectively compared to summer. The BASE, CHEM and SSALT runs represented observed radiation well in summer, where mean model-observation differences fell within satellite uncertainty bounds. In all seasons, the SSALT run reported the closest mean radiation values to observations, and the PMO run reported the largest difference (Appendix Tables 73, 74, 75, & 76).

SW TOA ↑ Radiation ($W\,m^{-2}$)	CERES-EBAF	BASE-CERES	PMO-CERES	CHEM-CERES	SSALT-CERES
Mean	107	111	114	111	109
Mean difference (%)		4.44 (6.64%)	7.48 (9.01%)	4.09 (6.09%)	1.80 (4.02%)
Correlation		1.00	1.00	1.00	1.00
Mean bias		4.44	7.48	4.09	1.80
NMBF		0.0416	0.0701	0.0383	0.0169
RMSE		5.74	7.77	5.27	4.67
NMAEF		0.0474	0.0701	0.0435	0.0403
IOA		1.00	0.994	1.00	1.00

Table 23: Comparison of CERES-EBAF observed and simulated SW TOA ↑ radiation, averaged over the Southern Ocean between 2016–2018. Simulated mean model-observation differences have been shaded if they are within the observational uncertainty ($2.5\,W\,m^{-2}$), as outlined in Appendix A.7.

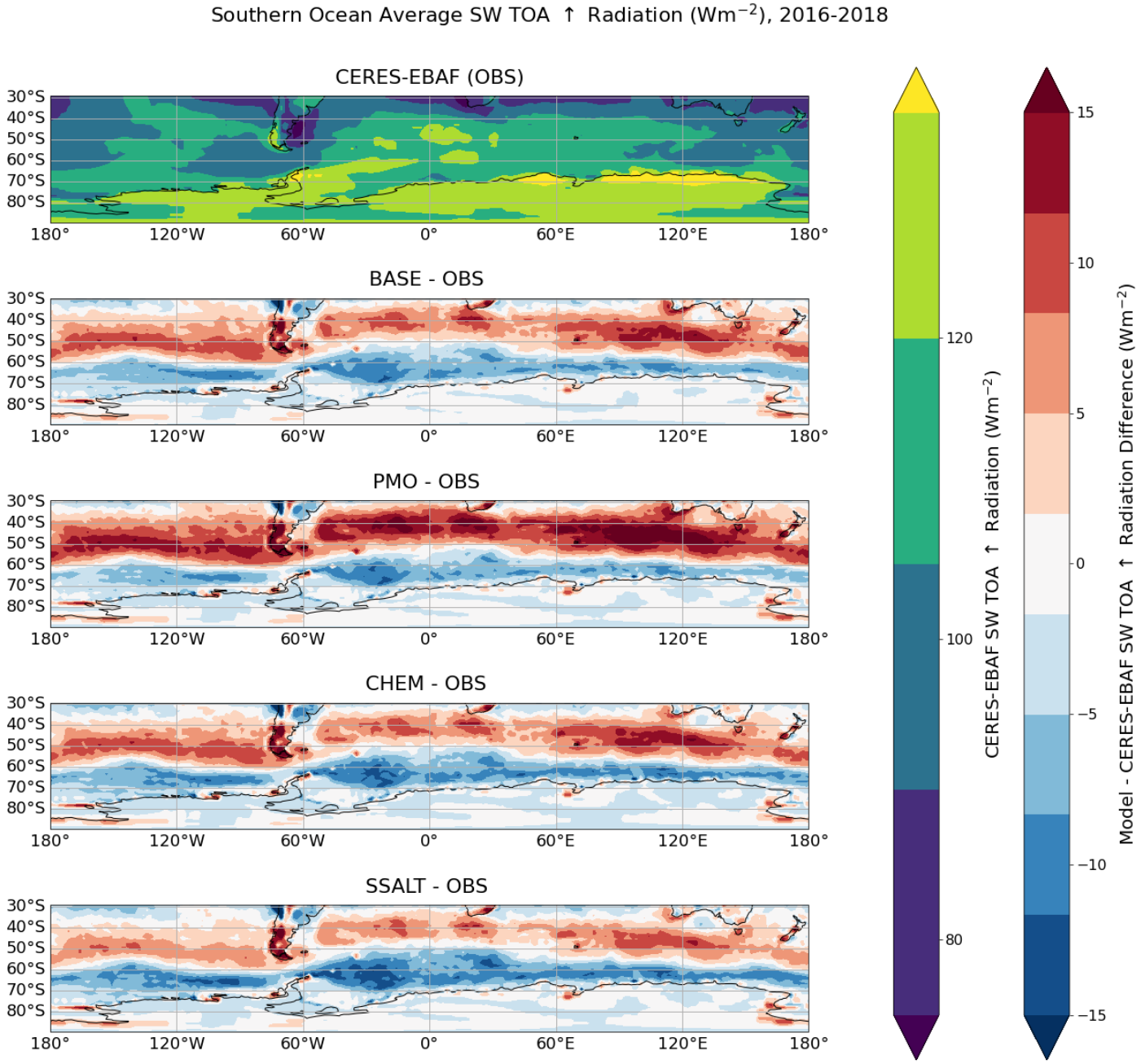


Figure 54: Average SW TOA ↑ radiation compared between model output and satellite-observed values. The top panel shows the absolute values of the CERES-EBAF observational dataset, and the following four plots show each model minus the satellite values. The satellite data has a monthly temporal resolution, so model output has been resampled to monthly values and averaged temporally from 2016–2018.

7.6.3 Low Cloud Fraction

Motivation for this study in Chapter 4 stated that most GCMs underestimate low Cloud Fraction (CF), contributing to Southern Ocean SST warm biases. ACCESS-CM2 consistently overestimates low CF by 0.181 (unitless), a relative difference of 36.1% compared to observations. All perturbation simulations had minimal impact on this bias, changing the mean simulated low CF by a maximum of 0.007 (1.2%) relative to the BASE run.

Figure 55 shows the PMO run increased simulated low CF by 0.006, and the CHEM and SSALT runs both decreased average low CF by 0.003 and 0.006 compared to the BASE run respectively (Table 24). The greatest changes to low CF were simulated within the 40–60°S domain. Seasonally, the PMO run recorded the highest increase in low CF in biologically-active spring and summer months. The CHEM and SSALT runs recorded the largest decreases in autumn and winter respectively. However, the magnitude of these differences were small; seasonal-averaged low CF varied by under 2% in the BASE run and under 6% in the PMO, CHEM and SSALT runs (Tables 77, 78, 79 & 80). The next section evaluates whether these perturbation changes have improved or worsened ACCESS-CM2 low CF bias compared to observations.

Cloud Fraction	BASE	PMO-BASE	CHEM-BASE	SSALT-BASE
Mean	0.776	0.782	0.773	0.770
Mean difference (%)		0.00644 (0.832%)	-0.00295 (-0.379%)	-0.00614 (-0.786%)
Correlation		0.994	0.997	0.993
Mean bias		0.00644	-0.00295	-0.00614
NMBF		0.00830	-0.00382	-0.00798
RMSE		0.00678	0.00337	0.00683
NMAEF		0.00830	0.00382	0.00798
IOA		0.968	0.992	0.965
Standard deviation	0.0190	0.0186	0.0184	0.0170

Table 24: Comparison of simulated low cloud fraction between ACCESS-CM2 simulations averaged over the Southern Ocean (40–60°S), 2016–2018.

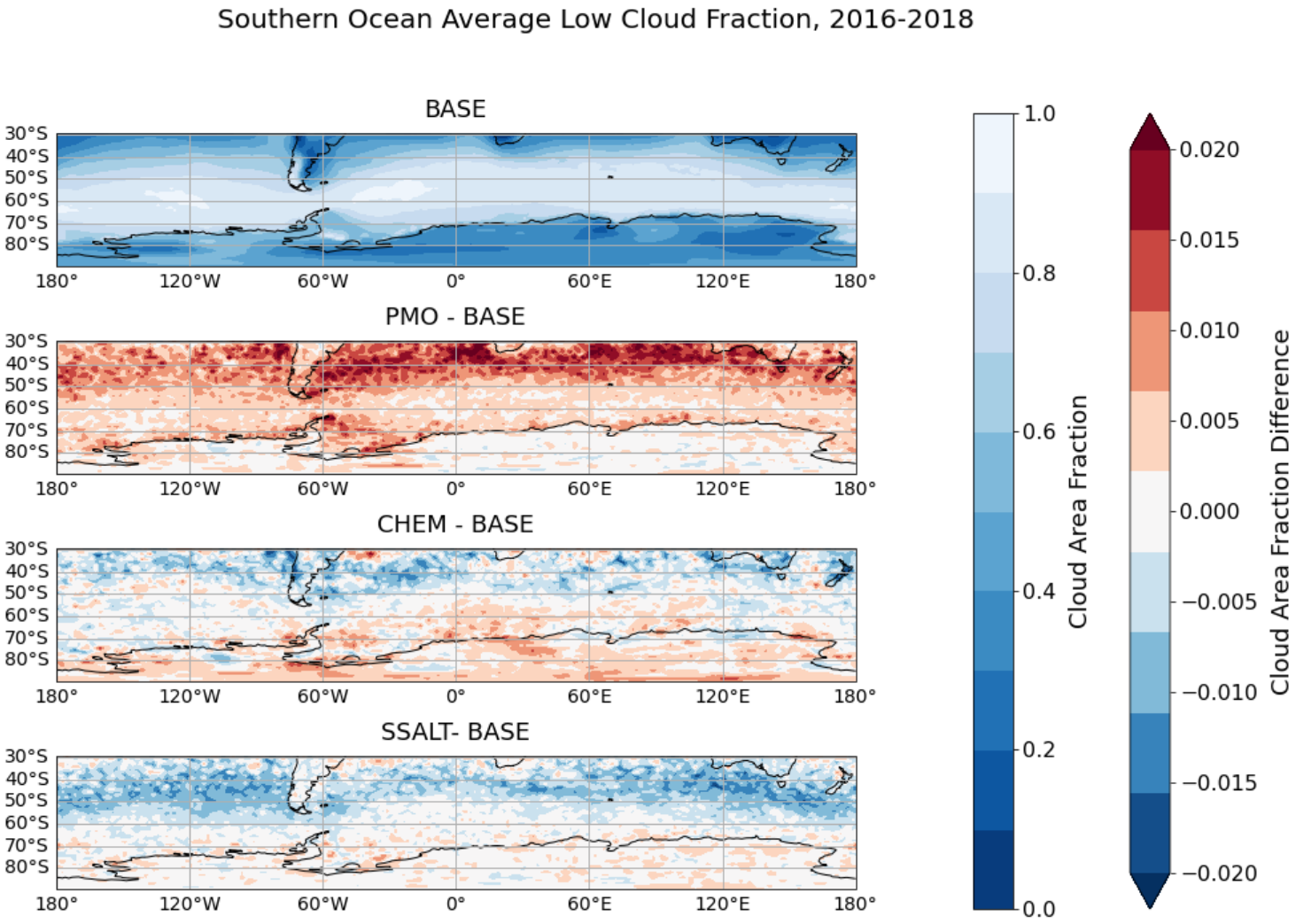


Figure 55: Comparison of BASE and perturbation model output low cloud fraction. The top plot shows the absolute values of cloud fraction output, and the following three plots show the difference of each perturbation simulation minus the BASE run values.

Comparison to observations

Figure 56 demonstrates the substantial positive bias of ACCESS-CM2 compared to CALIPSO-GOCCP satellite observations, and the negligible impact of aerosol-chemistry perturbations to overall simulated low CF. Averaged over the study spatial and temporal domain, the BASE, PMO, CHEM, and SSALT runs showed consistent increases in low CF of 0.181, 0.188, 0.178, and 0.175 respectively (Table 72). This is in contrast to the effects of perturbation simulations on radiation, where both the CHEM and SSALT runs resulted in a mean decrease of SW TOA ↑ radiation.

Seasonally, the largest model bias was noted in the PMO run in winter with an NMBF of 0.370 (outside of the observational variability range), and the lowest NMBF was reported by the SSALT run in summer of 0.237 (compared against observations). Spatially, the models exhibited a homogeneous positive bias from approximately 40–80°S, with no delineation between positive and negative bias at 60°S as seen in SW TOA ↑ radiation model-observation comparisons (Figure 56). These results have been discussed further in Section 8.3.

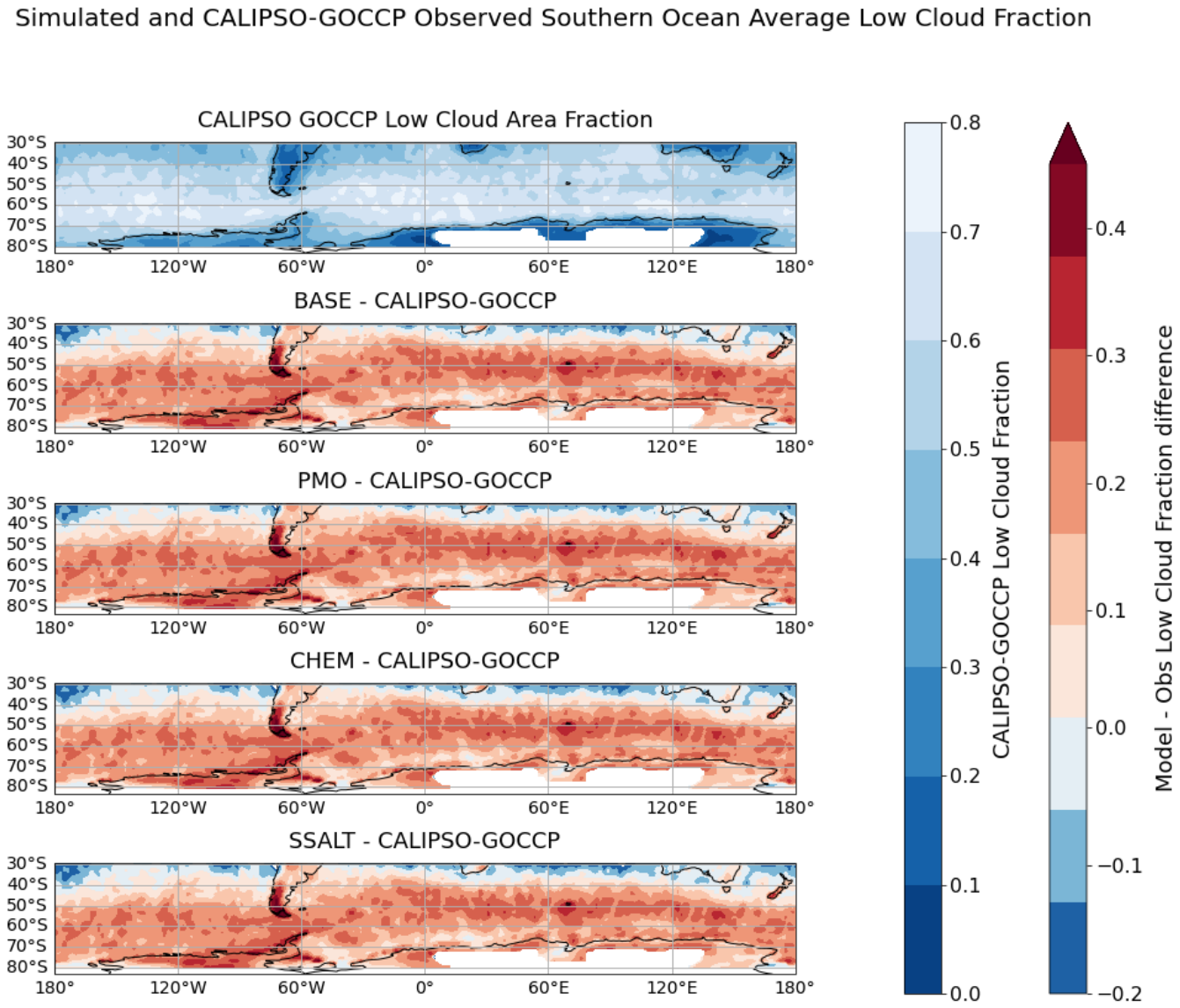


Figure 56: Comparison of simulated low cloud fraction and CALIPSO-GOCCP satellite observations, averaged temporally over 2016–2017. The first plot shows the absolute values of the satellite-based product CALIPSO-GOCCP Low Cloud Area Fraction, and the following plots show each perturbation run minus the satellite data. Areas of white between 70–80°S indicate missing data in the satellite dataset. Land values have been included in this plot for context but have been removed in the following statistical analysis.

Cloud Fraction	CALIPSO-GOCCP	BASE-CALIPSO	PMO-CALIPSO	CHEM-CALIPSO	SSALT-CALIPSO
Mean	0.608	0.777	0.784	0.774	0.770
Mean difference (%)		0.181 (36.1%)	0.188 (37.3%)	0.178 (35.4%)	0.175 (34.8%)
Correlation		0.487	0.490	0.491	0.490
Mean bias		0.181	0.188	0.178	0.175
NMBF		0.305	0.316	0.300	0.294
RMSE		0.228	0.232	0.225	0.223
NMAEF		0.328	0.336	0.324	0.319
IOA		0.409	0.397	0.419	0.424
Standard deviation	0.143	0.136	0.133	0.138	0.137

Table 25: Comparison of CALIPSO-GOCCP observed and simulated low cloud fraction averaged over the Southern Ocean, 2016–2017. All simulated mean model-observation differences are larger than the observational temporal variability (0.171) (see Appendix A.7).

Radiation and cloud fraction summary:

Analysis in this section has showed that:

- Perturbation simulations exhibited similar changes in simulated CNDC as CCN with corresponding spatial distributions dependent on [chl-a], online chemistry processes and prevailing wind-speeds for the PMO, CHEM, and SSALT runs respectively.
- ACCESS-CM2 featured a 4.44 $\mathrm{W\,m^{-2}}$ positive radiation bias between 40–60°S with a clear zonal structure shifting to a negative bias at higher latitudes.
- ACCESS-CM2 exhibited a consistent positive low CF bias from 40–80°, on average 36.1% larger than satellite observations. The radiation zonal bias sign change at 60°S was not noted in model low CF bias, indicating additional complexity within the radiation scheme beyond the influence of low cloud fraction.
- Perturbation simulations had little effect on simulated TOA SW ↑ radiation and low CF bias, with maximum perturbation differences of 2.62% and 1.2% relative to the BASE run, respectively.

8 Discussion of Research Questions

Chapter 7 characterised the representation and bias of simulated meteorological terms, chemical species and processes, AOD, CCN, radiation, and Cloud Fraction in ACCESS-CM2 and perturbation runs. This Chapter utilises the results gained in Chapter 7 to evaluate the study's three objectives outlined in Section 4.1.

8.1 How well does ACCESS-CM2 represent aerosols over the Southern Ocean in terms of AOD and CCN bias?

ACCESS-CM2 overestimates Southern Ocean AOD

ACCESS-CM2 exhibited a substantial positive AOD bias over the Southern Ocean. At Cape Grim, mean BASE-simulated AOD was larger than observations by a factor of over 1.5, and was poorly correlated (R = 0.349). Analysis of the PDF in Figure 37 showed that modelled AOD distributions exhibited an increased tail towards higher values, contributing to the positive bias. Simulated bias compared to observations varied between stations and seasons. Overall, ACCESS-CM2 exhibited improved model performance in summer compared to winter with reduced bias, error and increased agreement at Cape Grim and Amsterdam Island. At Macquarie Island, the opposite was true (discussed in Section 7.4.4). Additionally, Figures 64, 65, & 66 indicated that BASE-simulated AOD was substantially more variable, with standard deviations higher by a factor of 1.2 compared to all AOD station observations. The degree to which the model agreed with observations varied at each station and by season.

Explanation of positive AOD bias

GCMs are complex systems with numerous inter-connected meteorology, aerosol, chemistry, and radiation schemes. Furthermore, the AOD metric is dependent on multiple environmental and aerosol microphysical factors. Having identified the sign and magnitude of the AOD bias, determining its complete cause(s) would warrant a full attribution study due to the aforementioned model complexity. However, we may identify biases within certain parameters that would contribute to the overall AOD bias.

In physical terms, the positive AOD bias may be attributed to an excess of particle number and/or a shifting of particle distribution towards optically-active (larger) sizes. The model-observation size-distribution in Figure 33 indicated that ACCESS-CM2 simulated fewer, but larger particles in comparison to observations, which was also noted in another Southern Ocean GLOMAP size distribution [Woodhouse et al., 2020]. While the observational data used in this comparison faces challenges in accurately sampling larger aerosols (discussed in Appendix A.8), ACCESS-CM2 simulated mean diameters which were larger

than observations by factors of approximately 2, 3, and 5 for the Aitken, accumulation and coarse modes respectively. Simulated particle numbers in the Aitken, accumulation and coarse modes were all lower than respective observations by a factor of approximately 10. We next consider what factors may contribute to this underestimation of particle number. Factors include a deficiency in particle formation through nucleation processes, additional sink terms including the condensation of H_2SO_4, or increased growth processes would would reduce particle number but increase particle size. Due to lacking observational data regarding nucleation processes, these terms will be discussed in comparison to the CHEM run later in this section.

Next, we consider why ACCESS-CM2 may exhibit a bias towards larger particle sizes compared to size-resolved AOD observations (discussed in Section 7.4.7). As the dominant source of aerosol mass in the Southern Ocean, and a substantial contributor to total AOD (shown in Section 7.4.6), we first examine sea-salt concentrations. ACCESS-CM2 overestimated coarse-mode AOD compared to observations at Macquarie Island with a NMBF of 0.526. Coarse-mode AOD was determined to be representative of sea-salt due to the sensitivity of modelled coarse-mode AOD to modifications in the SSALT run. Therefore, we conclude that ACCESS-CM2 overestimates coarse-mode sea-salt as a substantial contributor to the total positive AOD bias. As a mass-dominated metric, this coarse-mode AOD overestimation does not clarify whether the model overestimates size or mass; increases in either would enhance AOD. In the absence of available coarse-mode sea-salt observations to provide an indication of mass bias, a representation of simulated size bias may be achieved through comparison of modelled fine-mode and coarse-mode AOD.

ACCESS-CM2 overestimated observed fine-mode AOD with an annual NMBF of 3.65. However, analysis against available accumulation-mode (fine-mode) sea-salt ACSM observations showed that this positive bias was not due to sea-salt (Section 7.2.1). The model underestimated observed accumulation-mode sea-salt (using a Cl^- ion proxy) by a factor of approximately six, and exhibited a fair correlation (R = 0.782). Instead, this fine-mode AOD bias was likely the result of over-estimations in nss-sulfates. Nss-sulfates would account for the simulated seasonal cycle that was not exhibited in observations, and therefore the worsened bias, error and correlation metrics in summer associated with increases of biological nss-sulfates not captured by observations. Therefore, we conclude that ACCESS-CM2 over-represents larger (coarse-mode) sea-salt, and under-represents smaller (fine-mode) sea-salt, substantiating the bias towards larger particle sizes.

In interpreting this bias, we must consider the model's underestimation of wind-speed in comparison to observational data showed in Section 7.1.1. Due to the dependency of the Gong [2003] sea-salt emission flux on U_{10} wind-speed, underestimations in wind-

speed would result in underestimations of wind-generated aerosols such as sea-salt. If the negative U_{10} zonal wind-speed bias in ACCESS-CM2 was adjusted towards realistic values, this would worsen the positive bias in coarse-mode sea-salt and AOD and hence is not recommended. Due to lacking observational data regarding the chemical species output in ACCESS-CM2 (discussed in Section 7.2.1), further comment on the role of aerosol chemical type impacting AOD cannot be made in this thesis.

Comparison of AOD bias against literature

The BASE-simulated AOD-wind-speed relationship plotted in Figure 39 demonstrated a positive bias in slope compared to observations. This is consistent with previous work which suggests the Gong [2003] function used in ACCESS-CM2 overestimates the dependency of SSA on wind-speed [Madry et al., 2011, Jaeglé et al., 2011a, Spada et al., 2015]. Previous model evaluations have found varying AOD bias over the SO due to diverse model aerosol representations. Table 26 summarises the AOD bias and error of previous model-observation evaluation studies relevant to the study region. The AOD bias established for ACCESS-CM2 in this study is consistent within the mean bias and RMSE ranges identified for the International Cooperative for Aerosol Prediction Multi-Model Ensemble (ICAP-MME), which used similar AERONET observations in Sessions et al. [2015]. The ACCESS-CM2 mean AOD bias was situated at the upper limit of the identified summer-autumn range in Sessions et al. [2015], but we note the difference in observational stations used for comparison in Table 26. Revell et al. [2019] provided annual model differences for HadGEM3-GA7.1, which shares the same General Atmosphere (GA7.1) as ACCESS-CM2. ACCESS-CM2 exhibited a larger model-observation difference compared to Revell et al. [2019] by factors ranging from 1.4 to 3.3, and increased error (RMSE) by factors ranging from 1.9 to 2.3. However, it must be noted that these comparisons use different datasets both in spatial resolution (satellite zonal averaged and station-based), and in their inherent biases. The combination of satellite measurements used in Revell et al. [2019] have been shown to overestimate Southern Ocean AERONET AOD due to cloud contamination, hence discrepancies between model-observation differences between these studies could be expected to be reduced due to satellite bias.

Model simulation	**Mean Bias**	**RMSE**
Sessions et al. [2015] Crozet Island Dec-May	-0.02 $\longrightarrow$ +0.05 MMM = +0.01	0.06 $\longrightarrow$ 0.11 MMM = 0.07
ACCESS-CM2 Cape Grim Amsterdam Island Dec-May	0.0500	0.0647
Sessions et al. [2015] Crozet Island Jun-Nov	+0.02 $\longrightarrow$ +0.09 MMM = +0.05	0.05 $\longrightarrow$ 0.11 MMM = 0.07
ACCESS-CM2 Cape Grim Amsterdam Island Jun-Nov	0.0587	0.0835
Model simulation	**M-O difference (relative %)**	**RMSE**
Revell et al. [2019] Annual (40-60°S)	0.016 (15.7%)	0.032
ACCESS-CM2 Cape Grim Macquarie Island Amsterdam Island	0.0502 (55.0%) 0.0219 (25.1%) 0.0532 (69.6%)	0.0752 0.0606 0.0749

Table 26: Comparison of ACCESS-CM2 AOD bias against previous model-observation evaluation studies in the Southern Ocean. Amsterdam Island was selected for comparison with Crozet Island as the closest available station ∼2350km (7 ACCESS-CM2 gridboxes North) away. This thesis has not used satellite observations for AOD, hence a like comparison of the zonal 40-60° band cannot be produced as in the Revell et al. [2019] study. Instead, model-observation differences have been shown for the three available stations. Mean bias and RMSE, Root Mean Square Error, have been defined in Table 8. M-O = Model minus Observations.

This section has demonstrated that, while ACCESS-CM2 exhibits a substantial AOD bias, it is within the expected bias range of previous simulations which use similar observational data for comparison. The following section evaluates model bias for simulated CCN.

ACCESS-CM2 has a negative bias in simulated CCN (0.5% SS)

Unlike the positive AOD bias, ACCESS-CM2 exhibited a substantial negative bias in CCN (0.5% SS) at all stations and voyages investigated, which varied in magnitude seasonally and spatially. Simulated NMBF ranged from -0.722 (55.2% lower than observations) at Cape Grim to a NMBF of -2.40 over the ACE Voyage (66.7% lower than observations). ACCESS-CM2 was able to capture the observed seasonal CCN cycle at Cape Grim and exhibited a general SO seasonal cycle at Macquarie Island (increased CCN in summer, reduced in winter). However, the model distinctly underestimated winter-time CCN concentration at Macquarie Island, and both summer and winter CCN sources at Cape Grim. Lacking CCN could likely be attributed to a missing source or an enhanced sink process that prohibits particles from growing to the critical 50nm diameter required to form CCN (0.5% SS). It has been established that biogenic aerosols, not sea-salt, control CCN

seasonality over the SO; biogenic aerosols contribute ∼80% of summer-time CCN and ∼35% of winter-time CCN [Vallina et al., 2007]. Hence, the lacking summer-time CCN concentration in ACCESS-CM2 is likely due to a missing biogenic source of CCN. The winter-time source of CCN notable at Macquarie Island is yet to be identified in literature and is discussed in the following section.

Explanation of negative CCN bias

Discrepancies between simulated and observed CCN are likely the result of variations in particle size or hygroscopicity. CCN particle size can be identified through comparison with observed AOD seasonal cycles, as AOD and CCN are dominated by different particle size ranges. Increased summer- and winter-time observed CCN concentrations were not reflected in AOD observations (see seasonal comparisons in Figures 40 & 50). Increases in CCN unaccounted for in AOD are likely due to upper-range Aitken-mode particles. Modal AOD contributions discussed in Section 7.4.6 showed that Aitken-mode particles contribute only ∼1.8% towards total simulated AOD, but do contribute substantially towards CCN number above 50nm diameter. Biogenic Aitken-mode particles have been shown to dominate CCN number at Cape Grim and are likely the result of DMS oxidation [Gras and Keywood, 2017, Bigg et al., 1984]. The online DMS oxidation scheme in the CHEM run produced mean CCN values closer to observations in summer months compared to the offline runs. Therefore, increased complexity within the online DMS scheme may provide an increased Aitken-mode biogenic source; further studies which output DMS oxidation flux terms could determine this hypothesis.

Differences in chemical composition may also account for model CCN bias. Aerosols which are more hygroscopic or have undergone more cloud-processing would more readily form CCN (described in Section 1.5), hence these processes may be lacking in ACCESS-CM2. Additionally, Section 3.1.2 identified lacking representations of cloud water pH which may contribute to simulated CCN bias. Further analysis of the CCN bias in this regard may not be conducted in this work due to lacking chemical composition and hygroscopicity data both simulated and observed.

Comparison of CCN bias against literature

Table 27 presents the limited previous model-observation comparison studies relevant to the study region. ACCESS-CM2 exhibits a far greater model-observation NMB by a factor of ∼100 compared against a previous GLOMAP CCN (0.23%SS) model-observation evaluation at Cape Grim. Compared against a global marine dataset made of station-based observations at varying supersaturations, ACCESS-CM2 exhibited NMB values which ranged within ∼4–46% of the published NMB values [Spracklen et al., 2011]. Such comparisons between CCN calculated at differing supersaturations are problematic. Aerosol

populations vary widely depending on the measured/simulated supersaturation, hence the model may exhibit strengths at a particular SS and weaknesses at another. Shortcomings in this literature comparison demonstrates the need for consistent CCN monitoring and model evaluations at standardised supersaturation values to facilitate inter-study comparisons.

Schmale et al. [2019] did not report statistical metrics for comparison with this study, but found similar GLOMAP-simulated underestimations of CCN (0.2%SS) by ∼50–80% compared to voyage-based observations. A Northern-Hemisphere station-based multi-model comparison found that all models underestimated observed CCN concentrations by at least 34% compared to observations at a range of supersaturations [Fanourgakis et al., 2019]. This study also identified hygroscopic properties of organic aerosol in summer and cloud-processing in winter as dominant sources of uncertainty, hence the study reached the same conclusions regarding model deficiencies as in this thesis [Fanourgakis et al., 2019].

This literature comparison has demonstrated that CCN bias varies widely between model simulations. We can conclude that the ACCESS-CM2 CCN bias is within an expected range of GCM model biases, but recommend further research to determine how the addition of ACCESS-CM2-UKCA components resulted in further discrepancies from the GLOMAP-only run at Cape Grim in Mann et al. [2010].

Model simulation	**NMB**	**Correlation**
Mann et al. [2010] Cape Grim	0.20 (1.2% SS) 0.78 (0.23% SS)	0.68 (1.2% SS) 0.41 (0.23% SS)
Spracklen et al. [2011] Global marine average	-77.2 (0.02-1.5% SS)	not published
ACCESS-CM2 Cape Grim Macquarie Island OBS1 Macquarie Island OBS2	-41.9 (0.5% SS) -68.4 (0.45% SS) -74.2 (0.55% SS)	0.403 (0.5% SS) 0.295 (0.45% SS) 0.317 (0.55% SS)

Table 27: Comparison of ACCESS-CM2 CCN bias against previous model-observation evaluation studies. NMB, Normalised Mean Bias and correlation have been defined in Table 8.

Summary of Research Question 1

This thesis has therefore concluded that the persistent AOD bias exhibited in ACCESS-CM2 is consistent within the range of mean bias and error of previous modelling efforts. This positive bias is likely due to an overestimation of sea-salt with a bias towards larger particle sizes as compared against observations. ACCESS-CM2 exhibits a substantial negative CCN bias which was consistent with previous GCM evaluations and is likely due to a missing biogenic Aitken-mode source in summer, lacking in-cloud sulfate production (cloud-processing), and/or poor representation of hygroscopicity aerosol characteristics in winter. The next section evaluates how the inclusion of aerosol-chemistry perturbations have impacted these AOD and CCN biases.

8.2 Does increasing the complexity of aerosol-chemistry schemes result in a more accurate representation of AOD and CCN?

This section discusses the impacts of incorporating the Gantt et al. [2012a] PMOA scheme, online chemistry, and the modified Hartery et al. [2020] SSA source function on simulated AOD and CCN bias within ACCESS-CM2. The physical processes resulting in changes to simulated AOD and CCN are explained, and the resulting perturbation-simulation biases are evaluated against available literature to determine whether these findings are supported.

8.2.1 Implications for AOD bias

PMO run increased AOD bias

The inclusion of the Gantt et al. [2012a] PMOA scheme saw the largest mean AOD increase of all perturbation runs in this study. Compared to the BASE run, PMO-simulated mean AOD was larger by 0.002 (1.83%) averaged over the SO, and was larger by factors of 1.2, 1.8, and 1.9 at Cape Grim, Macquarie Island and Amsterdam Island respectively.

Increases in PMO-simulated mean AOD have been attributed to the simulation of larger Aitken-mode particles, and more numerous accumulation-mode particles. We recall that the Gantt et al. [2012a] scheme injects the majority of OM_{SSA} into the upper Aitken-insoluble mode, which accounts for the skew towards larger particle sizes and the 354% increase in Aitken-insoluble AOD observed in Figure 45. Injected OM_{SSA} is quickly transformed into the accumulation-mode, accounting for the average peak increase in accumulation-mode particle number by 51.8% shown in Figure 32 (compared against the BASE run). As discussed in Section 8.1, all ACCESS-CM2 simulations under-represented modal particle number. Increases in PMO-simulated accumulation-mode particle number

brought the model closer towards observed accumulation-mode size distribution measurements in Figure 33.

The PMO run simulated a similar seasonal representation as the BASE run, but departed to higher AOD values during biologically-active summer-time months. Spatially, increased PMO AOD was attributed to regions of enriched [chl-a] due to its use in the Gantt et al. [2012a] parameterisation (shown in Figures 42 & 43). Given the existing positive bias of ACCESS-CM2 over all SO sites used, the PMO scheme hence worsened model bias. This positive AOD bias would be particularly enhanced in regions of high [chl-a], although lacking in-situ data prevents quantification of regional bias. This was shown in Section 7.4.6, where contributions to total Aitken-mode and accumulation-mode AOD increased by 819% and 7.97% respectively over the PMO-enriched area compared to the zonal 40-60° average.

Comparison against literature
Tsigaridis et al. [2013] noted the implementation of a marine POA source saw total simulated SO optical depth increase by 115% compared to a reference run. The study utilised a similar satellite [chl-a] product in the Gong [2003] SSA function as in the Gantt et al. [2012a] parameterisation. Despite the lack of further relevant studies, these findings suggest increases in ACCESS-CM2 simulated AOD due to inclusion of OM_{frac} in SSA are consistent with literature.

CHEM run decreased AOD bias
Averaged over the Southern Ocean, the CHEM run reduced mean AOD by 0.021 (13.9%). The CHEM run reduced model NMBF at at all stations/voyages by up to a factor of 4.7 at Macquarie Island where mean CHEM-simulated AOD was only 3.97% larger than observations. Despite reductions in mean simulated AOD, the CHEM run was still overall positively biased compared to observations. CHEM AOD bias varied between seasons and stations, where both bias (NMBF) and error (NMAEF) were reduced in summer at Cape Grim (compared to winter). Model strengths in reduced bias and error were instead seen in winter at Macquarie Island, with a largely consistent seasonal bias at Amsterdam Island.

Chemical analysis in Section 7.2 attributed these improvements in AOD bias to changed oxidation pathways and decreased sea-salt concentration. Increases in summer-time cloud-processing saw increases in accumulation-mode particle number, marked by increased Hoppel minimums in Figure 35 (compared against the BASE run). However, increases in AOD due to more numerous accumulation-mode particles were mitigated inadvertently by reductions in sea-salt. Section 7.4.6 suggested that increased cloud-processing shifted mass

towards the accumulation-mode. Larger accumulation-mode particles are then susceptible to wet and dry deposition processes. This provided an increased sink term for larger particles, which reduced the coarse-mode diameter peak by 292nm compared to the BASE run in Figure 32. Reduced AOD was also the result of a shifting to smaller accumulation-mode particle sizes due to cloud-processing. Increased numbers of Aitken-mode particles undoing aqueous-phase oxidation resulted in a 2.29% reduction in accumulation-mode AOD compared to the BASE run in Figure 45.

Comparison against literature

Few studies have run similar online perturbation experiments in the Southern Ocean. Revell et al. [2019] included more complicated DMS oxidation chemistry schemes in a perturbation experiment and compared simulations against satellite observations. The study noted that more complex chemistry schemes decreased model-observation RMSE by 0.004 relative to a reference run without altered chemistry. In this thesis, the CHEM run was similarly able to reduce model-observation RMSE compared to the BASE run across all stations and voyages, with reductions ranging from 0.0113 at Cape Grim to 0.385 over the RV Investigator 2018 voyage.

SSALT run was the most effective perturbation in reducing the AOD bias

The SSALT run effectively reduced simulated AOD by 0.0644 (43.4%) compared to the BASE run averaged over the SO. Compared to station observations, the SSALT run not only reduced, but changed the previously positive bias sign (in the BASE run) to negative at all stations analysed. The SSALT run reduced BASE-simulated NMBF values against observations from 0.541 at Cape Grim to 0.982 at Amsterdam Island. Notably, this perturbation exhibited a lower inter-annual variability compared to all observations and constrained the simulated AOD distribution towards higher frequencies at lower AOD values (seen on the PDFs shown in Figure 37). Seasonally, the SSALT run performed well in summer but struggled in winter-time with a greater bias at all stations/voyages. However, Section 7.4.6 showed that SSALT-simulated coarse-mode AOD was the closest to observational values in winter. Therefore, ACCESS-CM2 encompasses larger sources of AOD bias beyond sea-salt overestimations, as the SSALT run exhibited the greatest bias in winter coincident with the best representations of sea-salt. These findings suggest as sea-salt is the largest contributor to total AOD, additional complexity within the SSA source function may be required; such as the inclusion of seawater composition and sea-surface temperature, which have been shown to increase model-observation agreement of sea-spray production [Jaeglé et al., 2011b, Spada et al., 2015, Forestieri et al., 2018].

Reductions in SSALT-simulated AOD were attributed to reduced accumulation- and particularly, coarse-mode AOD. AOD reductions are attributable to the Hartery et al. [2020] SSA source function, which decreased total sea-salt output as a function of wind-speed. Comparison against fine- and coarse-mode AOD in Section 7.4.6 showed that the greatest reduction of sea-salt was in the coarse mode.

Comparison against literature

These findings are consistent with the results of ACCMIP models (introduced in Section 3.2.1), which overestimated annual mean simulated sea-salt between 50-60° in comparison to AERONET observations [Shindell et al., 2013]. Revell et al. [2019] similarly implemented the Hartery et al. [2020] SSA source function, and reported uniform reductions in AOD by 0.07 (unitless) in March–November between 40-60°S, in comparison to a reference run. In this study, the SSALT run decreased AOD in the same temporal and spatial domain by up to 0.770 (see Appendix Figures 68 & 69). The Revell et al. [2019] study utilised the same physical atmosphere (GA7.1) and chemical scheme (online CheST) as ACCESS-CM2, showing results of this study have been supported in a similar model.

8.2.2 Implications for CCN bias

This section evaluates the impacts of each perturbation simulation on modelled CCN in terms of bias and seasonal representation.

PMO run decreased Southern Ocean CCN bias

Similarly to AOD, the PMO run increased average SO simulated CCN by 19.9cm^{-3} (34.1%) compared to the BASE run. Increased CCN improved the already negative model bias in ACCESS-CM2, and hence decreased BASE-simulated NMBF values from 0.176 at Cape Grim to 1.05 over the MARCUS voyage. We note that PMO-simulated NMBF was lowest over voyages, which were coincident seasonally with improved summer-time bias noted at all stations. PDFs shown in Figure 49 demonstrated that despite increases in mean simulated CCN, the PMO run failed to capture the higher tail values of observations entirely. The maximum observed CCN value was larger than PMO-simulated CCN by factors ranging from 1.05 to 6.10 over the four sites and voyages. Similarly to PMO-simulated AOD, increases in simulated CCN were attributed spatially to biologically-active regions in Figure 51.

Factors contributing to the simulated CCN positive bias were the same as those accounting for the AOD bias in the PMO run discussed in Section 8.1. However, the CCN bias would also include the role of increased Aitken-mode particles, which were 40.5% more numerous than the BASE run. Increased Aitken-mode particles over 50nm would increase CCN (0.5%SS) number, but are too small to significantly contribute towards AOD as previously discussed.

Comparison against literature

Meskhidze et al. [2011] utilised a similar PMOA scheme as in this study, and found increases of CCN (0.2%SS) up to 20% over biologically-productive waters, compared to CCN increases of 120–125% in biologically-active regions simulated in the PMO run. Westervelt et al. [2012] added PMOA to sea-spray emissions as OM_{frac} in a GCM (similarly to the Gantt et al. [2012a] parameterisation) and found increases in CCN (0.2%SS) by up to 50% averaged over the SO (spatial domain not defined) compared to a reference run. The PMO-run in this study only increased average CCN over the SO (40-60°) by ∼20% compared to the BASE run. The treatment of PMOA schemes varies widely between models, hence we do not expect the PMO-run to replicate previous CCN-simulations. All studies using similar PMOA schemes also reported increases of simulated CCN, supporting the PMOA-scheme induced increases in CCN in this study.

CHEM run reduced CCN bias

The CHEM run increased mean simulated CCN by 25.9 cm^{-3} (44.5%) averaged over the SO compared to the BASE run. Online chemistry decreased BASE-simulated NMBF by 0.406 at Cape Grim and up to 1.09 along the MARCUS voyage. Increases in CCN concentration were attributed to increased cloud-processing, a known source of CCN uncertainty, leading to higher accumulation-mode number. Seasonally, the CHEM run saw increased CCN number in summer and spring. For example, summer-time months saw a reduction in NMBF of 0.167 and 1.70 at Cape Grim and Macquarie Island (0.45%SS) (compared to winter months NMBF). Spatially, the CHEM run saw a largely homogeneous increase in CCN zonally between 40-60°, with notable increases surrounding coastal areas outside of the scope of this thesis. This study recommends the use of online chemistry implemented for future land-based studies, particularly over the Antarctic continent due to increased CCN sensitivity to coupled chemistry in the region.

Enhanced nucleation processes were attributed to CHEM-simulated reductions of CCN. Increased emissions of the OH oxidant enabled increased gas-phase oxidation, particularly in summer-time at lower latitudes. Increased summer-time nucleation efficiency increased nucleation-mode particle number by 15.8% compared to the BASE run. Increased nucleation-mode number had knock-on effects to neighbouring modes through

particle growth, shown by a 24.8% increase in CHEM-simulated Aitken-mode particle number (compared to the BASE run). Aitken particles above 50nm in diameter contribute towards CCN, hence combined with aforementioned increases in accumulation-mode particle number, CCN concentration increased. CCN increases hence occurred particularly in summer and spring months more conducive to oxidation through increased incident radiation and photolysis. As gas-phase chemistry is not dictated by the presence of clouds (as in aqueous-phase oxidation), the resulting increase in CCN was more spatially homogeneous across the Southern ocean.

Comparison against literature

Similarly to the online chemistry evaluation for AOD, there are few relevant studies for comparison. The Revell et al. [2019] used the same chemistry scheme as ACCESS-CM2 (UKCA CheST), with varying modifications to the DMS chemistry. Simulations changed CCN by -18% - +25% relative to a reference run, and enhancements in CCN were attributed to increased accumulation-mode aerosol number. In this study, size distributions presented in Section 7.3 saw a similar increases in CHEM-simulated accumulation-mode number, which was further attributed to increased cloud-processing. This suggests that increased chemical complexity in the Revell et al. [2019] study supports the suggested mechanisms leading to increased CCN using online chemistry in ACCESS-CM2.

SSALT run increased the CCN bias

The SSALT run simulated a decreased CCN concentration by 8.4 cm^{-3} (15.8%) averaged over the SO compared against the BASE run. The decrease in sea-salt shown in Figure 24 worsened the already negative bias simulated in the BASE run by 0.253 along the MARCUS voyage to 1.33 at Macquarie Island (CCN 0.55%SS). Similarly to PDF distributions of AOD, PDF distributions of SSALT-simulated CCN (Figure 49) exhibited a narrow distribution biased towards low values, and featured a substantially lower representation of inter-annual variability (standard deviation) compared to observations (shown in Figures 49, 72, 73, & 74). Seasonally, the SSALT-run performed the worst in winter, with NMBF increasing by a factor of 1.58 and 2.30 between summer to winter at Cape Grim and Macquarie Island (0.45%SS). This is in opposition to the simulated AOD bias where reduced sea-salt aerosol abundance in the SSALT run saw the best improvements in winter-time NMBF at all stations.

While analysis of the size-distribution has not taken place (due to lacking output in the SSALT model), a reasonable explanation of changes in CCN may be obtained. Sea-salt is emitted into the accumulation and coarse-modes; both which are larger than the 50nm threshold for CCN at 0.5%SS. Therefore, reductions sea-salt particle number in either mode would directly reduce CCN concentration output. For seasons where we saw the largest decrease in SSALT-simulated sea-salt, we also saw the largest decrease in simulated CCN.

Comparison against literature

These results are consistent with the findings of Revell et al. [2019], wherein the modified Hartery et al. [2020] sea-salt source function decreased simulated CCN by ∼13% relative to a reference run (also between 40-60°S). Spatially, the SSALT run followed the same spatial reduction of CCN as it did with AOD in zonal patterns following the dominant U_{10} wind-speed. Lower reductions in CCN resulted from lower wind-speeds given the exponential nature of the [Hartery et al., 2020] SSA source function (Equation 7).

Summary of Research Question 2:

This thesis has shown that AOD in ACCESS-CM2 combined with GLOMAP and UKCA responds most effectively to reductions in sea-salt. The CHEM run exhibited favourable decreases in bias which were largely attributed to decreases in sea-salt, and the SSALT run was consequently most effective in reducing overall AOD bias. Evaluation of the SSALT run has shown that the Hartery et al. [2020] SSA source function reduces output sea-salt too much, shown by an underestimation of coarse-mode AOD and a negative AOD bias at some stations/voyages (Figures 45 & 7.4.1).

Improvements in AOD NMBF were not accompanied by improvements in CCN NMBF in the SSALT run. Reductions in accumulation and coarse-mode sea-salt in the SSALT run resulted in the greatest worsening of the already negative CCN bias. The PMO run was able to reduce the CCN bias, but would largely do so inhomogeneously over areas of increased [chl-a], and hence could not be applied to GCMs with the aim of reducing mean CCN bias. The best modification in terms of reducing the bias of both AOD and CCN is the use of online chemistry, which was the most effective at reducing NMBF at all stations/voyages for CCN bias, and similarly reduced NMBF for AOD bias, albeit not as effectively as the SSALT run.

This thesis has noted a lack of simulated Aitken-mode biogenic aerosols which substantiate part of the modelled CCN bias in summer. The winter-time CCN bias was attributed to lacking cloud-processing or poor representations of aerosol hygroscopicity. While the CHEM run simulated increased cloud-processing, it was only able to marginally capture observed increases in CCN (illustrated in Figure 50). This thesis makes a number of recommendations for future work aiming to increase the simulated representation of AOD and CCN:

1. ACCESS-CM2 overestimates coarse-mode sea-salt, largely contributing to the AOD bias. A modified SSA source function should be adopted to reduce sea-salt bias, but with reductions of a lesser magnitude than the Hartery et al. [2020] modification.

2. Reducing the coarse-mode sea-salt bias will have negative effects on CCN concentration. We recommend further work is conducted to include biogenic summer-time Aitken-mode aerosols. Increased Aitken-mode aerosols would not contribute significantly towards the AOD bias but would mitigate decreases in sea-salt on CCN concentration.

3. Promising results shown in AOD and CCN bias reductions lead to the recommendation for adoption of online chemistry where possible in GCMs.

4. The cost of online chemistry prevents its application in large-scale simulations, such as CMIP6 simulations used to forecast climate change. Therefore, we recommend the implementation of more complex modified sea-salt and Aitken-mode aerosol parameterisations as outlined in points 1 & 2 to achieve similar goals without the computational cost. We also recommend further observations be taken regarding hygroscopicity and cloud-processing for further investigation regarding model bias in this regard.

8.3 Can the overall radiation and cloud fraction bias in the Southern Ocean be improved through increasing the complexity of aerosol-chemistry schemes?

ACCESS-CM2 overestimates Low Cloud Fraction

In principle, causes for a positive SW TOA ↑ radiation bias would be too many simulated clouds, or too bright clouds. In terms of aerosol, too many clouds would refer to the second indirect aerosol effect of increasing cloud lifetime, and too bright clouds would indicate the increase in cloud albedo due to the first indirect effect (discussed in 1.6). Averaged over the SO domain, ACCESS-CM2 overestimated low CF by 0.181; an increase of ∼36% compared to observations with an NMBF of 0.305. This indicates that ACCESS-CM2 has an inherent cloud bias through either the simulation of too much cloud, or, as CF is largely used as a proxy for cloud lifetime, that the first indirect effect is over-represented in the model. It is important to note that the positive low CF bias was consistent over latitudes 40-80°S.

Radiation bias of ACCESS-CM2

Section 7.6.2 established that ACCESS-CM2 features an annual positive SW TOA ↑ radiation bias of of 4.44 Wm^{-2}, 6.64% larger than CERES-EBAF satellite observations between 40-60°S. While this thesis focuses on latitudes between 40-60°S, a marked switch of bias sign was observed from 60°S to higher latitudes with a negative bias. These results are consistent with the Cloud Feedback Model Intercomparison Project Phase 2, which concluded that most models reflected too little solar radiation over the SO, and noted the switch in sign at approximately 60-70°S [Bodas-Salcedo et al., 2014]. In the section above, we noted that ACCESS-CM2 featured a consistent positive low CF bias from 40-80°. Hence, it is unlikely that the cloud fraction bias accounts for the positive SW TOA ↑ radiation bias, given the change in sign at 60°. The next section evaluates whether perturbations of the aerosol-chemistry scheme were able to reduce this bias.

Aerosol schemes do not explain the radiation bias

Section 7.6.1 showed that perturbation simulations changed CDNC concentration spatially and seasonally similar to changes in simulated CCN, which would be expected given consistent cloud liquid water. The PMO and CHEM simulations were able to increase mean CDNC by 41.5% and 9.7%, and the SSALT scheme reduced mean CDNC by 18.4%. We would expect increased CDNC to increase cloud albedo due to the first indirect effect, therefore we could expect the PMO and CHEM runs to increase SW TOA ↑ radiation, and the SSALT to decrease radiation. This proved to be the case for the PMO and SSALT runs, with a further complicated relationship in the CHEM run which

exhibited a mean negative bias of SW TOA ↑ radiation. In answering this research question, it is important to note the difference in magnitude between changes in simulated CNDC, and the resulting effect on radiation bias between simulations. Each perturbation simulation had a substantial effect on mean simulated CDNC, but negligible effects when incorporated into the larger radiation scheme. For example, implementation of the PMO scheme within ACCESS-CM2 saw an average 40.6% increase in 1km simulated CNDC, which translated into a 2.27% increase in SW TOA ↑ radiation relative to the BASE run. The most effective simulation in reducing radiation bias was the SSALT run which was able to bring mean simulated SW TOA ↑ radiation within 4.02% of CERES-EBAF observations (within observational uncertainty thresholds), but this provided only a 2.62% advantage over the BASE run.

Research Question 3 Summary

Comparison of perturbation simulations has shown the lack of sensitivity to aerosol-chemistry changes within the radiation scheme. This thesis has shown that altering the aerosol-chemistry representation within ACCESS-CM2 is not able to bring about substantial reductions in modelled SOA TOA ↑ radiation bias. The most likely explanation for the SW TOA ↑ radiation bias is the type of cloud simulated. Bodas-Salcedo et al. [2014] found that wrongly-assigned cloud types in mid-level clouds substantially contributed to model underestimation of TOA outgoing radiation. South of 60°S, supercooled liquid clouds dominate the liquid cloud population (particularly between latitudes 60-65°S) [Bodas-Salcedo et al., 2016]. The contribution of supercooled and mixed-phase clouds have been shown to contribute between 27-38% to the total TOA reflected radiation flux [Bodas-Salcedo et al., 2016].

9 Conclusion

The representation of aerosols within GCMs is the largest contributor to global radiative forcing uncertainty. Over the Southern Ocean, GCMs struggle to achieve accurate representations of mean and seasonal cycles of AOD and CCN, which contributes to the significant SW radiation bias in the region. The Southern Ocean aerosol community has identified addressing such biases, particularly the SO SW radiation bias, as an area of priority which has necessitated a number of field campaigns that have collected aerosol data in the region. With the upcoming submission of ACCESS-CM2 to CMIP6, this thesis aimed to identify the inherent biases of ACCESS-CM2 regarding key aerosol properties; chemical species concentration, AOD, CCN, Radiation and Low Cloud Fraction. Additionally, with increasing interest in coupled chemistry-climate models, this thesis sought the determine whether a more physically representative model of aerosols would be able to reduce the bias in aerosol metrics such as AOD and CCN, and ultimately the radiation bias.

To achieve these aims, this study ran a series of ACCESS-CM2 perturbation simulations, each with a modification regarding the inclusion of PMOAs, a more complex chemistry scheme, and an altered sea-salt emission flux. Model simulations were compared against each other in terms of concentration output for a number of relevant chemical species, oxidation pathways, size distribution, AOD, CCN, CDNC, Cloud Fraction and Radiation to establish the effects of each perturbation simulation on such variables compared to the BASE run. In order to identify model bias, a suite of ground-based observational data was gathered for differing variables which were subject to the same data-screening methods, or used the same instrument and were screened for quality control. Models were compared against available ground-based observational data for a number of factors including meteorology, sea-salt concentration, size distribution, AOD and CCN. CERES-EBAF and CALIPSO-GOCCP satellite observational datasets were utilised for comparison against simulated mean values of SW TOA $\uparrow$ radiation and Low Cloud Fraction respectively.

ACCESS-CM2 exhibited numerous fundamental biases in meteorology, sea-salt concentration, particle size and number, AOD, and CCN. Firstly, ACCESS-CM2 was shown to largely underestimate zonal 10m wind-speed compared to station observations, dependent on station. It was also shown that ACCESS-CM2 only represents observed wind-direction within a 45° angle approximately only half of the time, which has important consequences for future baseline screening applications. ACCESS-CM2 overestimated AOD by up to a factor of 1.7 (at Amsterdam Island). This was attributed to an over-prediction of larger-sized sea-salt particles through comparison against coarse-mode AOD and size distribution observations. ACCESS-CM2 underestimated mean observed CCN

for all stations and voyages by up to a factor of 3.40 (over the ACE voyage). Additionally, the model did not capture seasonal increases observed in CCN, which is likely indicative of a missing summer-time Aitken-mode source in summer, and lacking cloud-processing or hygroscopic parameterisation during the winter. ACCESS-CM2 featured a duality in SOA TW ↑ radiation bias, with a positive bias between 40-60° and a negative bias from 60° southwards, and overestimated low Cloud Fraction over the Southern Ocean by 0.181 (relative difference of 36%) compared to CALIPSO-GOCCP observations.

Implementation of the PMO scheme saw increased AOD and CCN values, marking an increase in AOD bias but a reduction in CCN bias. This occurred through increased particle number concentration in the upper Aitken and accumulation modes, as a function of the injection size of OM in the Gantt et al. [2012a] scheme and resulting increased condensation sink of H_2O_2. Improvements in CCN were largely seen over areas of high [chl-a] as a function of the PMO scheme, and hence the scheme cannot be broadly applied to increase simulated CCN over the Southern Ocean domain.

The use of fully coupled online chemistry saw both improvements in the simulated AOD and CCN bias. Increased aqueous-phase oxidation resulted in increased accumulation-mode particle numbers, with a shift of accumulation-mode particle sizes towards the Aitken-mode. The most significant impact on total AOD was through a decrease in simulated sea-salt, likely through enhanced deposition processes which highlights the sensitivity of simulated AOD to coarse-mode particles such as sea-salt. CHEM-simulated CCN was increased due to increased nucleation processes, which in turn increased Aitken-mode particle numbers – thus increasing CCN without substantially affecting AOD.

The SSALT run demonstrated the sensitivity of simulated AOD and CCN to simulated sea-salt concentration, and largely worsened both AOD and CCN bias. While the positive AOD NMBF was reduced by up to a factor of 2.5 at Amsterdam Island, this reduction was too extreme and all stations exhibited a negative bias. Underestimations of observed CCN worsened, where mean SSALT-simulated CCN was up to a factor of 4.80 times lower than observed CCN (at Macquarie Island, 0.45%SS). This was attributed to reductions in SSALT-simulated sea-salt concentration by 55.9%, averaged over the Southern Ocean, which reduced the model's fine-mode AOD positive bias by a factor of approximately 3 in winter (compared to observations). In contrast, the SSALT run increased model bias (negatively) by a factor of 1.18 in annual coarse-mode AOD at Macquarie Island. This perturbation simulation has shown that improvements to ACCESS-CM2's AOD and sea-salt bias can be made through reducing the simulated sea-salt concentration, however the Hartery et al. [2020] modification has reduced sea-salt concentrations too much compared to observations.

The effect of aerosol-chemistry scheme perturbations on the Southern Ocean radiation bias were investigated. While each perturbation simulation was able to exhibit substantial impacts on CDNC (up to a 40.6% increase in the PMO run), these effects were not translated substantially into the radiation scheme with a maximum difference of 2.62% compared to the BASE run.

Key points gained from this thesis show that the use of online chemistry saw the best improvements in AOD and CCN bias, and should be adopted in GCM simulations with a small temporal or spatial domain due to computational limits. For improved aerosol representation in longer-term GCM simulations, this thesis makes a number of pragmatic recommendations in reducing both AOD and CCN bias. The most substantive impacts on AOD bias resulted from a reduction in simulated sea-salt concentrations. This research contributes to an increasing body of work in the aerosol modelling community which recognises that the widely-used Gong [2003] parameterisation results in overestimated sea-salt concentrations in the high wind-speed environment of the Southern Ocean. Instead, we recommend a change to a parameterisation with a reduction in sea-salt emissions, but to a lesser extent than the Hartery et al. [2020] parameterisation. Implementing such a scheme would have detrimental impacts for the existing negative CCN bias in ACCESS-CM2 due to reduced accumulation- and coarse-mode particle number. Hence, this thesis recommends the use of a parameterisation encompassing increased biogenic Aitken-mode aerosol which would address CCN number deficiencies, particularly in summer, without substantially compromising necessary decreases in AOD. While the PMO Gantt et al. [2012a] parameterisation increased biogenic Aitken aerosol number, increases were insufficient for agreement with observations, and were spatially dependent on [chl-a] which provided little improvement at land-based stations such as Cape Grim and Macquarie Island. We recommend additional research into evaluating the hygroscopicity of simulated aerosols against observations, and in confirming whether cloud-processing in ACCESS-CM2 constitutes an appreciable part of the CCN bias as suggested in Section 7.5.

Finally, this thesis concludes that while each perturbation run made significant changes to simulated aerosol-chemistry properties, the cause of the SW TOA $\uparrow$ radiation and Cloud Fraction bias does not lie within the aerosol scheme. Noting the consistent positive CF bias from 40-80° and switch in sign of the radiation bias, the issue likely remains within the cloud scheme. This thesis recommends further research into evaluating the representation of supercooled liquid clouds and INPs in ACCESS-CM2, which are known areas of bias and uncertainty within GCMs.

A Appendix

A.1 Köhler theory

Köhler theory describes the combination of the solute effect (Raoult's Law), and the Kelvin effect. The solute effect describes the phenomenon where the addition of solute particles to a solution reduces the vapour pressure, and occludes the evaporation of solute particles. This effect opposes the Kelvin effect, which describes how small aerosols have increased curvature and lower surface tension which increases evaporation rates. The combined Köhler theory is described below:

$$\ln(\frac{p_w(D_p)}{p^0}) = \frac{4M_w\sigma_w}{RT\rho_w D_p} - \frac{6n_s M_w}{\pi\rho_w D_p^3} \tag{14}$$

Equation 14: Köhler theory equation describing the process by which water vapour condenses onto aerosols to form liquid cloud drops. The first term on the right side of the equation indicates the Kelvin term, and the second term indicates the Raoult term, where: p_w is the droplet water vapour pressure, p^0 is the saturation vapour pressure over a flat surface, σ_w is the droplet surface tension, p_w is the density of water, n_s is the moles of solute, M_w is the molecular weight of water, and D_p is the cloud drop diameter.

Köhler theory theory is relevant to this research through the activity of PMOAs on CCN concentration, discussed in Section 1.5. Many compounds in PMOAs act as surfactants which facilitate cloud droplet activation through lowering the surface tension (σ_w) of nucleating cloud droplets (Kelvin effect) [Ovadnevaite et al., 2017].

A.1.1 Calculation of AOD and CCN from model output

Section 5.2.1 described how all model output was carefully selected to reduce computational cost and storage, and that as a result, both CCN and AOD were calculated 'offline' from model output. The following section describes both of those calculations.

Calculation of CCN

The cumulative total number of particles at a given radius was calculated for each aerosol mode as follows:

$$N_d = \left(\frac{N}{2.0}\right) \times \left(1.0 + \epsilon\left[log\left(\frac{r}{\bar{r}}\right) \Big/ \frac{\sqrt{2.0}}{l} og(\sigma_g)\right]\right) \tag{15}$$

where N_d is the total number of particles within a specific aerosol mode above a certain diameter (e.g: number of Aitken soluble particles above 50 nm diameter). N refers to the number of particles within that aerosol mode, r is the dry particle radius of that aerosol

mode, $\bar{r}$ is the modal mean radius and σ_g is the geometric standard deviation of the mode. ϵ refers to the python command *scipy.special.erf*, which returns the error function of the following complex argument. CCN was calculated as the sum of particle numbers within each aerosol mode above a dry diameter of 50 nm (representative of CCN at 0.5% SS), as shown in Figure 57 below.

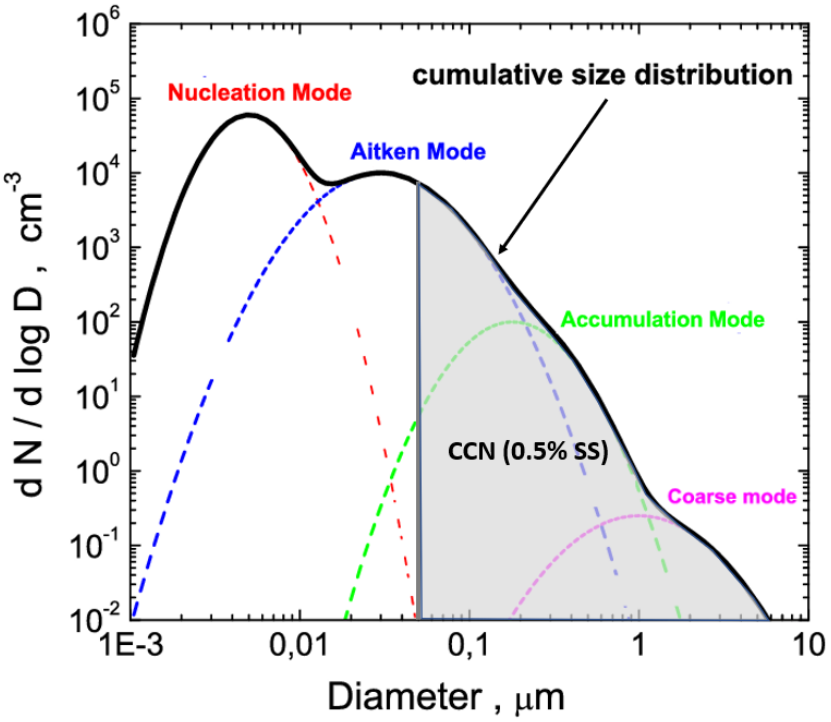


Figure 57: Schematic of the calculation of the cumulative total particle number above 50nm diameter. This diagram shows CCN as the area under the size distribution curve of modes above 50 nm in diameter, which corresponds to CCN at a supersaturation of 0.5% SS). Figure has been adapted from Veira [2011] and shaded to represent the portion of CCN within an idealised aerosol size distribution.

Calculation of AOD

Total AOD was not output directly by the model and needed to be calculated. ACCESS-CM2 outputs AOD at 6 wavelengths for each aerosol mode and solubility. The wavelength corresponding to AOD at 550 nm was selected and AOD_{550nm} was calculated as the sum of each aerosol mode as follows:

$$\mathrm{AOD}_{550nm} = \mathrm{AOD}_{Aitsol} + \mathrm{AOD}_{Aitins} + \mathrm{AOD}_{Accsol} + \mathrm{AOD}_{Coasol} + \mathrm{AOD}_{Dust} \tag{16}$$

where Aitsol = Aitken soluble, Aitins = Aitken insoluble, Accsol = accumulation soluble, and Coasol = coarse soluble. Particles in the nucleation mode are regarded as too small to be optically active and are neglected in the calculation of AOD_{550nm} [Abraham

et al., 2016]. All aerosol mode components from ACCESS-CM2 regard AOD at a 550 nm wavelength.

A.2 Calculation of AOD in observations

To calculate the AOD, the extinction coefficient (σ^{ext}) is first determined as follows.

$$\begin{aligned} \sigma^{sca} &= \int_0^\infty \pi r^2 Q^{sca}(r) n(r) dr \\ \sigma^{abs} &= \int_0^\infty \pi r^2 Q^{abs}(r) n(r) dr \end{aligned} \tag{17}$$

Equation 17: Scattering coefficient (σ^{sca}) and Absorption coefficient (σ^{abs}), units m^{-1}, which are a function of local atmospheric properties. Q^{sca} and Q^{abs} = ratio of the scattering and absorption cross sections and the geometric cross section of a spherical particle (respectively), r = radius, n(r) = size distribution [Boucher, 2015].

$$\sigma^{ext} = \sigma^{sca} + \sigma^{abs} \tag{18}$$

Equation 18: Extinction coefficient (σ^{ext}), units m^{-1}, calculated as the sum of the degree of scattering and absorption encountered by the laser beam. [Boucher, 2015].

AOD is then calculated as the integral of the extinction coefficient from the ground to the TOA (Equation 19). A value of 0.01 corresponds to clear-sky atmospheres, 0.4 indicates hazy conditions and a value of 1 identifies cloudy or high radiation-scattering conditions (due to aerosols) [NOAA, 2015].

$$\tau = \int_{Surface}^{TOA} \sigma^{ext}(z) dz \tag{19}$$

Equation 19: Calculation of the AOD (τ) as an integral of the extinction coefficient with height from the surface to the TOA [He et al., 2016].

Aerosol optical properties (and hence the AOD) vary depending on the wavelength used. The most commonly used wavelength is centered ∼500 nm (at the peak of TOA solar spectral irradiance). At this wavelength, the scattering efficiency of aerosols peaks at 1 μm, hence aerosols in the accumulation mode are the most optically active compared to other size modes.

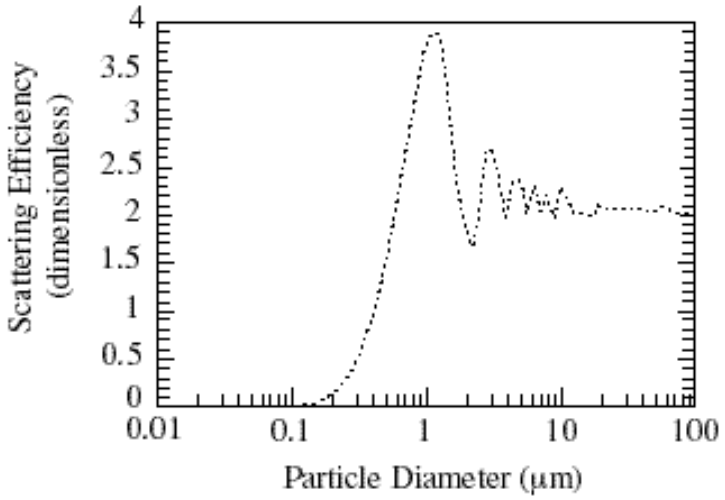


Figure 58: Scattering efficiency of green light (wavelength of 500 nm) by a liquid water sphere as a function of the sphere diameter [Jacobson, 2005].

A.3 Measurement of AOD

AOD is a useful tool which has been described as *"the single most comprehensive variable to remotely access the aerosol burden..."*, which holds true today [Holben et al., 2001]. At the surface, AOD is commonly measured through the use of a laser system or sun-photometers. Sun-photometers are ground-based instruments which are pointed at the sun and calculate optical depth from spectral extinction of direct beam radiation at a number of wavelengths (ranging from 340−1020 nm).

Sun photometers measure the spectral sky radiance at known angular distances from the sun (see schematic diagram in Figure 59. The solar intensity of a particular wavelength measured through a sun photometer can be written as:

$$\hat{I}(\lambda) = (\frac{r_0}{r})^2 I_{\odot}(\lambda) exp[-\tau(\lambda) m(\theta_0)] \tag{20}$$

Equation 20: Solar intensity of a given wavelength, where r and r_0 are the actual and mean sun-earth distances, $I\odot$ is the known solar intensity at the top of the atmosphere (which corresponds to r_0, θ_0 is the solar zenith angle, $m(\theta_0) = 1/\cos\theta_0$ and $\tau(\lambda)$ corresponds to the optical depth.

The total optical depth is written as the sum of individual contributing values from aerosols:

$$\tau(\lambda) = \tau_A(\lambda) + \tau_R(\lambda) + \tau_3(\lambda) + \tau_2(\lambda) \tag{21}$$

Equation 21: Total optical depth with contributions from aerosols (λ_A), Rayleigh molecules (λ_R), ozone (λ_3) and nitrogen dioxide (λ_2)

AOD is calculated through estimating and removing light attenuation due to Rayleigh scatter and absorption by ozone and nitrogen dioxide gases, described in Equation 21. Wavelengths in the visible spectrum are often used as absorption due to water vapor can be neglected [Liou, 2002]. AERONET sun-photometers utilise measurements in 8 spectral bands between 340nm and 1020nm, although this thesis has used wavelengths at 550nm. See full instrument details in Holben et al. [1998].

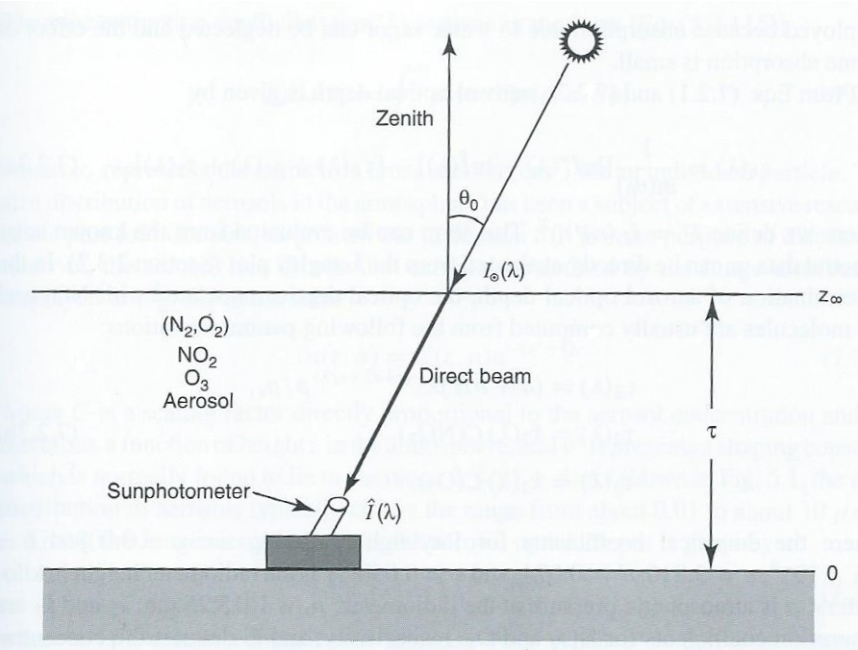


Figure 59: Schematic of a ground-based sun photometer measuring a direct solar beam, where θ_0 is the solar zenith angle, τ is the optical depth, $I_\odot$ and $\hat{I}$ are the solar intensity and measured intensity respectively at wavelength, λ [Liou, 2002].

Spectral Deconvolution Algorithm

This research also utilises an AERONET product that determines between to determine the fine and coarse mode contribution to AOD to enable further interpretation of model bias. This product uses a Spectral Deconvolution Algorithm (SDA) to separate measured aerosols into fine and coarse mode at 500nm (algorithm details described in [O'Neill et al., 2003]). This algorithm functions under the assumption of a largely bimodal aerosol particle size distribution - while this is inherently true for most aerosol populations, care must be taken when interpreting these values as absolute truths in the lack of size-resolved observational data for validation.

A.4 Model nudging

In order to realistically reproduce the physical state of the atmosphere at a given time, dynamical variables of free-running GCMs are adjusted towards meteorological reanalysis data. Nudging in ACCESS-CM2 is conducted within the UM, which uses Newtonian

relaxation to adjust zonal (U) and meridional (V) wind components, and potential temperature Θ towards ERA-Interim reanalysis data products of the same variables at 6-hourly intervals [Dee et al., 2011]. Reanalysis data is included in the model through the addition of non-physical relaxation terms to model equations [Dalvi, 2015]. The rate of change of a variable in the model is then described as:

$$\Delta X = F(X) + G(X_{ana} - X_{mod}) \tag{22}$$

Equation 22: F is the change of the variable X due to all factors over the dynamical time-step, X_{ana} is the value of the variable in ERA-Interim and X_{mod} is the value of the variable in the model to be nudged. G is the constant relaxation parameter, which is calculated as 1/(time interval (in seconds) between reanalysis data) [Telford et al., 2008].

While nudging interferes with a GCM's ability to respond to dynamic feedback systems, nudging a model is necessary when comparing against observational measurements, or in perturbation experiments where multiple simulations over the same time period are used to compare the effect of a small change. By ensuring the meteorology in the model is representative of the 'real world', meteorological-based variations are reduced in the model that may otherwise impact the variable of focus.

A.5 A-factors

The A-factor, also known as the pre-exponential factor, is a constant that represents the frequency of collisions between reactant species at a standard concentration. The A-factor is utilised in the Arrhenius equation which describes relationships between temperature and rate coefficient below.

$$k = Ae^{E_a/RT} \tag{23}$$

Equation 23: Arrhenius equation, where A = A-factor, E_a = activation energy (the energy that must be provided to result in a chemical reaction), T = temperature.

The A-factor is dependent on a number of factors including molecular alignment. For the purposes of this thesis the A-factor has been provided for chemical reactions within the CheST and Offline Oxidant chemistry schemes as a method of comparing reaction rates (as the A-factor has the same units as the rate constant, k).

A.6 Drawbacks of using ground-based observations

This research takes advantage of multiple recent research voyages that have taken place in the Southern Ocean region between 2016–2018 to enhance aerosol evaluation. There are, however, a number of drawbacks of using ground-based observations in comparison to satellite-based observations which are discussed below.

Immediately obvious from figure 60 is that there is a lack of Southern Ocean observations of AOD in winter, and towards higher-latitudes. Optical measurements such as AOD require clear-sky conditions in order to be conducted. SO observations are largely collected on ship-based voyages or land-based campaigns, which lack temporal density compared to satellite operations, and require rigorous screening to exclude ship-stack emission or land-signal contamination (described in Section A.10). Most voyage data is collected during summer months when Antarctic resupply missions occur and ships are able to travel further in pack ice, which biases analysis due to increased data density in summer months. Satellite observations provide a higher temporal coverage, but suffer from similar lacking observations at high-latitudes, largely due to persistent cloud cover preventing accurate retrievals [Bellouin et al., 2013b].

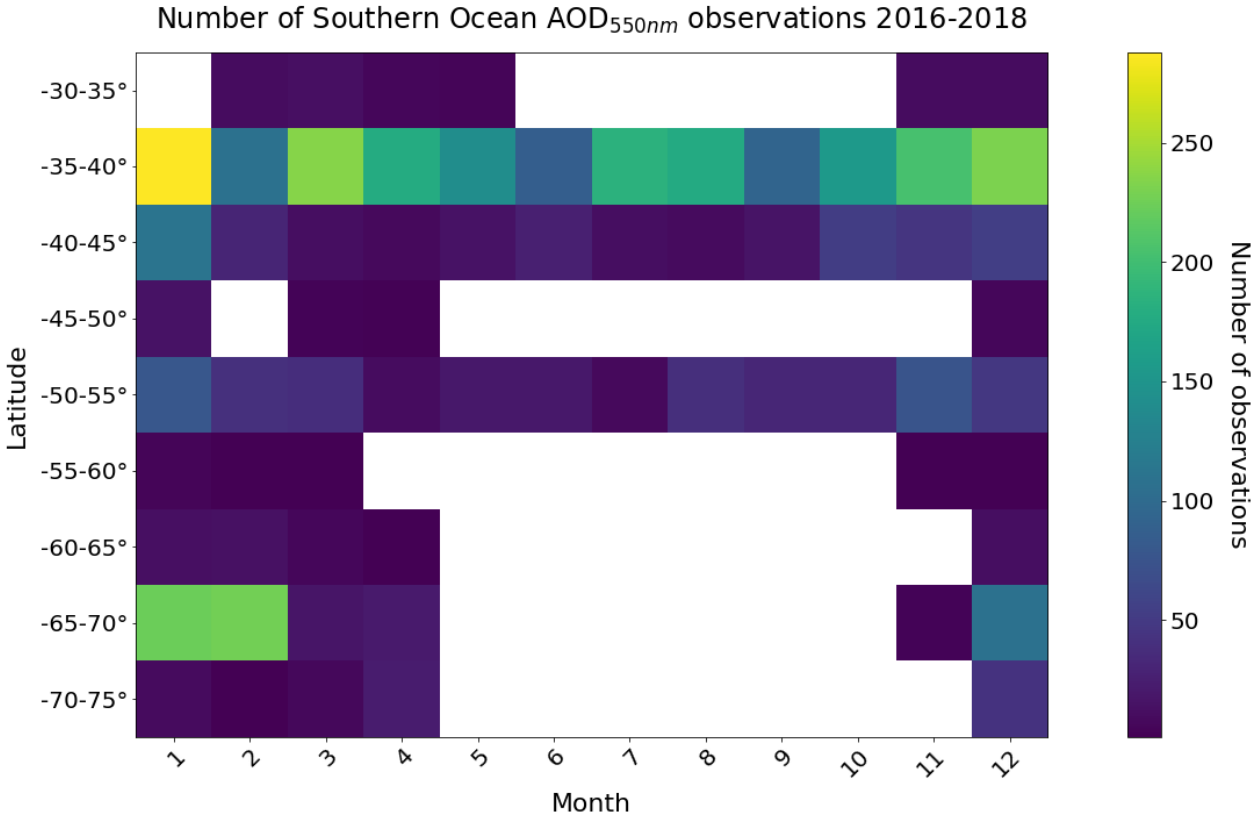


Figure 60: Number of AOD_{550nm} measurements taken over the Southern Ocean used in this thesis (see Table 28 for a list of all AOD observations). Increased data density between 30-40° shows the long-term monitoring stations, Amsterdam Island and Cape Grim.

One of the most notable disadvantages of ground-based data, is the multiple and differing uncertainties accompanying each source of observational data. Section A.7 discusses this concept further.

A.7 Observational and simulated uncertainty

This section discusses the uncertainty surrounding observational instruments and simulated parameters modelled in ACCESS-CM2.

Identifying uncertainty within a GCM is a challenging task. The calculation of model parameters such as AOD, CCN, and radiation involves multiple parameters and processes; each of which provides a compounding uncertainty towards the total calculated product. Most GCM evaluation studies avoid this issue by using an ensemble approach, defining the multi-model mean and the range of mean simulated values as a proxy for uncertainty. However, this approach is not feasible in perturbation studies due to the computing cost and storage restraints. Hence a lack of ensemble members in this study prevents such a metric of uncertainty range, and also prevents the testing of significance spatially.

Within a single model, sources of uncertainty include the resolution used (where higher resolution models often exhibit lower uncertainty), the inherent uncertainty in parameterisations, and the resulting error propagation [Flato et al., 2013]. For example, we consider uncertainty surrounding the UKCA Abdul-Razzak and Ghan [2000] parameterisation, which calculates CDNC and passes it to the radiation scheme to inform indirect effect calculations. Uncertainties in the calculation of CDNC would then propagate to the calculation of the indirect effect in the radiation scheme [Abraham et al., 2016]. Therefore parametric uncertainty increases with the complexity of model. As a new model, efforts to quantify the uncertainty surrounding physical processes in ACCESS-CM2 have not been published. There have, however, been efforts to qualify the uncertainty surrounding CCN in GLOMAP. Lee et al. [2012] utilised an emulation approach and found that found that the primary contributors to CCN uncertainty in the Southern Ocean are uncertainties surrounding the scavenging diameter, which describes the size at which aerosols are activated to form cloud droplets, and sea-spray emissions, which accounted for 60% of variance shown in the Southern Ocean region. From the Lee et al. [2012] study, we can infer that all perturbation simulations in this study will each have a different uncertainty surrounding simulated CCN. While the BASE, PMO, and CHEM runs use the same source of sea-salt, the CHEM run exhibited a changed sea-salt output and the SSALT run used a modified sea-spray emission source, hence variations in uncertainty between parameterisations are expected.

Characterising and quantifying parametric uncertainty within GCMs is an entire research field and outside of the possible scope of this thesis. Discussion above has described how we are unable to assign a ± uncertainty range to each modelled variable due to compounding parametric uncertainties. The lack of model uncertainty values limits the statistical accuracy of comparisons made in this thesis. Hence, there is an inherent assumption that modelled values in this thesis represent a "true" value with no uncertainty associated. Differences in uncertainty between simulations is important for understanding the significance of perturbation simulations. For example, if a perturbation simulation produced a mean value larger than the reference run by six units, but the reference model uncertainty was ±10 units, we would be able to characterise this result as unsubstantial given the inherent model uncertainty.

Useful comparisons regarding overall bias may still be made, which is the overall aim of this study. In the absence of a model uncertainty metric, we can instead determine whether the modelled means of certain parameters fall within published uncertainties or observational temporal variances in order to identify how closely the model agrees with observations. The available uncertainty for each observational dataset has been provided in Section 6. For comparisons between mean simulated and observed parameters, these uncertainty values have been taken into consideration to determine whether changes in the model are appreciable, or fall within the uncertainty of observations. For example, the overall uncertainty of CERES-EBAF SW TOA ↑ radiation has been defined as 2.5 W/m^2 [Loeb et al., 2018]. If the mean simulated SW TOA ↑ radiation value fell within ±2.5 of the mean observed value, the simulation could be regarded as capturing the mean observed radiation within uncertainty limits. For variables where uncertainty has not been defined, such as for CCN measurements and CALIPSO-GOCCP cloud-fraction, we have used a measure of temporal variability through calculating the standard deviation of that particular observational dataset. Statistical tables have been shaded appropriately to denote mean model-observation differences which fall within uncertainty/temporal variability thresholds. Values for each uncertainty/variability threshold have been included on all statistical tables.

A.8 Challenges facing observations in field campaigns

This section describes known challenges in measuring aerosols at stations or on voyages. This thesis makes references to challenges in determining sea-salt using the ACSM instrument, and in measuring coarse-mode particles using the APS instrument.

Sampling challenges arise for both of these instruments when utilised in a field environment (such as a voyage). While the APS is documented as having an upper detection limit of 20μm, in observational field campaigns it is well acknowledged that the long inlet tubing leading to the instrument can result in a loss of particles from impaction before reaching the instrument, particularly at higher particle sizes. Varying lengths of inlet tubing depend on the individual instrumental set-up of each voyage. The impaction of larger particles onto inlet tubing applies to all instruments used on voyages which utilise a similar set-up; including the APS and SMPS instruments which provide size distribution data, and CCN counters which provide CCN concentration. Therefore, confidence surrounding model-observation comparisons between simulated and observed values at higher particle sizes is decreased; this is relevant for the model-observation size distribution comparisons in Section 7.3.

Additionally, instrumental observations such as the ACSM are largely affected by a *cut-off shift* feature due to aerosol hygroscopic growth. While instruments often use an inlet head to cut off particles larger than a certain size, they operate under ambient RH (resulting in 'wet' particles). Particle diameter is greatly influenced by aerosol liquid water (ALW) content - for ambient, highly hygroscopic aerosols such as sea-salt with variable ALW (based on RH), this creates a shift between the cut-off diameter set, and the size of particles actually recorded [Chen et al., 2018]. This cut-off shift in observational studies is difficult to quantify and is therefore an unknown quantity that must be taken into consideration. Additionally, the height of the inlet varies between voyages and monitoring stations which provides an additional source of uncertainty between observations and the model, which defines the 'surface' height at 20m. Due to these issues, observations of aerosols can provide a measure by which to compare model bias (as has been done in this thesis) but cannot be interpreted as absolute truth.

Sea-salt observations (using a Cl^- ion proxy)

Measuring sea-salt using an Aerosol Chemical Speciation Monitor, ACSM, is difficult as most compounds in SSA are refractory and not effectively vaporised in the instrument (required for efficient analysis). Despite not measuring sea-salt directly, it is possible to obtain a sea-salt signal from ACSM measurements by scaling with a factor of 51, as NaCl is the dominant compound in sea-spray [Ovadnevaite et al., 2012]. It should be noted

that this method of scaling was developed using a different instrument to an ACSM, a Time-of-Flight Aerosol Mass Spectrometer which also measures non-refractory submicron aerosol chemical composition. The scaling method also used a $NaCl^+$ ion signal instead of the Cl^- ion used in this instance, and the instrument would have a different calibration to the ACSM used on the CAPRICORN II voyage in this study. Hence this scaling technique comes with caveats but can nonetheless provide a good estimate for bias and correlation, and has been successfully implemented in ACSM data in [Alroe et al., 2020].

The previous paragraph discussed how a sea-salt signal may be achieved from the ACSM Cl^- signal. It must also be noted that the ACSM instrument does not capture the full size distribution of sea-salt particles. ACSM instruments measure aerosols ranging in size from 0.004μm to 1μm despite factor adjustments mentioned above, and therefore would struggle to represent coarse-mode sea-salt particles [Watson, 2017]. Instead, this study has used the ACSM observations as a metric for accumulation-mode sea-salt, which fall within the measured size range.

A.9 Summary of observational ground-based datasets

Parameter	Instrument	Station/Voyage	Reference
Wind-speed	Synchrotac Vane Anemometer - Type 706 S/N	Macquarie Island King Island Cape Grim	Bureau of Meteorology
Wind-direction	Synchrotac Vane Anemometer - Type 706 S/N	Macquarie Island King Island Cape Grim	Bureau of Meteorology
Chloride (proxy for sea-salt)	Aerodyne Time of Flight Aerosol Chemical Speciation Monitor (ACSM)	CAPRICORN II, RV Investigator (IN2016 V02)	Personal communication, Humphries [2019], Fröhlich et al. [2013]
Size distribution	Aerodynamic Particle Sizer (APS) TSI 3320 Scanning Mobility Particle Sizer Spectrometer TSI 3938	Ice to Equator Voyage, RV Investigator (IN2016 V03)	Personal communication, Alroe [2020]
Aerosol Optical Depth (AOD)	Carter Scott SPO2 sun-photometer	Cape Grim	Personal communication, Wilson [2019]
Aerosol Optical Depth (AOD)	Cimel sun-photometer	Macquarie Island Amsterdam Island	Holben [2019b] Goloub [2019]
Continued over the next page...			

Parameter	Instrument	Station/Voyage	Reference
Aerosol Optical Depth (AOD)	Microtops II sun-photometer (AERONET Maritime Aerosol Network)	Agulhas II 2015-2016	Broccardo and Holben [2019]
		AK Fedorov 2015-2016	Vladimir and Holben [2019]
		AK Fedorov 2016-2017	Holben and Radionov [2019a]
		AK Fedorov 2017-2018	Holben and Radionov [2019b]
		AK Fedorov 2018-2019	Holben and Radionov [2019c]
		AK Treshnikov 2016-2017	Schmale and Holben [2019]
		AK Treshnikov 2018	Holben and Radionov [2019d]
		Aurora Australis 2018	Holben and Schofield [2019b]
		Aurora Australis 2018_1	Holben and Schofield [2019a]
		$HMNZS2016$	Holben [2019a]
		$RV Investigator2017$	Humphries and Holben [2019a]
		$RV Investigator2018$	Humphries and Holben [2019b]
		$RogerRevelle2016$	Nelson and Holben [2019]
		$Tangaroa2018$	Harvey and Holben [2019]
Cloud Condensation Nuclei	CCN-100 Counter (DMT)	Cape Grim	Personal communication, Keywood [2019]
Cloud Condensation Nuclei	CCN-100 Counter (DMT)	Macquarie Island	Personal communication, Humphries [2020]
Condensation	CCN-100 Counter (DMT)	ACE Voyage	Tatzelt et al. [2019]
Condensation	CCN-100 Counter (DMT)	MARCUS Voyage	Personal communication, Humphries [2020]

Table 28: Summary of ground-based observational data used in this thesis. AOD data provided through the AERONET MAN Network is labelled by the name of the ship and year of voyage.

A.9.1 Summary of observational satellite datasets

Parameter	Instrument	Reference
SW TOA ↑ Radiation	Clouds Clouds and Earth's Radiant Energy System (CERES) - Energy Balanced and Filled (EBAF) - TOA Edition 4.1	Loeb et al. [2018]. Data available for download at: https://ceres-tool.larc.nasa.gov/ord-tool/jsp/EBAF41Selection.jsp
Cloud Fraction	GCM-Oriented Cloud-Aerosol Lidar and Infrared Pathfinder Satellite Observation Cloud Product (CALIPSO-GOCCP)	Chepfer et al. [2010]. Data available by FTP at: ftp://ftp.climserv.ipsl.polytechnique.fr/cfmip/GOCCP_v3/2D_Maps/grid_2x2xL40/

Table 29: Summary of satellite-based observational data used in this thesis.

A.10 Observational data processing

This thesis uses multiple sources of observations as a comparative tool against model simulations. For each parameter used, all instruments have undergone similar data processing which screens for important factor affecting quality, including cloud contamination and exhaust screening for voyage data.

Cape Grim AOD

The following section utilises information provided by Wilson [2020]. AOD was measured at Cape Grim using Carter Scott SPO2 sun-photometers. One sun-photometer provided data between 01/2016–05/2017, which was replaced by another instrument (same make and model) for calibration and refurbishment purposes, and was used to provide the remainder of the data used in this thesis through 2018. Data processing includes the removal of weekend data, where contamination on the front window of the sun-photometer could have built up. AOD data was calibrated using the 'General method', which identifies temporal periods in the morning and afternoon unaffected by cloud, and extrapolates a calibration estimate [Forgan, 1994]. The calibrations are inspected for any evidence of drift, and none were observed. Drift describes unexpected changes in instrument readings which 'drift' into inaccurate values. All calibration values were then averaged for each wavelength measured, which have a 95% Confidence Interval of 0.01. Sun-photometer measurements are filtered for periods impacted by cloud using objective algorithms prescribed by [Harrison and Michalsky, 1994]. Cloud-filtered data output at minute intervals were converted into 10 minute averages.

Macquarie Island and Amsterdam Island AOD

AOD measurements at Macquarie Island and Amsterdam Island were measured using

Cimel sun-photometers (sun-sky radiometers) as part of AERONET. All AERONET data was selected at a Level 2.0 of data quality, which signifies cloud-cleared, manually quality-controlled data which has pre- and post- field calibrations applied. AERONET instruments are calibrated against a master Cimel sun-photometer pre-deployment, and are returned every 6-12 months for calibration. Computation of AOD and cloud screening has been described in detail in Giles et al. [2019].

This thesis also uses fine and coarse mode AOD which has been determined using a Spectral Deconvolution Algorithm (discussed in Section A.3). SDA AOD was also screened at a level 2.0 quality, which has a number of criteria imposed described in Giles [no date provided]. Outliers are removed according to the following criterion:

$$|AOD_{500nm} - AOD_{SDA500nm}| > (0.01 + AOD_{500nm} * 0.005)$$

AERONET MAN Voyage AOD

AERONET MAN AOD was measured using Microtops (II) sun-photometers. Microtops II instruments are calibrated against a master Cimel sun-photometer [Smirnov et al., 2009]. Each AOD measurement is made of the average of at least 5 measurements taken. The Version 2 AERONET direct sun algorithm is used to compute AOD, which is described in Giles [2017]. AERONET MAN AOD data has been selected at a level 2.0 quality, which applies final post-deployment calibration values to the data-set. The instruments are evaluated for any potential issues such as filter degradation or data anomalies, and AOD data is manually inspected for possible cloud-contaminated outliers following Smirnov et al. [2000].

While AERONET stations provide measurements every 15 minutes, AERONET MAN voyage data reports AOD more infrequently in the SO due to the scarcity of clear-sky conditions required. Level 2 quality data-processing algorithms often remove much of this data due to cloud-contamination which is a major feature of the Southern Ocean.

Cloud Condensation Nuclei

All CCN data has been quality controlled using standardised filtering and flagging processes, such as the processes detailed in Stratmann & Gysel, M. (no date provided) . CCN-100 counters measure at a range of supersaturations, and the closest SS have been chosen in this study (0.5% SS at Cape Grim, ACE and MARCUS Voyages, and both 0.45% SS and 0.55% SS at Macquarie Island). A Cape Grim CCN study has recently been published and provided measurement details, see Gras and Keywood [2017]. For voyage data (ACE and MARCUS), potential sources of contamination include ship stack exhaust. Particularly on the MARCUS campaign, the positioning of the inlet resulted in

∼90% of data being contaminated with exhaust, highlighting challenges of field campaigns and the importance for exhaust filtration in datasets. Exhaust signals are identified in CCN data as orders of magnitude higher than ambient data, and of a differing composition to background air. These signals are identified using an automated exhaust identification algorithm which utilises aerosol number concentration, black carbon concentration, carbon monoxide and carbon dioxide mixing ratios [Humphries et al., 2019].

Size distribution observational instruments

Size distribution data was provided by SMPS and APS instruments. Both instruments provide information on the size of submicrometer particles by their aerodynamic diameter (the size of an idealised spherical particle which has the same particle density and velocity as the measured particle). Both datasets were flagged for periods of ship exhaust, continental influence and instrument maintenance, and were filtered accordingly to ensure quality control. Identification of ship emissions and characterisation of continental air masses have been detailed for a similar research voyage in Alroe et al. [2020].

Aerosol Chemical Speciation Monitor

Chloride data is used as a proxy for sea-salt in this research, which was measured using an Aerodyne Time of Flight Aerosol Chemical Speciation Monitor (ACSM). Instrumental design and operation is provided in [Fröhlich et al., 2013]. THe ACSM measurements were recorded on the CAPRICORN II voyage, and hence were screened for exhaust contamination using a m/z 57 (mass to charge ratio) which provides a tracer for combustion that could be removed from the dataset. Cleaned data in this dataset accounts for method detection limits to ensure quality control.

A.10.1 Introduced Statistical metrics; NMBF and NMAEF

Traditional metrics of bias (NMB) and error (Mean Normalised Absolute Error) create issues of asymmetry and inflation, depending on the sign of the model bias. When the model overestimates observations, the NMB may grow unbounded; whereas for underestimates, the NMB is limited by -100%, creating issues of asymmetry. For cases where the model exhibits a large bias (where the observed denominator value is relatively low), the NMB value can be greatly inflated. This poses an issue for atmospheric chemistry evaluations, where species analysed are often low in value. The statistic, Normalised Mean Bias Factor (NMBF), overcomes this asymmetry problem through utilising the ratio of the modelled to observed values in order to denote the sign of the statistic. The introduced error statistic, Normalised Mean Absolute Error Factor (NMAEF), addresses asymmetry by ranging from 0 to $+\infty$. Both NMBF and NMAEF have the advantage of avoiding issues of inflation through utilising normalisation (which avoids having small values on

the denominator), and maintain symmetry [Yu et al., 2006].

A.11 Meteorology

A.11.1 Statistical summaries of simulated and observed wind-speed

Southern Ocean Average	BASE	ERA-I
Mean	9.07	9.55
Minimum	8.97	9.41
Maximum	9.28	9.79
Relative Difference (%)		-4.93
Correlation		0.999
Bias		-0.471
NMBF		-0.0519
RMSE		0.472
NMAEF		0.0519
IOA		0.309

Table 30: Statistical summary of simulated wind-speed compared to ERA-I wind-speed averaged spatially over the Southern Ocean, summer months 2016-2018.

Southern Ocean Average	BASE	ERA-I
Mean	10.15	10.7
Minimum	10.00	10.59
Maximum	10.2	10.8
Relative Difference (%)		-5.02
Correlation		0.973
Bias		-0.536
NMBF		-0.0528
RMSE		0.538
NMAEF		0.0528
IOA		0.094

Table 31: Statistical summary of simulated wind-speed compared to ERA-I wind-speed averaged spatially over the Southern Ocean, winter months 2016-2018.

Cape Grim Summer	BASE	ERA-I	OBS
Mean	5.33	6.82	9.91
Minimum	4.73	6.68	9.81
Maximum	5.84	7.05	10.0
Standard deviation	0.459	0.168	0.096
Relative Difference (%)		-21.8	-46.2
Correlation		0.214	-0.138
Bias		-1.49	-4.57
NMBF		-0.278	-0.858
RMSE		1.55	4.60
NMAEF		0.278	0.858
IOA		0.027	-0.001

Table 32: Statistical summary of simulated wind-speed compared to ERA-I wind-speed averaged temporally over summer months at Cape Grim, 2016-01-01 to 2018-10-22.

Cape Grim Winter	BASE	ERA-I	OBS
Mean	7.63	8.35	10.2
Minimum	7.17	7.47	9.31
Maximum	8.26	9.30	11.03
Standard deviation	0.459	0.748	0.709
Relative Difference (%)		-8.41	-25.4
Correlation		0.978	0.919
Bias		-0.724	-2.61
NMBF		-0.0949	-0.343
RMSE		0.789	2.64
NMAEF		0.0949	0.343
IOA		0.683	0.147

Table 33: Statistical summary of simulated wind-speed compared to ERA-I wind-speed averaged temporally over winter months at Cape Grim, 2016-01-01 to 2018-10-22.

Macquarie Island Summer	BASE	ERA-I	OBS
Mean	9.91	10.3	9.4
Minimum	9.45	9.97	8.73
Maximum	10.4	10.7	9.93
Relative Difference (%)		-4.19	5.37
Correlation		1.00	0.981
Bias		-0.431	0.496
NMBF		-0.0435	0.0527
RMSE		0.438	0.520
NMAEF		0.043	0.053
IOA		0.693	0.730

Table 34: Statistical summary of simulated wind-speed compared to ERA-I wind-speed averaged temporally over summer months at Macquarie Island, 2016-01-01 to 2018-10-22.

Macquarie Island Winter	BASE	ERA-I	OBS
Mean	10.7	10.9	10.3
Minimum	10.0	10.5	10.0
Maximum	11.5	11.3	11.0
Relative Difference (%)		-2.23	3.35
Correlation		0.983	0.916
Bias		-0.236	0.349
NMBF		-0.0221	0.0338
RMSE		0.354	0.427
NMAEF		0.0305	0.0338
IOA		0.863	0.848

Table 35: Statistical summary of simulated wind-speed compared to ERA-I wind-speed averaged temporally over winter months at Macquarie Island, 2016-01-01 to 2018-10-22.

King Island Summer	BASE	ERA-I	OBS
Mean	4.91	6.82	6.15
Minimum	4.51	6.68	5.97
Maximum	5.18	7.05	6.27
Relative Difference (%)		-28.0	-12.7
Correlation		0.704	0.997
Bias		-1.90	-1.05
NMBF		-0.387	-0.144
RMSE		1.92	1.05
NMAEF		0.387	0.144
IOA		0.036	0.665

Table 36: Statistical summary of simulated wind-speed compared to ERA-I wind-speed averaged temporally over summer months at King Island, 2016-01-01 to 2018-10-22.

King Island Winter	BASE	ERA-I	OBS
Mean	7.30	8.4	6.88
Minimum	6.38	7.47	6.07
Maximum	8.19	9.30	7.74
Relative Difference (%)		-12.69	6.07
Correlation		1.00	1.00
Bias		-1.05	0.420
NMBF		-0.144	0.0610
RMSE		1.05	0.426
NMAEF		0.144	0.0610
IOA		0.665	0.917

Table 37: Statistical summary of simulated wind-speed compared to ERA-I wind-speed averaged temporally over winter months at King Island, 2016-01-01 to 2018-10-22.

A.11.2 Land-Ocean Fraction as a source of simulated wind-speed bias

The representation of land and ocean in ACCESS-CM2 was investigated as a source of bias in simulated wind-speed. Land and ocean have separate parameters that contribute to wind-speed, such as surface roughness and temperature. Coarse-scale models parameterise surface interactions at coastal sites using the fraction of land to ocean in a gridbox to calculate the contribution of each surface to meteorological parameters using a 'buddy' system [Hewitt et al., 2011]. King Island and Macquarie Island are regarded as being completely ocean and exhibited higher model-observation wind-speed correlation values compared to Cape Grim which has a land fraction of 0.2 (see Figure 61). While this negative relationship may be noted, the small amount of suitable meteorological stations prevents this relationship from being stated with confidence.

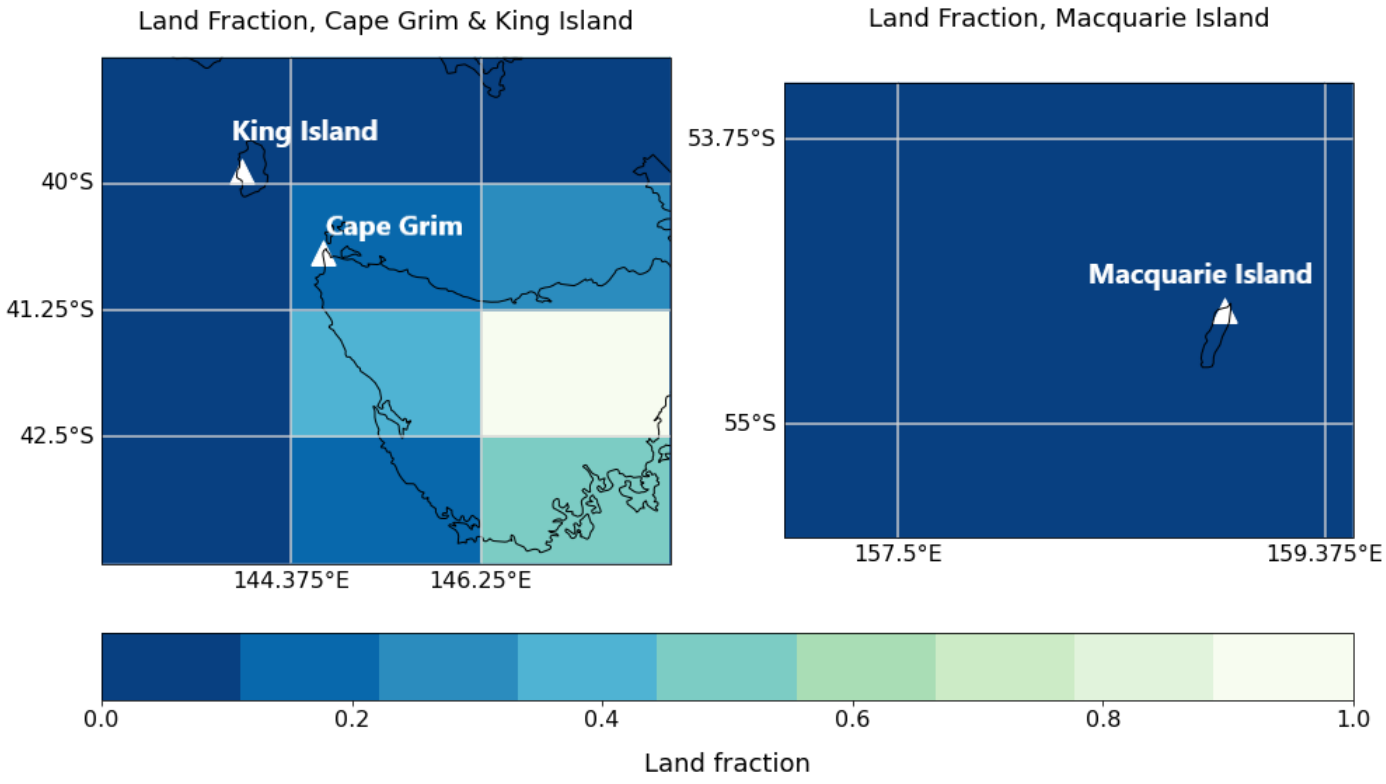


Figure 61: Land fraction of available meteorological stations, King Island, Cape Grim, and Macquarie Island. The latitude/longitude lines on the plot are aligned with ACCESS-CM2 grid-spaces (1.25° Latitude by 1.85° Longitude).

A.12 Size distributions

Aerosol Mode mean diameter (nm)	BASE	PMO	CHEM
Nucleation	(undetected)	10.5932689	(undetected)
Aitken	48.9	80.4	49.8
Accumulation	271	243	266
Coarse	2056	2019	1807

Table 38: Summer Average Southern Ocean aerosol mode mean diameter (nm).

Aerosol Mode peak particle number (dN/dlogDp)	BASE	PMO	CHEM
Nucleation	(undetected)	3.55	(undetected)
Aitken	104	60.3	136
Accumulation	116	197	126
Coarse	2.96	2.99	3.26

Table 39: Summer Average Southern Ocean aerosol mode peak particle number (dN/dlogDp).

Aerosol Mode mean diameter (nm)	BASE	PMO	CHEM
Nucleation	11.8	11.0	12.5
Aitken	44.6	76.0	46.2
Accumulation	266	243	247
Coarse	2133	2133	1841

Table 40: Autumn Average Southern Ocean aerosol mode mean diameter (nm).

Aerosol Mode peak particle number (dN/dlogDp)	BASE	PMO	CHEM
Nucleation	19.2	17.2	12.2
Aitken	67.3	49.1	56.5
Accumulation	87.9	123.9	91.8
Coarse	2.8	2.8	3.1

Table 41: Autumn Average Southern Ocean aerosol mode peak particle number (dN/dlogDp).

Aerosol Mode mean diameter (nm)	BASE	PMO	CHEM
Nucleation	11.0	10.8	11.4
Aitken	45.4	(not detected)	44.6
Accumulation	261	252	238
Coarse	2173	2173	1910

Table 42: Winter Average Southern Ocean aerosol mode mean diameter (nm).

Aerosol Mode peak particle number (dN/dlogDp)	BASE	PMO	CHEM
Nucleation	14.8	12.7	15.0
Aitken	16.8	(not detected)	24.6
Accumulation	73.0	87.4	74.2
Coarse	2.63	2.61	2.88

Table 43: Winter Average Southern Ocean aerosol mode peak particle number (dN/dlogDp).

Aerosol Mode mean diameter (nm)	BASE	PMO	CHEM
Nucleation	11.0	10.8	11.2
Aitken	45.4	(not detected)	43.8
Accumulation	271	242.7	252
Coarse	2133	2133	1875

Table 44: Spring Average Southern Ocean aerosol mode mean diameter (nm).

Aerosol Mode peak particle number (dN/dlogDp)	BASE	PMO	CHEM
Nucleation	29.8	24.1	45.2
Aitken	51.2	(not detected)	80.3
Accumulation	76.4	126	81.5
Coarse	2.66	2.65	2.93

Table 45: Spring Average Southern Ocean aerosol mode peak particle number (dN/dlogDp).

A.13 AOD

A.13.1 Average simulated and observed AOD statistical comparisons

Cape Grim	OBS	BASE	PMO	CHEM	SSALT
Mean	0.0912	0.1414	0.1436	0.1208	0.0751
Relative Difference		0.0502 (55.0%)	0.0524 (57.5%)	-0.0296 (32.4%)	-0.0162 (7.12%)
Correlation		0.349	0.346	0.335	0.318
Bias		0.0295	0.0306	0.0120	-0.0165
NMBF		0.322	0.335	0.132	-0.219
RMSE		0.0752	0.0756	0.0639	0.0617
NMAEF		0.602	0.607	0.493	0.537
IOA		0.620	0.653	0.579	0.365

Table 46: Statistical summary of modeled and observed AOD at Cape Grim. Model-observation difference have been shaded if they fall within the observational uncertainty (0.01), see Appendix A.7.

Macquarie Island	OBS	BASE	PMO	CHEM	SSALT
Mean	0.0871	0.109	0.110	0.0906	0.0624
Relative Difference		0.0219 (25.1%)	0.0231 (26.5%)	0.00346 (3.97%)	0.0247 (-19.5%)
Correlation		0.376	0.377	0.372	0.251
Bias		0.0195	0.0202	0.00416	-0.0240
NMBF		0.226	0.234	0.048	-0.385
RMSE		0.0606	0.0576	0.0461	0.0442
NMAEF		0.467	0.467	0.391	0.559
IOA		0.446	0.449	0.513	0.317

Table 47: Statistical summary of modeled and observed AOD at Macquarie Island. Model-observation difference have been shaded if they fall within the observational uncertainty (0.01), see Appendix A.7.

Amsterdam Island	OBS	BASE	PMO	CHEM	SSALT
Mean	0.0764	0.130	0.132	0.114	0.0601
Relative Difference		0.0532 (69.6%)	0.0560 (73.4%)	0.0373 (48.8%)	-0.0163 (-10.0%)
Correlation		0.633	0.637	0.626	0.381
Bias		0.0540	0.0566	0.0366	-0.0170
NMBF		0.700	0.735	0.475	-0.282
RMSE		0.0749	0.0784	0.0545	0.0392
NMAEF		0.745	0.778	0.553	0.479
IOA		0.517	0.505	0.609	0.479

Table 48: Statistical summary of modeled and observed AOD at Amsterdam Island. Model-observation difference have been shaded if they fall within the observational uncertainty (0.01), see Appendix A.7.

Southern Ocean Voyages	OBS	BASE	PMO	CHEM	SSALT
Mean	0.0746	0.161	0.166	0.141	0.0956
Relative difference (%)		0.0860 (115%)	0.0910 (122%)	0.0663 (88.9%)	0.0210 (48.7%)
Correlation		0.463	0.433	0.414	0.429
Bias		0.0860	0.0910	0.0663	0.0210
NMBF		1.15	1.22	0.889	0.281
RMSE		0.116	0.121	0.0898	0.0438
NMAEF		1.17	1.24	0.915	0.452
IOA		0.288	0.260	0.313	0.533

Table 49: Statistical summary of modeled and observed AOD over 14 Southern Ocean AERONET MAN Voyages. Model-observation difference have been shaded if they fall within the observational uncertainty (0.02), see Appendix A.7.

A.13.2 Seasonal simulated and observed AOD statistical comparisons

Cape Grim Summer, N =1996	OBS	BASE	PMO	CHEM	SSALT
Mean	0.108	0.149	0.151	0.128	0.0950
Relative Difference (%)		0.0414 (38.5%)	0.0437 (40.6%)	0.0201 (18.7%)	-0.0126 (-11.7%)
Correlation		-0.327	-0.309	-0.265	-0.287
Bias		0.0414	0.0437	0.0201	-0.013
NMBF		0.385	0.406	0.187	-0.133
RMSE		0.0548	0.0565	0.0376	0.032
NMAEF		0.385	0.406	0.291	0.288
IOA		0.909	0.895	0.894	-0.311

Table 50: Statistical summary of seasonal modeled and observed AOD, Cape Grim Summer (2016-2018). Model-observation difference have been shaded if they fall within the observational uncertainty (0.01), see Appendix A.7.

Cape Grim Winter, N =1960	OBS	BASE	PMO	CHEM	SSALT
Mean	0.0474	0.130	0.131	0.109	0.0680
Relative Difference (%)		0.0827 (174%)	0.0834 (176%)	0.0613 (129%)	0.0206 (43.4%)
Correlation		0.989	0.979	0.946	0.781
Bias		0.0827	0.0834	0.0613	0.0206
NMBF		1.74	1.76	1.29	0.434
RMSE		0.0838	0.0845	0.0621	0.0215
NMAEF		1.74	1.76	1.29	0.434
IOA		0.909	0.895	0.894	0.165

Table 51: Statistical summary of seasonal modeled and observed AOD, Cape Grim Winter (2016-2018). Model-observation difference have been shaded if they fall within the observational uncertainty (0.01), see Appendix A.7.

Macquarie Island Summer, N =146	OBS	BASE	PMO	CHEM	SSALT
Mean	0.0839	0.129	0.132	0.110	0.0807
Relative Difference (%)		0.0448 (53.3%)	0.0481 (57.3%)	0.0257 (30.7)	-0.00328 (-3.90%)
Correlation		-0.988	-0.909	-1.000	-0.980
Bias		0.0448	0.0481	0.0257	-0.00328
NMBF		0.533	0.573	0.307	-0.0406
RMSE		0.0496	0.0516	0.0333	0.0151
NMAEF		0.533	0.573	0.307	0.185
IOA		0.609	0.619	0.576	0.117

Table 52: Statistical summary of seasonal modeled and observed AOD, Macquarie Island Summer (2016-2018). Model-observation difference have been shaded if they fall within the observational uncertainty (0.01), see Appendix A.7.

Macquarie Island Winter, N =69	OBS	BASE	PMO	CHEM	SSALT
Mean	0.0861	0.0929	0.0915	0.0661	0.0431
Relative Difference (%)		0.0068 (7.91%)	0.0054 (6.22%)	0.0201 (-23.3%)	-0.0430 (-49.9%)
Correlation		0.493	0.630	0.634	0.776
Bias		0.00681	0.00535	-0.0201	-0.0430
NMBF		0.0791	0.0622	-0.304	-0.996
RMSE		0.0167	0.0138	0.0226	0.0439
NMAEF		0.157	0.136	0.304	0.996
IOA		0.438	0.431	0.524	0.132

Table 53: Statistical summary of seasonal modeled and observed AOD, Macquarie Island Winter (2016-2018). Model-observation difference have been shaded if they fall within the observational uncertainty (0.01), see Appendix A.7.

Amsterdam Island Summer, N =636	OBS	BASE	PMO	CHEM	SSALT
Mean	0.0766	0.125	0.130	0.115	0.0859
Relative Difference (%)		0.0488 (63.7%)	0.0536 (70.0%)	0.0381 (49.7%)	0.00928 (12.1%)
Correlation		0.965	0.975	0.990	0.999
Bias		0.0488	0.0536	0.0381	0.00928
NMBF		0.637	0.700	0.497	0.121
RMSE		0.0498	0.0547	0.0385	0.00938
NMAEF		0.637	0.700	0.497	0.121
IOA		0.516	0.493	0.595	0.783

Table 54: Statistical summary of seasonal modeled and observed AOD, Amsterdam Island Summer (2016-2018). Model-observation difference have been shaded if they fall within the observational uncertainty (0.01), see Appendix A.7.

Amsterdam Island Winter, N =450	OBS	BASE	PMO	CHEM	SSALT
Mean	0.0769	0.135	0.135	0.113	0.0674
Relative Difference (%)		0.0577 (75.0%)	0.0585 (76.0%)	0.0362 (47.0%)	-0.00953 (-12.4%)
Correlation		0.998	0.998	0.999	0.902
Bias		0.0577	0.0585	0.0362	-0.0095
NMBF		0.750	0.760	0.470	-0.141
RMSE		0.0582	0.0589	0.0363	0.0106
NMAEF		0.750	0.760	0.470	0.141
IOA		0.502	0.510	0.627	0.777

Table 55: Statistical summary of seasonal modeled and observed AOD, Amsterdam Island Winter (2016-2018). Model-observation difference have been shaded if they fall within the observational uncertainty (0.01), see Appendix A.7.

A.13.3 Relationship between wind-direction and AOD bias

Pollution Rose:

Section 7.4.2 utilised a pollution rose in Figure 38 to identify sources of increased AOD bias. Figure 62 provides the same pollution rose figure, which shows increased sources of AOD originating from multiple wind-directions through areas of orange and red, as would be expected for a small island in the Southern Ocean. In comparison, Cape Grim is situated on a larger land mass, and exhibits a distinct Southern Ocean signature in the baseline sector (shown in Figure 38).

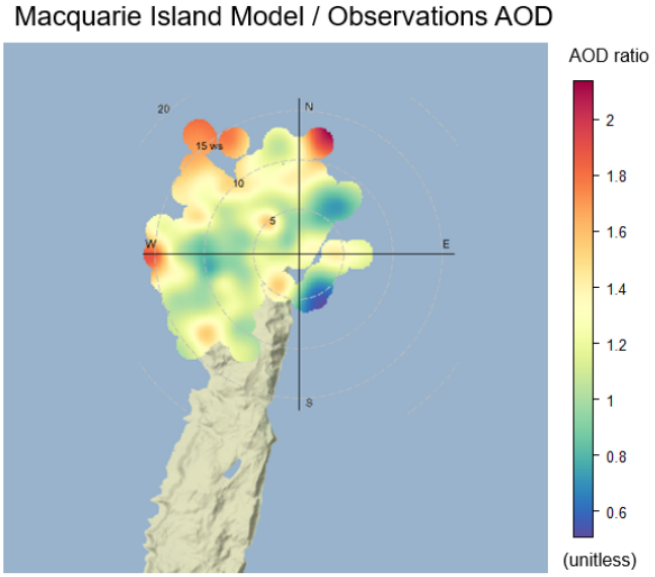


Figure 62: Pollution Rose of AOD_{550nm} at Macquarie Island. AOD ratio calculated as the ratio of ACCESS-CM2 simulated AOD/Observed AOD for all data (not baseline-screened.

Conditional Probability Function

To investigate sources of the highest AOD bias further, the Conditional Probability Function (CPF) was used. CPF is used to show wind directions that dominate high concentrations of a pollutant, as follows:

$$CPF = \frac{m_{\theta,j}}{n_{\theta,j}} \tag{24}$$

Equation 24: Conditional Probability Function (CPF), where $m_{\theta,j}$ is the number of samples above a specified concentration within a wind sector, θ and wind speed interval, j. $n_{\theta,j}$ defines the total number of samples within the same wind-direction speed interval.

The plot below illustrates the probability of AOD bias in the 90th percentile (over a ratio of 2.6) occurring by wind direction [Carslaw, 2019]. In Figure 63, a higher AOD bias is

much more likely (CPF probability up to 0.8) in directions of SWW (corresponding to the baseline region shown in Figure 38, and another area at the NE direction, which was not as clearly depicted in Figure 38. As this wind direction is near, but not within the specified baseline region, it may represent outflow from the Australian continental region. This suggests that the model may exhibit a strong signal of high AOD from continental sources, and care must be taken to ensure that data used at Cape Grim is filtered for baseline wind directions. The separated 'dots' shown in Figure 38 are likely an artefact of lacking data density. We recommend that this CPF function be applied to a longer-term dataset to increase the number of data points and decrease uncertainty surrounding the identified regions of increased AOD.

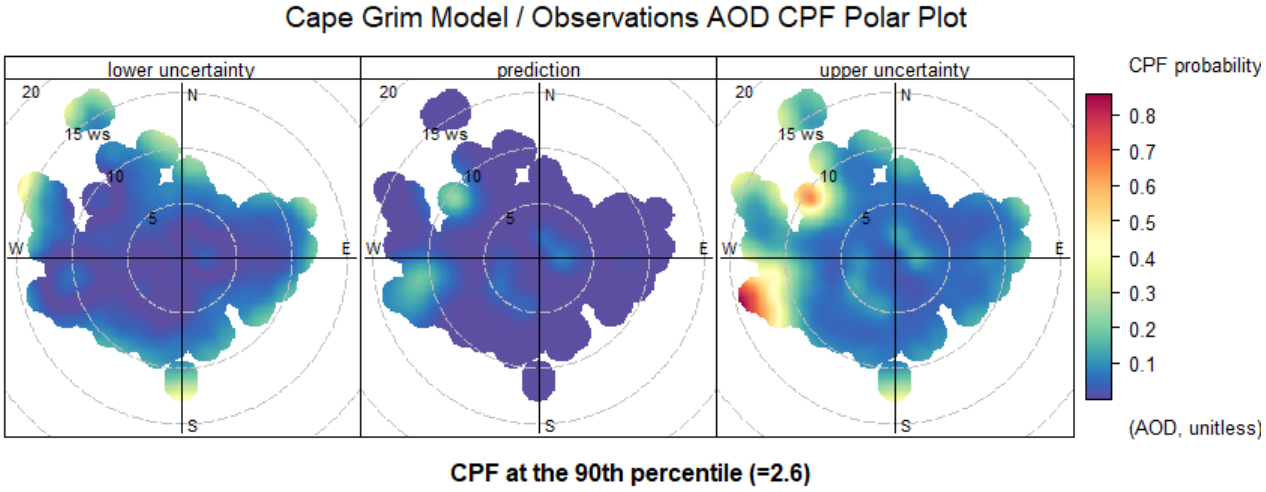


Figure 63: This figure is divided into the central prediction (middle) and the lower and upper 95% estimated uncertainties. This has been done as if the central feature exists in all uncertainty plots, then the feature is 'real' and not an artifact of too few data values, as the observational dataset used was more temporally sparse than the model input.

Another method of filtering Cape Grim data for the Baseline is through the use of Radon data. Radon-222 is a species ubiquitous to most terrestrial soils and rocks, and is measured at 2-3 orders of magnitude larger than in oceanic environments [Chambers et al., 2015]. When recorded over the same temporal and spatial domain as the parameter investigated, Radon data provides a useful terrestrial marker which can identify air parcels of terrestrial provenance. This thesis has employed wind-direction data screening processes following Cape Grim aerosol/chemistry observational studies [Crawford et al., 2017, Slemr et al., 2015]. Given the increased signature of AOD bias in non-baseline conditions (shown in Figure 63), we recommend the use of Radon-screening methods in further studies to isolate the Southern Ocean signal further. Terrestrial air parcels may be recirculated and approach the Cape Grim monitoring station from baseline wind-directions; the use of Radon data would remove air parcels flagged as containing terrestrial elements.

A.13.4 Simulated inter-annual variability of AOD

Inter-annual variability, AOD

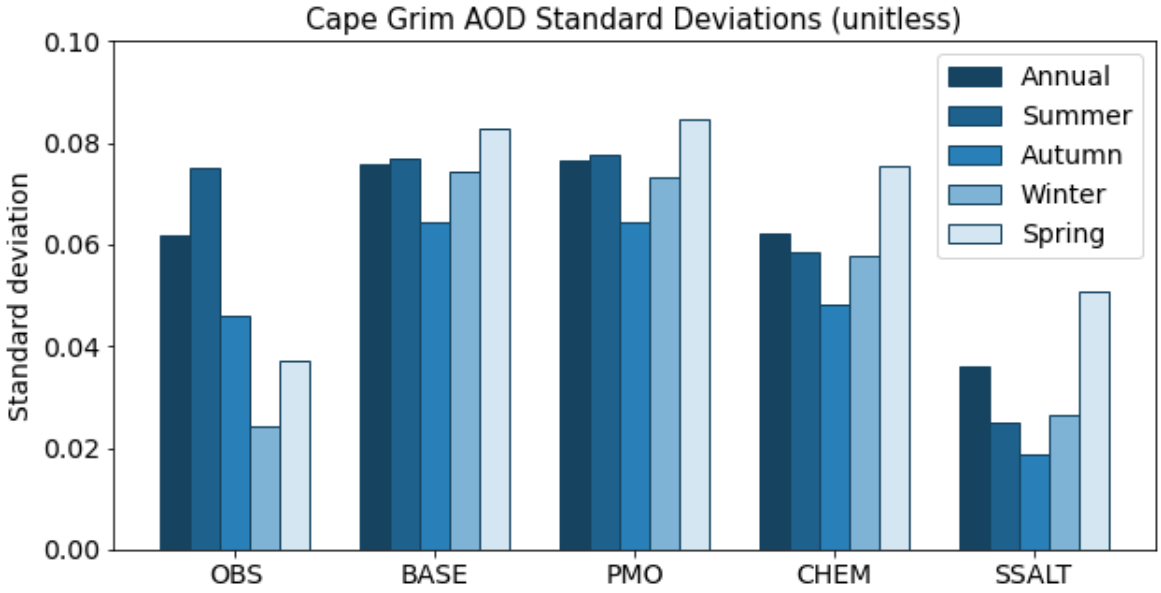


Figure 64: Observed and simulated AOD inter-annual variability at Cape Grim

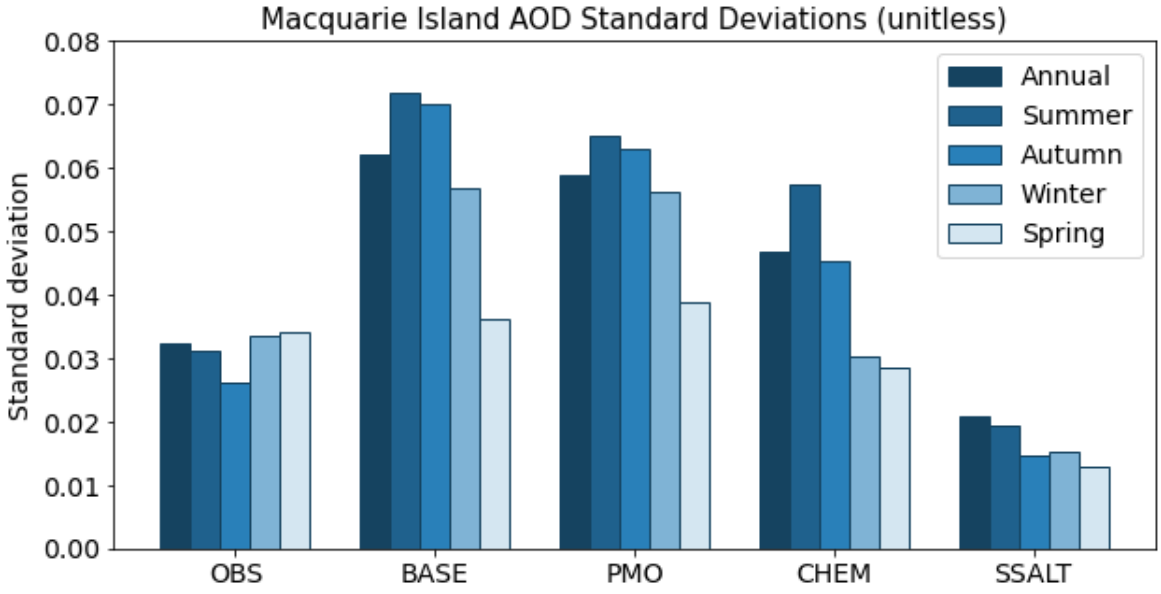


Figure 65: Observed and simulated AOD inter-annual variability at Macquarie Island

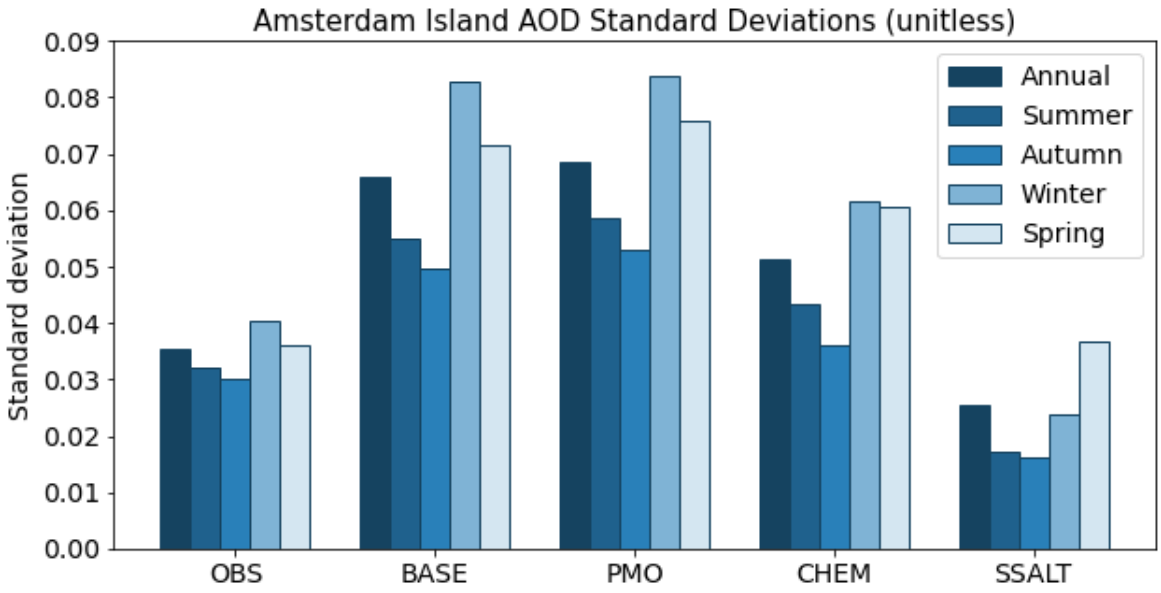


Figure 66: Observed and simulated AOD inter-annual variability at Amsterdam Island

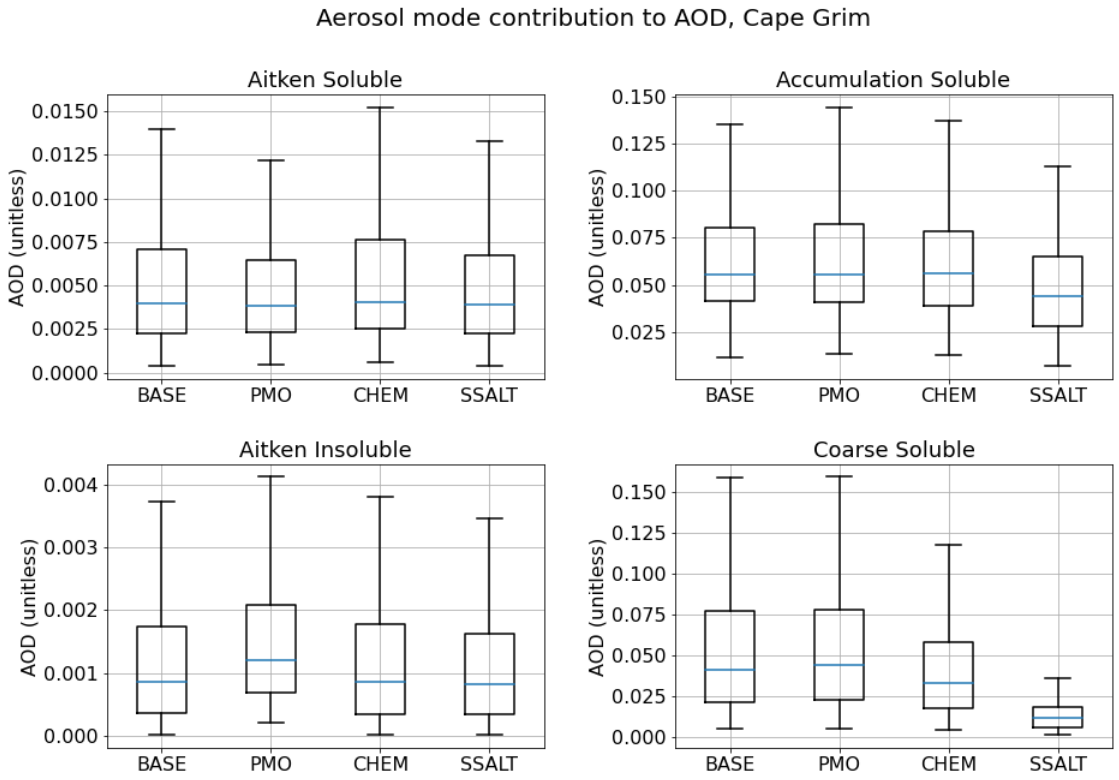


Figure 67: Aerosol mode contribution to AOD, Cape Grim. This figure also demonstrates similar changes in aerosol modes in perturbation runs relative to the BASE run as shown averaged over the Southern Ocean.

A.13.5 Comparison of zonal simulated AOD against Revell et al. [2019] results

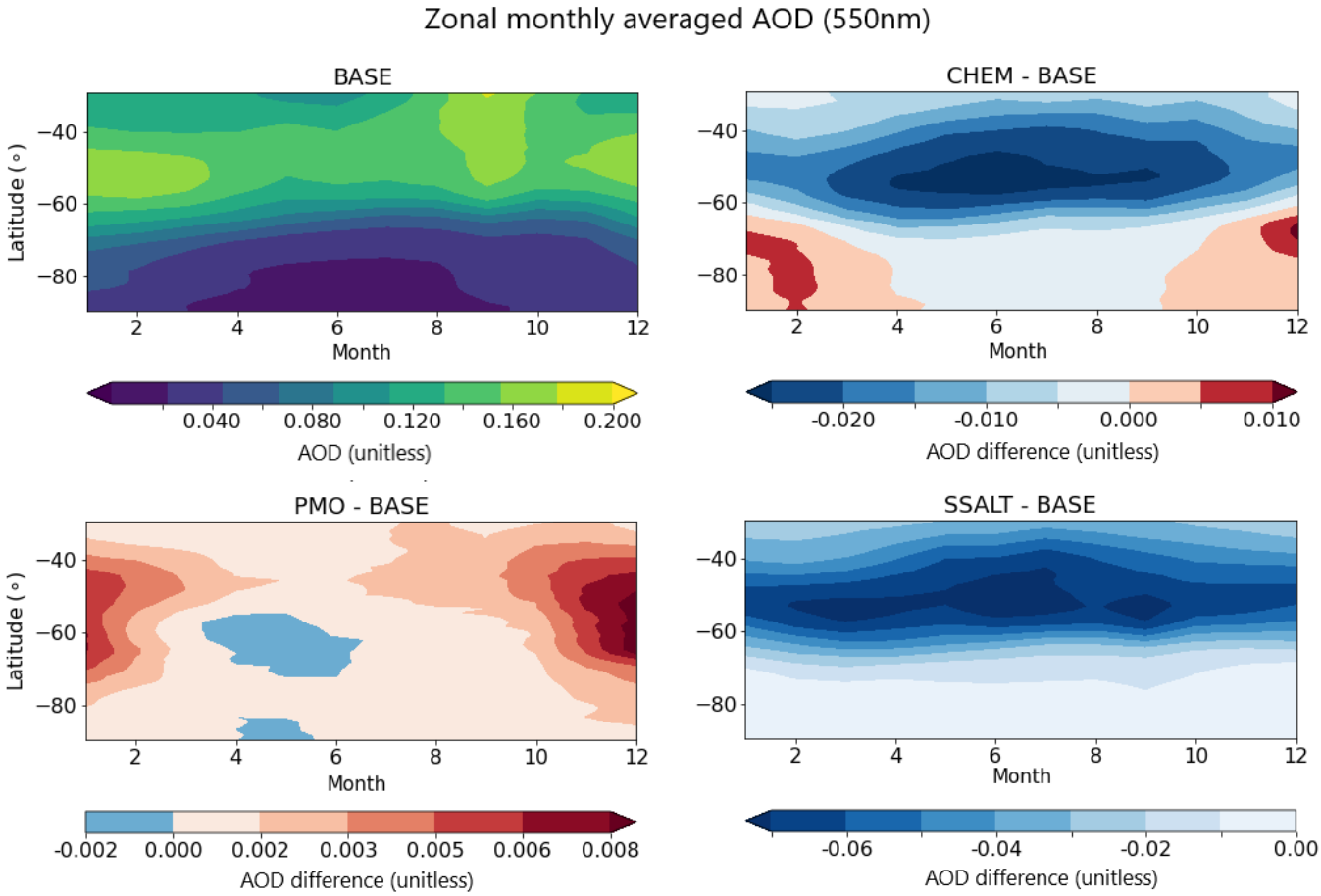


Figure 68: Simulated zonal averages of AOD_{550nm}. The top left figure shows the simulated AOD output for the BASE run, and the remaining plots show each perturbation run minus the BASE run. Model values have been plotted in this configuration for comparison against the [Revell et al., 2019] study, which utilised the same [Hartery et al., 2020] modified sea-salt source function, see Figure 69 below.

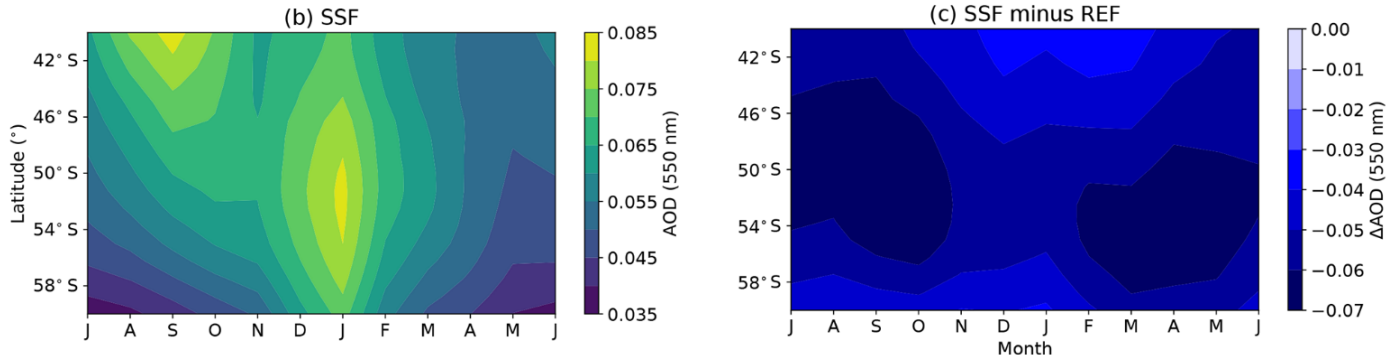


Figure 69: HadGEM3-GA7.1-simulated zonal averages of AOD_{550nm}. This figure has been adapted from Figure 3 in the Revell et al. [2019] study for comparison with Figure 68 above

In the Revell et al. [2019] study shown in Figure 68, the "SSF" model run denoted the model run with the modified sea-salt source function (similar to the SSALT run in this study), and the "REF" run used the same model structure as the SSF run, but without the modified sea-salt function (akin to the "BASE" run in this study. It is important to remember that whilst the two models share a physical atmosphere and chemistry scheme (GA7.1 and UKCA CheST), they are different models, ACCESS-CM2 and HadGEM3-GA7.1, hence AOD simulation will be different due to varying biases and model processes. Note the offset on x-axis between the two Figures, where Summer months are located in the centre of this plot, but are located at the beginning of the x-axis in Figure 68

A.14 CCN

A.14.1 Average simulated and observed CCN statistical comparisons

Cape Grim, N = 1258	OBS	BASE	PMO	CHEM	SSALT
Mean	132	76.4	87.4	99.9	74.6
Min	6.67	7.69	9.39	8.04	4.56
Max	3151	958	1116	1132	1013
Relative Difference (%)		-55.2 (-13.7%)	-44.2 (2.8%)	-31.7 (15.0%)	-57.0 (-16.0%)
Correlation		0.403	0.373	0.387	0.375
Bias		-55.2	-44.2	-31.7	-57.0
NMBF		-0.722	-0.505	-0.317	-0.764
RMSE		162	160	159	165
NMAEF		1.08	0.900	0.841	1.15
IOA		0.436	0.413	0.491	0.421
Standard deviation	166	75.9	73.4	94.9	79.4

Table 56: Statistical summary of average modeled and observed CCN at Cape Grim (2016-2018). Model-observation difference have been shaded if they fall within the observational temporal variability (166), see Appendix A.7.

Macquarie Island CCN(0.45%SS), N = 14323	OBS	BASE	PMO	CHEM	SSALT
Mean	130	41.2	57.5	61.2	29.7
Min	10.8	4.78	6.46	5.35	3.01
Max	1223	207	234	521	175
Relative Difference (%)		-88.3 (-55.9%)	-72.0 (-38.8%)	-68.3 (-36.5%)	-99.8 (-68.8%)
Correlation		0.295	0.275	0.212	0.240
Bias		-88.3	-72.0	-68.3	-99.8
NMBF		-2.15	-1.25	-1.12	-3.36
RMSE		127	117	119	136
NMAEF		2.20	1.36	1.32	3.39
IOA		0.145	0.201	0.218	0.101
Standard deviation	95.8	24.3	32.7	49.1	22.9

Table 57: Statistical summary of average modeled and observed CCN at Macquarie Island (2016-2018). Model-observation difference have been shaded if they fall within the observational temporal variability (99.3), see Appendix A.7.

Macquarie Island CCN(0.55%SS), N = 14323	OBS	BASE	PMO	CHEM	SSALT
Mean	143	41.2	57.5	61.2	29.7
Min	10.8	4.78	6.46	5.35	3.01
Max	1429	207	234	521	175
Relative Difference (%)		-101 (-59.6%)	-85.1 (-44.1%)	-81.4 (-42.2%)	-113 (-71.6%)
Correlation		0.317	0.304	0.239	0.271
Bias		-101	-85.1	-81.4	-113
NMBF		-2.46	-1.48	-1.33	-3.80
RMSE		144	133	134	153
NMAEF		2.50	1.56	1.49	3.82
IOA		0.137	0.194	0.219	0.102
Standard deviation	107	24.3	32.71	49.1	22.9

Table 58: Statistical summary of average modeled and observed CCN at Macquarie Island (2016-2018). Model-observation difference have been shaded if they fall within the observational temporal variability (126), see Appendix A.7.

ACE Voyage, N = 5226	OBS	BASE	PMO	CHEM	SSALT
Mean	176	51.9	82.2	81.5	42.4
Min	3.90	13.8	19.4	18.0	7.93
Max	1388	1158	1327	1314	1120
Relative Difference (%)		-124 (-66.7%)	-94.1 (-41.0%)	-94.7 (-44.6%)	-134 (-74.5%)
Correlation		0.440	0.364	0.368	0.441
Bias		-124	-94.1	-94.7	-134
NMBF		-2.40	-1.14	-1.16	-3.16
RMSE		159	143	148	167
NMAEF		2.53	1.30	1.39	3.31
IOA		0.370	0.390	0.407	0.353
Standard deviation	101	83.5	89.0	101	85.0

Table 59: Statistical summary of average modeled and observed CCN, ACE Voyage (2016-2017). Model-observation difference have been shaded if they fall within the observational temporal variability (101), see Appendix A.7.

MARCUS Voyage, N = 131	OBS	BASE	PMO	CHEM	SSALT
Mean	226	67.5	98	100	62.8
Min	39.1	12.3	24.8	16.5	7.19
Max	1020	335	321	384	359
Relative Difference (%)		-158 (-66.2%)	-127 (-45.0%)	-125 (-50.1%)	-163 (-70.6%)
Correlation		0.736	0.686	0.701	0.743
Bias		-158	-127	-125	-163
NMBF		-2.34	-1.29	-1.25	-2.59
RMSE		205	186	177	207
NMAEF		2.35	1.33	1.27	2.60
IOA		0.386	0.385	0.509	0.401
Standard deviation	164	54.3	48.1	70.7	58.4

Table 60: Statistical summary of average modeled and observed CCN, MARCUS Voyage (2017-2018). Model-observation difference have been shaded if they fall within the observational temporal variability (164), see Appendix A.7.

A.14.2 Probability Density Functions, Southern Ocean CCN

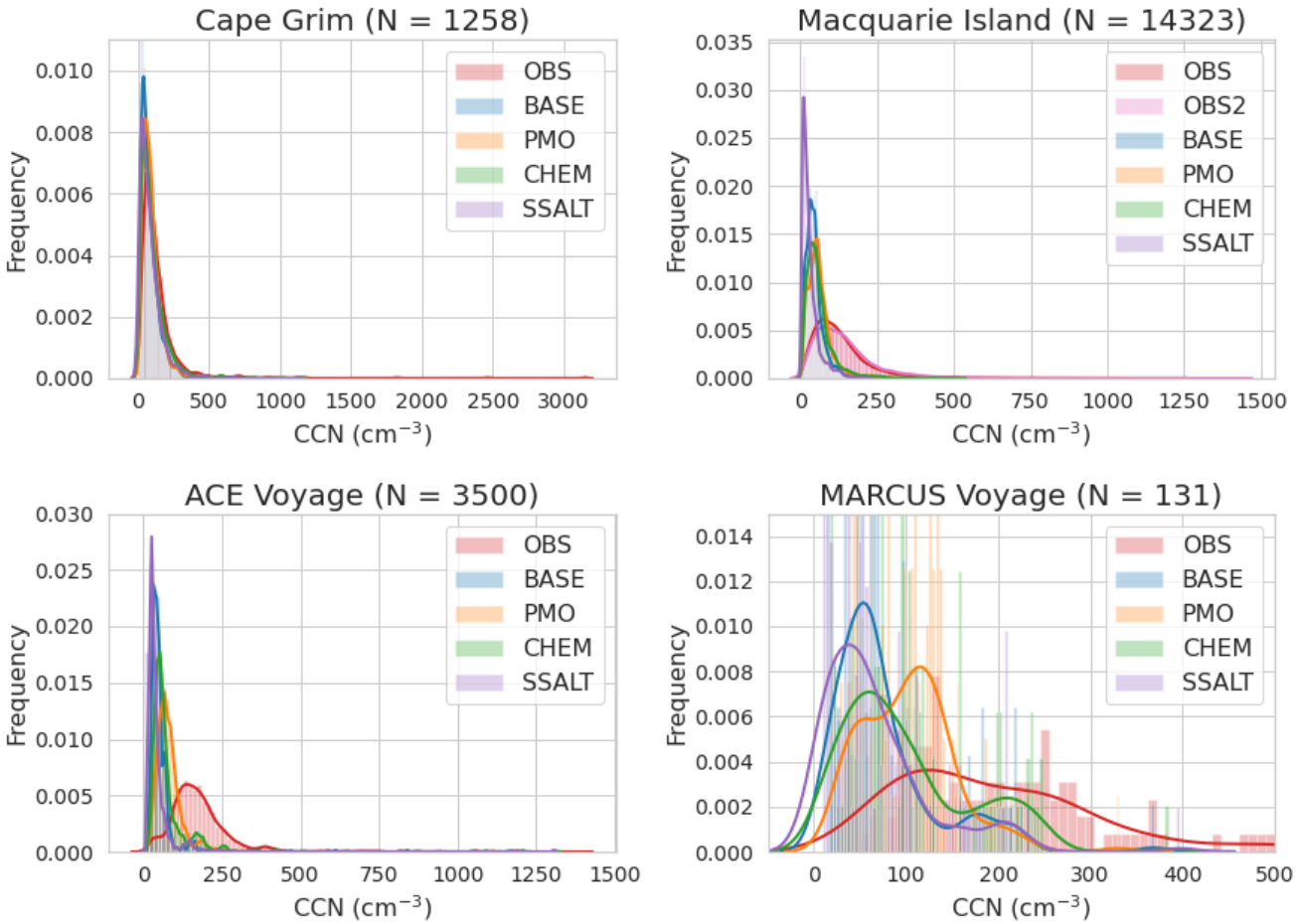


Figure 70: Histogram of observed and modeled CCN at Cape Grim, Macquarie Island and over the ACE and MARCUS Voyage Campaigns. Figure has been left un-cropped to show the magnitude of the peaks in the models compared to observations.

A.14.3 Monthly mean CCN time-series, Cape Grim and Macquarie Island

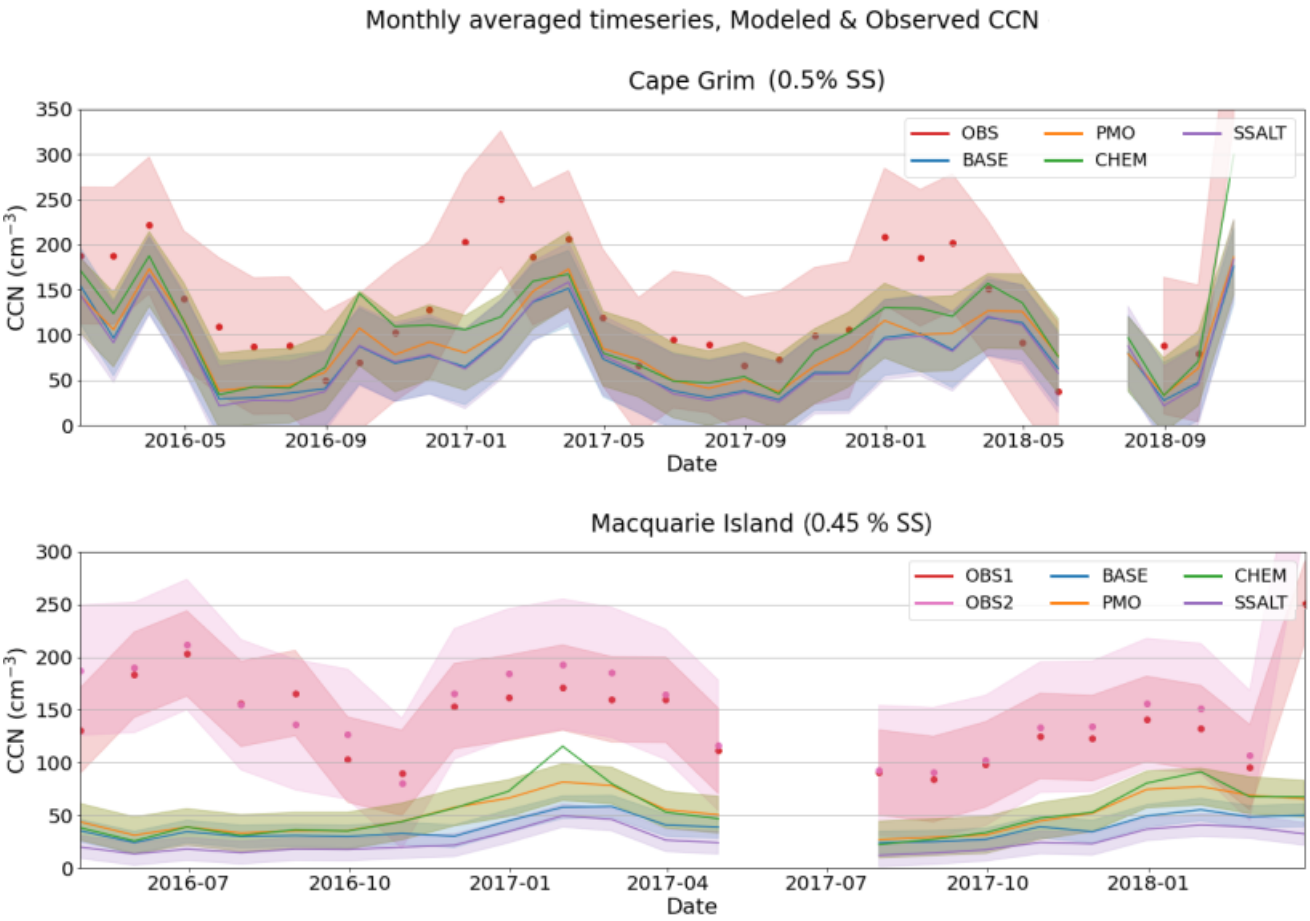


Figure 71: Monthly averaged timeseries of observed and modeled CCN, Cape Grim and Macquarie Island. Shaded regions show ± 1 standard deviation for each respective dataset.

A.14.4 Seasonal simulated and observed CCN statistical comparisons

Cape Grim Summer, N =330	OBS	BASE	PMO	CHEM	SSALT
Mean	204	104	112	132	101
Min	9.17	23.6	27.3	32.0	19.2
Max	3151	751	707	748	676
Relative Difference (%)		-99.8 (-23.9)	-91.6 (-17.1)	-71.9 (-3.1)	-103 (-26.2)
Correlation		0.412	0.374	0.384	0.375
Bias		-99.8	-91.6	-71.9	-103
NMBF		-0.959	-0.815	-0.544	-1.02
RMSE		219	219	210	223
NMAEF		1.14	1.00	0.829	1.21
IOA		0.371	0.321	0.401	0.336
Standard deviation	214	80.4	70.6	90.3	78.8

Table 61: Statistical summary of seasonal modeled and observed CCN, Cape Grim Summer (2016-2018). Model-observation difference have been shaded if they fall within the observational temporal variability (214), see Appendix A.7.

Cape Grim Winter, N =330	OBS	BASE	PMO	CHEM	SSALT
Mean	82.4	35.2	46.5	48.1	31.5
Min	6.67	8.55	9.39	8.06	4.56
Max	701	143	154	207	152
Relative Difference (%)		-47.1 (-29.5%)	-35.9 (-3.1%)	-34.2 (-2.6%)	-50.9 (-35.7%)
Correlation		0.231	0.165	0.209	0.199
Bias		-47.1	-35.9	-34.2	-50.9
NMBF		-1.34	-0.771	-0.711	-1.62
RMSE		95.4	92.3	91.7	98.1
NMAEF		1.57	1.15	1.15	1.86
IOA		0.157	0.151	0.228	0.148
Standard deviation	85.2	21.5	27.0	34.9	24.5

Table 62: Statistical summary of seasonal modeled and observed CCN, Cape Grim Winter (2016-2018). Model-observation difference have been shaded if they fall within the observational temporal variability (85.2), see Appendix A.7.

Cape Grim Autumn, N =330	OBS	BASE	PMO	CHEM	SSALT
Mean	136.0	96.5	108	114	96.3
Min	18.5	7.69	13.1	8.04	4.56
Max	2466	957	1116	1021	1013
Relative Difference (%)		-29.6 (12.3%)	-18.1 (27.8%)	-12.5 (32.4%)	-29.8 (11.1%)
Correlation		0.256	0.243	0.277	0.256
Bias		-29.6	-18.1	-12.5	-29.8
NMBF		-0.307	-0.168	-0.110	-0.309
RMSE		181	182	182	183
NMAEF		0.856	0.766	0.794	0.896
IOA		0.340	0.336	0.396	0.351
Standard deviation	178	92.7	96.6	110	98.9

Table 63: Statistical summary of seasonal modeled and observed CCN, Cape Grim Autumn (2016-2018). Model-observation difference have been shaded if they fall within the observational temporal variability (178), see Appendix A.7.

Cape Grim Spring, N =330	OBS	BASE	PMO	CHEM	SSALT
Mean	103	63.2	76.4	95.7	62.8
Min	12	12.3 16.4	11.7	8.8	
Max	1827	744	731	1132	771
Relative Difference (%)		-39.9 (-14.1%)	-26.7 (5.34%)	-7.4 (30.7%)	-40.3 (-14.3%)
Correlation		0.476	0.488	0.455	0.441
Bias		-39.9	-26.7	-7.36	-40.3
NMBF		-0.631	-0.350	-0.0769	-0.641
RMSE		110	105	114	114
NMAEF		1.05	0.803	0.791	1.13
IOA		0.539	0.551	0.619	0.530
Standard deviation	116	63.9	59.6	98.8	71.1

Table 64: Statistical summary of seasonal modeled and observed CCN, Cape Grim Spring (2016-2018). Model-observation difference have been shaded if they fall within the observational temporal variability (116), see Appendix A.7.

Macquarie Island Summer, N =4320	OBS	BASE	PMO	CHEM	SSALT
Mean	162	52.2	75.1	84.6	41.3
Min	13.2	7.20	13.3	7.17	4.33
Max	1100	207	234	521	175
Relative Difference (%)		-110 (-57.4%)	-87.4 (-38.4%)	-77.9 (-32.5%)	-121.1 (-66.5%)
Correlation		0.194	0.161	0.117	0.151
Bias		-110	-87.4	-77.9	-121
NMBF		-2.11	-1.16	-0.921	-2.93
RMSE		146	131	133	155
NMAEF		2.14	1.25	1.14	2.95
IOA		0.0787	0.109	0.133	0.0582
Standard deviation	97.2	24.1	33.8	59.8	25.2

Table 65: Statistical summary of seasonal modeled and observed CCN, Macquarie Island Summer (2016-2018). Model-observation difference have been shaded if they fall within the observational temporal variability (84.5), see Appendix A.7.

Macquarie Island Winter, N =3154	OBS	BASE	PMO	CHEM	SSALT
Mean	94.7	24.2	28.0	26.4	13.4
Min	11.6	4.78	6.46	5.35	3.01
Max	1429	103	102	122	80.8
Relative Difference (%)		-70.6 (-58.4%)	-66.7 (-51.0%)	-68.3 (-54.7%)	-81.3 (-76.3%)
Correlation		0.199	0.179	0.205	0.177
Bias		-70.6	-66.7	-68.3	-81.3
NMBF		-2.92	-2.38	-2.59	-6.06
RMSE		114	112	113	122
NMAEF		2.96	2.46	2.64	6.06
IOA		0.0720	0.0722	0.0821	0.0348
Standard deviation	91.4	13.9	14.9	15.1	8.22

Table 66: Statistical summary of seasonal modeled and observed CCN, Macquarie Island Winter (2016-2018). Model-observation difference have been shaded if they fall within the observational temporal variability (95.2), see Appendix A.7.

Macquarie Island Autumn, N =2498	OBS	BASE	PMO	CHEM	SSALT
Mean	141	39.8	53.0	49.4	25.3
Min	14.0	7.08	11.9	8.04	5.13
Max	1192	143	143	182	121
Relative Difference (%)		-101 (-58.1%)	-87.7 (-41.8%)	-91.3 (-45.9%)	-115 (-72.6%)
Correlation		0.290	0.220	0.175	0.181
Bias		-101	-87.7	-91.3	-115
NMBF		-2.54	-1.66	-1.85	-4.56
RMSE		149	141	144	160
NMAEF		2.59	1.74	1.93	4.60
IOA		0.0974	0.0848	0.0724	0.0431
Standard deviation	113	18.2	18.5	20.5	14.2

Table 67: Statistical summary of seasonal modeled and observed CCN, Macquarie Island Autumn (2016-2018). Model-observation difference have been shaded if they fall within the observational temporal variability (126), see Appendix A.7.

Macquarie Island Spring, N =4351	OBS	BASE	PMO	CHEM	SSALT
Mean	135	33.1	46.7	47.4	21.8
Min	10.8	5.12	8.66	8.18	3.74
Max	1056	189	193	223	158
Relative Difference (%)		-102 (-63.7%)	-88.0 (-50.2%)	-87.3 (-49.2%)	-113 (-76.3%)
Correlation		0.367	0.405	0.376	0.359
Bias		-102	-88.0	-87.3	-113
NMBF		-3.07	-1.89	-1.84	-5.16
RMSE		149	139	138	158
NMAEF		3.13	1.94	1.91	5.20
IOA		0.147	0.205	0.222	0.106
Standard deviation	115	22.6	26.6	31.6	17.8

Table 68: Statistical summary of seasonal modeled and observed CCN, Macquarie Island Spring (2016-2018). Model-observation difference have been shaded if they fall within the observational temporal variability (104), see Appendix A.7.

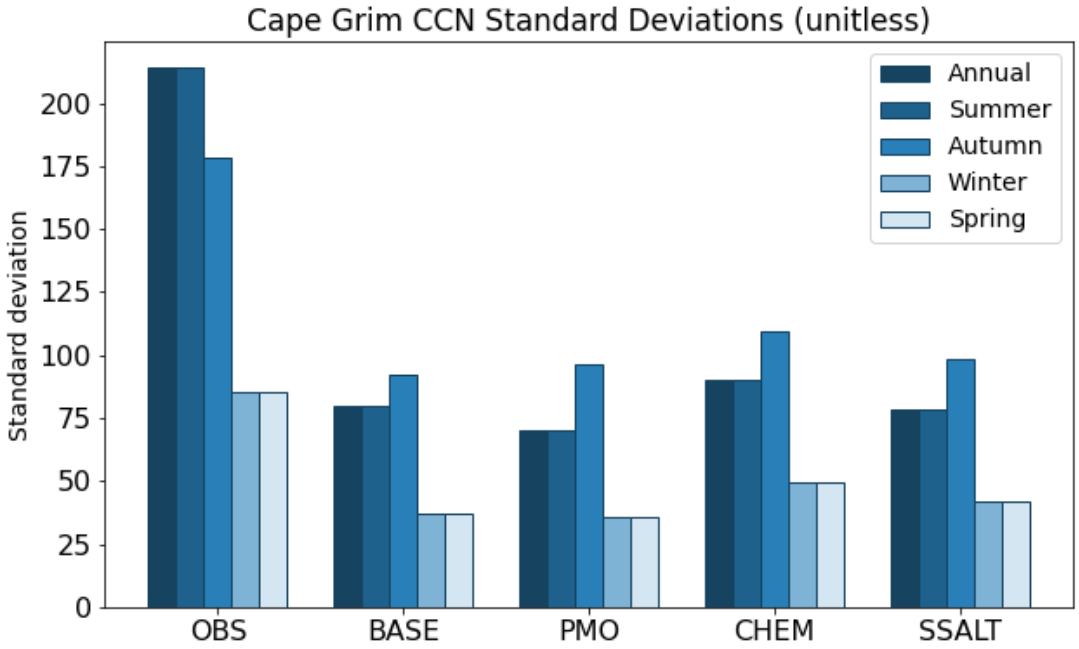


Figure 72: Cape Grim Standard Deviations of simulated and observed CCN (showing inter-annual variability) grouped by season.

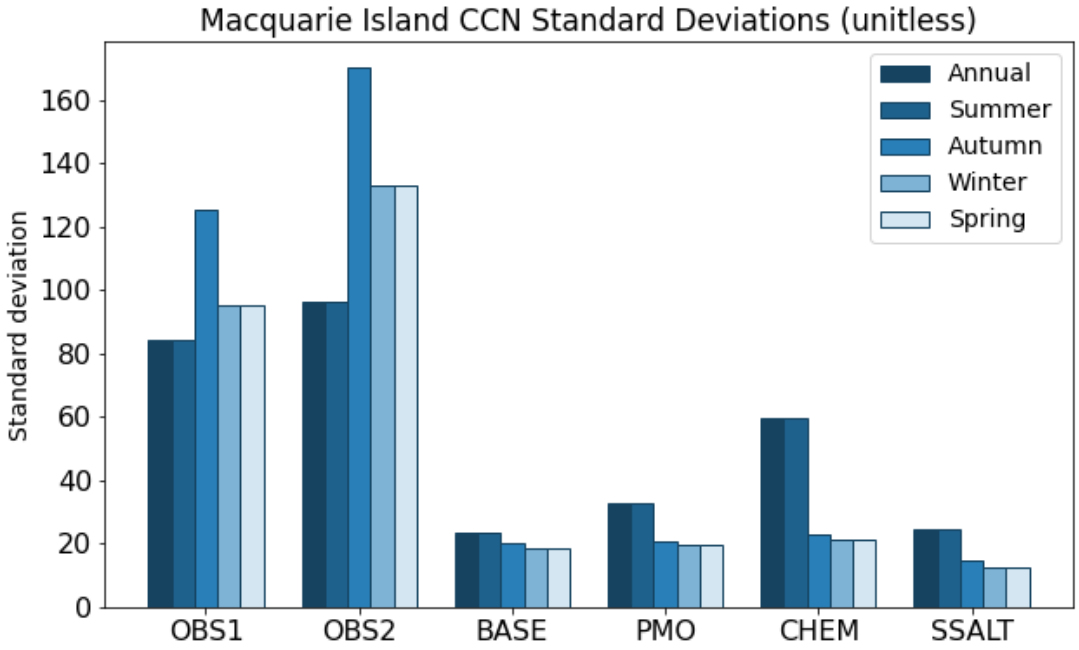


Figure 73: Macquarie Island Standard Deviations of simulated and observed CCN (showing inter-annual variability) grouped by season.

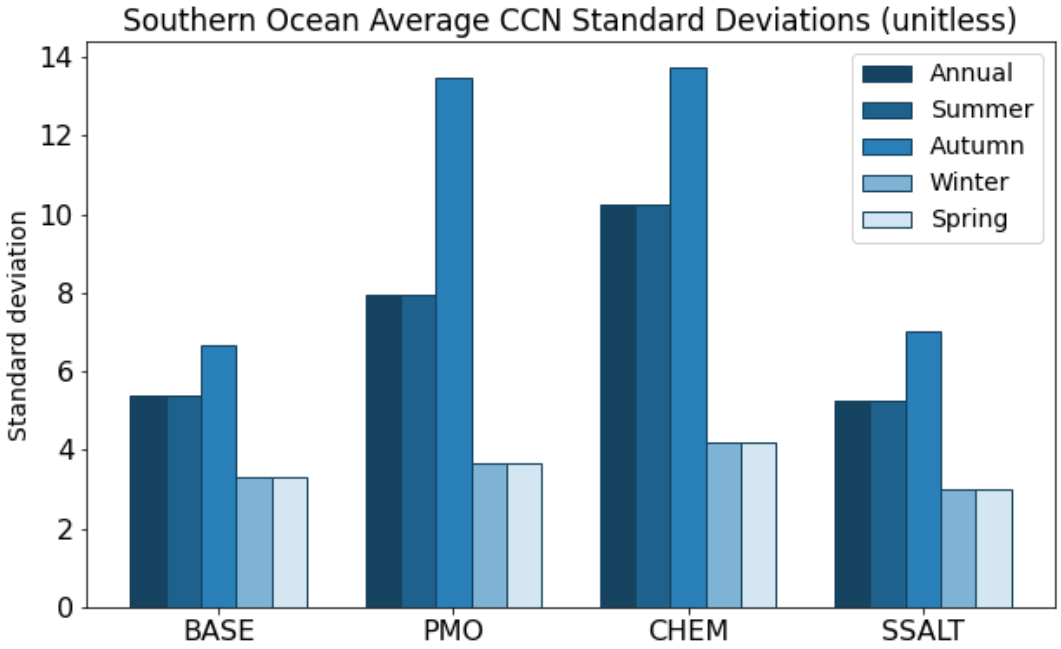


Figure 74: Average Southern Ocean Standard Deviations of simulated and observed CCN (showing inter-annual variability) grouped by season.

A.15 CDNC, Radiation & Low Cloud Fraction

A.15.1 Seasonal simulated CDNC statistical comparisons

Summer CDNC	BASE	PMO-BASE	CHEM-BASE	SSALT-BASE
Mean	44.8	69.3	50.1	41.4
Mean difference (%)		24.5 (55.3%)	5.33 (12.0%)	-3.37 (-7.54%)
Correlation		0.210	0.999	1.00
Mean bias		24.5	5.33	-3.37
NMBF		0.548	0.119	-0.0814
RMSE		24.7	5.36	3.37
NMAEF		0.548	0.119	0.0814
IOA		0.00103	0.428	0.697

Table 69: Comparison of summer-time simulated CNDC values between ACCESS-CM2 BASE and perturbation models, averaged over the Southern Ocean from 2016–2018.

Winter CDNC	BASE	PMO-BASE	CHEM-BASE	SSALT-BASE
Mean	23.3	27.6	24.4	17.3
Mean difference (%)		4.33 (18.6%)	1.07 (4.56%)	-5.96 (-25.6%)
Correlation		0.801	0.996	0.979
Mean bias		4.33	1.07	-5.96
NMBF		0.186	0.0459	-0.344
RMSE		4.37	1.14	5.97
NMAEF		0.186	0.0459	0.344
IOA		0.0709	0.570	0.0408

Table 70: Comparison of winter-time simulated CNDC values between ACCESS-CM2 BASE and perturbation models, averaged over the Southern Ocean from 2016–2018.

Autumn CDNC	BASE	PMO-BASE	CHEM-BASE	SSALT-BASE
Mean	31.5	43.4	34.1	26.3
Mean difference (%)		11.9 (36.4%)	2.61 (8.21%)	-5.19 (-17.2%)
Correlation		1.00	1.00	1.00
Mean bias		11.9	2.61	-5.19
NMBF		0.378	0.0829	-0.197
RMSE		12.8	2.67	5.22
NMAEF		0.378	0.0829	0.197
IOA		0.550	0.942	0.808

Table 71: Comparison of autumn-time simulated CNDC values between ACCESS-CM2 BASE and perturbation models, averaged over the Southern Ocean from 2016–2018.

Spring CDNC	BASE	PMO-BASE	CHEM-BASE	SSALT-BASE
Mean	26.4	41.4	30.0	21.6
Mean difference (%)		15.0 (54.8%)	3.53 (13.1%)	-4.83 (-18.5%)
Correlation		0.900	0.981	0.983
Mean bias		15.0	3.53	-4.83
NMBF		0.567	0.133	-0.224
RMSE		17.8	3.73	4.87
NMAEF		0.567	0.133	0.224
IOA		0.204	0.635	0.450

Table 72: Comparison of spring-time simulated CNDC values between ACCESS-CM2 BASE and perturbation models, averaged over the Southern Ocean from 2016–2018.

A.15.2 Seasonal simulated and observed SW TOA ↑ radiation statistical comparisons

Summer SW TOA ↑ Radiation ($W\,m^{-2}$)	CERES-EBAF	BASE-CERES	PMO-CERES	CHEM-CERES	SSALT-CERES
Mean	167	168	174	168	165
Mean difference (%)		0.816 (0.639%)	6.317 (3.90%)	0.945 (0.708%)	-2.498 (-1.34%)
Correlation		1.00	1.00	1.00	1.00
Mean bias		0.816	6.32	0.945	-2.50
NMBF		0.005	0.038	0.006	-0.015
RMSE		2.88	6.55	2.76	3.94
NMAEF		0.0134	0.0378	0.0124	0.0220
IOA		0.987	0.943	0.988	0.976

Table 73: Statistical summary of summer CERES-EBAF observed and simulated SW TOA ↑ radiation over the Southern Ocean, 2016-2018. Model-observation difference have been shaded if they fall within the observational uncertainty (2.5 $\mathrm{W\,m^{-2}}$), see Appendix A.7.

Winter SW TOA ↑ Radiation ($W\,m^{-2}$)	CERES-EBAF	BASE-CERES	PMO-CERES	CHEM-CERES	SSALT-CERES
Mean	47.6	53.6	54.1	53.0	52.1
Mean difference (%)		5.94 (12.4%)	6.49 (13.5%)	5.39 (11.3%)	4.52 (9.37%)
Correlation		1.00	1.00	1.00	1.00
Mean bias		5.94	6.49	5.39	4.52
NMBF		0.125	0.136	0.113	0.095
RMSE		6.18	6.76	5.58	4.71
NMAEF		0.125	0.136	0.113	0.095
IOA		0.943	0.934	0.953	0.965

Table 74: Statistical summary of winter CERES-EBAF observed and simulated SW TOA ↑ radiation over the Southern Ocean, 2016-2018. Model-observation difference have been shaded if they fall within the observational uncertainty (2.5 $\mathrm{W\,m^{-2}}$), see Appendix A.7.

Autumn SW TOA ↑ Radiation ($W\,m^{-2}$)	CERES-EBAF	BASE-CERES	PMO-CERES	CHEM-CERES	SSALT-CERES
Mean	78.5	85.2	87.0	84.5	83.2
Mean difference (%)		6.76 (9.43%)	8.52 (11.53%)	6.07 (8.51%)	4.79 (6.86%)
Correlation		1.000	1.000	1.000	1.000
Mean bias		6.76	8.52	6.07	4.79
NMBF		0.0861	0.1087	0.0774	0.0610
RMSE		6.78	8.63	6.08	4.82
NMAEF		0.0861	0.1087	0.0774	0.0610
IOA		0.983	0.974	0.987	0.991

Table 75: Statistical summary of autumn CERES-EBAF observed and simulated SW TOA ↑ radiation over the Southern Ocean, 2016-2018. Model-observation difference have been shaded if they fall within the observational uncertainty (2.5 $\mathrm{W\,m^{-2}}$), see Appendix A.7.

Spring SW TOA ↑ Radiation ($W\,m^{-2}$)	CERES-EBAF	BASE-CERES	PMO-CERES	CHEM-CERES	SSALT-CERES
Mean	134	138	142	137	134
Mean difference (%)		4.24 (4.13%)	8.60 (7.12%)	3.96 (3.88%)	0.386 (1.20%)
Correlation		1.00	1.00	1.00	1.00
Mean bias		4.24	8.60	3.96	0.39
NMBF		0.0317	0.0644	0.0296	0.00289
RMSE		6.26	8.84	5.94	5.13
NMAEF		0.0395	0.0644	0.0376	0.0321
IOA		0.986	0.975	0.987	0.990

Table 76: Statistical summary of spring CERES-EBAF observed and simulated SW TOA ↑ radiation over the Southern Ocean, 2016-2018. Model-observation difference have been shaded if they fall within the observational uncertainty 2.5 ($\mathrm{W\,m^{-2}}$), see Appendix A.7.

A.15.3 Seasonal simulated Low Cloud Fraction statistical comparisons

Summer Cloud Fraction	BASE	PMO-BASE	CHEM-BASE	SSALT-BASE
Mean	0.770	0.742	0.734	0.733
Mean difference (%)		0.00680 (0.927%)	-0.00159 (-0.215%)	-0.00246 (-0.334%)
Correlation		1.00	1.00	1.00
Mean bias		0.00680	-0.00159	-0.00246
NMBF		0.00925	-0.00216	-0.00335
RMSE		0.00685	0.00170	0.00246
NMAEF		0.00925	0.00216	0.00335
IOA		0.875	0.991	0.984

Table 77: Comparison of summer simulated low cloud fraction between models averaged over the Southern Ocean (40-60°S), 2016-2018.

Winter Cloud Fraction	BASE	PMO-BASE	CHEM-BASE	SSALT-BASE
Mean	0.782	0.787	0.778	0.772
Mean difference (%)		0.00509 (0.651%)	-0.00385 (-0.496%)	-0.00969 (-1.239%)
Correlation		0.997	1.000	0.996
Mean bias		0.00509	-0.00385	-0.00969
NMBF		0.00651	-0.00495	-0.0126
RMSE		0.00515	0.00450	0.00977
NMAEF		0.00651	0.00495	0.01256
IOA		0.928	0.954	0.757

Table 78: Comparison of winter simulated low cloud fraction between models averaged over the Southern Ocean (40-60°S), 2016-2018.

Autumn Cloud Fraction	BASE	PMO-BASE	CHEM-BASE	SSALT-BASE
Mean	0.776	0.782	0.772	0.770
Mean difference (%)		0.00551 (0.709%)	-0.00440 (-0.568%)	-0.00607 (-0.781%)
Correlation		1.000	1.000	0.989
Mean bias		0.00551	-0.00440	-0.00607
NMBF		0.00710	-0.00570	-0.00788
RMSE		0.00552	0.00441	0.00625
NMAEF		0.00710	0.00570	0.00788
IOA		0.911	0.941	0.872

Table 79: Comparison of autumn simulated low cloud fraction between models averaged over the Southern Ocean (40-60°S), 2016-2018.

Spring Cloud Fraction	BASE	PMO-BASE	CHEM-BASE	SSALT-BASE
Mean	0.776	0.786	0.774	0.770
Mean difference (%)		0.00942 (1.22%)	-0.00239 (-0.307%)	-0.00637 (-0.818%)
Correlation		0.999	0.999	0.999
Mean bias		0.00942	-0.00239	-0.00637
NMBF		0.0121	-0.00309	-0.00828
RMSE		0.00963	0.00258	0.00655
NMAEF		0.0121	0.00309	0.00828
IOA		0.917	0.994	0.961

Table 80: Comparison of spring simulated low cloud fraction between models averaged over the Southern Ocean (40-60°S), 2016-2018.

A.15.4 Seasonal simulated and observed Low Cloud Fraction statistical comparisons

Summer Cloud Fraction	CALIPSO-GOCCP	BASE-CALIPSO	PMO-CALIPSO	CHEM-CALIPSO	SSALT-CALIPSO
Mean	0.590	0.770	0.777	0.767	0.764
Mean difference (%)		0.184(40.7%)	0.190(42.1%)	0.180(40.0%)	0.177(39.5%)
Correlation		0.420	0.419	0.422	0.420
Mean bias		0.184	0.190	0.180	0.177
NMBF		0.313	0.324	0.308	0.302
RMSE		0.241	0.246	0.239	0.237
NMAEF		0.349	0.357	0.346	0.342
IOA		0.378	0.365	0.386	0.389

Table 81: Comparison of summer simulated low cloud fraction between CALIPSO-GOCCP and models averaged over the Southern Ocean (40-60°S), 2016. Model-observation difference have been shaded if they fall within the observational temporal variability (0.188), see Appendix A.7.

Winter Cloud Fraction	CALIPSO-GOCCP	BASE-CALIPSO	PMO-CALIPSO	CHEM-CALIPSO	SSALT-CALIPSO
Mean	0.569	0.782	0.787	0.778	0.772
Mean difference (%)		0.213 (44.6%)	0.218 (45.7%)	0.209 (43.8%)	0.203 (42.7%)
Correlation		0.509	0.512	0.511	0.508
Mean bias		0.213	0.218	0.209	0.203
NMBF		0.374	0.383	0.367	0.357
RMSE		0.253	0.256	0.250	0.245
NMAEF		0.387	0.395	0.383	0.374
IOA		0.377	0.368	0.3872	0.395

Table 82: Comparison of winter simulated low cloud fraction between CALIPSO-GOCCP and models averaged over the Southern Ocean (40-60°S), 2016. Model-observation difference have been shaded if they fall within the observational temporal variability (0.186), see Appendix A.7.

Autumn Cloud Fraction	CALIPSO-GOCCP	BASE-CALIPSO	PMO-CALIPSO	CHEM-CALIPSO	SSALT-CALIPSO
Mean	0.590	0.776	0.782	0.772	0.770
Mean difference (%)		0.186 (40.1%)	0.192 (41.2%)	0.182 (39.1%)	0.180 (39.0%)
Correlation		0.478	0.483	0.481	0.479
Mean bias		0.186	0.192	0.182	0.180
NMBF		0.316	0.325	0.308	0.306
RMSE		0.239	0.242	0.235	0.234
NMAEF		0.346	0.352	0.340	0.338
IOA		0.416	0.409	0.4272	0.428

Table 83: Comparison of autumn simulated low cloud fraction between CALIPSO-GOCCP and models averaged over the Southern Ocean (40-60°S), 2016. Model-observation difference have been shaded if they fall within the observational temporal variability (0.196), see Appendix A.7.

Spring Cloud Fraction	CALIPSO-GOCCP	BASE-CALIPSO	PMO-CALIPSO	CHEM-CALIPSO	SSALT-CALIPSO
Mean	0.599	0.776	0.786	0.774	0.770
Mean difference (%)		0.177 (36.9%)	0.187 (38.8%)	0.175 (36.3%)	0.171 (35.7%)
Correlation		0.621	0.622	0.624	0.620
Mean bias		0.177	0.187	0.175	0.171
NMBF		0.296	0.312	0.292	0.285
RMSE		0.221	0.228	0.219	0.217
NMAEF		0.314	0.326	0.311	0.306
IOA		0.539	0.519	0.547	0.552

Table 84: Comparison of spring simulated cloud fraction between CALIPSO-GOCCP and models averaged over the Southern Ocean (40-60°S), 2016. Model-observation difference have been shaded if they fall within the observational temporal variability (0.199), see Appendix A.7.

References

H. Abdul-Razzak and S. J. Ghan. A parameterization of aerosol activation 2. Multiple aerosol types. Journal of Geophysical Research Atmospheres, 105(D5):6837–6844, 3 2000. ISSN 01480227. doi: 10.1029/1999JD901161.

N. L. Abraham, T. Archibald, A, N. Bellouin, O. Boucher, P. Braesicke, A. Bushell, K. Carslaw, B. Collins, M. Dalvi, K. Emmerson, G. Folberth, J. Haywood, C. Johnson, Z. Kipling, H. Macintyre, G. Mann, P. Telford, J. Merikanto, O. Morgenstern, F. O'Connor, C. Ordonez, S. Osprey, K. Pringle, J. Pyle, J. Rae, C. Reddington, N. Savage, D. Spracklen, P. Stier, and R. West. United Model Documentation Paper No. 84: United Kingdom Chemistry and Aerosol (UKCA) Technical Description MetUM Version 8.4. Technical report, Met Office, Exeter, 2016.

J. Alroe. Personal communication, 27/07/2020, 2020.

J. Alroe, L. T. Cravigan, B. Miljevic, G. R. Johnson, P. Selleck, R. S. Humphries, M. D. Keywood, S. D. Chambers, A. G. Williams, and Z. D. Ristovski. Marine productivity and synoptic meteorology drive summer-time variability in Southern Ocean aerosols. Atmospheric Chemistry and Physics, 20(13):8047–8062, 7 2020. ISSN 1680-7324. doi: 10.5194/acp-20-8047-2020. URL `https://www.atmos-chem-phys.net/20/8047/2020/`.

M. O. Andreae and D. Rosenfeld. Aerosol-cloud-precipitation interactions. Part 1. The nature and sources of cloud-active aerosols. Earth-Science Reviews, 89(1-2):13–41, 7 2008. ISSN 00128252. doi: 10.1016/j.earscirev.2008.03.001.

G. Ayers, J. Ivey, and R. Gillet. Coherence between seasonal cy- cles of dimethylsulfide, methanesulfonate, and sulfate in marine air. Nature, 349:404–406, 1991.

G. P. Ayers, J. M. Cainey, R. W. Gillett, and J. P. Ivey. Atmospheric sulphur and cloud condensation nuclei in marine air in the Southern Hemisphere. Philosophical Transactions of the Royal Society B: Biological Sciences, 352(1350):203–211, 1997a. ISSN 09628436. doi: 10.1098/rstb.1997.0015.

P. Ayers, G, M. Cainey, J, W. Gillett, R, S. Saltzman, E, and M. Hooper. Sulfur dioxide and dimethyl sulfide in marine air at Cape Grim, Tasmania. Tellus, 49:292–299, 1997b.

N. Bellouin, G. W. Mann, M. T. Woodhouse, C. Johnson, K. S. Carslaw, and M. Dalvi. Geoscientific Instrumentation Methods and Data Systems Impact of the modal aerosol scheme GLOMAP-mode on aerosol forcing in the Hadley Centre Global Environmental Model. Atmospheric Chemistry and Physics, 13:3027–3044, 2013a.

N. Bellouin, G. W. Mann, M. T. Woodhouse, C. Johnson, K. S. Carslaw, and M. Dalvi. Impact of the modal aerosol scheme GLOMAP-mode on aerosol forcing in the hadley centre global environmental model. Atmospheric Chemistry and Physics, 13:3027–3044, 2013b. doi: 10.5194/acp-13-3027-2013.

F. A. Bender, L. Frey, D. T. McCoy, D. P. Grosvenor, and J. K. Mohrmann. Assessment of aerosol–cloud–radiation correlations in satellite observations, climate models and reanalysis. Climate Dynamics, 52(7-8):4371–4392, 4 2019. ISSN 14320894. doi: 10.1007/s00382-018-4384-z.

A. Benedetti, J.-J. Morcrette, O. Boucher, A. Dethof, R. J. Engelen, M. Fisher, H. Flentje, N. Huneeus, L. Jones, J. W. Kaiser, S. Kinne, A. Mangold, M. Razinger, A. J. Simmons, and M. Suttie. Aerosol analysis and forecast in the European Centre for Medium-Range Weather Forecasts Integrated Forecast System: 2. Data assimilation. Journal of Geophysical Research, 114(D13205), 2009.

D. Bi, M. Dix, S. Marsland, S. O'Farrell, A. Sullivan, R. Bodman, R. Law, I. Harman, J. Srbinovsky, H. Rashid, P. Dobrohotoff, C. Mackallah, H. Yan, A. Hirst, A. Savita, F. Boeira Dias, M. Woodhouse, R. Fielder, and A. Heerdegen. Configuration and spin-up of ACCESS-CM2, the new generation Australian Community Climate and Earth System Simulator Coupled Model. Unpublished manuscript, 2020.

E. K. Bigg, J. L. Gras, and C. Evans. Origin of Aitken Particles in Remote Regions of the Southern Hemisphere. Journal of Atmospheric Chemistry, 1:203–214, 1984.

A. Bodas-Salcedo, M. J. Webb, S. Bony, H. Chepfer, J. L. Dufresne, S. A. Klein, Y. Zhang, R. Marchand, J. M. Haynes, R. Pincus, and V. O. John. COSP: Satellite simulation software for model assessment. Bulletin of the American Meteorological Society, 92(8): 1023–1043, 8 2011. ISSN 00030007. doi: 10.1175/2011BAMS2856.1.

A. Bodas-Salcedo, K. D. Williams, M. A. Ringer, I. Beau, . J. N. S. Cole, J.-L. Dufresne, T. Koshiro, B. Stevens, Z. Wang, and T. Yokohata. Origins of the Solar Radiation Biases over the Southern Ocean in CFMIP2 Models. Journal of Climate, 27:41–56, 2014. doi: 10.1175/JCLI-D-13. URL `http://dx.doi.org/10.1175/JCLI-D-13-`.

A. Bodas-Salcedo, P. G. Hill, K. Furtado, K. D. Williams, P. R. Field, J. C. Manners, P. Hyder, and S. Kato. Large contribution of supercooled liquid clouds to the solar radiation budget of the Southern Ocean. Journal of Climate, 29(11):4213–4228, 6 2016. ISSN 08948755. doi: 10.1175/JCLI-D-15-0564.1.

O. Boucher. Atmospheric Aerosols: Properties and Climate Impacts. Springer, Netherlands, 2015.

K. W. Bowman, D. T. Shindell, H. M. Worden, J. F. Lamarque, P. J. Young, D. S. Stevenson, Z. Qu, M. De La Torre, D. Bergmann, P. J. Cameron-Smith, W. J. Collins, R. Doherty, S. B. Dalsøren, G. Faluvegi, G. Folberth, L. W. Horowitz, B. M. Josse, Y. H. Lee, I. A. MacKenzie, G. Myhre, T. Nagashima, V. Naik, D. A. Plummer, S. T. Rumbold, R. B. Skeie, S. A. Strode, K. Sudo, S. Szopa, A. Voulgarakis, G. Zeng, S. S. Kulawik, A. M. Aghedo, and J. R. Worden. Evaluation of ACCMIP outgoing longwave radiation from tropospheric ozone using TES satellite observations. Atmospheric Chemistry and Physics, 13(8):4057–4072, 4 2013. ISSN 16807324. doi: 10.5194/acp-13-4057-2013.

S. Broccardo and B. Holben. 2015-2016 RV SA Agulhas II Cruise Level 2.0 AOD Measurements, 2019. URL `https://aeronet.gsfc.nasa.gov/new_web/cruises_new/Agulhas_15_16.html`.

D. Carslaw. The openair manual - open-source tools for analysing air pollution data. Manual for version 2.6-6. Technical report, University of York, 2019. URL `https://github.com/davidcarslaw/openair`.

K. S. Carslaw, L. A. Lee, C. L. Reddington, K. J. Pringle, A. Rap, P. M. Forster, G. W. Mann, D. V. Spracklen, M. T. Woodhouse, L. A. Regayre, and J. R. Pierce. Large contribution of natural aerosols to uncertainty in indirect forcing. Nature, (503):67–73, 2013.

S. Chambers, A. Williams, J. Crawford, A. Griffiths, P. Krummel, L. Steele, R. Law, M. van der Schoot, I. Galbally, and B. Molloy, S. A Radon-only technique for characterising atmospheric 'baseline' constitutent concentrations at Cape Grim. Technical report, Baseline Atmospheric Program (Australia) 2011-2013, 2015. URL `https://www.researchgate.net/publication/280028388`.

Y. Chen, O. Wild, Y. Wang, L. Ran, M. Teich, J. Größ, L. Wang, G. Spindler, H. Herrmann, D. van Pinxteren, G. McFiggans, and A. Wiedensohler. The influence of impactor size cut-off shift caused by hygroscopic growth on particulate matter loading and composition measurements. Atmospheric Environment, 195:141–148, 12 2018. ISSN 18732844. doi: 10.1016/j.atmosenv.2018.09.049.

H. Chepfer, S. Bony, D. Winker, G. Cesana, J. L. Dufresne, P. Minnis, C. J. Stubenrauch, and S. Zeng. The GCM-oriented CALIPSO cloud product (CALIPSO-GOCCP). Journal of Geophysical Research Atmospheres, 115(5), 2010. ISSN 01480227. doi: 10.1029/2009JD012251.

P. Colarco, A. Da Silva, M. Chin, and T. Diehl. Online simulations of global aerosol distributions in the NASA GEOS-4 model and comparisons to satellite and ground-

based aerosol optical depth. Journal of Geophysical Research Atmospheres, 115(14), 2010. ISSN 01480227. doi: 10.1029/2009JD012820.

J. W. Collins, J. F. Lamarque, M. Schulz, O. Boucher, V. Eyring, I. M. Hegglin, A. Maycock, G. Myhre, M. Prather, D. Shindell, and J. S. Smith. AerChemMIP: Quantifying the effects of chemistry and aerosols in CMIP6. Geoscientific Model Development, 10 (2), 2017. ISSN 19919603. doi: 10.5194/gmd-10-585-2017.

J. Crawford, D. D. Cohen, E. Stelcer, and A. J. Atanacio. Long term fine aerosols at the Cape Grim global baseline station: 1998 to 2016. Atmospheric Environment, 166: 34–46, 2017.

P. Crippa, D. Spracklen, and S. C. Pryor. Satellite-derived estimates of ultrafine particle concentrations over eastern North America. Journal of Geophysical Research Atmospheres, 118(17):9968–9981, 9 2013. ISSN 21698996. doi: 10.1002/jgrd.50707.

J. Curtius. Nucleation of atmospheric aerosol particles, 11 2006. ISSN 16310705.

M. Dalvi. Unified Model Documentation Paper 083: Nudging the Unified Model. Technical report, Met Office, Exeter, 2015.

D. P. Dee, S. M. Uppala, A. J. Simmons, P. Berrisford, P. Poli, S. Kobayashi, U. Andrae, M. A. Balmaseda, G. Balsamo, P. Bauer, P. Bechtold, A. C. Beljaars, L. van de Berg, J. Bidlot, N. Bormann, C. Delsol, R. Dragani, M. Fuentes, A. J. Geer, L. Haimberger, S. B. Healy, H. Hersbach, E. V. Hólm, L. Isaksen, P. Kållberg, M. Köhler, M. Matricardi, A. P. Mcnally, B. M. Monge-Sanz, J. J. Morcrette, B. K. Park, C. Peubey, P. de Rosnay, C. Tavolato, J. N. Thépaut, and F. Vitart. The ERA-Interim reanalysis: Configuration and performance of the data assimilation system. Quarterly Journal of the Royal Meteorological Society, 137:553–597, 2011.

S. Dhomse, G. Mann, K. Carslaw, J. Flemming, J. Morcrette, R. Engelen, S. Remy, O. Boucher, F. Benduhn, W. Hewson, and M. Woodhouse. Evaluation of aerosol properties simulated by the high resolution global coupled chemistry-aerosol-microphysics model C-IFS-GLOMAP. In EGU GEeneral Assembly Conference Abstracts, Vienna, Austria, 2016.

J. Duplissy, M. Gysel, M. R. Alfarra, J. Dommen, A. Metzger, A. S. Prevot, E. Weingartner, A. Laaksonen, T. Raatikainen, N. Good, S. F. Turner, G. McFiggans, and U. Baltensperger. Cloud forming potential of secondary organic aerosol under near atmospheric conditions. Geophysical Research Letters, 35(3), 2 2008. ISSN 00948276. doi: 10.1029/2007GL031075.

S. Elliott. Dependence of DMS global sea-air flux distribution on transfer velocity and concentration field type. Journal of Geophysical Research: Biogeosciences, 114(2), 6 2009. ISSN 01480227. doi: 10.1029/2008JG000710.

T. Fan and O. B. Toon. Modeling sea-salt aerosol in a coupled climate and sectional microphysical model: Mass, optical depth and number concentration. Atmospheric Chemistry and Physics, 11(9):4587–4610, 2011. ISSN 16807316. doi: 10.5194/acp-11-4587-2011.

T. Fan, C. Zhao, X. Dong, X. Liu, X. Yang, F. Zhang, C. Shi, Y. Wang, and F. Wu. Quantify contribution of aerosol errors to cloud fraction biases in CMIP5 Atmospheric Model Intercomparison Project simulations. International Journal of Climatology, 38 (7):3140–3156, 6 2018. ISSN 10970088. doi: 10.1002/joc.5490.

G. S. Fanourgakis, M. Kanakidou, A. Nenes, S. E. Bauer, T. Bergman, K. S. Carslaw, A. Grini, D. S. Hamilton, J. S. Johnson, V. A. Karydis, A. Kirkeväg, J. K. Kodros, U. Lohmann, G. Luo, R. Makkonen, H. Matsui, D. Neubauer, J. R. Pierce, J. Schmale, P. Stier, K. Tsigaridis, T. Van Noije, H. Wang, D. Watson-Parris, D. M. Westervelt, Y. Yang, M. Yoshioka, N. Daskalakis, S. Decesari, M. Gysel-Beer, N. Kalivitis, X. Liu, N. M. Mahowald, S. Myriokefalitakis, R. Schrödner, M. Sfakianaki, A. P. Tsimpidi, M. Wu, and F. Yu. Evaluation of global simulations of aerosol particle and cloud condensation nuclei number, with implications for cloud droplet formation. Atmospheric Chemistry and Physics, 19(13):8591–8617, 7 2019. ISSN 16807324. doi: 10.5194/acp-19-8591-2019.

G. Flato, J. Marotzke, B. Abiodun, P. Braconnot, C. Chou, S, W. Collins, P. Cox, F. Driouech, S. Emori, V. Eyring, C. Forest, P. Gleckler, E. Guilyardi, C. Jakob, V. Kattsov, C. Reason, and M. Rummukainen. Evaluation of Climate Models. In: Climate Change 2013: The Physical Science Basis. Contribution of Working Group I to the Fifth Assessment Report of the Intergovernmental Panel on Climate Change. Technical report, Cambridge, United Kingdom and New York, NY,USA, 2013.

S. D. Forestieri, K. A. Moore, R. Martinez Borrero, A. Wang, M. D. Stokes, and C. D. Cappa. Temperature and Composition Dependence of Sea Spray Aerosol Production. Geophysical Research Letters, 45(14):7218–7225, 7 2018. ISSN 19448007. doi: 10.1029/2018GL078193.

B. Forgan. General method for calibrating Sun photometers. Applied Optics, 33(21): 4841–4850, 1994.

K. N. Fossum, J. Ovadnevaite, D. Ceburnis, M. Dall'Osto, S. Marullo, M. Bellacicco, R. Simó, D. Liu, M. Flynn, A. Zuend, and C. O'Dowd. Summertime Primary and

Secondary Contributions to Southern Ocean Cloud Condensation Nuclei. Scientific Reports, 8(1), 12 2018. ISSN 20452322. doi: 10.1038/s41598-018-32047-4.

R. Fröhlich, M. J. Cubison, J. G. Slowik, N. Bukowiecki, A. S. Prévôt, U. Baltensperger, J. Schneider, J. R. Kimmel, M. Gonin, U. Rohner, D. R. Worsnop, and J. T. Jayne. The ToF-ACSM: A portable aerosol chemical speciation monitor with TOFMS detection. Atmospheric Measurement Techniques, 6(11):3225–3241, 11 2013. ISSN 18671381. doi: 10.5194/amt-6-3225-2013.

A. A. Frossard, L. M. Russell, S. M. Burrows, S. M. Elliott, T. S. Bates, and P. K. Quinn. Sources and composition of submicron organic mass in marine aerosol particles. Journal of Geophysical Research Atmospheres, 119(22):977–13, 11 2014. ISSN 21698996. doi: 10.1002/2014JD021913.

B. Gantt and N. Meskhidze. The physical and chemical characteristics of marine primary organic aerosol: A review. Atmospheric Chemistry and Physics, 13(8):3979–3996, 4 2013. ISSN 16807324. doi: 10.5194/acp-13-3979-2013.

B. Gantt, M. S. Johnson, N. Meskhidze, J. Sciare, J. Ovadnevaite, D. Ceburnis, and C. D. O'Dowd. Model evaluation of marine primary organic aerosol emission schemes. Atmospheric Chemistry and Physics, 12(18):8553–8566, 2012a. ISSN 16807316. doi: 10.5194/acp-12-8553-2012.

B. Gantt, J. Xu, N. Meskhidze, Y. Zhang, A. Nenes, S. J. Ghan, X. Liu, R. Easter, and R. Zaveri. Global distribution and climate forcing of marine organic aerosol-Part 2: Effects on cloud properties and radiative forcing. Atmospheric Chemistry and Physics, 12(14):6555–6563, 2012b. ISSN 16807316. doi: 10.5194/acp-12-6555-2012.

D. Giles. Aerosol Optical Depth - Direct Sun Measurements. SDA Retrieval Quality Levels. . URL `https://aeronet.gsfc.nasa.gov/new_web/aot_levels_versions.html#Versions`.

D. Giles. AERONET Version 2 Direct Sun Algorithm. Technical Report 4, 2 2017. URL `Accessedfrom:https://aeronet.gsfc.nasa.gov/new_web/man_data.htmlhttps://aeronet.gsfc.nasa.gov/new_web/Documents/version2_table.pdf`.

D. M. Giles, A. Sinyuk, M. G. Sorokin, J. S. Schafer, A. Smirnov, I. Slutsker, T. F. Eck, B. N. Holben, J. R. Lewis, J. R. Campbell, E. J. Welton, S. V. Korkin, and A. I. Lyapustin. Advancements in the Aerosol Robotic Network (AERONET) Version 3 database - Automated near-real-time quality control algorithm with improved cloud screening for Sun photometer aerosol optical depth (AOD) measurements.

Atmospheric Measurement Techniques, 12(1):169–209, 1 2019. ISSN 18678548. doi: 10.5194/amt-12-169-2019.

J. Gliß, A. Mortier, M. Schulz, E. Andrews, Y. Balkanski, S. Bauer, A. Benedictow, H. Bian, R. Checa-Garcia, M. Chin, P. Ginoux, J. Griesfeller, A. Heckel, Z. Kipling, A. Kirkevåg, H. Kokkola, P. Laj, P. Le Sager, M. T. Lund, C. Lund Myhre, H. Matsui, G. Myhre, D. Neubauer, T. van Noije, P. North, D. Olivié, L. Sogacheva, T. Takemura, K. Tsigaridis, and S. Tsyro. Multi-model evaluation of aerosol optical properties in the AeroCom phase III Control experiment, using ground and space based columnar observations from AERONET, MODIS, AATSR and a merged satellite product as well as surface in-situ observations from GAW sites. Atmospheric Chemistry and Physics, pages 1–62, 2020. ISSN 1680-7316. doi: 10.5194/acp-2019-1214.

P. Goloub. Amsterdam Island AERONET Aerosol Optical Depth (AOD), 2019. URL `https://aeronet.gsfc.nasa.gov/cgi-bin/webtool_aod_v3?stage=3&region=Indian_Ocean&state=Amsterdam_Island&site=Amsterdam_Island&place_code=10&if_polarized=0`.

S. L. Gong. A parameterization of sea-salt aerosol source function for sub- and super-micron particles. Global Biogeochemical Cycles, 17(4):n/a–n/a, 12 2003. ISSN 0886-6236. doi: 10.1029/2003gb002079.

L. J. Gras and M. Keywood. Cloud condensation nuclei over the Southern Ocean: Wind dependence and seasonal cycles. Atmospheric Chemistry and Physics, 17(7):4419–4432, 4 2017. ISSN 16807324. doi: 10.5194/acp-17-4419-2017.

C. A. Gueymard and D. Yang. Worldwide validation of CAMS and MERRA-2 reanalysis aerosol optical depth products using 15 years of AERONET observations. Atmospheric Environment, 225, 3 2020. ISSN 18732844. doi: 10.1016/j.atmosenv.2019.117216.

R. Guzman, H. Chepfer, V. Noel, T. Vaillant De Guélis, J. E. Kay, P. Raberanto, G. Cesana, M. A. Vaughan, and D. M. Winker. Direct atmosphere opacity observations from CALIPSO provide new constraints on cloud-radiation interactions. Journal of Geophysical Research: Atmospheres, 122:1066–1085, 2017.

L. Harrison and J. Michalsky. Objective algorithms for the retrieval of optical depths from ground-based measurements. Applied Optics, 33(22):5126–5132, 1994.

S. Hartery, D. Toohey, L. Revell, K. Sellegri, P. Kuma, M. Harvey, and A. J. McDonald. Constraining the Surface Flux of Sea Spray Particles From the Southern Ocean. Journal of Geophysical Research: Atmospheres, 125(4), 2 2020. ISSN 21698996. doi: 10.1029/2019JD032026.

M. Harvey and B. Holben. 2018 RV Tangaroa Cruise Level 2.0 AOD Measurements, 2019. URL https://aeronet.gsfc.nasa.gov/new_web/cruises_new/Tangaroa_18_0.html.

M. Hawcroft, J. M. Haywood, M. Collins, A. Jones, A. C. Jones, and G. Stephens. Southern Ocean albedo, inter-hemispheric energy transports and the double ITCZ: global impacts of biases in a coupled model. Climate Dynamics, 48:2279–2295, 2017.

G. D. Hayman, F. M. O'Connor, M. Dalvi, D. B. Clark, N. Gedney, C. Huntingford, C. Prigent, M. Buchwitz, O. Schneising, J. P. Burrows, C. Wilson, N. Richards, and M. Chipperfield. Comparison of the HadGEM2 climate-chemistry model against in situ and SCIAMACHY atmospheric methane data. Atmospheric Chemistry and Physics, 14(23):13257–13280, 12 2014. ISSN 16807324. doi: 10.5194/acp-14-13257-2014.

M. He, Y. Hu, J. P. Huang, K. Stamnes, . Y. Hu, K. Stamnes, M. Vaughan, J. Pelon, C. Weimer, D. Wu, M. Cisewski, W. Sun, P. Yang, B. Lin, A. Omar, D. Flittner, C. Hostetler, C. Trepte, D. Winker, G. Gibson, M. Santa-Maria, . A. H. Omar, D. M. Winker, M. A. Vaughan, Y. Hu, C. R. Trepte, R. A. Ferrare, K.-P. Lee, C. A. Hostetler, C. Kittaka, R. R. Rogers, R. E. Kuehn, and Z. Liu. Aerosol optical depth under clear sky conditions derived from sea surface reflection of lidar signals. Optics Express, 24 (26), 2016.

J. Heintzenberg, D. Covert, and R. Van Dingenen. Size distribu- tion and chemical composition ofmarine aerosols: a compilation and review. Tellus B: Chemical and Physical Meteorology, 52(4):1104–1122, 2000. doi: 10.3402/tellusb.v52i4.17090.

H. T. Hewitt, D. Copsey, I. D. Culverwell, C. M. Harris, R. S. Hill, A. B. Keen, A. J. McLaren, and E. C. Hunke. Design and implementation of the infrastructure of HadGEM3: The next-generation Met Office climate modelling system. Geoscientific Model Development, 4(2):223–253, 2011. ISSN 1991959X. doi: 10.5194/gmd-4-223-2011.

T. Hirst, D. Bi, H. Yan, S. Marsland, M. Dix, and A. Sullivan. The ACCESS-CM2 coupled climate model – status and plans including contribution to CMIP6. In Conference Abstract, Greenhouse, 27-30 October, Hobart, 2015. CSIRO. URL http://hdl.handle.net/102.100.100/91600?index=1.

B. Holben. 2016 HMNZS Wellington Cruise Level 2.0 AOD Measurements, 2019a. URL https://aeronet.gsfc.nasa.gov/new_web/cruises_new/HMNZS_16_2.html.

B. Holben. Macquarie Island AERONET Aerosol Optical Depth (AOD), 2019b. URL https://aeronet.gsfc.nasa.gov/cgi-bin/webtool_aod_v3?stage=3&region=

Australia_and_Pacific&state=Australia&site=ARM_Macquarie_Is&place_code=10&if_polarized=0.

B. Holben and V. Radionov. 2016-2017 RV Akademic Fedorov Cruise Level 2.0 AOD Measurements, 2019a. URL https://aeronet.gsfc.nasa.gov/new_web/cruises_new/Ak_Fedorov_16_17.html.

B. Holben and V. Radionov. 2017-2018 RV Akademic Fedorov Cruise Level 2.0 AOD Measurements, 2019b. URL https://aeronet.gsfc.nasa.gov/new_web/cruises_new/Ak_Fedorov_17_18.html.

B. Holben and V. Radionov. 2018-2019 RV Akademic Fedorov Cruise Level 2.0 AOD Measurements, 2019c. URL https://aeronet.gsfc.nasa.gov/new_web/cruises_new/Ak_Fedorov_18_19.html.

B. Holben and V. Radionov. 2018 RV Akademic Treshnikov Cruise Level 2.0 AOD Measurements, 2019d. URL https://aeronet.gsfc.nasa.gov/new_web/cruises_new/Ak_Treshnikov_18_0.html.

B. Holben and R. Schofield. 2018-2019 RV Aurora Australis Cruise Level 2.0 AOD Measurements, 2019a. URL https://aeronet.gsfc.nasa.gov/new_web/cruises_new/Aur_Australis_18_1.html.

B. N. Holben, T. F. Eck, I. Slutsker, D. Tanré, J. P. Buis, A. Setzer, E. Vermote, J. A. Reagan, Y. J. Kaufman, T. Nakajima, F. Lavenu, I. Jankowiak, and A. Smirnov. AERONET-A Federated Instrument Network and Data Archive for Aerosol Characterization tion of a new Sun-sky scanning radiometer system that. Technical report, 1998. URL http://spamer.gsfc.nasa.gov.

B. N. Holben, D. Tanré, A. Smirnov, T. F. Eck, I. Slutsker, N. Abuhassan, W. W. Newcomb, J. S. Schafer, B. Chatenet, F. Lavenu, Y. J. Kaufman, J. Vande Castle, A. Setzer, B. Markham, D. Clark, R. Frouin, R. Halthore, A. Karneli, N. T. O'Neill, C. Pietras, R. T. Pinker, K. Voss, and G. Zibordi. An emerging ground-based aerosol climatology: Aerosol optical depth from AERONET. Journal of Geophysical Research Atmospheres, 106(D11):12067–12097, 6 2001. ISSN 01480227. doi: 10.1029/2001JD900014.

R. Holben and R. Schofield. 2018 RV Aurora Australis Cruise Level 2.0 AOD Measurements, 2019b. URL https://aeronet.gsfc.nasa.gov/new_web/cruises_new/Aur_Australis_18_0.html.

L. Hu, C. A. Keller, M. S. Long, T. Sherwen, B. Auer, A. Da Silva, J. E. Nielsen, S. Pawson, M. A. Thompson, A. L. Trayanov, K. R. Travis, S. K. Grange, M. J. Evans,

and D. J. Jacob. Global simulation of tropospheric chemistry at 12.5 km resolution: Performance and evaluation of the GEOS-Chem chemical module (v10-1) within the NASA GEOS Earth system model (GEOS-5 ESM). Geoscientific Model Development, 11(11):4603–4620, 11 2018. ISSN 19919603. doi: 10.5194/gmd-11-4603-2018.

R. Humphries. Personal communication, 19/06/2019, 2019.

R. Humphries. Personal Communication, 18/05/2020, 2020.

R. Humphries and B. Holben. 2017 RV Investigator Cruise Level 2.0 AOD Measurements, 2019a. URL `https://aeronet.gsfc.nasa.gov/new_web/cruises_new/Investigator_17_0.html`.

R. Humphries and B. Holben. 2018 RV Investigator Cruise Level 2.0 AOD Measurements, 2019b. URL `https://aeronet.gsfc.nasa.gov/new_web/cruises_new/Investigator_18_0.html`.

R. S. Humphries, I. M. McRobert, W. A. Ponsonby, J. P. Ward, M. D. Keywood, Z. M. Loh, P. B. Krummel, and J. Harnwell. Identification of platform exhaust on the RV Investigator. Atmospheric Measurement Techniques, 12(6):3019–3038, 6 2019. ISSN 18678548. doi: 10.5194/amt-12-3019-2019.

P. Hyder, J. M. Edwards, R. P. Allan, H. T. Hewitt, T. J. Bracegirdle, J. M. Gregory, R. A. Wood, A. J. Meijers, J. Mulcahy, P. Field, K. Furtado, A. Bodas-Salcedo, K. D. Williams, D. Copsey, S. A. Josey, C. Liu, C. D. Roberts, C. Sanchez, J. Ridley, L. Thorpe, S. C. Hardiman, M. Mayer, D. I. Berry, and S. E. Belcher. Critical Southern Ocean climate model biases traced to atmospheric model cloud errors. Nature Communications, 9(1), 12 2018. ISSN 20411723. doi: 10.1038/s41467-018-05634-2.

A. Inness, F. Baier, A. Benedetti, I. Bouarar, S. Chabrillat, H. Clark, C. Clerbaux, P. Coheur, R. J. Engelen, Q. Errera, J. Flemming, M. George, C. Granier, J. Hadji-Lazaro, V. Huijnen, D. Hurtmans, L. Jones, J. W. Kaiser, J. Kapsomenakis, K. Lefever, J. Leitão, M. Razinger, A. Richter, M. G. Schultz, A. J. Simmons, M. Suttie, O. Stein, J.-N. Thépaut, V. Thouret, M. Vrekoussis, and C. Zerefos. The MACC reanalysis: An 8-year data set of atmospheric composition. Technical report, 2012. URL `http://www.ecmwf.int/publications/`.

IUPAC. Evaluated Kinetic Data International Union of Pure and Applied Chemistry, 2006. URL `http://www.iupac-kineti.ch.cam.ac.uk/index.html`.

M. Jacobson. Fundamentals of Atmospheric Modeling. Cambridge University Press, Cambridge, 2 edition, 2005. doi: doi:10.1017/CBO9781139165389.

L. Jaeglé, P. K. Quinn, T. S. Bates, B. Alexander, and J.-T. Lin. Global distribution of sea salt aerosols: new constraints from in situ and remote sensing observations. Atmospheric Chemistry and Physics, 11:3137–3157, 2011a.

L. Jaeglé, P. K. Quinn, T. S. Bates, B. Alexander, and J.-T. Lin. Global distribution of sea salt aerosols: new constraints from in situ and remote sensing observations. Atmospheric Chemistry and Physics, 11:3137–3157, 2011b.

B. Jourdain and M. Legrand. Seasonal variations of atmospheric dimethylsulfide, dimethylsulfoxide, sulfur dioxide, methanesulfonate, and non-sea-salt sulfate aerosols at Dumont d'Urville (coastal Antarctica) (December 1998 to July 1999). Journal of Geophysical Research, 106:14391–14408, 2001.

M. Keywood. Personal Communication, 24/01/2019, 2019.

Z. Kipling, P. Stier, C. E. Johnson, G. W. Mann, N. Bellouin, S. E. Bauer, T. Bergman, M. Chin, T. Diehl, S. J. Ghan, T. Iversen, A. Kirkevåg, H. Kokkola, X. Liu, G. Luo, T. Van Noije, K. J. Pringle, K. Von Salzen, M. Schulz, Seland, R. B. Skeie, T. Takemura, K. Tsigaridis, and K. Zhang. What controls the vertical distribution of aerosol? Relationships between process sensitivity in HadGEM3-UKCA and inter-model variation from AeroCom Phase II. Atmospheric Chemistry and Physics, 2016. ISSN 16807324. doi: 10.5194/acp-16-2221-2016.

I. Koren, O. Altaratz, and G. Dagan. Aerosol effect on the mobility of cloud droplets. Environmental Research Letters, 10(104011), 2015.

H. Korhonen, K. S. Carslaw, D. V. Spracklen, G. W. Mann, and M. T. Woodhouse. Influence of oceanic dimethyl sulfide emissions on cloud condensation nuclei concentrations and seasonality over the remote Southern Hemisphere oceans: A global model study. Journal of Geophysical Research Atmospheres, 113(15), 2008. ISSN 01480227. doi: 10.1029/2007JD009718.

E. A. Kowalczyk, L. Stevens, R. M. Law, M. Dix, Y. P. Wang, I. N. Harman, K. Haynes, J. Srbinovsky, B. Pak, and T. Ziehn. The land surface model component of ACCESS: description and impact on the simulated surface climatology. Technical report, 2013. URL `http://lis.gsfc.nasa.gov/`.

S. M. Kreidenwies, C. J. Walcek, G. Feingold, W. Gong, M. Z. Jacobson, C. H. Kim, X. Liu, J. E. Penner, A. Nenes, and J. H. Seinfeld. Modification of aerosol mass and size distribution due to aqueous-phase SO2 oxidation in clouds: Comparisons of several models. Journal of Geophysical Research D: Atmospheres, 108(7), 4 2003. ISSN 01480227. doi: 10.1029/2002jd002697.

P. Kuma, A. J. McDonald, O. Morgenstern, S. P. Alexander, J. J. Cassano, S. Garrett, J. Halla, S. Hartery, M. J. Harvey, S. Parsons, G. Plank, V. Varma, and J. Williams. Evaluation of Southern Ocean cloud in the HadGEM3 general circulation model and MERRA-2 reanalysis using ship-based observations. Atmospheric Chemistry and Physics Discussions, pages 1–37, 4 2019. ISSN 1680-7375. doi: 10.5194/acp-2019-201.

J. F. Lamarque, D. T. Shindell, B. Josse, P. J. Young, I. Cionni, V. Eyring, D. Bergmann, P. Cameron-Smith, W. J. Collins, R. Doherty, S. Dalsoren, G. Faluvegi, G. Folberth, S. J. Ghan, L. W. Horowitz, Y. H. Lee, I. A. MacKenzie, T. Nagashima, V. Naik, D. Plummer, M. Righi, S. T. Rumbold, M. Schulz, R. B. Skeie, D. S. Stevenson, S. Strode, K. Sudo, S. Szopa, A. Voulgarakis, and G. Zeng. The atmospheric chemistry and climate model intercomparison Project (ACCMIP): Overview and description of models, simulations and climate diagnostics. Geoscientific Model Development, 6(1): 179–206, 2013. ISSN 1991959X. doi: 10.5194/gmd-6-179-2013.

C. S. Law, M. J. Smith, M. J. Harvey, T. G. Bell, L. T. Cravigan, F. C. Elliott, S. J. Lawson, M. Lizotte, A. Marriner, J. Mcgregor, Z. Ristovski, K. A. Safi, E. S. Saltzman, P. Vaattovaara, and C. F. Walker. Overview and preliminary results of the Surface Ocean Aerosol Production (SOAP) campaign. Atmospheric Chemistry and Physics, 17:13645–13667, 2017.

L. A. Lee, K. S. Carslaw, K. J. Pringle, and G. W. Mann. Mapping the uncertainty in global CCN using emulation. Atmospheric Chemistry and Physics, 12(20):9739–9751, 2012. ISSN 16807316. doi: 10.5194/acp-12-9739-2012.

L. A. Lee, K. J. Pringle, C. L. Reddington, G. W. Mann, P. Stier, D. V. Spracklen, J. R. Pierce, and K. S. Carslaw. The magnitude and causes of uncertainty in global model simulations of cloud condensation nuclei. Atmospheric Chemistry and Physics, 13(17): 8879–8914, 2013. ISSN 16807316. doi: 10.5194/acp-13-8879-2013.

R. C. Levy, S. Mattoo, L. A. Munchak, L. A. Remer, A. M. Sayer, F. Patadia, and N. C. Hsu. The Collection 6 MODIS aerosol products over land and ocean. Atmospheric Measurement Techniques, 6(11):2989–3034, 2013. ISSN 18671381. doi: 10.5194/amt-6-2989-2013.

S. S. Lewis, E. Sea Salt Aerosol Production: Mechanisms, Methods, Measurements and Models - A Critical Review. Washington DC American Geophysical Union Geophysical Monograph Series, 152:1–413, 2004.

J. L. Li, D. E. Waliser, G. Stephens, S. Lee, T. L'Ecuyer, S. Kato, N. Loeb, and H. Y. Ma. Characterizing and understanding radiation budget biases in CMIP3/CMIP5 GCMs,

contemporary GCM, and reanalysis. Journal of Geophysical Research Atmospheres, 118:8166–8184, 2013.

N. Liou, K. Application of Radiative Transfer Principles to Remote Sensing. In An Introduction to Atmospheric Radiation, chapter 7, pages 348–434. Elsevier Science, San Diego, London, 2 edition, 2002. ISBN 0-12-451451-0.

N. G. Loeb, D. R. Doelling, H. Wang, W. Su, C. Nguyen, J. G. Corbett, L. Liang, C. Mitrescu, F. G. Rose, and S. Kato. Clouds and the Earth'S Radiant Energy System (CERES) Energy Balanced and Filled (EBAF) top-of-atmosphere (TOA) edition-4.0 data product. Journal of Climate, 31(2):895–918, 1 2018. ISSN 08948755. doi: 10.1175/JCLI-D-17-0208.1.

M. S. Long, W. C. Keene, D. J. Kieber, D. J. Erickson, and H. Maring. A sea-state based source function for size- and composition-resolved marine aerosol production. Atmospheric Chemistry and Physics, 11(3):1203–1216, 2011. ISSN 16807316. doi: 10.5194/acp-11-1203-2011.

S. J. Lowe, D. G. Partridge, J. F. Davies, K. R. Wilson, D. Topping, and I. Riipinen. Key drivers of cloud response to surface-active organics. Nature Communications, 10(1), 12 2019. ISSN 20411723. doi: 10.1038/s41467-019-12982-0.

W. L. Madry, O. B. Toon, and C. D. O'Dowd. Modeled optical thickness of sea-salt aerosol. Journal of Geophysical Research Atmospheres, 116(8), 2011. ISSN 01480227. doi: 10.1029/2010JD014691.

C. Malm, W, A. Schichtel, B, B. Ames, R, and A. Gebhart, K. A 10-year spatial and temporal trend of sulfate across the United States. Journal of Geophysical Research, 107(D22)(4627), 2002. doi: 10.1029/2002JD002107.

G. Mann. UKCA Chemistry and Aerosol Tutorial 10, 2014. URL `http://www.ukca.ac.uk/wiki/index.php/UKCA_Chemistry_and_Aerosol_Tutorial_10`.

G. W. Mann, K. S. Carslaw, D. V. Spracklen, D. A. Ridley, P. T. Manktelow, M. P. Chipperfield, S. J. Pickering, and C. E. Johnson. Geoscientific Model Development Description and evaluation of GLOMAP-mode: a modal global aerosol microphysics model for the UKCA composition-climate model. Geoscientific Model Development, 3: 519–551, 2010.

R. Marchand, R. Wood, C. Bretherton, G. Mcfarquhar, A. Protat, S. Siems, C. Jakob, S. Alexander, S. Ghan, C. Hostetler, G. De Boer, J. Mace, P. Kollias, R. Moore,

T. Wilson, D. Hartmann, J. Jensen, J. Kay, L. Russell, J. Scheff, E. Maroon, S. Burrows, S. Tucker, J. Stith, J. Hudson, J. Russell, Y. Feng, P. Demott, T. Lachlan-cope, P. Ceppi, D. Grosvenor, D. Mccoy, N. Meskhidze, C. Fairall, S. Gille, T. Bates, C. Gaston, E. Dolinar, R. Stanfield, K. Williams, A. Bodas-salcedo, B. Rauber, M. Harvey, A. Clarke, M. Orellana, A. Muhlbauer, L. Polvani, Y. Hu, S. Collis, A. G. Hallar, Y. Li, A. J. Mcdonald, K. Furtado, G. Roberts, A. Fridlind, A. Ackerman, C. Clayson, and B. Hillman. The Southern Ocean Clouds, Radiation, Aerosol Transport Experimental Study. Technical report, University of Washington, 2014.

J. V. Martins, D. Tanré, L. Remer, Y. Kaufman, S. Mattoo, and R. Levy. MODIS Cloud screening for remote sensing of aerosols over oceans using spatial variability. Geophysical Research Letters, 29(12), 2002.

S. Mason, J. K. Fletcher, J. M. Haynes, C. Franklin, A. Protat, and C. Jakob. A hybrid cloud regime methodology used to evaluate Southern Ocean cloud and shortwave radiation errors in ACCESS. Journal of Climate, 28(15):6001–6018, 2015. ISSN 08948755. doi: 10.1175/JCLI-D-14-00846.1.

D. T. Mccoy, S. M. Burrows, R. Wood, D. P. Grosvenor, S. M. Elliott, P.-L. Ma, P. J. Rasch, and D. L. Hartmann. Natural aerosols explain seasonal and spatial patterns of Southern Ocean cloud albedo. Science Advances, 1:1–12, 2015a.

D. T. Mccoy, S. M. Burrows, R. Wood, D. P. Grosvenor, S. M. Elliott, P.-L. Ma, P. J. Rasch, and D. L. Hartmann. Natural aerosols explain seasonal and spatial patterns of Southern Ocean cloud albedo. Science Advances, 1:1–12, 2015b.

G. McFarquhar. Measurements of Aerosols, Radiation, and Clouds over the Southern Ocean (MARCUS) Science Plan. U.S Department of Energy, Atmospheric Radiation Measurement Climate Research Facility, pages 1–49, 2016.

J. Merikanto, D. V. Spracklen, G. W. Mann, S. J. Pickering, and K. S. Carslaw. Atmospheric Chemistry and Physics Impact of nucleation on global CCN. Technical report, 2009. URL `www.atmos-chem-phys.net/9/8601/2009/`.

N. Meskhidze, J. Xu, B. Gantt, Y. Zhang, A. Nenes, S. J. Ghan, X. Liu, R. Easter, and R. Zaveri. Global distribution and climate forcing of marine organic aerosol: 1. Model improvements and evaluation. Atmospheric Chemistry and Physics, 11(22): 11689–11705, 2011. ISSN 16807316. doi: 10.5194/acp-11-11689-2011.

A. M. Middlebrook, D. M. Murphy, and D. S. Thomson. Observations of organic material in individual marine particles at Cape Grim during the First Aerosol Characterization

Experiment (ACE 1). Journal of Geophysical Research Atmospheres, 103(D13):16475–16483, 7 1998. ISSN 01480227. doi: 10.1029/97JD03719.

A. K. Mishra, I. Koren, and Y. Rudich. Effect of aerosol vertical distribution on aerosol-radiation interaction: A theoretical prospect. Heliyon, 1(2), 11 2015. ISSN 24058440. doi: 10.1016/j.heliyon.2015.e00036.

A. Misra, V. P. Kanawade, and S. N. Tripathi. Quantitative assessment of AOD from 17 CMIP5 models based on satellite-derived AOD over India. Annales Geophysicae, 34 (8):657–671, 8 2016. ISSN 14320576. doi: 10.5194/angeo-34-657-2016.

C. J. Morcrette. Improvements to a prognostic cloud scheme through changes to its cloud erosion parametrization. Atmospheric Science Letters, 13(2):95–102, 4 2012. ISSN 1530261X. doi: 10.1002/asl.374.

J. Morcrette, O. Boucher, L. Jones, D. Salmond, P. Bechtold, A. Beljaars, A. Benedetti, A. Bonet, W. Kaiser, J, M. Razinger, M. Schulz, S. Serrar, A. J. Simmons, M. Sofiev, M. Suttie, M. Tompkins, A, and A. Untch. Aerosol analysis and forecast in the European Centre for Medium-Range Weather Forecasts Integrated Forecast System: 3. Evaluation by means of case studies. Journal of Geophysical Research Atmospheres, 114(D06206), 2011.

O. Morgenstern, P. Braesicke, F. M. O 'connor, A. C. Bushell, C. E. Johnson, S. M. Osprey, and J. A. Pyle. Evaluation of the new UKCA climate-composition model – Part 1: The stratosphere. Geoscientific Model Development, 2:43–57, 2009.

M. Murphy, D, R. Anderson, J, K. Quinn, P, M. McInnes, L, M. Brechtelk, F, M. Kreidenweisk, S, M. Middlebrook, A, M. Posfai, S. Thomson, D, and R. Buseck, P. Influence of sea-salt on aerosol radiative properties in the Southern Ocean marine boundary layer. Nature, 392:62–65, 1998. doi: https://doi.org/10.1038/32138.

G. Myhre, D. Shindell, M. Bréon, F, W. Collins, J. Fuglestvedt, J. Huang, D. Koch, F. Lamarque, J, D. Lee, B. Mendoza, T. Nakajima, A. Robock, G. Stephens, T. Takemura, and Z. Zhang. Anthropogenic and Natural Radiative Forc-ing. In: Climate Change 2013: The Physical Science Basis. Contribution of Working Group I. In D. Q. G.-K. P. M. T. S. A. Stocker, T.F., Y. X. V. B. J. Boschung, A. Nauels, and P. Midgley, editors, Anthropogenic and Natural Radiative Forcing: Climate Change 2013: The Physical Science Basis. Contribution of Working Group I to the Fifth Assessment Report of the Intergovernmental Panel on Climate Change, chapter 8, pages 659–740. Cambridge University Press, Cambridge, United Kingdom and New York, NY, USA., 2013.

N. Nelson and B. Holben. 2016 RV Roger Revelle Cruise Level 2.0 AOD Measurements, 2019. URL https://aeronet.gsfc.nasa.gov/new_web/cruises_new/Roger_Revelle_16_0.html.

D. Neubauer, S. Ferrachat, C. Siegenthaler-Le Drian, P. Stier, D. G. Partridge, I. Tegen, I. Bey, T. Stanelle, H. Kokkola, and U. Lohmann. The global aerosol-climate model ECHAM6.3-HAM2.3-Part 2: Cloud evaluation, aerosol radiative forcing, and climate sensitivity. Geoscientific Model Development, 12(8):3609–3639, 8 2019. ISSN 19919603. doi: 10.5194/gmd-12-3609-2019.

B. C. Nguyen, N. Mihalopoulos, J. P. Putaud, A. Gaudry, L. Gallet, W. C. Keene, and J. N. Galloway. Covariations in Oceanic Dimethyl Sulfide, its Oxidation Products and Rain Acidity at Amsterdam Island in the Southern Indian Ocean. Technical report, 1992.

. NOAA. SURFRAD Aerosol Optical Depth. Global Radiation Group, 2015. URL https://www.esrl.noaa.gov/gmd/grad/surfrad/aod/.

F. M. O'Connor, C. E. Johnson, O. Morgenstern, N. L. Abraham, P. Braesicke, M. Dalvi, G. A. Folberth, M. G. Sanderson, P. J. Telford, A. Voulgarakis, P. J. Young, G. Zeng, W. J. Collins, and J. A. Pyle. Evaluation of the new UKCA climate-composition model-Part 2: The troposphere. Geoscientific Model Development, 7(1):41–91, 1 2014. ISSN 1991959X. doi: 10.5194/gmd-7-41-2014.

S. J. Oltmans, A. S. Lefohn, J. M. Harris, I. Galbally, H. E. Scheel, G. Bodeker, E. Brunke, H. Claude, D. Tarasick, B. J. Johnson, P. Simmonds, D. Shadwick, K. Anlauf, K. Hayden, F. Schmidlin, T. Fujimoto, K. Akagi, C. Meyer, S. Nichol, J. Davies, A. Redondas, and E. Cuevas. Long-term changes in tropospheric ozone. Atmospheric Environment, 40(17):3156–3173, 6 2006. ISSN 13522310. doi: 10.1016/j.atmosenv.2006.01.029.

N. T. O'Neill, T. F. Eck, A. Smirnov, B. N. Holben, and S. Thulasiraman. Spectral discrimination of coarse and fine mode optical depth. Journal of Geophysical Research: Atmospheres, 108(17), 9 2003. ISSN 01480227. doi: 10.1029/2002jd002975.

J. Ovadnevaite, D. Ceburnis, G. Martucci, J. Bialek, C. Monahan, M. Rinaldi, M. C. Facchini, H. Berresheim, D. R. Worsnop, and C. O'Dowd. Primary marine organic aerosol: A dichotomy of low hygroscopicity and high CCN activity. Geophysical Research Letters, 38(21), 11 2011. ISSN 00948276. doi: 10.1029/2011GL048869.

J. Ovadnevaite, D. Ceburnis, M. Canagaratna, H. Berresheim, J. Bialek, G. Martucci, D. R. Worsnop, and C. O'Dowd. On the effect of wind speed on submicron sea salt

mass concentrations and source fluxes. Journal of Geophysical Research Atmospheres, 117(16), 2012. ISSN 01480227. doi: 10.1029/2011JD017379.

J. Ovadnevaite, A. Zuend, A. Laaksonen, J. Sanchez, K, G. Roberts, D. Ceburnis, S. Decesari, M. Rinaldi, N. Hodas, C. Facchini, M, H. Seinfeld, J, and C. O'Dowd. Surface tension prevails over solute effect in organic-influenced cloud droplet activation. Nature, 546:637–641, 2017. URL `https://doi-org.ezp.lib.unimelb.edu.au/10.1038/nature22806`.

C. O'Dowd, C. Facchini, M, F. Cavalli, D. Ceburnis, M. Mircea, S. Decesari, S. Fuzzi, J. Yoon, Y, and P. Putaud, J. Biogenically driven organic contribution to marine aerosol. Nature, 431:676–680, 2004. doi: 10.1038/nature02970.

M. Pham, J.-f. Miiller, G. P. Brasseur, and C. Granier. A three-dimensional study of the tropospheric sulfur cycle. Technical Report D12, 1995.

K. J. Pringle, K. S. Carslaw, D. V. Spracklen, G. M. Mann, and M. P. Chipperfield. The relationship between aerosol and cloud drop number concentrations in a global aerosol microphysics model. Technical report, 2009. URL `www.atmos-chem-phys.net/9/4131/2009/`.

P. K. Quinn and T. S. Bates. The case against climate regulation via oceanic phytoplankton sulphur emissions, 12 2011. ISSN 00280836.

P. K. Quinn, T. S. Bates, K. S. Schulz, D. J. Coffman, A. A. Frossard, L. M. Russell, W. C. Keene, and D. J. Kieber. Contribution of sea surface carbon pool to organic matter enrichment in sea spray aerosol. Nature Geoscience, 7(3):228–232, 2014. ISSN 17520908. doi: 10.1038/ngeo2092.

C. L. Reddington, K. S. Carslaw, D. V. Spracklen, M. G. Frontoso, L. Collins, J. Merikanto, A. Minikin, T. Hamburger, H. Coe, M. Kulmala, P. Aalto, H. Flentje, C. Plass-Dülmer, W. Birmili, A. Wiedensohler, B. Wehner, T. Tuch, A. Sonntag, C. D. O'Dowd, S. G. Jennings, R. Dupuy, U. Baltensperger, E. Weingartner, H. C. Hansson, P. Tunved, P. Laj, K. Sellegri, J. Boulon, J. P. Putaud, C. Gruening, E. Swietlicki, P. Roldin, J. S. Henzing, M. Moerman, N. Mihalopoulos, G. Kouvarakis, V. Ždímal, N. Zíková, A. Marinoni, P. Bonasoni, and R. Duchi. Primary versus secondary contributions to particle number concentrations in the European boundary layer. Atmospheric Chemistry and Physics, 11(23):12007–12036, 2011. ISSN 16807316. doi: 10.5194/acp-11-12007-2011.

L. E. Revell, S. Kremser, S. Hartery, M. Harvey, J. P. Mulcahy, J. Williams, O. Morgenstern, A. J. Mcdonald, V. Varma, L. Bird, and A. Schuddeboom. The sensitivity of Southern Ocean aerosols and cloud microphysics to sea spray and sulfate aerosol production in the HadGEM3-GA7.1 chemistry-climate model. Atmospheric Chemistry and Physics, 19(24):15447–15466, 12 2019. ISSN 16807324. doi: 10.5194/acp-19-15447-2019.

K. Riahi, D. P. van Vuuren, E. Kriegler, J. Edmonds, B. C. O'Neill, S. Fujimori, N. Bauer, K. Calvin, R. Dellink, O. Fricko, W. Lutz, A. Popp, J. C. Cuaresma, S. KC, M. Leimbach, L. Jiang, T. Kram, S. Rao, J. Emmerling, K. Ebi, T. Hasegawa, P. Havlik, F. Humpenöder, L. A. Da Silva, S. Smith, E. Stehfest, V. Bosetti, J. Eom, D. Gernaat, T. Masui, J. Rogelj, J. Strefler, L. Drouet, V. Krey, G. Luderer, M. Harmsen, K. Takahashi, L. Baumstark, J. C. Doelman, M. Kainuma, Z. Klimont, G. Marangoni, H. Lotze-Campen, M. Obersteiner, A. Tabeau, and M. Tavoni. The Shared Socioeconomic Pathways and their energy, land use, and greenhouse gas emissions implications: An overview. Global Environmental Change, 42:153–168, 1 2017. ISSN 09593780. doi: 10.1016/j.gloenvcha.2016.05.009.

G. J. Roelofs. Atmospheric Chemistry and Physics A GCM study of organic matter in marine aerosol and its potential contribution to cloud drop activation. Technical report, 2008. URL `www.atmos-chem-phys.net/8/709/2008/`.

W. Rolf. Neumayer (DE0060G) - CPC particle number concentration, 1999. URL `http://ebas.nilu.no/Pages/DataSetList.aspx?key=0350D1C3599341AF968739F70B4A2F43`.

D. Rosenfeld, Y. Zheng, E. Hashimshoni, M. L. Pöhlker, A. Jefferson, C. Pöhlker, X. Yu, Y. Zhu, G. Liu, Z. Yue, B. Fischman, Z. Li, D. Giguzin, T. Goren, P. Artaxo, H. M. Barbosa, U. Pöschl, and M. O. Andreae. Satellite retrieval of cloud condensation nuclei concentrations by using clouds as CCN chambers. Proceedings of the National Academy of Sciences of the United States of America, 113(21):5828–5834, 5 2016. ISSN 10916490. doi: 10.1073/pnas.1514044113.

E. S. Saltzman. Marine Aerosols. In Surface Ocean-Lower Atmosphere Processes, pages 17–35. Wiley Blackwell, 3 2013. ISBN 9781118670330. doi: 10.1029/2008GM000769.

A. M. Sayer, N. C. Hsu, C. Bettenhausen, and M. J. Jeong. Validation and uncertainty estimates for MODIS Collection 6 "deep Blue" aerosol data. Journal of Geophysical Research Atmospheres, 118(14):7864–7872, 7 2013. ISSN 21698996. doi: 10.1002/jgrd.50600.

J. Schmale and B. Holben. 2016-2017 RV Akademic Treshnikov Cruise Level 2.0 AOD Measurements, 2019. URL https://aeronet.gsfc.nasa.gov/new_web/cruises_new/Ak_Treshnikov_16_17.html.

J. Schmale, A. Baccarini, I. Thurnherr, S. Henning, A. Efraim, L. Regayre, C. Bolas, M. Hartmann, A. Welti, K. Lehtipalo, F. Aemisegger, C. Tatzelt, S. Landwehr, R. L. Modini, F. Tummon, J. S. Johnson, N. Harris, M. Schnaiter, A. Toffoli, M. Derkani, N. Bukowiecki, F. Stratmann, J. Dommen, U. B. Sperger, H. Wernli, D. Rosenfeld, M. Gysel-Beer, and K. S. Carslaw. Overview of the antarctic circumnavigation expedition: Study of preindustrial-like aerosols and their climate effects (ACE-SPACE). Bulletin of the American Meteorological Society, 100(11):2260–2283, 2019. ISSN 00030007. doi: 10.1175/BAMS-D-18-0187.1.

U. Schulzweida. CDO User Guide. Technical report, MPI for Meteorology, 2019. URL https://code.mpimet.mpg.de/projects/cdo/embedded/cdo.pdf.

H. Seinfeld, J and N. Pandis, S. Atmospheric Chemistry and Physics : From Air Pollution to Climate Change. chapter Part III: Aerosols, pages 323–657. John Wiley & Sons, Hoboken, New Jersey, 3 edition, 2016a. ISBN 9781119221173.

H. Seinfeld, J and N. Pandis, S. Atmospheric Trace Constituents. In Atmospheric Chemistry and Physics: From Air Pollution to Climate Change, chapter 2, pages 47–59. John Wiley & Sons, Hoboken, New Jersey, 3 edition, 2016b. ISBN 9781119221173.

W. R. Sessions, J. S. Reid, A. Benedetti, P. R. Colarco, A. Da Silva, S. Lu, T. Sekiyama, T. Y. Tanaka, J. M. Baldasano, S. Basart, M. E. Brooks, T. F. Eck, M. Iredell, J. A. Hansen, O. C. Jorba, H. M. Juang, P. Lynch, J. J. Morcrette, S. Moorthi, J. Mulcahy, Y. Pradhan, M. Razinger, C. B. Sampson, J. Wang, and D. L. Westphal. Development towards a global operational aerosol consensus: Basic climatological characteristics of the International Cooperative for Aerosol Prediction Multi-Model Ensemble (ICAP-MME). Atmospheric Chemistry and Physics, 15(1):335–362, 1 2015. ISSN 16807324. doi: 10.5194/acp-15-335-2015.

D. T. Shindell, J. F. Lamarque, M. Schulz, M. Flanner, C. Jiao, M. Chin, P. J. Young, Y. H. Lee, L. Rotstayn, N. Mahowald, G. Milly, G. Faluvegi, Y. Balkanski, W. J. Collins, A. J. Conley, S. Dalsoren, R. Easter, S. Ghan, L. Horowitz, X. Liu, G. Myhre, T. Nagashima, V. Naik, S. T. Rumbold, R. Skeie, K. Sudo, S. Szopa, T. Takemura, A. Voulgarakis, J. H. Yoon, and F. Lo. Radiative forcing in the ACCMIP historical and future climate simulations. Atmospheric Chemistry and Physics, 13(6):2939–2974, 3 2013. ISSN 16807324. doi: 10.5194/acp-13-2939-2013.

F. Slemr, H. Angot, A. Dommergue, O. Magand, M. Barret, A. Weigelt, R. Ebinghaus, E. G. Brunke, K. A. Pfaffhuber, G. Edwards, D. Howard, J. Powell, M. Keywood, and F. Wang. Comparison of mercury concentrations measured at several sites in the Southern Hemisphere. Atmospheric Chemistry and Physics, 15(6):3125–3133, 3 2015. ISSN 16807324. doi: 10.5194/acp-15-3125-2015.

A. Smirnov, B. N. Holben, T. F. Eck, O. Dubovik, and I. Slutsker. Cloud-Screening and Quality Control Algorithms for the AERONET Database. Remote Sensing of Environment, 73:337–349, 2000.

A. Smirnov, B. N. Holben, I. Slutsker, D. M. Giles, C. R. McClain, T. F. Eck, S. M. Sakerin, A. Macke, P. Croot, G. Zibordi, P. K. Quinn, J. Sciare, S. Kinne, M. Harvcy, T. J. Smyth, S. Piketh, T. Zielinski, A. Proshutinsky, J. I. Goes, N. B. Nelson, P. Larouche, V. F. Radionov, P. Goloub, K. Krishna Moorthy, R. Matarrese, E. J. Robertson, and F. Jourdin. Maritime Aerosol Network as a component of Aerosol Robotic Network. Journal of Geophysical Research Atmospheres, 114(6), 3 2009. ISSN 01480227. doi: 10.1029/2008JD011257.

C. J. Smith, R. J. Kramer, G. Myhre, P. M. Forster, B. J. Soden, T. Andrews, O. Boucher, G. Faluvegi, D. Fläschner, Hodnebrog, M. Kasoar, V. Kharin, A. Kirkevåg, J. F. Lamarque, J. Mülmenstädt, D. Olivié, T. Richardson, B. H. Samset, D. Shindell, P. Stier, T. Takemura, A. Voulgarakis, and D. Watson-Parris. Understanding Rapid Adjustments to Diverse Forcing Agents. Geophysical Research Letters, 45(21):023–12, 11 2018. ISSN 19448007. doi: 10.1029/2018GL079826.

A. Sockol and J. Small Griswold. Intercomparison between CMIP5 model and MODIS satellite-retrieved data of aerosol optical depth, cloud fraction, and cloud-aerosol interactions. Earth and Space Science, 4:485–505, 2017.

M. Spada, O. Jorba, C. Pérez García-Pando, Z. Janjic, and M. Baldasano, J. On the evaluation of global sea-salt aerosol models at coastal/orographic sites. Atmospheric Environment, 101:41–48, 2015. doi: 10.1016/j.atmosenv.2014.11.019.

D. V. Spracklen, K. S. Carslaw, M. Kulmala, V.-M. Kerminen, G. W. Mann, and S.-L. Sihto. The contribution of boundary layer nucleation events to total particle concentrations on regional and global scales. Technical report, 2006. URL `www.atmos-chem-phys.net/6/5631/2006/`.

D. V. Spracklen, S. R. Arnold, J. Sciare, K. S. Carslaw, and C. Pio. Globally significant oceanic source of organic carbon aerosol. Geophysical Research Letters, 35(12), 6 2008. ISSN 00948276. doi: 10.1029/2008GL033359.

D. V. Spracklen, K. S. Carslaw, J. Merikanto, G. W. Mann, C. L. Reddington, S. Pickering, J. A. Ogren, E. Andrews, U. Baltensperger, E. Weingartner, M. Boy, M. Kulmala, L. Laakso, H. Lihavainen, N. Kivekäs, M. Komppula, N. Mihalopoulos, G. Kouvarakis, S. G. Jennings, C. O'Dowd, W. Birmili, A. Wiedensohler, R. Weller, J. Gras, P. Laj, K. Sellegri, B. Bonn, R. Krejci, A. Laaksonen, A. Hamed, A. Minikin, R. M. Harrison, R. Talbot, and J. Sun. Explaining global surface aerosol number concentrations in terms of primary emissions and particle formation. Atmospheric Chemistry and Physics, 10 (10):4775–4793, 2010. ISSN 16807316. doi: 10.5194/acp-10-4775-2010.

D. V. Spracklen, K. S. Carslaw, U. Pöschl, A. Rap, and P. M. Forster. Global cloud condensation nuclei influenced by carbonaceous combustion aerosol, 2011. ISSN 16807316.

P. Stier, J. Feichter, and S. Kinne. The aerosol-climate model ECHAM5-HAM. Atmospheric Chemistry and Physics, 5:1125–1156, 2005. doi: 10.5194/acp-5-1125-2005.

F. Stratmann and M. Gysel. WP3-NA3: In-situ chemical, physical and optical properties of aerosols Deliverable D3.11: Standardized protocol for CCN measurements. Technical report, ACTRIS, 2015. URL `www.actris.net/Portals/97/Publications/quality%20standards/aerosol%20insitu/WP3_D3.13_M24_CCNC_SOP_v130514.pdf`.

S. Swart, S. T. Gille, B. Delille, S. Josey, M. Mazloff, L. Newman, A. F. Thompson, J. Thomson, B. Ward, M. D. Du Plessis, E. C. Kent, J. Girton, L. Gregor, H. Petra, P. Hyder, L. P. Pezzi, R. B. De Souza, V. Tamsitt, R. A. Weller, and C. J. Zappa. Constraining Southern ocean air-sea-ice fluxes through enhanced observations, 2019. ISSN 22967745.

C. Tatzelt, S. Henning, F. Tummon, M. Hartmann, A. Baccarini, A. Welti, L. Katrianne, and J. Schmale. Cloud Condensation Nuclei number concentrations over the Southern Ocean during the austral summer of 2016/2017, 2019.

E. Taylor, K, D. Williamson, and W. Zweirs, F. Program for Climate Model Diagnosis and Intercomparison AMIP Sea Surface Temperature and Sea Ice Concentration Boundary Conditions, 2015. URL `http://www-pcmdi.llnl.gov/projects/amip/AMIP2EXPDSN/BCS/index.php`.

I. Tegen, D. Neubauer, S. Ferrachat, C. S. L. Drian, I. Bey, N. Schutgens, P. Stier, D. Watson-Parris, T. Stanelle, H. Schmidt, S. Rast, H. Kokkola, M. Schultz, S. Schroeder, N. Daskalakis, S. Barthel, B. Heinold, and U. Lohmann. The global aerosol-climate model echam6.3-ham2.3 -Part 1: Aerosol evaluation. Geoscientific Model Development, 12(4):1643–1677, 4 2019. ISSN 19919603. doi: 10.5194/gmd-12-1643-2019.

P. Telford, P. Braesicke, O. Morgenstern, and J. Pyle. Technical Note: Description and assessment of a nudged version of the new dynamics Unified Model. Atmospheric Chemistry and Physics, 8:1701–1712, 2008.

C. Textor, M. Schulz, S. Guibert, S. Kinne, Y. Balkanski, S. Bauer, T. Berntsen, T. Berglen, O. Boucher, M. Chin, F. Dentener, T. Diehl, R. Easter, H. Feichter, D. Fillmore, S. Ghan, P. Ginoux, S. Gong, A. Grini, J. Hendricks, L. Horowitz, P. Huang, I. Isaksen, T. Iversen, S. Kloster, D. Koch, A. Kirkevåg, J. E. Kristjansson, M. Krol, A. Lauer, J. F. Lamarque, and X. Liu. Analysis and quantification of the diversities of aerosol life cycles within AeroCom. Atmos. Chem. Phys. Atmospheric Chemistry and Physics, 6:1777–1813, 2006. URL `www.atmos-chem-phys.net/6/1777/2006/`.

T. J. Thorsen and Q. Fu. CALIPSO-inferred aerosol direct radiative effects: Bias estimates using ground-based raman lidars. Journal of Geophysical Research, 120(12):209–220, 2015.

K. Tsigaridis, D. Koch, and S. Menon. Uncertainties and importance of sea spray composition on aerosol direct and indirect effects. Journal of Geophysical Research Atmospheres, 118(1):220–235, 1 2013. ISSN 21698996. doi: 10.1029/2012JD018165.

S. T. Turnock, G. W. Mann, M. T. Woodhouse, M. Dalvi, F. M. O'Connor, K. S. Carslaw, and D. V. Spracklen. The Impact of Changes in Cloud Water pH on Aerosol Radiative Forcing. Geophysical Research Letters, 46(7):4039–4048, 4 2019. ISSN 19448007. doi: 10.1029/2019GL082067.

S. Twomey. Pollution and the planetary albedo. Atmospheric Environment (1967), 1974. ISSN 00046981. doi: 10.1016/0004-6981(74)90004-3.

UKCA. Chemistry of the Stratosphere and Troposphere, 2011. URL `https://www.ukca.ac.uk/wiki/index.php/Chemistry_of_the_Stratosphere_and_Troposphere`.

S. M. Vallina, R. Simó, S. Gassó, C. de Boyer-Montégut, E. del Río, E. Jurado, and J. Dachs. Analysis of a potential solar radiation dose-dimethylsulfide-cloud condensation nuclei link from globally mapped seasonal correlations. Global Biogeochemical Cycles, 21(2), 6 2007. ISSN 08866236. doi: 10.1029/2006GB002787.

H. Vehkamäki, M. Kulmala, I. Napari, K. E. Lehtinen, C. Timmreck, M. Noppel, and A. Laaksonen. An improved parameterization for sulfuric acid-water nucleation rates for tropospheric and stratospheric conditions. Journal of Geophysical Research Atmospheres, 107(22):3–1, 2002. ISSN 01480227. doi: 10.1029/2002JD002184.

A. Veira. Dakar's urban pollution plume: A SAMUM-II case study on the plume structure and the influence of urban emissions on dust physico-chemical and radiative properties. Technical report, 2011.

J. Vergara-Temprado, K. Miltenberger, A, K. Furtado, D. Grosvenor, J. Shipway, B, A. Hill, A, M. Wilkinson, J, R. Field, P, J. Murray, B, and S. Carslaw, K. Strong control of Southern Ocean cloud reflectivity by ice-nucleating particles. 115(11):2687–2692, 2018. doi: 10.5518/317.

E. Vignati, M. C. Facchini, M. Rinaldi, C. Scannell, D. Ceburnis, J. Sciare, M. Kanakidou, S. Myriokefalitakis, F. Dentener, and C. D. O'Dowd. Global scale emission and distribution of sea-spray aerosol: Sea-salt and organic enrichment. Atmospheric Environment, 44(5):670–677, 2 2010. ISSN 13522310. doi: 10.1016/j.atmosenv.2009.11.013.

R. Vladimir and B. Holben. 2015-2016 RV Akademic Fedorov Cruise Level 2.0 AOD Measurements, 2019. URL `https://aeronet.gsfc.nasa.gov/new_web/cruises_new/Ak_Fedorov_15_16.html`.

D. Walters, A. J. Baran, I. Boutle, M. Brooks, P. Earnshaw, J. Edwards, K. Furtado, P. Hill, A. Lock, J. Manners, C. Morcrette, J. Mulcahy, C. Sanchez, C. Smith, R. Stratton, W. Tennant, L. Tomassini, K. Van Weverberg, S. Vosper, M. Willett, J. Browse, A. Bushell, K. Carslaw, M. Dalvi, R. Essery, N. Gedney, S. Hardiman, B. Johnson, C. Johnson, A. Jones, C. Jones, G. Mann, S. Milton, H. Rumbold, A. Sellar, M. Ujiie, M. Whitall, K. Williams, and M. Zerroukat. The Met Office Unified Model Global Atmosphere 7.0/7.1 and JULES Global Land 7.0 configurations. Geoscientific Model Development, 12(5):1909–1963, 5 2019. ISSN 19919603. doi: 10.5194/gmd-12-1909-2019.

Y. Wang. Aerosol-Cloud Interactions from Urban, Regional, to Global Scales. PhD thesis, Texas A&M University, 2015.

T. Watson. Aerosol Chemical Speciation Monitor (ACSM) Instrument Handbook. Technical report, U.S Department of Energy, Office of Science. ARM Climate Research Facility, 2017.

M. Werner, , M. Kryza, , K. Walaszek, , M. Vieno, , and A. J. Dore. EMEP4PL and WRF-Chem—Evaluation of the Modelling Results. In C. Mensink, editor, Air Pollution Modeling and its Application XXV, pages 117–122. Springer International Publishing, 2018.

D. M. Westervelt, R. H. Moore, A. Nenes, and P. J. Adams. Effect of primary organic sea spray emissions on cloud condensation nuclei concentrations. Atmospheric Chemistry and Physics, 12(1):89–101, 2012. ISSN 16807316. doi: 10.5194/acp-12-89-2012.

C. J. Willmott. Some Comments on the Evaluation of Model Performance. Technical report, 1982. URL http://journals.ametsoc.org/bams/article-pdf/63/11/1309/3719364/1520-0477.

D. R. Wilson, A. C. Bushell, A. M. Kerr-Munslow, J. D. Price, and C. J. Morcrette. PC2: A prognostic cloud fraction and condensation scheme. I: Scheme description. Quarterly Journal of the Royal Meteorological Society, 134(637):2093–2107, 2008. ISSN 00359009. doi: 10.1002/qj.333.

S. Wilson. Personal Communication, 20/08/2019, 2019.

S. Wilson. Personal communication, 27/08/2020. 2020.

D. M. Winker, J. L. Tackett, B. J. Getzewich, Z. Liu, M. A. Vaughan, and R. R. Rogers. Geoscientific Instrumentation Methods and Data Systems The global 3-D distribution of tropospheric aerosols as characterized by CALIOP. Atmospheric Chemistry and Physics, 13:3345–3361, 2013.

M. Witek, D. Diner, and M. Garay. Satellite assessment of sea spray aerosol productivity: Southern Ocean case study. Journal of Geophysical Research: Atmospheres, 121:872–894, 2016. doi: 10.1002/2015JD023726.

M. L. Witek, M. J. Garay, D. J. Diner, and A. Smirnov. Aerosol optical depths over oceans: A view from MISR retrievals and collocated MAN and AERONET in situ observations. Journal of Geophysical Research Atmospheres, 118(12):620–633, 2013.

M. Woodhouse, L. Cravigan, M. Harvey, S. Lawson, T. Bell, Z. Ristovski, S. Fiddes, S. Arnold, and H. Walker. Simulating marine organic contributions to aerosol. in prep, 2020.

M. T. Woodhouse, K. S. Carslaw, G. W. Mann, S. M. Vallina, M. Vogt, P. R. Halloran, and O. Boucher. Low sensitivity of cloud condensation nuclei to changes in the sea-air flux of dimethyl-sulphide. Atmospheric Chemistry and Physics, 10(16):7545–7559, 2010. ISSN 16807316. doi: 10.5194/acp-10-7545-2010.

S. Woodward. Hadley Centre Technical Note 87, Mineral Dust in HadGEM2. Technical report, Met Office, Exeter, 2011.

World Meteorological Organization, Global Atmosphere Watch, World Weather Research Programme, World Climate Research Programme, and European Cooperation in the Field of Scientific and Technical Research. Coupled Chemistry-Meteorology/Climate Modelling (CCMM): Status and Relevance for Numerical Weather Prediction, Atmospheric Pollution and Climate Research. GAW Report No. 226, WCRP Report No.9/2016. Technical report, World Meteorological Organisation, Geneva, Switzerland, 2015. URL https://www.wcrp-climate.org/documents/GAW_226_10_May.pdf.

S. Yu, B. Eder, R. Dennis, S.-H. Chu, and S. E. Schwartz. New unbiased symmetric metrics for evaluation of air quality models. Atmospheric Science Letters, 7(1):26–34, 1 2006. ISSN 1530-261X. doi: 10.1002/asl.125.